Tropical waves and rainfall over Africa: Variability, mechanisms and potential for forecasting

Zur Erlangung des akademischen Grades eines

DOKTORS DER NATURWISSENSCHAFTEN (Dr. rer. nat)

von der KIT-Fakultät für Physik des Karlsruher Instituts für Technologie (KIT)

angenommene Dissertation

von

ANDREAS SCHLÜTER (M. Sc.)

Referent:
Prof. Dr. Peter Knippertz

Korreferent:
Prof. Dr. Andreas H. Fink

Tag der mündlichen Prüfung:
26.04.2019

Karlsruhe Institute of Technology

Who gave a course to violent showers,
*   or a way for noisy thunder:*
That it should rain on the earth without man,
*   in the wilderness, where no mortal dwelleth:*
That it should fill the desert and desolate land,
*   and should bring forth green grass?*
Who is the father of rain?
*   or who begot the drops of dew?*

— Book of Job

Abstract

Excessive rains or prolonged drought can have severe impacts on the economy, agriculture, water resources, spread of diseases and ecosystems in many African countries. As current global numerical weather prediction systems fail to deliver accurate rainfall forecasts over tropical Africa, novel forecasting strategies are needed. Tropical waves are known to modulate precipitation over this region on timescales of a few days to several weeks. The aim of this dissertation is to quantify the influence of all major waves on rainfall variability over Africa, to investigate the involved mechanisms and, to test their potential for forecasting rainfall, with a focus on northern tropical Africa during the extended monsoon season.

Despite the importance of rainfall variability for vulnerable societies in tropical Africa, the relative influence of tropical waves for this region is largely unknown. This thesis closes this gap and presents the first systematic comparison of the impact of six wave types on precipitation over northern tropical Africa during the transition and full monsoon seasons, using two satellite products and a dense rain gauge network. Composites of rainfall anomalies based on different datasets show comparable modulation intensities in the West Sahel and at the Guinea Coast, varying from less than 2 to above $7\,\mathrm{mm\,d^{-1}}$ depending on the wave type. Tropical disturbances (TDs, including African Easterly Waves, AEWs) and Kelvin waves dominate the 3-hourly to daily timescale and explain 10–30 % of precipitation variability locally. On longer timescales (7—20 days), only the Madden-Julian Oscillation (MJO) and Equatorial Rossby (ER) waves remain as modulating factors and explain up to one third of rainfall variability. Eastward inertio-gravity (EIG) waves and mixed Rossby-gravity (MRG) waves are comparatively unimportant. An analysis of wave superposition shows that low-frequency waves (MJO, ER) in their wet phase amplify the activity of high-frequency waves (TD, MRG) and suppress them in the dry phase.

Furthermore, this dissertation gives the first systematic comparison of the dynamics and thermodynamics associated with tropical waves affecting rainfall variability over northern tropical Africa: Reanalysis and radiosonde data were analyzed for the period 1981—2013 based on space-time filtering of outgoing longwave radiation. The identified circulation patterns are largely consistent with equatorial shallow water theory. The slow modes, MJO and ER, mainly impact precipitable water, whereas the faster TDs, Kelvin waves, and MRG waves primarily modulate moisture convergence. Monsoonal inflow intensifies during wet phases of the MJO, ER, and MRG waves, associated with a northward shift of the intertropical discontinuity for MJO and ER waves. This study reveals that MRG waves over Africa have a distinct dynamical structure that differs significantly from AEWs. During passages of vertically tilted imbalanced wave modes, such as MJO, TDs, Kelvin, and partly MRG waves, increased vertical wind shear and improved conditions for up- and downdrafts facilitate the organization of mesoscale convective systems. The balanced ER waves are not tilted and rainfall is triggered by large-scale moistening and stratiform lifting. The MJO and ER waves interact with intraseasonal variations of the Indian monsoon and extratropical Rossby wave trains. The latter causes a trough over the Atlas Mountains associated with a tropical plume and rainfall over the Sahara. The presented results unveil which dynamical processes need to be modeled realistically to represent the coupling between tropical waves and rainfall in northern tropical Africa.

The potential of tropical waves as predictors for African rainfall was tested. The spatio-temporal correlation patterns of tropical waves highlight their potential for synoptic rainfall forecasting. The observed spatio-temporal properties agree with values predicted by shallow-water theory, with the exception of MRG and EIG waves, which have a strong phase dispersion at low wavenumbers. Unfiltered precipitation fields show correlations patterns that are physically explainable by tropical waves and other atmospheric phenomena such as the position of the tropical rainbelt. These correlations serve as predictors in a logistic regression model. It was shown that this model successfully predicts rainfall occurrence over Africa with a lead time of one day. The statistical model is calibrated and outperforms the climatological forecast and current numerical weather prediction models by about 20 %. The fact that tropical waves explain large portions of synoptic to intraseasonal rainfall variability in almost the entire tropics emphasize the potential of the proposed statistical model. This PhD thesis has laid the foundation to exploit this potential and to significantly improve short-term weather forecasts in Africa and throughout the tropics.

Kurzfassung

Übermäßige Regenfälle oder anhaltende Dürre können in vielen afrikanischen Ländern schwerwiegende Auswirkungen auf Wirtschaft, Landwirtschaft, Wasserressourcen, Ausbreitung von Krankheiten und Ökosystemen haben. Da die derzeitigen globalen numerischen Wettervorhersagesysteme keine genauen Niederschlagsvorhersagen über tropischem Afrika liefern, sind neue Vorhersagestrategien erforderlich. Tropische Wellen sind dafür bekannt, den Niederschlag über dieser Region auf Zeitskalen von einigen Tagen bis mehreren Wochen zu modulieren. Das Ziel dieser Arbeit ist es, den Einfluss aller wesentlichen Wellen auf die Niederschlagsvariabilität über Afrika zu quantifizieren, die beteiligten Mechanismen zu untersuchen und ihr Potenzial für die Niederschlagsvorhersage zu testen. Der Schwerpunkt dieser Arbeit liegt auf dem nördlichen tropischen Afrika während der verlängerten Monsunzeit.

Trotz der Bedeutung von Niederschlagsvariabilität für vulnerable Gesellschaften im tropischen Afrika ist der relative Einfluss der tropischen Wellen auf diese Region weitestgehend unbekannt. Diese Arbeit schließt diese Lücke und präsentiert den ersten systematischen Vergleich der Auswirkungen von sechs Wellentypen auf den Niederschlag über dem nördlichen tropischen Afrika während der Übergangs- und der vollen Monsunzeit in zwei Satellitenprodukten und einem dichten Regenmessernetzwerk. Komposite von Niederschlagsanomalien, die auf diesen verschiedenen Datensätzen basieren, zeigen vergleichbare Modulationsintensitäten im westlichen Sahel und an der Guinea-Küste, die je nach Wellentyp von weniger als 2 bis über $7\,\mathrm{mm\,d^{-1}}$ variieren. *Tropical disturbances* (TDs, inklusive *African Easterly Waves*, AEWs) und Kelvinwellen dominieren die 3-Stunden- bis Tageszeitskala und erklären lokal 10–30 % der Niederschlagsvariabilität. Bei längeren Zeiträumen (7–20 Tage) verbleiben nur die *Madden-Julian Oscillation* (MJO) und *Equatorial Rossby* (ER) Wellen als modulierende Faktoren erhalten und erklären bis zu einem Drittel der Niederschlagsvariabilität. *Eastward inertio-*

gravity (EIG) und *mixed Rossby-gravity* (MRG) sind vergleichsweise unbedeutend. Eine Analyse der Wellenüberlagerung zeigt, dass niederfrequente Wellen (MJO, ER) in ihrer feuchten Phase die Aktivität von hochfrequenten Wellen (TD, MRG) verstärken und in der trockenen Phase unterdrücken.

Desweiteren liefert diese Dissertation den ersten systematischen Vergleich der Dynamik und Thermodynamik der tropischen Wellen, die Niederschlagsvariabilität über dem nördlichen tropischen Afrika beeinflussen: Basierend auf der raum-zeitlichen Filterung von ausgehender langwelliger Strahlung wurden Reanalyse- und Radiosondendaten für den Zeitraum 1981–2013 analysiert. Die identifizierten Zirkulationsmuster stimmen weitgehend mit der äquatorialen Flachwassertheorie überein. Die langsamen Moden, MJO und ER-Welle, wirken sich hauptsächlich auf das ausfällbare Niederschlagswasser aus, während die schnelleren TDs, Kelvinwellen und MRG-Wellen in erster Linie die Feuchtekonvergenz modulieren. Die Monsunströmung wird während der feuchten Phasen der MJO-, ER- und MRG-Wellen verstärkt, verbunden mit einer nordwärts Verschiebung der intertropischen Diskontinuität bei MJO und ER Wellen. Diese Studie zeigt, dass MRG-Wellen über Afrika eine eindeutige dynamische Struktur haben, die sich deutlich von AEWs unterscheidet. Während der Passage von den vertikal geneigten, unbalancierten Wellenmoden MJO, TDs, Kelvin und teilweise MRG-Wellen erleichtern erhöhte vertikale Windscherung und verbesserte Bedingungen für Auf- und Abwinde die Organisation mesoskaliger konvektiver Systeme. Die balancierten ER-Wellen sind vertikal nicht geneigt und der Niederschlag wird durch großflächige Anfeuchtung und stratiforme Hebung ausgelöst. Die MJO und ER-Wellen interagieren mit der intrasäsonalen Variabilität des indischen Monsuns und extratropischen Rossby-Wellenzügen. Letztere erzeugen einen Trog über dem Atlasgebirge, der verbunden mit einer *tropical plume* und Niederschlägen über der Sahara ist. Die vorgestellten Ergebnisse zeigen, welche dynamischen Prozesse korrekt modelliert werden müssen, um die Kopplung zwischen tropischen Wellen und Regenfällen im nördlichen tropischen Afrika realistisch zu repräsentieren.

Tropischer Wellen wurden auf ihr Potenzial als Prädiktoren für Niederschlag über Afrika getestet. Die raum-zeitlichen Korrelationsmuster tropischer Wellen unterstreichen ihr Potenzial für die synoptische Niederschlagsvorhersage. Die beobachteten raum-zeitlichen Eigenschaften stimmen mit den von der Flach-wassertheorie vorhergesagten Werten überein; mit Ausnahme von MRG- und EIG-Wellen, die eine starke Phasendispersion bei niedrigen Wellenzahlen aufweisen. Ungefilterte Niederschlagsfelder zeigen Korrelationsmuster, die durch tropische

Wellen und andere atmosphärische Phänomene wie die Position des tropischen Regenbands physikalisch erklärbar sind. Diese Korrelationen dienen als Prädiktoren in einem logistischen Regressionsmodell. Es zeigte sich, dass dieses Modell erfolgreich Niederschlagsereignisse über Afrika mit einer Vorhersagezeit von einem Tag prognostiziert. Das statistische Modell ist kalibriert und übertrifft die klimatologische Vorhersage sowie aktuelle numerischen Wettervorhersagemodelle um etwa 20 %. Die Tatsache, dass tropische Wellen große Teile der synoptischen bis intrasäsonalen Niederschlagsvariabilität in fast den ganzen Tropen erklären, unterstreicht das Potenzial des vorgeschlagenen statistischen Modells. Diese Dissertation hat den Grundstein gelegt, um dieses Potenzial zu nutzen und kurzfristige Wettervorhersagen in Afrika und den Tropen deutlich zu verbessern.

Preface

The PhD candidate confirms that the research presented in this thesis contains significant scientific contributions by himself. This thesis reuses material from the following publications:

Schlueter, A., A. H. Fink, P. Knippertz, and P. Vogel, 2019a: A Systematic Comparison of Tropical Waves over Northern Africa. Part I: Influence on Rainfall. *Journal of Climate*, **32 (5)**, 1501–1523, doi: 10.1175/JCLI-D-18-0173.1

Schlueter, A., A. H. Fink, and P. Knippertz, 2019b: A Systematic Comparison of Tropical Waves over Northern Africa. Part II: Dynamics and Thermodynamics. *Journal of Climate*, doi: 10.1175/JCLI-D-18-0651.1

Schlueter, A., 2019: Synoptic to intraseasonal variability of African rainfall (under review). *Oxford Research Encyclopedia of Climate Science: Climate of Africa*

The abstract and Chapters 1, 3, 4, 5, 8, 9, and the appendix A.1 reuse material from Schlueter et al. (2019a). © 2019, American Meteorological Society. Used with permission. Moreover, the abstract and Chapters 1, 3, 4, 6, 8, 9, and the appendix A.2 reuse material from Schlueter et al. (2019b). © 2019, American Meteorological Society. Used with permission. Furthermore, reused material in the abstract, Chapter 1, 2, 8, and 9 include a submitted draft of a chapter that is under review for publication by Oxford University Press in the forthcoming book "Oxford Research Encyclopedia of Climate Science" edited by Hans von Storch due for publication in 2019. Reproduced by permission of Oxford University Press, `http://climatescience.oxfordre.com/`.

The research leading to these results has been accomplished within project C2 "Prediction of wet and dry periods of the West African Monsoon" of the Transregional Collaborative Research Center SFB / TRR 165 "Waves to Weather"

funded by the German Science Foundation (DFG). The research proposal of this project was written by Peter Knippertz, Andreas H. Fink, and Tilmann Gneiting. Analyses in Schlueter et al. (2019a) and Schlueter et al. (2019b), were solely performed by the candidate, who also wrote the text with advice from Peter Knippertz and Andreas H. Fink and comments from all co-authors during the manuscript preparation. Section 7.3 is based on joint work in the C2 Project with Peter Vogel, Manuel Klar, Tilmann Gneiting, Peter Knippertz, and Andreas H. Fink. The mathematical design of the statistical model presented in this section was developed in a leading role by Peter Vogel, Manuel Klar, and Tilmann Gneiting.

The candidate confirms that appropriate credit has been given within the thesis where reference has been made to the work of others. This copy has been supplied on the understanding that this is copyright material and that no quotation from the thesis may be published without proper acknowledgment.

Contents

Acronyms

AEJ . . . . . . African Easterly Jet

AEW . . . . . African Easterly Wave

AMMA . . . . African Monsoon Multidisciplinary Analysis

AO . . . . . . Arctic Oscillation

BSS . . . . . . Brier Skill Score

CAPE . . . . . Convective Available Potential Energy

CCEW . . . . Convectively coupled equatorial wave

CHIRPS . . . Climate Hazards Group InfraRed Precipitation with Station data

CIN . . . . . . Convective inhibition

ECMWF . . . European Centre for Medium-Range Weather Forecasts

EIG wave . . . Eastward inertio-gravity wave

EL . . . . Equilibrium level

ENSO . . . . . El-Niño/Southern Oscillation

EPC . . . . . . Ensemble probabilistic climatology

EPS . . . . . . Ensemble prediction system

ER wave . . . Equatorial Rossby wave

EWS . . . . . Early warning system

GPCP . . . . . Global Precipitation Climatology Project

GPM . . . . . Global Precipitation Measurement

IG wave . . . . Inertio-gravity wave

IGRA . . . . . Integrated Global Radiosonde Archive

ITD . . . . . . Inter-tropical discontinuity

KASS-D . . . Karlsruhe African Surface Station Database

KDE . . . . . . Kernel density estimation

LFC . . . . . . Level of free convection

MCS . . . . . Mesoscale convective system

MJO . . . . . . Madden-Julian Oscillation

MRG wave . . Mixed Rossby-gravity wave

NAO   . . . . . North Atlantic Oscillation

NOAA   . . . . National Oceanic and Atmospheric Administration

NWP   . . . . . Numerical weather prediction

OLR . . . . . . Outgoing longwave radiation

PDF . . . . . . Probability density functions

PNA . . . . . . Pacific/North American pattern

PV . . . . Potential vorticity

PW   . . . . . . Precipitable water

QBZD . . . . . Quasi-biweekly zonal dipole

RH   . . . . . . Relative humidity

RMM   . . . . . Real-time Multivariate MJO index

SHL . . . . . . Saharan heat low

TD . . . . Tropical disturbance

TRMM   . . . . Tropical Rainfall Measuring Mission

TTT . . . . . . Tropical temperate trough

WAM   . . . . . West African monsoon

Wave-CISK   . Wave conditional instability of the second kind

WIG wave   . . Westward Inertio-gravity wave

WISHE   . . . . Wind induced surface heat exchange

1 | Introduction

Africa, the second largest and second most populated continent of the our planet (CIA, 2019), harbors a wide variety of climates. It is home to the world-largest non-polar desert, the Sahara (Goudie and Seely, 2011), and the second largest rain forest of the world in Central and West Africa (Malhi et al., 2013). The mean annual rainfall ranges from less than $5\,\mathrm{mm\,yr^{-1}}$ in the eastern Saharan desert (Kelley, 2014) to more than $10\,000\,\mathrm{mm\,yr^{-1}}$ at the foot of Mount Cameroon (Houérou, 2009). In the course of the year, different zones experience periods, where rainfall is enhanced or reduced relative to the mean seasonal climatology. These variations, typically, occur on the synoptic timescale of approximately 2 to 10 days and the intraseasonal timescale, which refers to variations of about 10 to 90 days (Janicot et al., 2011; Lau and Waliser, 2012). These deviations from climatology can imply excessive rains or prolonged droughts, which, in consequence, often result in natural disasters.

Across Africa, societies are impacted by rainfall variability in various ways. In Sub-Saharan Africa, 93 % of agricultural fields are rainfed (FAO, 2016a). Thus, the agricultural sector, which employs 55 % of the work force (ILO, 2019) and contributes 17 % of the gross domestic product (FAO, 2016b), is highly weather-dependent. More than 40 % of the population live below the international poverty line (World Bank, 2019) and 23 % are undernourished (FAO, 2017). Therefore, drought-induced famines regularly lead to fatalities of thousands of people across Africa (Kadomura, 2005; Taye et al., 2010), most notably of infants (Kudamatsu et al., 2012). Moreover, wet periods favor the spread of vector-borne diseases such as malaria (Zhou et al., 2004; Kudamatsu et al., 2012), Rift Valley fever (Caminade et al., 2011), and plague (Moore et al., 2012), whereas waterborne diarrhea prevalence is higher during dry periods (Bandyopadhyay et al., 2012). Besides the influence on human society, rainfall variability has stabilizing and destabilizing effects on ecosystems. Rainfall fluctuations are a necessary component of ecosystems as they increase biodiversity through "noise-induced stability", which is necessary for the existence of niche species (Borgogno et al., 2007). On the other hand, prolonged drought facilitates forest fires (Littell et al., 2016) and deforestation

(Staal et al., 2015), and can thus lead to a loss of biodiversity (Tilman and El Haddi, 1992; Desbureaux and Damania, 2018).

Even though rainfall over Africa is rather stochastic by nature, predictability exists on different temporal and spatial scales. Like many physical systems, the atmosphere allows the existence of inherent wave modes (Laplace, several works between 1778 – 1825, reprinted Laplace 2017). As fundamental phenomena observed in nature, these waves result from a disturbance from a state of equilibrium and the restoring inertial, gravity and pressure gradient forces (Hough, 1897, 1898). In the tropics, several different wave types are preferred natural oscillations of the atmosphere, which stand out against the background noise of tropical rainfall (Wheeler and Kiladis, 1999). These waves have periods of less than a day to several weeks and spatial scales of less than hundred to several thousand kilometers. Furthermore, each wave type is associated with a specific horizontal circulation pattern (e.g. Matsuno, 1966). These waves can couple with deep convection and subsequently modulate rainfall on the synoptic to subseasonal timescale throughout the tropics.

Although rainfall variability is an integral part of the climate system and despite its great importance for African societies and ecosystems, major operational global weather prediction models still struggle to deliver skillful short-range precipitation forecasts over most of tropical Africa (Vogel et al., 2018; Vogel, 2019). This corroborates the need for an improved understanding of rainfall variability over Africa and the underlying processes. This study places a geographical focus on northern tropical Africa (5°–15°N). As tropical waves are the main driver of rainfall variability over tropical Africa, it raises the question to what extent they can be used as predictors. The **overarching research aim** of this dissertation therefore is:

- to quantify the influence of tropical waves on rainfall variability over Africa,
- to investigate the involved mechanisms and,
- to test their potential for forecasting rainfall.

The thesis provides, first, a comprehensive review of existing literature on synoptic to intraseasonal modes of rainfall variability over Africa and the challenges in rainfall prediction in Chapter 2. Then, the research questions that need to be answered to achieve the overarching research aim are elaborated in Chapter 3. After the description of the employed data and methods in Chapter 4, the influence of tropical waves on rainfall variability are analyzed in Chapter 5. Chapter 6 shows the involved mechanisms and in Chapter 7 the potential of tropical waves

for forecasting rainfall over Africa is investigated. The conclusions in Chapter 8 and an outlook in Chapter 9 complete this study.

2 | Literature review

This chapter reviews individual synoptic and intraseasonal atmospheric modes, which govern rainfall variability over Africa. Section 2.1 outlines a brief history of research on rainfall variability and discuss first observations made during colonial times as well as describe the development of theoretical understanding of rainfall variability in the tropics during the second half of the 20th century. Section 2.2 presents observational evidences of several synoptic to intraseasonal modes of variability affecting African rainfall. Finally, Section 2.3 discusses the predictability of African rainfall variability and highlights some challenges involved in rainfall forecasting. For additional background information on the local climate of African regions, which can not be discussed here in detail, the reader is referred to review articles describing the climate of the Mediterranean Region (García-Herrera and Barriopedro, 2018), the Sahel and West Africa (Nicholson, 2018), western and central equatorial Africa (Dezfuli, 2017), eastern Africa (Camberlin, 2018), and southern Africa (Reason, 2017).

2.1 Historical review

Long before the rise of modern science, local communities in Africa have experienced rainfall variability and collected their repeated observations in oral traditions (Warren, 1991). In order to master their everyday activities, hunter-gatherers, farmers, or pastoralists depended on their traditional knowledge about weather and climate. Across Africa, several predictors were used by these communities as signs for imminent rains, dry spells, for early or late onset and cessation dates of the rainy seasons. Example of such indicators range from insects, birds, mammals, plants, over atmospheric variables such as winds, air temperature, to the appearance of sun, moon, and stars (Roncoli et al., 2002; Sanni et al., 2012; Kijazi et al., 2013; Shoko and Shoko, 2013; Jiri et al., 2015; Ebhuoma and Simatele, 2017). As the afore-cited studies reveal, indigenous knowledge on rainfall
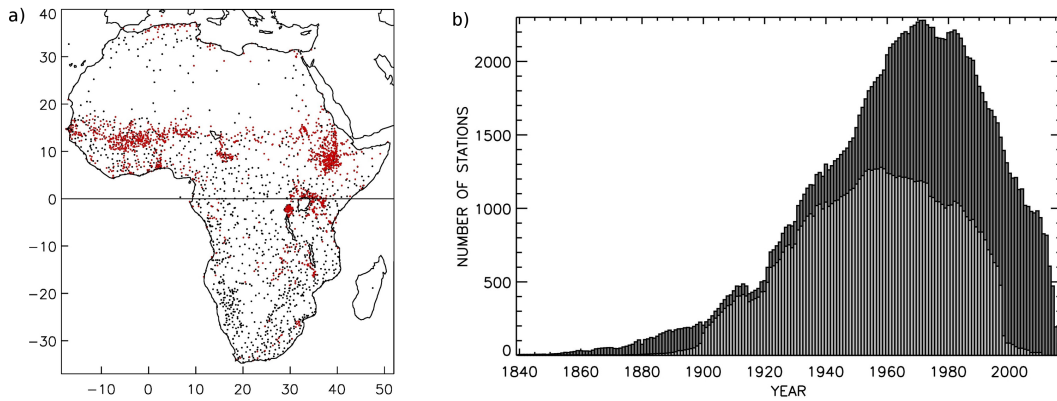
Figure 2.1: (a) Map of all rainfall stations available between 1840 and 2014 and (b) temporal evolution of reporting stations per year in two comprehensive datasets (dark and light gray). Reprinted from Nicholson et al. (2018) with permission. © 2018 Elsevier CC BY NC ND 4.0 ⓒⓘⓢⓔ.

variability continues to exist across Africa and local communities still rely on it for their daily life.

The rainfall variability, which has been observed by African communities since millennia, follows regular wave-like patterns. Scientific advances in the 19th and 20th century led to the current understanding of African rainfall variability. In the following, an overview of research on African rainfall variability during colonial times is provided. Then, this section reviews fundamental theoretical developments in the research of Rossby waves, which are the dominant wave type in the extratropics, and equatorial waves and presents the major intraseasonal mode, the Madden-Julian Oscillation (MJO). Finally, this section concludes with a brief discussion of the most important filtering methods used for tropical wave modes.

2.1.1 Research during colonial times

With ongoing colonization of many African countries and the development of modern rain gauges, first systematic weather observations of rainfall over Africa began to be recorded in the 1840s (Nicholson et al., 2012, 2018). During the second half of the 19th century, relatively few observations were still made, but the station network grew constantly and reached a maximum of reporting stations during the 1970s (Fig. 2.1b). After the independence of most African states, the measurement network deteriorated in many countries in the 1970s and 1980s and it became increasingly difficult to access the data. Even during the peak time, the spatial resolution of the measurements was very sparse in most regions of Africa (Fig. 2.1a), limiting detailed research on rainfall variability. A review of the history of rainfall records in Africa can be found in Nicholson (2017).

6

Despite the scarcity of meteorological data over Africa, first evidences of synoptic rainfall variability over West Africa were observed independently before the second world war by the two German meteorologists Regula and Piersig (Fink, 2012). Analyzing observations of coastal weather stations, seaplanes and zeppelins, Regula (1936) concluded on the existence of regular surface pressure disturbances with a periodicity of about four days. Due to their direction of motion, they were called African Easterly Waves (AEWs). In the rest of the tropics, these easterly waves are generally termed tropical disturbances (TDs). Regula found that this mode of variability is associated with wind modulation at upper levels and increased occurrence of squall lines during periods of increasing pressure. Analyzing weather observations between 1881 and 1911, Piersig (1936) (translated into English 1944) first noted the seasonal cycle with maximum occurrence during boreal summer and the relation of these waves with tropical storms in the Atlantic. Little later, the French meteorologist Hubert (1939) was the first to track AEWs. He showed that they propagate with an average speed of 6–14 m s^{-1} across West Africa. Their dominant contribution to annual rainfall in West Africa has been known since the 1950s (Eldridge, 1957). Around this time, significant advances in the understanding of theses waves were also obtained, which are discussed in the next subsection. In the 1960s and 1970s, the international scientific community united despite cold-war tensions under the Global Atmospheric Research Program (GARP). Arguably the most important international measurement resulting from GARP was the GARP Atlantic Tropical Experiment (GATE) in 1974 (Kuettner and Parker, 1976). During GATE, extensive observations of AEWs could be obtained (e.g. Burpee 1975; Reed et al. 1977; Albignat and Reed 1980). The next large international research project of this scale in this region would only come thirty years later with the African Monsoon Multidisciplinary Analysis (AMMA) (Redelsperger et al., 2006).

2.1.2 Rossby waves

AEWs are only one particular African wave mode, which dynamically force rainfall variability. Yet, several more wave modes exist affecting precipitation over Africa. The theoretical foundation for the study of atmospheric variability was laid in the late 18th century by Laplace (Laplace, several works between 1778 – 1825, reprinted Laplace 2017). His set of tidal equations was the earliest form of the so-called "shallow-water equations", which describes motions of a shallow layer of homogeneous fluid on a rotating sphere where the horizontal motions are much larger than vertical motions. Hough (1897, 1898) found analytical solutions to these equations, which predict the existence of two classes of atmospheric waves: The

first class refers to gravity waves, which are covered in detail in the next subsection. The second class are planetary-scale waves. These waves were later named after Rossby and collaborators (1939), who described their existence in the atmosphere and correctly identified the change of Coriolis force (Coriolis, 1835) with latitude as their restoring mechanism. In a barotropic setting the pressure gradient is parallel to the temperature gradient and the Coriolis force is balanced with the pressure gradient force in Rossby waves. All motions satisfying this balance are called geostrophic. In such a barotropic shallow-water system, the absolute vorticity, which consists of the earth-relative vorticity of the flow ζ and the planetary vorticity f, scaled by the depth h is conserved in time and thus

$$\frac{D}{Dt}\left(\frac{\zeta+f}{h}\right)=0. \tag{2.1}$$

Barotropic Rossby waves feature no vertical winds. In baroclinic regions where the temperature gradient is not aligned with pressure gradient, the winds are accelerated due to horizontal temperature gradients along isobars, which results in additional divergence and, thus, vertical winds. As they deviate slightly from geostrophy, these motions are therefore called quasi-geostrophic (Kundu et al., 2016). Mathematically, baroclinic Rossby waves can be described in various ways. One common mathematical framework is the Ertel potential vorticity (PV) (Ertel 1942, translated Schubert et al. 2004). The PV on constant geopotential height is defined as

$$PV=\frac{1}{\rho}(\zeta+f)\frac{\partial\theta}{\partial z}, \tag{2.2}$$

and relates absolute vorticity with the vertical gradient of potential temperature θ, which is a measure for static stability, and density ρ. In analogy to the barotropic case, baroclinic Rossby waves conserve PV (Hoskins et al., 1985).

Riehl (1945) revealed that easterly waves can be dynamically explained with the conservation of PV. Burpee (1972) showed that AEWs exhibit a baroclinic vertical tilt and a barotropic horizontal tilt. He first proved that the meridional PV gradient of the African Easterly Jet (AEJ), which acts as a waveguide to the AEWs, satisfies the Charney-Stern criterion for instability (Charney and Stern, 1962). To first order, AEWs can thus be seen as balanced (quasi-geostrophic) disturbances, which grow and are sustained by barotropic and baroclinic conversions of energy from the AEJ (Albignat and Reed, 1980).
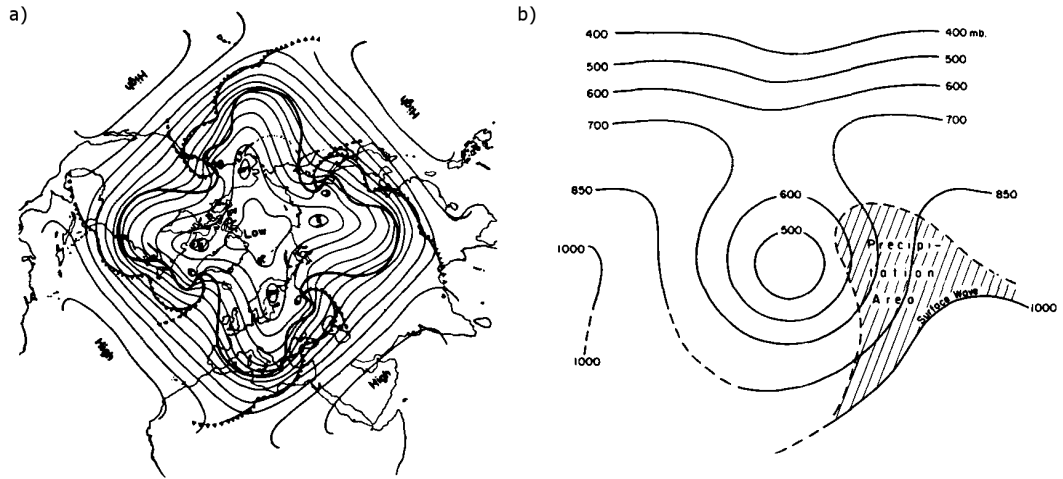
Figure 2.2: (a) Schematic of a planetary Rossby wave as seen in the 500 hPa geopotential (thin lines) with the associated surface front (thick lines). (b) Illustration of a trough in a mid-latitude Rossby wave and its relationship with precipitation. Reprinted from Palmén (1949). © 1949 John Wiley & Sons, Inc. Used with permission.

Another common diagnostic framework for describing baroclinic Rossby waves and the associated vertical motions is the quasi-geostrophic omega equation (Holton and Hakim, 2013).

$$\omega \propto \frac{\partial}{\partial z} \mathbf{V}_h \cdot \nabla_p (\zeta + f) + \mathbf{V}_h \cdot \nabla_p (T). \qquad (2.3)$$

Assuming no diabatic effects, it states that the vertical velocity ω depends on the differential advection of absolute vorticity with height and the horizontal advection of temperature. Positive differential vorticity advection and warm air advection result in large-scale lifting and, in case of saturation, precipitation. Most prominently, Rossby waves manifest themselves as planetary disturbances of the polar jet in the upper troposphere and as such they are the main driver of synoptic to intraseasonal rainfall variability in the extratropics (Fig. 2.2a). According to Eq. (2.3), air masses are lifted ahead of troughs, which leads to moistening of the air column and potentially precipitation (Fig. 2.2b). A model to explain hyper-baroclinic zones in organized frontal structures observed at the surface of extratropical Rossby waves is the polar front theory developed by a school of Norwegian meteorologists at Bergen under the leadership of Bjerknes (Bjerknes, 1919). These polar fronts are responsible for the majority of rainfall in the extratropics. For a detailed mathematical treatment of Rossby waves the reader is referred to the pertinent literature (e.g. Holton and Hakim 2013; Kundu et al. 2016). As a final note, extratropical Rossby waves commonly occur in entire wave trains,

so-called Rossby wave packets, which serve as predictors of rainfall variability on the intraseasonal timescale (Wirth et al., 2018).

In the first half of the 20th century, the upper troposphere in the tropics was considered to be relatively stable. With radiosonde data obtained during the end of the Second World War, Riehl (1950) revealed that the tropical upper troposphere is highly variable. He gave first evidences that tropical disturbances can influence the circulation in the extratropics. The coupling of synoptic to intraseasonal tropical modes with Rossby waves in the extratropics was later found to be an important pathway for tropical-extratropical interactions (Stan et al., 2017). In equatorial regions of westerly flow, so-called 'westerly ducts', Rossby waves can traverse the equator and influence the circulation on the other hemisphere (Webster and Holton, 1982). Due to their mutual influence, intraseasonal variability in the tropics and extratropics are nowadays often seen as a global phenomenon. Predictability of intraseasonal rainfall variability in the extratropics largely stems from the tropics (Waliser et al. 2003; Vitart and Robertson 2018).

2.1.3 Equatorial waves

As the previous subsection laid out, the theoretical understanding of fluid dynamics in the beginning of the 20th century already predicted that all atmospheric motions can be described as either quasi-geostrophically balanced or unbalanced flow. Despite the progress made in extratropical dynamics, it was not until the late 1960s that the theoretical foundations were laid for the study of wave dynamics in the tropics and their influence on rainfall variability. As the Coriolis force vanishes at the equator, the assumptions by Rossby and collaborators 1939 to solve the equations of motion in the extratropics break down. Before the groundbreaking theoretical work by Matsuno (1966), it was not clear whether large-scale motions in the tropics can be quasi-geostrophically balanced. First theoretical considerations on equatorial waves were done by Ichiye (1959) and Stern (1963), but not until 1966, Matsuno proved that large-scale motions at the equator exist, which can indeed be quasi-geostrophically balanced. Due to their similarity to extratropical Rossby waves, these motions are summarized under the term of equatorial Rossby (ER) waves. These waves were first observed in the atmosphere in form of tropical cyclone pairs during the early 1980s (Keen, 1982).

Besides ER waves, several further wave solutions exist for motions at the equator. Matsuno derived full analytical solutions for the near-equatorial shallow-water equations. More specifically, he solved the hydrostatic shallow water equations of an incompressible, inviscid fluid of homogeneous density on a rotating
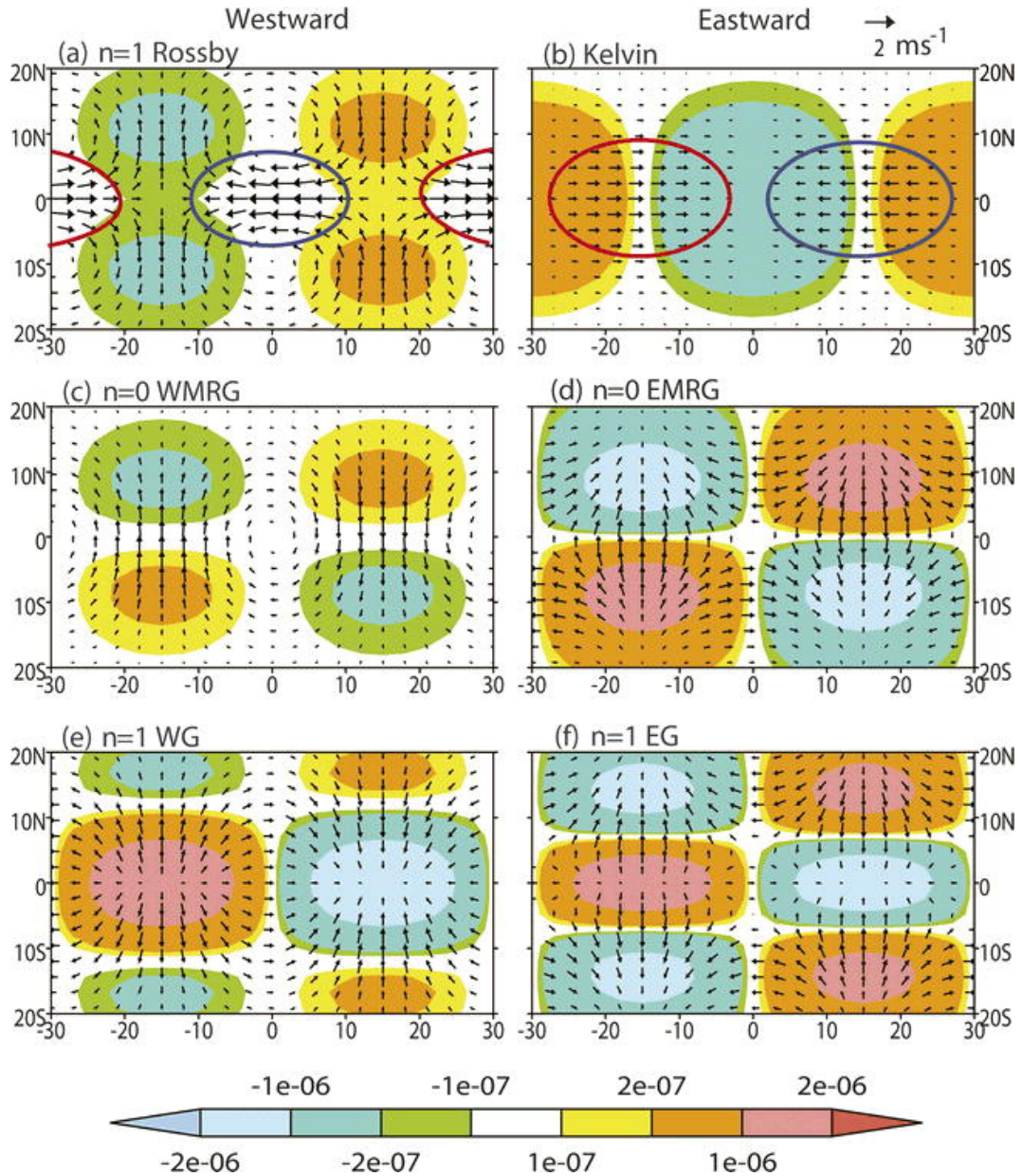
Figure 2.3: Wave solutions of the near-equatorial shallow water system showing winds (vectors) and divergence (shading, in s^{-1}) of (a) ER n=1, (b) Kelvin n=-1, (c) westward MRG n=0, (d) eastward MRG n=0 (also called EIG n=0), (e) WIG n=1, and (f) EIG n=1. Ellipses in (a) and (b) indicate regions where significant wind induced surface energy fluxes are expected. Reprinted from Yang et al. (2007b). © American Meteorological Society. Used with permission.

sphere. Furthermore, he assumed no background flow and approximated the Coriolis parameter f as increasing linearly with latitude y, which is called the equatorial β-plane approximation ($f = \beta y$). The mathematical derivation of the wave solutions and a detailed discussion of the different wave types obtained can be found in Matsuno (1966); Kiladis et al. (2009); Wheeler and Nguyen (2015). Briefly speaking, several wave solutions can exist under these constraints. Matsuno showed that the solutions for the zonally propagating waves with a zonal wavenumber k and frequency ω in a shallow water system with an equivalent depth h_e satisfy the relationship

$$\frac{\sqrt{gh_e}}{\beta}\left(\frac{\omega^2}{gh_e} - k^2 - \frac{k}{\omega}\beta\right) = 2n+1, \quad n = 0, 1, 2, ..., \tag{2.4}$$

whereby g is the gravitational acceleration and n is the number of meridional modes (Kiladis et al., 2009). The equivalent depth h_e of the shallow water system should not be understood as a measurable length. Yet, it is an important theoretical parameter, which determines the scale of several wave properties such as their speed and scale. Aforementioned balanced ER waves are the low-frequency solution of Eq. (2.4) and their dispersion relation is

$$\omega_{\mathrm{ER}} \approx \frac{-\beta k}{k^2 + (2n+1)\beta/\sqrt{gh_e}}. \tag{2.5}$$

First observational evidences of Matsuno's theory were provided by Yanai and Maruyama (1966) who analyzed five months of radiosonde measurements taken as supporting information for nuclear tests in the central equatorial Pacific. Later, they discovered lower stratospheric meridional winds exhibit westward propagating oscillations. These waves were later identified as mixed Rossby-Gravity (MRG) waves. Their dispersion relation

$$\omega_{\mathrm{MRG}} = k\sqrt{gh_e}\left[\frac{1}{2} \pm \frac{1}{2}\left(1 + \frac{4\beta}{k^2\sqrt{gh_e}}\right)^{1/2}\right] \tag{2.6}$$

is obtained from Eq. (2.4) with $n = 0$. MRG waves are antisymmetric along the equator and feature a strong cross-equatorial wind component (Fig. 2.3c-d). They have been observed over the central and western Pacific region affecting rainfall variability there (Takayabu and Nitta, 1993; Holder et al., 2008; Kiladis et al., 2016). They are quasi-geostrophically balanced when traveling westward and behave as inertio-gravity (IG) waves when traveling eastward. Therefore, eastward traveling

MRG waves are often referred to as eastward inertio-gravity waves (EIG, n=0), which are treated next.

At high frequencies, Eq. (2.4) yields

$$\omega_{\text{IG}} \approx \pm \left[(2n+1)\beta \sqrt{gh_e} + k^2 gh_e \right]^{1/2}, \qquad (2.7)$$

as the dispersion relation of IG waves (Fig. 2.3d-f). These waves are solutions where the restoring force is not the horizontal pressure gradient as for Rossby waves, but the vertically oriented gravity force. In the extratropics, IG waves are often triggered by jets or fronts (Plougonven and Zhang, 2007). In the tropics, EIG waves are most prominent in the stratosphere and mesosphere (Mayr et al., 2003, 2004; Tindall et al., 2006a,b). If observed in the troposphere, EIG waves have their main influence on upper levels (Yang et al., 2003, 2007b; Kiladis et al., 2009). They are known to interact with westward MRG waves, although the exact mechanism is not clear (Kiladis et al., 2016; Dias and Kiladis, 2016).

A third class of waves exists next to the Rossby and IG waves predicted by Hough (Longuet-Higgins, 1968). As additional solution to Eq. (2.4), the dispersion relation of Kelvin waves is

$$\omega_{\text{Kelvin}} = \sqrt{gh_e}k. \qquad (2.8)$$

The solution can be also obtained by setting $n = -1$ in Eq. (2.4). This wave type is called Kelvin ($n = -1$) wave after Lord Kelvin who described them first at the end of the 19th century (Thomson, 1880). Kelvin waves exist due to trapping at a boundary, along which they travel. In the tropics, their waveguide is the equator because the Coriolis parameter has opposite signs in the southern and northern hemisphere. Kelvin waves are a hybrid of Rossby and IG waves as they share properties of both. In their propagation direction, which is eastward, equatorial Kelvin waves behave like IG waves, whereas in perpendicular to their propagation in meridional direction they are quasi-geostrophically balanced. Equatorial Kelvin waves only modulate zonal winds (Fig. 2.3b). They are the only non-dispersive equatorial wave mode and, thus, their speed is independent of the wave length.

Figure 2.4 displays the dispersion relationship of the most important wave modes in the zonal wavenumber-frequency domain. These lower-order ($n \leq 1$) wave solutions are commonly observed in the tropics. Their associated horizontal circulation patterns are shown in Fig. 2.3. In contrast, higher order waves (not shown in Figs. 2.4–2.3) exhibit even more complex circulation patterns and are thus hardly discernible in raw weather data.
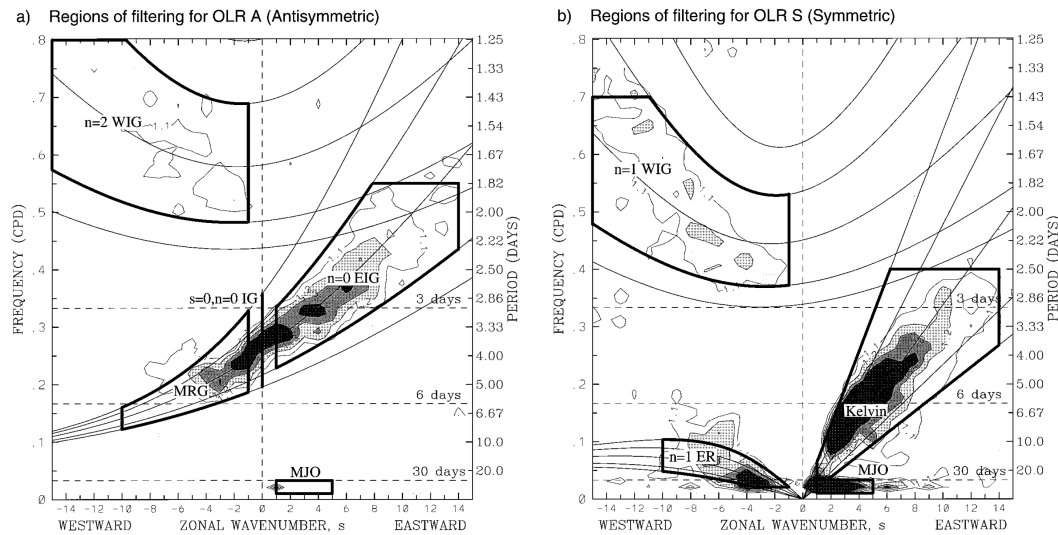
Figure 2.4: (a) Symmetric and (b) antisymmetric power spectrum of OLR between 15°S–15°N in the wavenumber-frequency domain. Black solid lines denote the theoretical dispersion relationship of the major equatorial wave types as obtained from equatorial shallow water theory with equivalent depth varying at 8, 12, 25, 50, and 90 m (from bottom to top). Reprinted from Wheeler and Kiladis (1999). © American Meteorological Society. Used with permission.

All waves influence divergence fields. IG waves are in general more divergent waves, whereas balanced modes behave more rotationally (Fig. 2.3, cf. Fig. 1 from Delayen and Yano 2009). Due to their influence on lower- and upper-tropospheric divergence, mass continuity leads to vertical velocity in all equatorial wave types. Therefore, they can modulate tropical cloud formation and rainfall generation. In areas where vertical motions lead to condensation and evaporation, diabatic heating and cooling modifies the properties of equatorial waves and acts as an additional wave forcing. Due to this coupling to convection, equatorial waves that are associated with rainfall are thus termed convectively coupled equatorial waves (CCEWs). The equivalent depth of CCEWs and therefore their speed is considerably lower ($h_e = 12$ to 50 m) than in dry waves ($h_e = 200$ m). Several theories exist, trying to explain the effect of latent heating and its relationship to the large-scale circulation such as the concepts of gross moist stability (Neelin and Held, 1987), wave conditional instability of the second kind (wave-CISK, Hayashi 1970), quasi equilibrium (Arakawa and Schubert, 1974), wind induced surface heat exchange (WISHE, Emanuel 1987), and stratiform instability (Mapes, 2000).

As a last remark on equatorial waves, although they were treated in this section as independent equatorial motions, equatorial waves are not independent from the extratropics. Extratropical forcing by Rossby waves has been proven theoretically (Hoskins and Yang, 2000) and observed repeatedly to trigger equatorial waves (ER waves: Kiladis and Wheeler 1995; MRG waves: Magaña and Yanai 1995;

14

Kelvin waves: Straub and Kiladis 2003). These interactions are relevant on the intraseasonal timescale as pointed out in the previous subsection.

2.1.4 Madden-Julian Oscillation

In the early 1970s, spectral analysis of station pressure and radiosonde wind observations in the Indian and Pacific Oceans revealed the existence of an intraseasonal oscillation, which stands out significantly against the background noise (Madden and Julian 1971; 1972). After their discoverers, this phenomenon is named "Madden-Julian Oscillation", although it is occasionally simply called the "intraseasonal oscillation". Figure 2.5 shows how the MJO propagates eastward affecting surface pressure, winds and convection. As a planetary wave mode, the MJO affects the circulation in the entire tropics, although the strength of coupling with convection depends on longitude. It couples strongly with convection over the warm western Pacific and eastern Indian Ocean, commonly termed the tropical warm pool, where it travels at an average speed of about $5\,\mathrm{m\,s}^{-1}$ (Weickmann et al., 1985). When moving over the eastern Pacific Ocean the strong coupling with convection vanishes and the MJO continues to travel as a (relatively) free wave at higher speeds of about 30–$35\,\mathrm{m\,s}^{-1}$ (Milliff and Madden, 1996; Matthews, 2000). In this dissertation, the term "equatorial waves" refers to all CCEWs and the MJO. The term "tropical waves" additionally includes all other tropical wave modes such as AEWs.

The exact underlying mechanisms of the MJO are not fully clear and therefore it has been regarded by some as the "holy grail" of tropical meteorology (Raymond, 2001). Several theories exist explaining the properties of the MJO. The MJO shares properties of an atmospheric Kelvin wave, and has thus been described as a Kelvin wave dampened through convection (Chang, 1977). The diabatic heating associated with convection causes a Rossby wave response, which can be seen in the twin gyres often observed off the equator. The resulting circulation pattern obtained from a coupling of Rossby and Kelvin waves resembles the Gill-pattern (Gill, 1980). Therefore, the MJO has been also described as a mixed Kelvin-Rossby mode (Wang and Rui, 1990; Wang and Li, 1994; Adames and Kim, 2016). Similar to CCEWs, the MJO has been considered to create its own forcing through moisture convergence (wave-CISK) and surface evaporation (WISHE, Emanuel 1987 and evaporation-wind feedback, Neelin and Held 1987). More recent research has again challenged the view that the MJO and Kelvin waves are dynamically distinguishable, suggesting instead that they form a continuum (Roundy, 2012; Powell, 2017). Additionally, some studies have suggested that the MJO can be
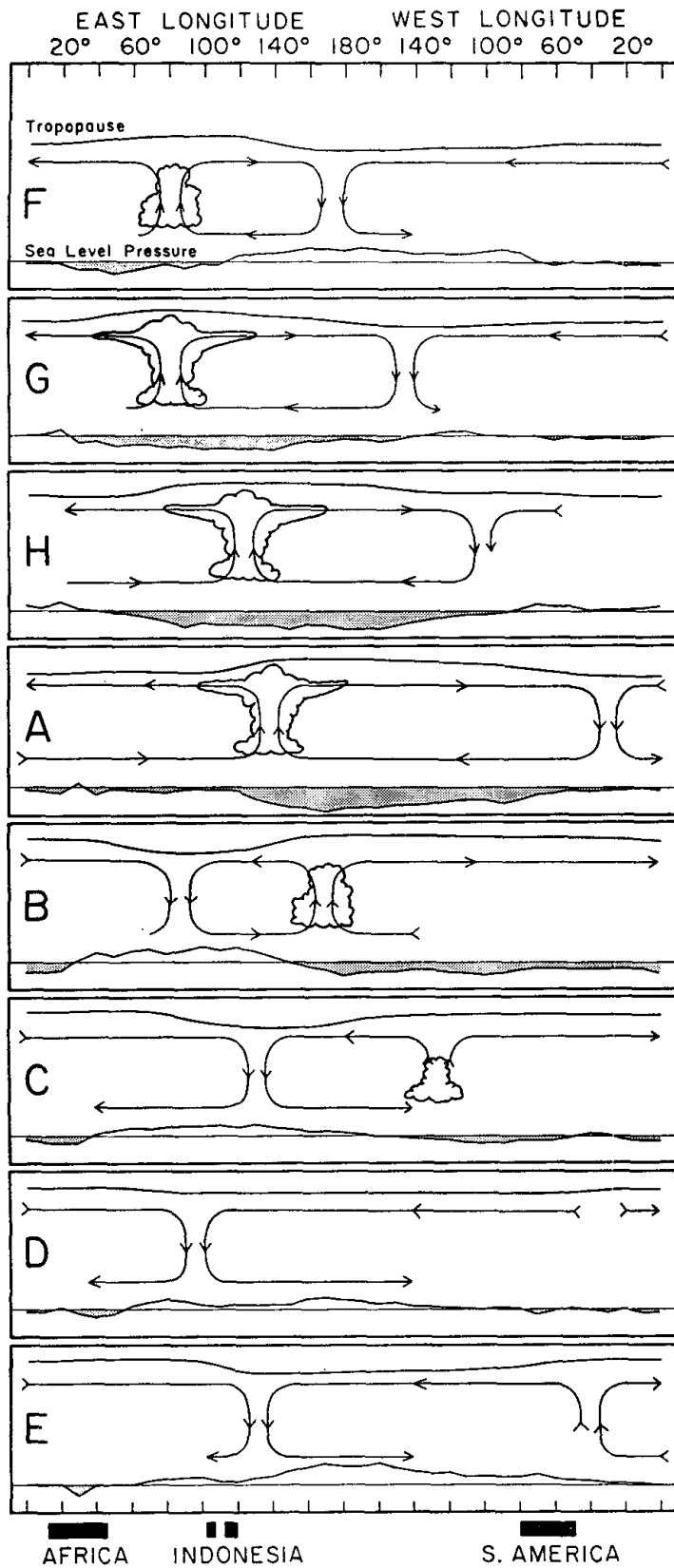
Figure 2.5: Schematic equatorial cross-section of the MJO depicting the eastward propagation and influence on circulation, convection, and surface pressure. Reprinted from Madden and Julian (1972). © American Meteorological Society. Used with permission.

understood as a response to an independent forcing such as a tropical intraseasonal stationary forcing (Yasunari, 1979; Lau and Chan, 1985), tropical stochastic forcing (Salby and Garcia, 1987), and lateral forcing (Lau and Peng, 1987), where the resultant propagation of the signal and coupling with convection is a secondary result. Additional factors affecting the propagation of the MJO include further diabatic effects such as radiation, water vapor and ocean-atmosphere interactions, which are not discussed in detail here. The reader is furthermore referred to the reviews by Madden and Julian (1994) and Zhang (2005; 2013) on the research history, mechanisms and impacts of the MJO.

2.1.5 Wave filtering and monitoring

When spatially and temporally gridded weather data became available, tropical waves could be observed more easily. Early studies of tropical waves mostly relied on spectral analysis of wind from radiosonde data (e.g. Chang et al. 1970; Yanai and Murakami 1970; Madden and Julian 1971). Due to the scarcity of measurements in the tropics, this approach could give only limited insight into the spatial properties of tropical waves. During the 1970s, first quasi-continuous observations of tropical weather from space began with the launch of the Geostationary Operational Environmental Satellite (GOES) series (House et al., 1986; Davis, 2007). As a proxy for rainfall in the tropics, remotely sensed outgoing longwave radiation (OLR) has been used since then (Arkin and Ardanuy, 1989). Since 1998, direct measurements of hydrometeors are collected by the precipitation radar and passive microwave sensors of the Tropical Rainfall Measuring Mission (TRMM) satellite. The TRMM rainfall products have been arguably the most accurate satellite-derived rainfall dataset until TRMM was replaced by the Global Precipitation Measurement (GPM) mission in 2014 (Skofronick-Jackson et al., 2017). As TRMM precipitation estimates differ considerably from rain gauge measurements over Africa at synoptic time scales, rain gauges remain a crucial part in validation of satellite products (Vogel et al., 2018).

Several filtering methods have been developed to isolate tropical waves and study their effect on rainfall variability. Wheeler and Kiladis (1999) established a filtering method to isolate tropical waves in the wavenumber-frequency spectrum using their known temporal and spatial properties (Fig 2.4). Several studies of tropical waves over Africa (and the rest of the tropics) have successfully used this approach to filter OLR, brightness temperature or TRMM precipitation (Mounier et al., 2007, 2008; Janicot et al., 2009, 2010; Ventrice and Thorncroft, 2013; Mekonnen and Thorncroft, 2016). This method needs data on entire latitudinal

bands. To obtain the local wave signal, Riley et al. (2011); Yasunaga and Mapes (2012) define a local phase diagram of the wave activity and the local time-derivative at a specific location. This method allows the quantification of eight local wave phases. Other filters for tropical waves have been developed by projecting onto theoretical horizontal patterns (Yang et al., 2003), using wavelet analysis (Kikuchi and Wang, 2010; Roundy, 2018), or 3D normal mode functions (Castanheira and Marques, 2015). Finally, the aforementioned decomposition of global three-dimensional flow into balanced and IG modes can be achieved using the theory of normal-mode functions (Kasahara and Puri, 1981; Žagar et al., 2015).

The MJO is a unique global mode and has thus been treated specifically. Several indices exist to monitor the propagation of the MJO as a global mode. The Real-time Multivariate MJO index (RMM) uses the two first principal components of a combination of 850 hPa and 200 hPa zonal wind, and OLR data to construct a phase diagram, which is then partitioned into eight phases (Wheeler and Hendon, 2004). More recent indices are the OLR-based MJO Index (Kiladis et al. 2014) and the revised RMM (Liu et al., 2016).

2.2 Synoptic and intraseasonal modes over Africa

After the previous section reviewed the historical development, which led to the current understanding of rainfall variability over Africa, this section describes each mode individually and their respective influences on rainfall. Several equatorial, (sub-)tropical and extratropical wave modes modulate precipitation on the synoptic to intraseasonal timescale. In the first part of this section, the equatorial modes (MJO and CCEWs) are discussed, then (sub-)tropical modes that are specific to the West African monsoon are treated and, finally, extratropical modes are described. Within the different groups, the modes are ordered according to their timescales, from slow modes to fast ones.

2.2.1 Equatorial waves

The MJO and CCEWs influence rainfall variability mainly over the tropical regions of Africa. These modes affect precipitation on a wide range of spatial and temporal scales. The influence of the equatorial waves on West African rainfall have been treated individually in detail in several studies performed during the AMMA measurement campaign (Janicot et al. 2011 and references therein).
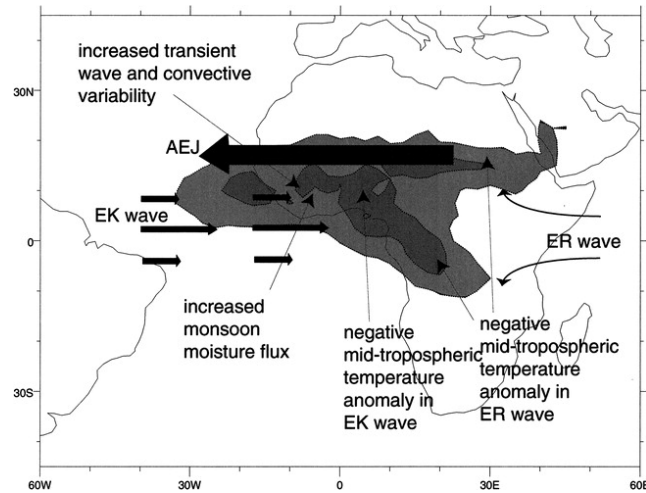
Figure 2.6: Conceptual illustration of the MJO over Africa as equatorial Kelvin wave (EK) and equatorial Rossby wave (ER) response of MJO bursts over the tropical warm pool. Reprinted from Matthews (2004). © American Meteorological Society. Used with permission.

a. Madden-Julian Oscillation

Since its discovery in the 1970s, most researchers considered the MJO to solely affect convection over the tropical warm pool and to have no or little impact on Africa (e.g Madden and Julian, 1972; Knutson et al., 1986; Murakami et al., 1986). In the 2000s, the intraseasonal rainfall signal over Africa received more attention and since then the influence of the MJO on African rainfall has been repeatedly treated (e.g Matthews 2004; Janicot et al. 2009; Pohl et al. 2009b; Berhane et al. 2015; Zaitchik 2017). As a intraseasonal oscillation, the MJO affects rainfall variability on the timescale of about 30–90 days. Matthews (2000, 2004) suggested that an MJO burst over the tropical warm pool about 20 days prior to the convective maximum over Africa triggers ER and Kelvin waves. These wave propagate westward and eastward with different propagation speed and meet over Africa where they create a standing oscillation over Africa (Matthews, 2004; Janicot et al., 2009; Alaka and Maloney, 2012) (Fig. 2.6). Due to its differences to the planetary MJO, the intraseasonal oscillation over Africa is also called the "African MJO" (Janicot et al., 2011; Louvet et al., 2016).

The MJO strongly modulates the zonal wind pattern and rainfall over West Africa. Rainfall increases during the phase of enhanced low-level westerlies and decreases in regions of easterly wind anomalies, respectively (Matthews, 2004). Along the Guinean belt, the modulation is more pronounced than farther north over the Sahel region (Gu, 2009; Pohl et al., 2009b). The precipitable water varies strongly during the passage of the MJO (Matthews, 2004; Alaka and Maloney, 2012). Lavender and Matthews (2009) argued that the precipitation moistens the

boundary layer. During the wet phase, the westerly anomalies at the southern flank of the AEJ induce an increased horizontal wind shear (Matthews, 2004; Ventrice et al., 2011), which reduces the barotropic stability of the AEJ (Fig. 2.6). This way, the MJO modulates the activity of AEWs and thus interacts with rainfall variability on shorter timescales (Alaka and Maloney, 2012, 2014; Ventrice et al., 2011).

The influence of the MJO on central African rainfall is strongest during boreal spring, when the MJO is still very active over the Indian and Pacific Oceans (Berhane et al., 2015). During the monsoon season, the rainbelt is farther in the north. The details of intraseasonal rainfall variability over the Congo basin still remain largely unknown, additionally hampered due to the lack of rainfall measurements in this region.

Over equatorial East Africa, the MJO affects both rainy seasons (March to May and October to December) (Pohl and Camberlin, 2006a,b). In contrast to the rest of Africa, the MJO shows here a clear eastward propagation (Pohl and Camberlin, 2006a). Due to the complex topography and the presence of multiple large water bodies, the modulation patterns are out of phase over the highlands in northern Tanzania and western Kenya and the coastal regions of equatorial East Africa. Over the highlands, low-level westerlies advect moisture from the Congo, whereas coastal regions experience enhanced rainfall when convection is suppressed over the rest of Africa and the Indian Ocean.

The rainfall modulation by the MJO is not only restricted to tropical areas but reaches far into the subtropics. The MJO affects the dry spell frequency in the West Sahel during boreal summer (Pohl et al., 2009b). During austral summer, the MJO also influences rainfall in southern Africa (Pohl et al., 2007). As the MJO passes over the Congo basin, it induces anomalous meridional moisture flux into the subtropics and subsequently leads to wet and dry periods up to 20°S. Yet, the modulation in the southern hemispheric subtropics is spatially not as homogeneous and strong as in the tropics.

b. Equatorial Rossby waves

ER waves modulate rainfall on the intraseasonal timescale. During boreal summer, two types of ER waves have been documented over West Africa (Janicot et al., 2010). The first mode acts on the timescale of 30 to 100 days. This longer mode explains about one third of the variability of ER waves. It is highly correlated to the African MJO and represents the ER response of the intraseasonal MJO signal (Sultan et al., 2009; Janicot et al., 2009). The shorter ER mode affects precipitation

on the timescale of 10 to 30 days and explains about one half of the OLR variance in the ER band. These ER waves feature deep vortex pairs, propagating westward. The circulation pattern resembles the theoretical wave solution of an $n = 1$ ER wave (Fig. 2.3a) displaced northward with a stronger response in the northern hemisphere (Janicot et al., 2010). Janicot et al. (2010) traced them back to an area around Lake Victoria, although they speculated on a possible connection to the Indian monsoon. The short intraseasonal ER mode features a poleward tilted pattern reaching from the Sahel over the Sahara up to the Mediterranean (Janicot et al., 2010). As a balanced wave mode, ER waves feature a deep equivalent barotropic structure (Roundy and Janiga, 2012; Yang and Hoskins, 2017). ER waves originating from the southern hemispheres affect both MRG and AEW activity over West Africa (Yang et al., 2018).

c. Kelvin waves

Kelvin waves are predominantly synoptic-scale disturbances, observed primarily in the equatorial regions of Africa. The tropical rainbelt serves as a wave guide to convectively coupled Kelvin waves (Dias and Pauluis, 2009, 2011); therefore, the influence of Kelvin waves shifts during the year with the propagation of the tropical rainbelt (Huang and Huang, 2011). When centered at the equator, Kelvin waves only modulate zonal winds (2.3b). An additional modulation of meridional winds exists, when Kelvin waves travel off the equator (Gill, 1980; Dias and Pauluis, 2009). Kelvin waves exist at a range of spatial and temporal scales (Fig. 2.4a). Yet, there speed is fairly constant at around 12-15 m s^{-1} (Nguyen and Duvel, 2008; Mounier et al., 2007; Mekonnen et al., 2008). On average they have a wavelength of about 8000 km and a quasi-weekly period (5–7 days). Kelvin waves are backward tilted with height. An area of low-level convergence leads the region of deep convection, which is trailed by upper level divergence (Kiladis et al., 2009).

Kelvin waves have a pronounced impact on synoptic-scale rainfall variability over tropical Africa. Over West Africa, they explain about 10–15 % of daily rainfall variability (Mekonnen and Thorncroft, 2016). Similar to the MJO, rainfall is enhanced during the passage of westerly anomalies at lower levels. Due to the off-equatorial forcing during boreal summer, an additionally southerly component enhances moisture inflow towards the north in its wet phase. As in the MJO, Kelvin waves influence the activity of AEWs due to increased cyclonic shear vorticity along the southern flank of the AEJ during their wet phase (Mekonnen et al., 2008; Ventrice and Thorncroft, 2013; Mekonnen and Thorncroft, 2016). Over central and East Africa, Kelvin waves modulate rainfall during boreal spring (Nguyen and

Duvel, 2008; Laing et al., 2011; Sinclaire et al., 2015). Over the Congo basin, passing waves facilitate mesoscale convective activity (Laing et al., 2011). When reaching East Africa, the complex topography modifies the propagation of Kelvin waves and their influence on circulation and rainfall (Sinclaire et al., 2015).

d. Mixed Rossby-gravity waves

The impact of MRG waves over Africa is not yet well documented. Their influence on synoptic-scale rainfall variability over West Africa is estimated to be ± 1–$2\,\mathrm{mm\,d^{-1}}$. Wave disturbances sharing properties of MRG waves and AEWs have been documented (Cheng et al., 2019), although the exact mechanisms of the interaction between them is not clear. MRG waves can transition to off-equatorial easterly waves (Takayabu and Nitta, 1993; Zhou and Wang, 2007) and when they are in phase with each other, MRG waves amplify AEWs (Yang et al., 2018). More research on this interaction is needed, as the theoretical models for both modes cannot fully explain individual vortices observed in reality (Knippertz et al., 2017).

e. Inertio-gravity waves

Little is known about the influence of EIG and WIG waves on African rainfall. As they modulate the circulation only weakly (Kiladis et al., 2016) and due to their fast propagation speed, convection is hardly affected by the passage of IG waves. Indications exists that squall lines, which are the most important rain bearing systems in the Sahel (Fink and Reiner, 2003), can be interpreted as convectively coupled WIG (Tulich and Kiladis, 2012).

2.2.2 Other (sub-)tropical modes

This subsection describes (sub-)tropical wave modes specific to the West African summer monsoon, which can not be explained with the equatorial shallow-water equations. First, AEWs are the most dominant synoptic-scale wave mode over northern tropical Africa. The "quasi-biweekly zonal dipole" (QBZD) and "Sahel mode" are two internal intraseasonal modes of the West African monsoon system (Mounier, 2004). These modes are obtained from spectral analysis of observations and empirical orthogonal functions, however, the mechanisms of both modes are not entirely clear.
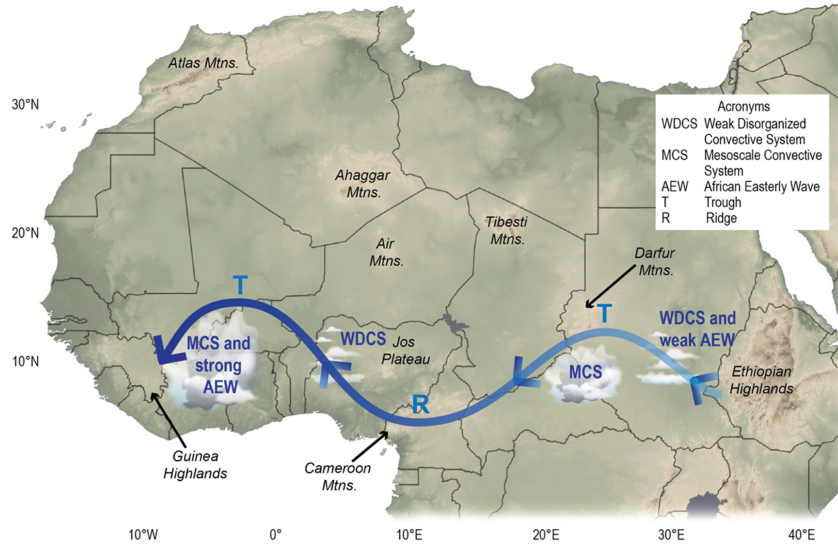
Figure 2.7: Schematic of AEWs and their relationship to synoptic scale rainfall over northern tropical Africa. Reprinted from Semunegus et al. (2017). © John Wiley and Sons, CC BY 4.0 ⓒⓘ.

a. African Easterly Waves

AEWs are the main synoptic weather system in the West African monsoon region. To first order, their existence can be explained by barotropic-baroclinic instability of the AEJ (Charney and Stern, 1962; Burpee, 1972; Thorncroft and Hoskins, 1994; Hsieh and Cook, 2005). As they are linked to the AEJ, AEWs are observed only during the wet monsoon season, when the AEJ forms due to the temperature gradient between the relatively cool monsoon air layer in equatorial Africa and the hot Saharan desert. Disturbances embedded in AEWs occur on a northerly and southerly track on both sides of the AEJ with maximum disturbances at about 850 and 700 hPa and a mean latitudinal position at around 17°N and 9°N, respectively (Reed et al., 1977; Pytharoulis and Thorncroft, 1999; Fink and Reiner, 2003). They have a period of 3–5 days (Burpee, 1972) and a phase speed of approximately 8-–10 m s^{-1} (Reed et al., 1977). Their zonal wavelength is about 3000–5000 m (Diedhiou et al., 1999; Kiladis et al., 2006). In reality, AEWs can take various forms and a unified model describing the different "tastes" of AEWs is still missing (Knippertz et al., 2017; Yang et al., 2018; Cheng et al., 2019). As described in 2.2.1, AEW activity is influenced by the MJO, ER, Kelvin, and MRG waves. Due to their strong coupling with squall lines, a dynamical influence from WIG waves might also exist (Tulich and Kiladis, 2012).

AEWs strongly couple with convection over tropical northern Africa. About one third of West African rainfall variability can be explained by AEWs (Dickinson

23

and Molinari, 2000; Lavaysse et al., 2006; Mekonnen et al., 2006). Their modulation intensity is about ± 2–$3\,\mathrm{mm\,d}^{-1}$. The link between the dynamic disturbance in the mid-troposphere and convection is not trivial. A primary region of enhanced rainfall exists ahead of and in the trough of the AEW, where low-level moisture converges and air is lifted quasi-geostrophically (Duvel, 1990; Fink and Reiner, 2003; Janiga and Thorncroft, 2016) (see Fig. 2.7). A secondary maximum of enhanced isolated shallow convection lies near the ridge of the wave in the region of moist southerlies (Fink and Reiner, 2003; Semunegus et al., 2017; Maranan et al., 2018). While moving towards the Atlantic, the relative position of rainfall maxima and dynamic forcing changes (Kiladis et al., 2006). AEWs mainly modulate precipitation by facilitating the organization of convection. About two third of the squall lines observed over West Africa are associated with the presence of AEWs (Fink and Reiner, 2003).

b. Quasi-biweekly zonal dipole

As the name suggests, the first West African intraseasonal mode, QBZD manifests itself as a predominantly stationary zonal dipole mode of convection with a periodicity of about 10–25 days. During its wet phase, convection is enhanced over equatorial Central and West Africa, whereas it decreases at the other pole over the equatorial Atlantic between 30° and 60°W. Between the two poles, an envelope of enhanced convection propagates eastwards. One dynamical key component of the QBZD are Kelvin waves. Additionally, Mounier et al. (2008) highlighted the role of radiative processes. If the influence of Kelvin waves is removed, the stationary character is more pronounced although a slight westward propagation is evident, raising the question of additional coupling with ER waves (Mounier et al. 2008, their Fig. 8).

c. Sahel mode

The other main mode relevant for the short intraseasonal timescale (10–25 days) over West Africa is the Sahel mode (Sultan et al., 2003). The convective signal starts over eastern equatorial Africa and travels westward until reaching the tropical Atlantic. During the passage of associated anticyclonic vortices, the monsoonal south-westerlies are enhanced. Additionally, the rainbelt moves northward and cloudiness (but not necessarily rainfall) can be observed over the Saharan Desert up to the Mediterranean coast. The Sahel mode modulates West African rainfall by about $\pm 2\,\mathrm{mm\,d}^{-1}$. About one third of the Sahel mode is explainable with ER waves
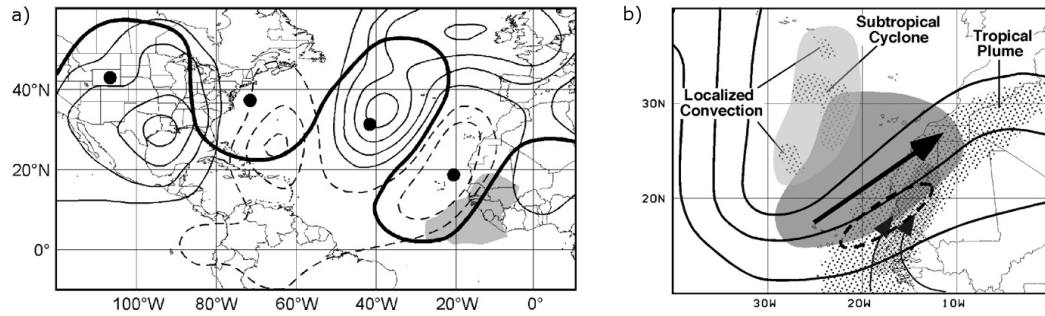
Figure 2.8: (a) Extratropical Rossby wave train leading to a tropical plume over West Africa. The wave train in 200 hPa is indicated in thick lines, with dots marking respective minima and maxima. Thin line shows 850 hPa streamfunction and shading areas of negative OLR anomalies. (b) Schematic of rainfall generation mechanism over West Africa by a tropical plume. Figures reprinted from Knippertz (2007) with permission, © 2007 Elsevier. Figures are based on data from (a) Kiladis and Weickmann (1997) and (b) Knippertz and Martin (2005).

(Janicot et al., 2010). In contrast to ER waves, the Sahel mode also influences equatorial Africa and displaces the tropical rainbelt northward. In addition to the contribution by ER wave dynamics, soil moisture and land surface interactions play an important role for the dynamics of the Sahel mode (Taylor, 2008; Lavender et al., 2010; Taylor et al., 2011).

2.2.3 Extratropical Rossby waves

Rossby waves carry most of the planetary wave energy in the extratropics (Žagar et al., 2015, 2017). Their influence on rainfall variability over Africa is mostly confined to subtropical Africa, although occasionally they interact with the tropical regime. This subsection describes how extratropical Rossby waves are known to influence African rainfall variability via tropical plumes, cold air surges, dry air intrusions and the variability of the Saharan Heat Low (SHL). Some of the mechanisms are related to each other and can occur concomitantly.

a. Tropical plumes

One possible mechanism of tropical-extratropical interactions are tropical plumes, which are "a continuous mid and upper level cloud band[s], at least 2000 km long, which cross 15°N" (McGuirk and Ulsh, 1990) extending from the tropics towards the extratropics. In the northern hemisphere, an extratropical Rossby wave train, which penetrates south-eastward towards the tropics, typically precedes a tropical plume (Fig. 2.8a). To the south-east of the upper-level trough tropical moisture is transported northward and air masses are lifted quasi-geostrophically, such that an elongated cloud band, consisting of a variety of cloud types, forms. This cloud
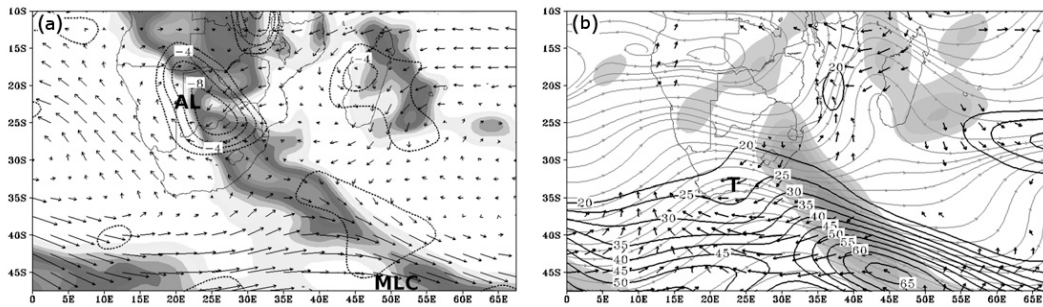
Figure 2.9: (a) Example of a tropical-temperate trough (OLR in shading) over southern Africa on January 1, 1998 and the position of the Angola low (AL) and a mid-latitude cyclone (MLC) as seen in low-level (850 hPa) winds (vectors) and convergence (contours). (b) Upper-level trough (T) and 250 hPa wind (streamlines), ageostrophic wind (vectors) and divergence (shading). Reprinted from Hart et al. (2010). © American Meteorological Society. Used with permission.

band exhibits a south-west to north-east horizontal tilt and often reaches thousands of kilometers from the tropics into the subtropics or even midlatitudes (Fig. 2.8b). The mean lifetime of a tropical plume over the North Atlantic is about 1.5 days (Fröhlich et al., 2013).

Tropical plumes are an important rainfall generating mechanism for semi-arid and arid regions of northwest Africa during late boreal summer, when the tropical rainbelt is furthest north, and early autumn, when upper-level troughs over the Atlantic Coast are more frequent (Knippertz et al., 2003). Tropical plumes explain up to 40 % of the annual rainfall amount at the southern foothills of the Atlas Mountains, which lead to additional orographic lifting. The contribution to the annual sum decreases toward the wetter Moroccan Atlantic coast (Knippertz, 2003).

Due to the proximity to the mid-latitudes, synoptic rainfall variability in southern Africa is related to the passage of extratropical Rossby waves. In this region, tropical plumes, which occur in relation to the South Indian convergence zone (Cook, 2000), have a slightly different mechanism than over northern Africa. They are also referred to as "tropical temperate troughs" (TTTs) (Fig. 2.9a). During the austral summer, TTTs are responsible for the majority of rainfall in southern Africa (Harrison, 1984). Extratropical Rossby waves, which are often abnormally strong, are a necessary precursor for TTTs (Vigaud et al., 2012; Macron et al., 2014). The upper-tropospheric extratropical wave interacts with a low-level tropical disturbance (Fig. 2.9) (Lyons, 1991). Due to the passing Rossby wave, the quasi-permanent low pressure system over Angola intensifies and leads to increased moisture convergence over southern Africa. The extratropical trough induces a poleward export of moisture and draws in moisture from the Atlantic and Indian Oceans and Mozambique Channel (Todd and Washington, 1999; Todd et al., 2004).

The resulting cloud band is tilted in the northwest-southeast direction and stretches from tropical southern Africa (10°S) to the southwest Indian Ocean (>40°S) (Todd et al., 2004; Fauchereau et al., 2009). Precipitation is additionally facilitated through destabilization of the atmosphere. Most TTTs propagate eastward from southern Africa to southern Madagascar (Fauchereau et al., 2009; Pohl et al., 2009a). Depending on their location, they strongly modulate intraseasonal regional rainfall variability (Todd and Washington, 1999; Washington and Todd, 1999). About one fifth of the South African seasonal rainfall is associated with TTTs, although interannually this contribution varies substantially (Macron et al., 2014).

b. Cold air surge

The orography in the western part of North Africa causes a climatological ridge over the Atlas Mountains and a trough further east over Libya and Egypt. The presence of orography facilitates surges of cooler Mediterranean air towards the tropics. A passing Rossby wave over North Africa can amplify the climatological mid-level trough and induce a shallow layer of cold air of about 2 km height. This dome of air is typically between 1 and 6 K colder than its environment. Thus, it creates a meridional pressure gradient and propagates equatorward with a typical width of 500--1000 km and an average speed of approximately $5.5\,\mathrm{m\,s}^{-1}$ (Garreaud, 2001; Vizy and Cook, 2009). During its progression through the East Sahara, surface fluxes heat the air. Thus, the surge is in some cases only identifiable due to its dryness and strong meridional winds when it reaches the tropics. Approximately six to ten cold air surges occur every summer over North Africa (Vizy and Cook, 2009). A strong surge can lead to a collapse of the SHL and, therefore, this mechanism is related to the intraseasonal variability of the SHL (Roehrig et al., 2011) discussed below.

Cold air surges influence synoptic-scale rainfall variability in the Sahel and tropical Africa. Strong surges during spring can suppress the onset of the West African monsoon (Roehrig et al., 2011). A surge during boreal summer is associated with a temporary strengthening of convection over the West Sahel 2–5 days prior to its arrival. About 4 days after its arrival over the eastern Sahel, a surge can lead to monsoon breaks for about 6 days (Vizy and Cook, 2009, 2014). During boreal winter, surges affect the rainfall variability over tropical Africa (0°N–8°N), although their cooling effect on the Sahara is weaker then.
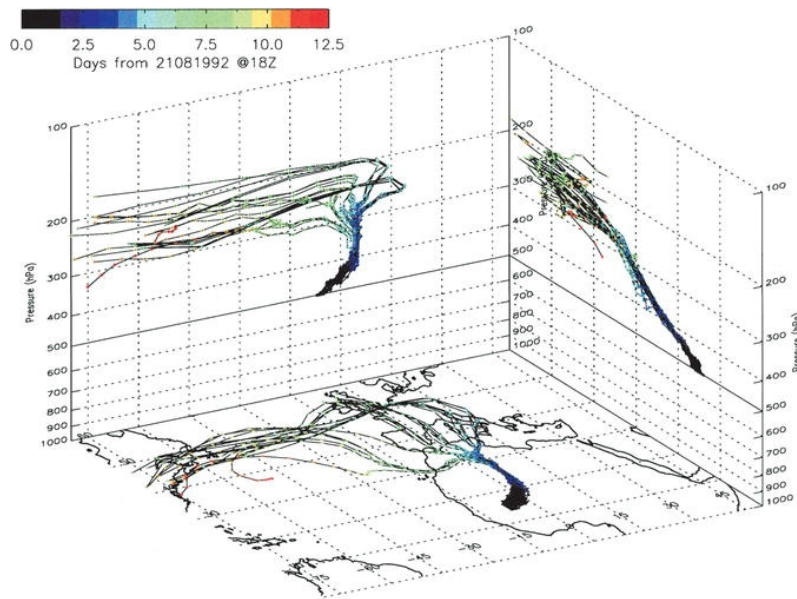
Figure 2.10: The trajectories of a dry intrusion case in August 1992 show the extratropical origin of air descending towards West Africa. Reprinted from Roca et al. (2005). © American Meteorological Society. Used with permission.

c. Dry intrusions

Extratropical Rossby waves influence moisture distribution and mesoscale convective activity over West Africa via dry intrusions. West African rainfall stems predominantly from squall lines and mesoscale convective systems (MCS) (Eldridge, 1957; Laing et al., 1999; Fink and Reiner, 2003). The evaporative downdrafts in these MCSs are intensified when dry mid-tropospheric air is present (Raymond and Jiang, 1990; Brown and Zhang, 1997). Consequently, the downdraft-induced cold pools reinforce the MCSs or help to trigger new convection (Zipser, 1977; Corfidi, 2003). Intrusions of dry air are related to a breaking extratropical Rossby wave and subsequent descent of upper-tropospheric air to mid-levels (Fig. 2.10) (Raveh-Rubin, 2017). During the monsoon period, convection over the East Sahel is favored when dry intrusions lead to very dry mid-levels from extratropical origin. With dry intrusions, MCSs last longer due to their importance for cold pools of squall lines (Roca et al., 2005). Dry intrusions can occur in connection to aforementioned cold air surges (Garreaud, 2001) and are related with the SHL variability (Chauvin et al., 2010).

d. Variability of the Saharan heat low

One key component of subtropical northern Africa during boreal summer is the SHL (Lavaysse et al. 2009; 2010a). The SHL connects and experiences modulation
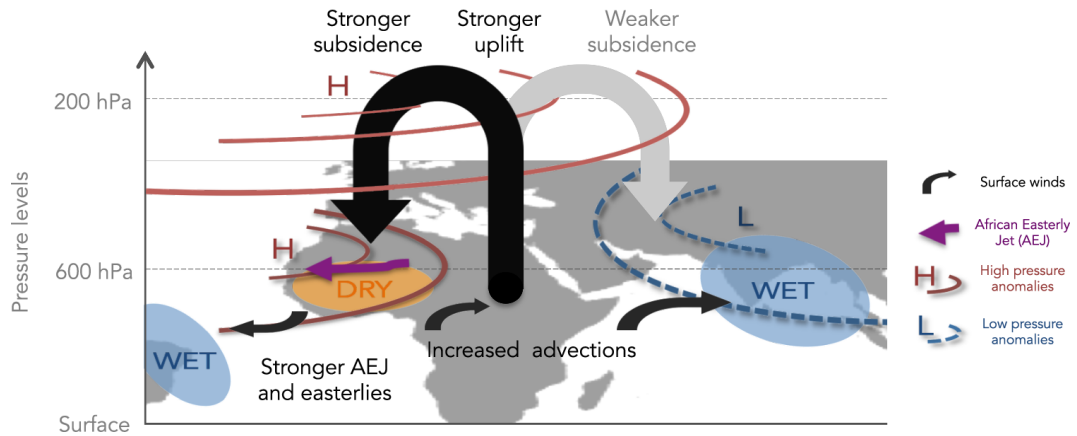
Figure 2.11: Teleconnection of the African and Indian monsoon systems. Reprinted from Vigaud and Giannini (2018). © Springer Nature. Used with permission.

by both, the tropical and the extratropical regime. It pulsates at the intraseasonal timescale of 10–25 days (Chauvin et al., 2010; Roehrig et al., 2011; Lavaysse et al., 2010b). Southward penetrating extratropical Rossby wave trains over North Africa affect the position and intensity of the SHL, mostly through increased ventilation at its western or eastern side. As an integral part of the West African monsoon system, the modification of the SHL impacts on the strength of both Harmattan and monsoonal winds and affects, therefore, rainfall variability in the Sahel approximately five days after the SHL modification. When the SHL is displaced towards the west, convection is enhanced over the Darfur region. The convective signal then propagates westward towards the Atlantic Ocean. One third of dry and wet spells in the Sahel can be explained by intraseasonal variability of the SHL (Roehrig et al., 2011). Finally, the SHL has been shown to be an important predictor of West African monsoon onset (Roehrig et al., 2011).

2.2.4 Intraseasonal teleconnections

On the intraseasonal timescale, teleconnections of remote modes affect African rainfall variability. In the extratropics, intraseasonal modes include the North Atlantic Oscillation (NAO) (Walker and Bliss, 1932), the Arctic Oscillation (AO) (Thompson and Wallace, 1998) and the Pacific/North American pattern (PNA) (Wallace and Gutzler, 1981). These extratropical intraseasonal modes also influence tropical modes such as the MJO through the excitation of Rossby wave trains (Stan et al. 2017 and references therein). Furthermore, the Indian monsoon modulates intraseasonal rainfall variability over Africa. The West African monsoon is linked to convection over the Indian subcontinent via the Walker circulation (Fig. 2.11). Wetter conditions over the Indian monsoon region correspond to drier conditions

over West Africa (Rodwell and Hoskins, 1996; Vigaud and Giannini, 2018). Due to the aforementioned links to several other modes, the intraseasonal variability has been considered a "global phenomenon", which should not be treated as a "either a purely tropical phenomenon or a purely extratropical phenomenon" (Hsu, 1996).

2.2.5 Modulation by climate modes

The discussed synoptic to intraseasonal rainfall modes are themselves affected by climate modes. Several oceanic basins feature interannual modes of variability which influence the global circulation patterns in the atmosphere such as the El-Niño/Southern Oscillation (ENSO) in the tropical Pacific (Wang et al., 2017), the Indian Ocean Dipole (Saji et al., 1999), or the Tropical Southern Atlantic mode (Enfield et al., 1999). These interannual modes modulate the activity of CCEWs (Huang and Huang, 2011). ENSO, for example, modulates the activity of Kelvin waves over Africa (Mekonnen et al., 2008; Sinclaire et al., 2015) and the MJO activity (Hendon et al., 1999). As ENSO modulates the interannual variability of the MJO, the related seasonal rainfall and the onset of the spring rainy season are modulated over East Africa (Pohl and Camberlin, 2006b). TTTs over southern Africa are also affected by the state of ENSO (Fauchereau et al., 2009; Pohl et al., 2009a), and furthermore the variability of sea surface temperature in the Atlantic (Williams et al., 2007), the Agulhas Current (Crimp et al., 1998), and the Indian Ocean (Fauchereau et al., 2009; Manhique et al., 2011). The intraseasonal variability of African rainfall also depends on even longer decadal timescales. Interannual rainfall variability over East Africa, e.g., experiences non-stationary teleconnections with several decadal climate modes (Bahaga et al., 2019). On the climate timescale scale, it has been estimated that a warming climate will lead to a 30 % stronger and more frequent MJO (Chang et al., 2015).

2.3 Predictability of rainfall variability

Accurate forecasts of rainfall variability are needed to facilitate timely actions by decision makers. Typically, this information is provided by numerical weather prediction (NWP). NWP models predict the future state of the atmosphere by numerically solving a set of primitive equations, which describes the physical cause-and-effect relationship of the atmosphere between two incremental steps in time. The initial values used to solve these equations are estimated from weather observations. Such deterministic forecasts can skillfully predict weather in the extratropics for about two weeks until the forecast error exceeds the error,
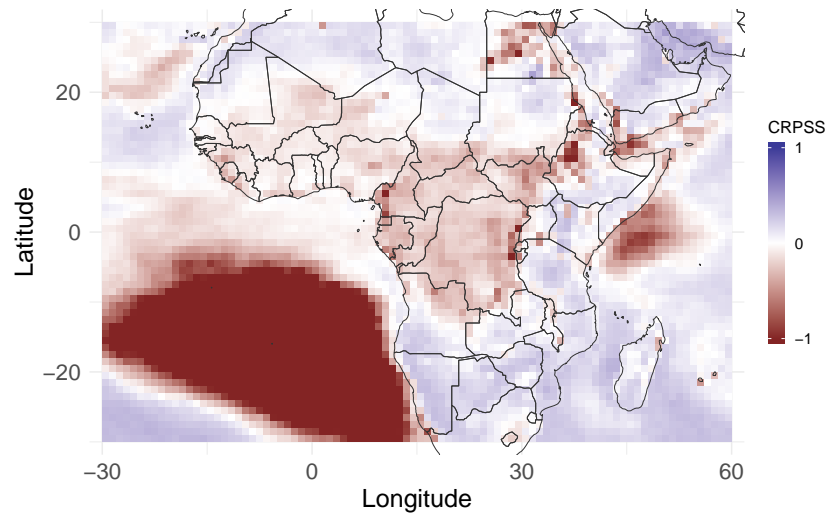
Figure 2.12: Skill of raw ECMWF forecast of 5-day accumulated rainfall over Africa during the monsoon season 2007–2014. Negative continuous ranked probability score (CRPSS) indicate no skill compared to climatology whereas a positive score denotes skill. A similar picture is obtained by Dias et al. (2018). Figure adapted from Vogel (2019). Used with permission. © 2019, Peter Vogel.

which would be obtained from a naive forecast such as climatology (Lorenz, 1982; Froude et al., 2013). Deterministic forecasts fail to represent the full non-linear, chaotic nature of the atmosphere because they only depict one of myriad possible future states of the atmosphere given the uncertainties in initial conditions (Lorenz, 1963). With increasing computational power, probabilistic NWP forecasts were therefore developed, which are used operationally since the mid 1980s (Lewis, 2005; Palmer, 2018). These ensemble prediction systems (EPSs) are similar to the Monte-Carlo method in representing model uncertainties by using an ensemble of several deterministic model runs with slightly perturbed initial values and/or slightly perturbed model physics. Finally, statistical models have been developed in addition to numerical models for rainfall prediction, which are based on mathematical relationships between current observations and a future state of the atmosphere.

In the following, this section describes the predictability and skill of deterministic and probabilisitic NWP forecasts as well as statistical forecasts of African rainfall variability on the synoptic and the intraseasonal timescale. Furthermore, several applications in early warning systems are discussed.

2.3.1 Synoptic forecasting

Despite the proven capabilities of NWP forecasts in the extratropics, the prediction of tropical rainfall remains a major challenge. Deterministic operational forecasts
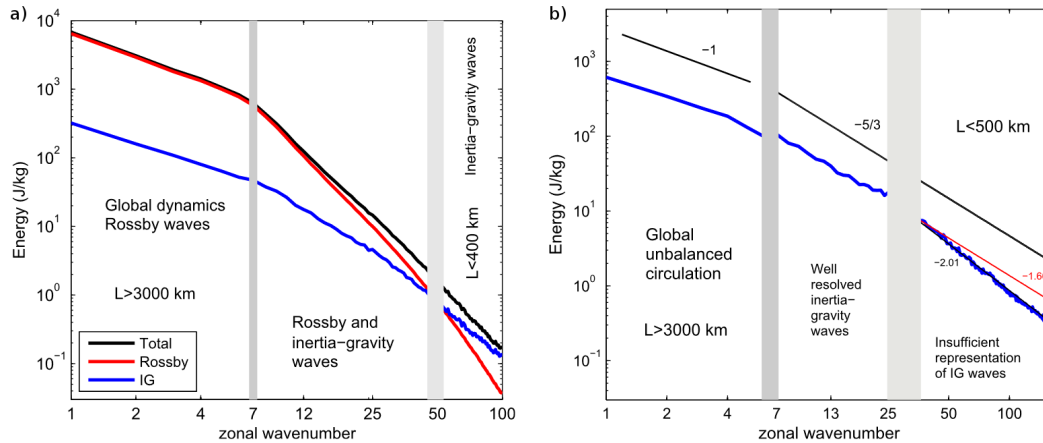
Figure 2.13: (a) Global energy in reanalysis data in dependence of zonal wavenumber. Large scale balanced waves dominate motions up to $k < 50$. (b) At smaller scales, IG wave dominate, which are not well represented in the model. Reprinted from Žagar et al. (2017). © American Meteorological Society. Used with permission.

of rainfall in the tropics with 1-day lead time were as skillful as forecasts in the extratropics for day six in 2010/2011 (Haiden et al., 2012). A thorough evaluation study over northern tropical Africa revealed that all major operational global EPS largely failed to deliver skillful predictions for one- to five-day accumulated rainfall during the period between 2007 and 2014 (Vogel et al., 2018). All raw ensembles were uncalibrated and unreliable due to model biases and underdispersive prediction of rainfall. Compared to a simple probabilistic climatological forecast, all models failed to deliver skillful predictions for even 1-day accumulated rainfall. Raw 5-day forecasts are only skillful over East Africa and in the subtropics (Fig. 2.12). The systematic errors in global EPSs stress the importance of statistical post-processing of ensemble forecasts, which often are delivered without calibration to end-users. Even after applying advanced post-processing methods, most global ensemble models could only show moderate skill, if at all. Due to the parametrization of convection, numerical models cannot adequately represent mesoscale organized convection, which is responsible for the majority of rainfall in tropical Africa (Vogel et al., 2018). Furthermore, operational analyses exhibit large errors due to few observations in this region (Parker et al., 2008; Meynadier et al., 2010; Roberts et al., 2015). In addition, errors in the intensity and phasing of atmospheric modes lead to wrong rainfall prediction, which are discussed in the next paragraph. Instead of forecasting rainfall numerically, Vogel et al. (2018); Vogel (2019) show that even a simple probabilistic climatological forecast is more skillfull in most of tropical Africa. Therefore, a promising pathway for short- to medium-range rainfall predictions will be statistical models based on spatio-temporal correlation patterns,
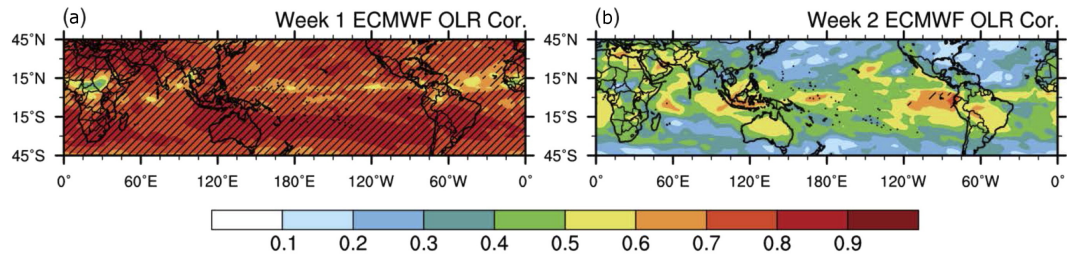
Figure 2.14: Correlation between observed and forecasted OLR with a lead time of (a) one week and (b) two weeks. Significant correlations are stippled. Reprinted from Janiga et al. (2018). © American Meteorological Society. Used with permission.

which might use additional predictors such as tropical waves from dynamical models (Vogel et al., 2018).

The skill of rainfall predictions depends on how well the phase and intensity of synoptic-scale tropical waves are forecasted. Operational forecasts of AEWs between 2007 and 2013 showed systematic errors in the position and intensity of the disturbances, although these errors have been reduced in the latter years (Elless and Torn, 2018). With increasing lead time, key features of the West African monsoon such as the AEJ disappear in global NWP models (Sultan et al., 2009). Furthermore, they lose equatorial wave energy (Dias et al., 2018). The propagation of the equatorial waves depends on convective parametrization (Lin et al., 2008; Frierson et al., 2011). The coupling between convection and wave forcing is not correctly represented in these NWP models. Inertio-gravity waves and higher-frequency Kelvin waves are predicted to propagate faster than in reality. The vertical tilt of equatorial waves in global NWP models is too low and precipitation is triggered too quickly by low-level convergence (Dias et al., 2018). A large portion of tropical motion are IG waves, whereas extratropical circulation is dominated by Rossby waves (Žagar et al., 2015, 2017). Unbalanced waves contribute to about 10% of global wave energy (Williams et al., 2008; Žagar et al., 2009) and dominate circulation at horizontal scales of approximately 500 km (Fig. 2.13a). However, global NWP models fail at assimilating and forecasting these smaller-scale unbalanced waves (Fig. 2.13b; Ying and Zhang 2017). Therefore, new assimilation schemes need to be developed specifically designed to also incorporate unbalanced motions (Žagar et al. 2005; 2012; 2016, Harlim and Majda 2013).

2.3.2 Intraseasonal forecasting

Intraseasonal forecasting is an integral part of seamless prediction (Fig. 2.14a) (Palmer et al., 2008; Ebert et al., 2013). The intrinsic predictability (Sun and Zhang, 2016) of intraseasonal rainfall is lower in the extratropics than in the
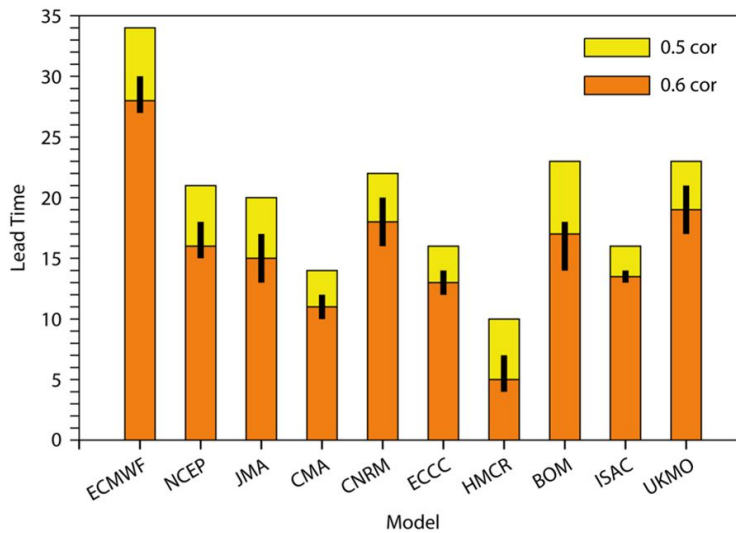
Figure 2.15: Forecast skill of the MJO in major global NWP models. Reprinted from Vitart and Robertson (2018). © Springer Nature, CC BY 4.0 ©①.

tropics, in contrast to synoptic forecasting, where it is the other way around (Fig. 2.14b) (Žagar, 2017). Predictability depends on the temporal and spatial scales of atmospheric features (Buizza and Leutbecher, 2015; Ying and Zhang, 2017). Most predictability on the intraseasonal timescale stems from the planetary-scale MJO (Zhang, 2013). The estimated theoretical limit of predictability lies at around 35–45 days (Neena et al., 2014). Since the discovery of the MJO in the 1970s, several numerical and statistical models have been developed with increasing ability to predict the phenomenon skillfully. Until the early 2000s, statistical models still outperformed numerical models (Kim et al., 2018). Since the introduction of probabilistic numerical forecasts, the forecast horizon of the MJO has been constantly extended (Fig. 2.15). Predicatbility of the MJO depends on its intensity (Waliser et al., 2003) and phase (Kim, 2017). Between 2006 and 2008, the phase and intensity biases were considerably reduced in the European Centre for Medium-Range Weather Forecasts (ECMWF) forecasts (Fig. 2.15) (Vitart and Robertson, 2018). Still, most EPS models struggle to accurately predict the propagation of the MJO into the Pacific and show a so-called "prediction barrier" over the Maritime Continent (Vitart et al., 2007; Kim et al., 2016; Liu et al., 2017). Furthermore, different models have systematic biases on the intraseasonal timescale in phase and amplitude of CCEWs (Janiga et al., 2018) and in important features such as the SHL and the Inter-tropical discontinuity (ITD) (Lélé and Lamb, 2010; Louvet et al., 2016). Finally, additional predictability of African rainfall on the intraseasonal scale stems from the Indian monsoon (Vigaud and Giannini, 2018).

2.3.3 Applications in early warning systems

Societies in Africa are vulnerable to rainfall variability as outlined in the introduction. Natural risk management relies on predictability at synoptic to intraseasonal timescales as valuable information (White et al., 2017). To avert detrimental impacts of prolonged droughts or excessive rains, early warning systems (EWS) support decision makers and prepare for natural disasters involved with rainfall variability (Scheffer et al., 2009; Lenton, 2013). Operational weather forecasters can consult real-time filtered information on tropical waves (Wheeler and Weickmann, 2001), the MJO (Wheeler and Hendon, 2004; Kiladis et al., 2014), and balanced and unbalanced wave modes (Žagar et al., 2015). Tailored weather forecasts are further disseminated via the internet such as in the National Oceanic and Atmospheric Administration (NOAA) Global African desk (Thiawa and Kumar, 2015) or by private companies such as Ignitia (`http://www.ignitia.se/`) via mobile phones (Caine et al., 2015). For agriculturalists valuable information stems from predictions of the monsoon onset (Fontaine et al., 2008; Vellinga et al., 2013), drought (Vicente-Serrano et al., 2012) and flood forecasts (Alfieri et al., 2013), as well as crop forecasts (Macdonald and Hall, 1980; Meinke and Stone, 2005), which use rainfall as predictors. Furthermore, famine relief organizations benefit from specific famine (Verdin et al., 2005) and livestock EWSs including forage and market forecasts (Kaitho et al., 2007). Finally, rainfall variability is considered in crop insurances (Barnett and Mahul, 2007; Jensen and Barrett, 2016), economic forecasting (Benson and Clay, 2004; Barrios et al., 2010; Rosenzweig and Udry, 2014), and malaria EWSs (Thomson and Connor, 2001; Cox and Abeku, 2007). Aforementioned forecast systems have several challenges including large model errors, missing model verification and quantification of uncertainty (White et al., 2017). An additional challenge is the adequate communication of the forecasts (Basher, 2006; Coughlan de Perez and Mason, 2014), in particular of probabilisitic information (Stephens et al., 2012).

3 | Research questions

The previous chapter has systematically reviewed different synoptic to intraseasonal modes of rainfall variability over Africa. As the different parts of the African continent exhibit very diverse meteorological conditions, this dissertation needs to focus on a specific region and places, therefore, a special emphasis on northern tropical Africa (5°–15°N). This region is socio-economically important due to its high population density and the strong dependence of the semi-arid Sahel zone on rainfall (Jalloh, 2013). Northern tropical Africa receives its main rainfall during the 'full monsoon' in the boreal summer and the months before and after the onset of the monsoon in the so-called 'transition season'. Thus, this study focuses on these two seasons. All fundamental tropical wave types that affect rainfall variability in northern tropical Africa, namely the MJO, ER, MRG, Kelvin, EIG waves and TDs (including AEWs), are specifically analyzed. The study puts the results in context with the other atmospheric modes described in the literature review, which are either largely explainable by aforementioned wave types (e.g. the QBZD and Sahel mode) or are of extratropical origin. In the following the research questions are elaborated, which contribute to reaching the overarching research aim of this dissertation. Following this aim, the study is structured in three parts. The first part quantifies the influence of tropical waves on rainfall variability. The second part investigates the involved mechanisms and the final part analyzes the potential of tropical waves for forecasting rainfall. In the following, the proposed research questions are motivated and, then, stated for all three parts.

Despite the importance of the different tropical wave modes on the variability of rainfall on synoptic to intraseasonal timescales, which the previous chapter outlined, as of today, a systematic investigation of the relative influence of the different wave types on rainfall variability over northern tropical Africa has not been performed. Several questions concerning the modulation of rainfall by the different waves remain open. The quantitative influence of tropical waves and the relative contribution to rainfall variability at the different timescales are not well documented and a consistent analysis for all waves using a unified method

is pending. Therefore, operational forecasters in the region mostly rely on their experience or subjective view when assessing tropical waves (B. Lamptey, personal communication, 2017). The aim of the first part of this dissertation is therefore to close this gap and compare the influence of the major types of tropical waves for northern tropical Africa using satellite products and in-situ measurements, and one consistent method for all waves. The forecast verification study of Vogel et al. (2018) has stressed the need to use data from rain gauge networks due to large discrepancies between satellite and rain gauge accumulations in this region at daily time scales. Thus, the present study also uses an extensive database of African rain gauges. The first part of the study in Chapter 5 addresses the following research questions in order to systematically compare the influence of tropical waves on precipitation over northern tropical Africa:

RQ 1a Where, in which season, and how strongly do tropical waves contribute to rainfall variability over northern tropical Africa?

RQ 1b What is their effect on spatial precipitation patterns and observed rainfall amounts?

RQ 1c What is their relative contribution to rainfall variability on different timescales?

RQ 1d Do different types of tropical waves superimpose in a non-linear way?

The influence of tropical waves on rainfall depend on their influence on the local dynamics and thermodynamics. Several studies have analyzed the (thermo-) dynamic signatures of single wave types over this region in detail (see literature review). The comparison of results for different waves is hampered by the use of different methodologies in the respective studies. So far no systematic comparison of all tropical waves has been performed using one consistent method. The aim of the second part of the study is to close this gap and to provide a comprehensive analysis of the modulation of the West African monsoon (WAM) by tropical waves. This part focuses specifically on the effect of tropical waves on important components of the WAM such as the monsoon layer, ITD position, SHL and AEJ. Additional attention is paid to the conditions for the organization of mesoscale convective systems (MCSs, Houze 2004), which are responsible for the majority of rainfall in West Africa (Eldridge, 1957; Laing et al., 1999; Fink and Reiner, 2003) and commonly cause extreme precipitation (Engel et al., 2017; Lafore et al., 2017). The first part of the study (Chapter 5) shows that the MJO

and ER waves over northern tropical Africa are associated with rainfall far into the subtropics during the extended monsoon season. The eastward-tilted precipitation pattern resembles tropical cloud plumes (Knippertz, 2003; Knippertz et al., 2003; Knippertz and Martin, 2005; Fröhlich et al., 2013). It is not known whether the precipitation patterns associated with ER waves and the MJO are triggered by the same dynamical process as in wintertime tropical plumes. In order to make use of as much data as possible in this data scarce region, reanalysis data and in-situ measurements by radiosondes are employed. This part of the study, presented in Chapter 6, addresses the following research questions:

> **RQ 2a** How do circulation patterns associated with tropical waves modify the WAM and the moisture distribution?
>
> **RQ 2b** How do tropical waves influence the vertical profile of temperature, moisture, and wind and what does this imply for rainfall generation and organization of MCSs?
>
> **RQ 2c** How is rainfall triggered over the Sahara by the MJO and ER waves and do they interact with the extratropical circulation?

The lack of skill in current global NWP forecasts in tropical Africa stresses the need for novel rainfall forecasting methods for this region (Vogel et al., 2018; Vogel, 2019). This raises the question whether alternative forecasting methods, such as statistical models, could exploit predictability from systematic spatio-temporal correlation patterns. We hypothesize that tropical waves carry predictability on the synoptic to intraseasonal timescale. To our knowledge, no statistical models for tropical rainfall based on spatio-temporal correlation patterns has been developed so far. Vogel et al. (2018) showed that even a relatively simple probabilistic climatology has the skill of current postprocessed global NWP forecasts. Therefore, we hypothesize that a statistical models based on the probabilistic climatology, which uses these spatio-temporal correlations as additional predictors, can outperform current NWP models. This part is more general than both previous parts and will also partially deal with rainfall variability in the entire tropics. The addressed research questions in the final part of the study in Chapter 7 are as follows:

RQ 3a What are the observed and theoretical spatio-temporal properties of tropical waves and what does this imply for their potential as predictors for rainfall variability?

RQ 3b How can statistical models exploit existing spatio-temporal correlation patterns in order to skillfully forecast rainfall variability over Africa?

RQ 3c What is the potential for applying such a statistical model to the forecasting rainfall variability in the rest of the tropics?

4 | Data and methods

4.1 Study area

This study focuses on two 5°-wide latitudinal bands in northern tropical Africa (Fig. 4.1): the Guinean (5°–10°N) and Sahelian band (10°–15°N). For a more detailed analysis, two boxes in West Africa were defined where most rain gauges are available: the Guinea Coast (5°W–5°E, 5°–10°N) and the West Sahel (5°W–5°E, 10°–15°N). The analysis was stratified in two seasons: the full monsoon ranges from July to September; the three months before the onset of the monsoon (April to June) and October are collectively labeled as the transition season (Sultan et al., 2003; Thorncroft et al., 2011); combining both, the extended monsoon season stretches from April to October.

4.2 Data

The modulating impact of tropical waves on rainfall over northern tropical Africa was examined in three different rainfall datasets. The Tropical Rainfall Measuring Mission (TRMM) 3B42 V.7 precipitation dataset Precipitation Processing System (PPS) at NASA GSFC (2018) is arguably the most accurate gridded rainfall product for the tropics (Maggioni et al., 2016), with a record long enough for climatological studies. TRMM 3B42 is a gauge-adjusted combined microwave-infrared precipitation estimate (Huffman et al., 2007). It has been used in several studies of tropical waves (e.g., Yasunaga and Mapes 2012; Lubis and Jacobi 2015). The 3-hourly product has a spatial resolution of 0.25°×0.25°. The analyzed time period ranges from 1998 to 2016. With full spatial coverage in the tropics and a high temporal and spatial resolution, the TRMM dataset is a preferable dataset for the study of tropical waves in a rain gauge sparse environment such as tropical Africa.

For a 33-year period from 1981 to 2013, the Climate Hazards Group InfraRed Precipitation with Station data V.2 (CHIRPS) provides daily, gauge-
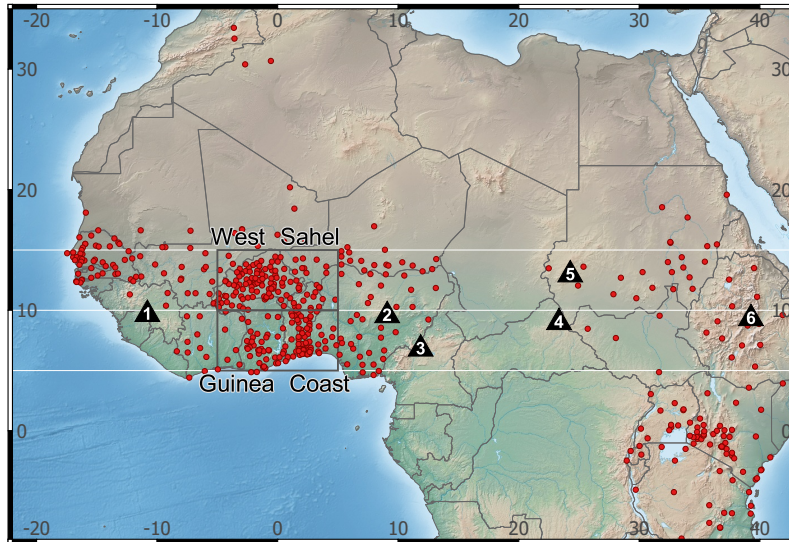
Figure 4.1: Topographic map of the study area. Available stations with a minimum of 50% observations during 1981 to 2013 are indicated by a red dot. The two boxes show the location of the Guinea Coast and West Sahel used in this study. Black triangles show prominent orographic features that are discussed in the text: 1. Guinea Highlands, 2. Jos Plateau, 3. Cameroon Line, 4. Bongo Massif, 5. Darfur Mountains, and 6. Ethiopian Highlands. Reprinted from Schlueter et al. (2019a). © 2019, American Meteorological Society. Used with permission.

calibrated, infra-red based precipitation estimates (Funk et al., 2015). The dataset has a resolution of $0.25° \times 0.25°$ and is available over land masses only. The daily CHIRPS product that was used is disaggregated from five-day accumulated values. Due to the disaggregation, CHIRPS can only be used with care at daily timescales and will likely underestimate the variability when compared to rain gauge observations (C. Funk, 2017, personal communication). At 0°E, the daily values range from 00 to 00UTC+1d. This dataset has the advantage of a long record and a high spatial resolution. On the other hand, it has a comparatively low temporal resolution and is only available over the continent.

In situ rain gauge measurements are essential to validate the results obtained from satellite observations. The Karlsruhe African Surface Station Database (KASS-D) provides daily measurements from an extended rain gauge network. The 24-h accumulation period ranges for most stations from 06 UTC to 06 UTC. Stations were required to have at least 50 % of observations during the period from 1981 to 2013 to match with the analyzed time period of the CHIRPS dataset. Additionally, stations with less than 1 % of non-zero observations were excluded, resulting in a total number of 524 stations (Fig. 4.1).

A good proxy for tropical convection is OLR (see review in Arkin and Ardanuy 1989). OLR has been successfully applied in other studies of tropical waves (e.g., Wheeler and Kiladis 1999; Roundy and Janiga 2012). Therefore, the

daily interpolated NOAA OLR dataset (Liebmann and Smith, 1996) was used to filter the waves in the period from 1981 to 2013. The spatial resolution of this dataset is 2.5°×2.5°. To demonstrate the effect of orography, we used the 5-minute gridded ETOPO5 elevation dataset (NOAA, 1988).

The modulation of dynamics and thermodynamics by tropical waves was examined using reanalysis data. Reanalysis products have the advantage of global coverage and a long temporal record. ERA-Interim is the most recent reanalysis product provided by the European Center for Medium-Range Weather Forecasts (ECMWF) (Dee et al., 2011), until it will be fully replaced by ERA-5. Several dynamical and thermodynamical fields were downloaded from the Meteorological Archival and Retrieval System (MARS) archive (`http://apps.ecmwf.int/datasets/`). The analyzed vertically integrated fields of Convective Available Potential Energy (CAPE), moisture flux, and moisture flux convergence are computed from surface to the top of the model domain (0.1 hPa) and were provided by the ECMWF.

Reanalyses have large biases in humidity fields but also in wind and temperature over the measurement-sparse African continent (Agustí-Panareda et al., 2010a,b; Roberts et al., 2015). Thus, in-situ measurements by radiosondes are a valuable supplement to accurately assess the modulation of atmospheric profiles. For this purpose, quality-controlled radiosonde measurements from the Integrated Global Radiosonde Archive (IGRA) Version 2 (Durre et al., 2016) were analyzed, which were downloaded from `https://data.nodc.noaa.gov/cgi-bin/iso?id=gov.noaa.ncdc:C00975`. Due to a relatively high data availability, 12 UTC ascents at Abidjan Airport (13.48°N, 2.17°E) and Niamey Airport (5.25°N, 3.93°W) were chosen to illustrate the modulation over the Guinea Coast box and the West Sahel box. Composites of radiosonde ascents from Abidjan were calculated for the more equatorial MRG and Kelvin waves, as both are predominantly equatorial phenomena, whereas the influence of ER waves and TDs was analyzed using the Niamey data, as both wave modes have a stronger imprint further to the north (see Figs. 5.2–5.4). Between April to October 1981 to 2013, 1370 measurements are available for Niamey (19.4 % of the study period) and 1214 measurements (17.2 %) for Abidjan. As reference for the observed rainfall, the daily rain gauge observations were obtained from the Karlsruhe African Surface Station Database (KASS-D).

The influence of the MJO was compared with the NAO, AO, and PNA. Daily normalized indices for these modes were downloaded from `ftp://ftp.cpc.ncep.noaa.gov/cwlinks`. Further information on how the indices

are calculated can be found at `http://www.cpc.ncep.noaa.gov/products/`
`precip/CWlink/daily_ao_index/history/method.shtml`.

4.3 Wave filtering

Six different wave types were analyzed in this study, sorted according to their scale: MJO, ER, MRG, Kelvin, TD, and EIG (n=0, hereafter simply called "EIG") waves. WIG and higher meridional mode EIG ($n > 1$) could not be analyzed because their frequency is too high to be filtered in daily data. The activities of the tropical waves were filtered in the wavenumber-frequency spectrum following the method developed by Wheeler and Kiladis (1999). The filter settings for wavenumber, frequency, and equivalent depth ranges are obtained from previous studies on tropical waves studies (Table 4.1). No symmetric/antisymmetric decomposition has been done as the analyzed bands are entirely north of the equator. A small overlap of the filter bands of Kelvin and EIG waves, and of TD and MRG waves exists, which is likely not important. It has to be noted that the wave signal, as captured by the filter bands, can be contaminated by random noise. The obtained signal must be interpreted as an overestimate of the wave modulation since wave motions generally stay out against the background noise by less than 30 % (Wheeler and Kiladis, 1999).

The modulation of precipitation by tropical waves was investigated for two periods: (a) for the shorter period 1998 to 2016, the influence of tropical waves was analyzed in the TRMM dataset; (b) for the longer period 1981 to 2013, CHIRPS and KASS-D were examined. Table 4.2 shows the structure of the results section and lays out which dataset has been used in which section of the study. For the analysis of the rainfall patterns and modulation intensities of each wave, OLR is used by default for the wave filtering to derive the local wave phase. Precipitation anomalies or quantile deviations are then projected onto this composite. TRMM data have also been used in place of OLR to determine the wave phase (supplemental material) to assess the robustness of the composite. For the analysis of the contribution of each wave to the rainfall variability and the wave interaction, TRMM has been wave-filtered directly because of its global coverage, which is required for the wave-filtering.

The filtering was done using the NCAR Command Language (NCL) *kf_filter* function. This function is based on a Fast Fourier Transform (FFT), which does not allow missing values in the entire analyzed latitudinal band. For the longer period from 1981 to 2013, we rely on the interpolated OLR dataset as a proxy

Table 4.1: Analyzed tropical waves with their corresponding wave characteristics. The filter settings for the period T, the planetary zonal wave number k, and the equivalent depth h_e were used to extract the wave signal. Corresponding references are given.

| Acronym	Wave	Direction	T (days)	k	h (m)	Source
MJO	Madden-Julian Oscillation	Eastward	30 – 96	0 – 9	-	Roundy and Frank (2004)
ER	Equatorial Rossby wave	Westward	9 – 72	1 – 10	1 – 90	Kiladis et al. (2009)
MRG	Mixed Rossby-gravity wave	Westward	3 – 8	1 – 10	8 – 90	Wheeler and Kiladis (1999)
Kelvin	Kelvin wave	Eastward	2.5 – 20	1 – 14	8 – 90	Wheeler and Kiladis (1999)
TD/AEW	Tropical disturbance/ African Easterly Wave	Westward	2.5 – 5	6 – 20	-	Lubis and Jacobi (2015)
EIG	Eastward inertio-gravity wave	Eastward	1 – 5	0 – 14	12 – 50	Yasunaga and Mapes (2012)

for precipitation, although, the relationship between OLR and precipitation is weak over West Africa (see Fig. A.1.1). CHIRPS is available only over the continents and could thus not be used for filtering. The 3-hourly TRMM product exhibits minor observational gaps. Over Africa, these gaps are negligible with an average amount of missing data of about 0.005 % to 0.05 %. All missing values in TRMM were filled with zeros. The effect of this primitive gap filling method for the wave filtering is expected to be negligible over Africa where gaps are rare. As a side remark, more caution should be applied when the 3-hourly TRMM product is used for wave filtering over the Maritime Continent for the period prior to 2007, where about 1% of the data is missing due to downtimes of a geostationary infrared satellite.

The filtering method has no constraints for the associated circulation. Wave signals can be contaminated by physically different phenomena, missed by the filter due to Doppler shifting, or double counted due to the partial overlap of wavenumber frequency spectra. Other filters have been developed that are based on the horizontal structure functions obtained from equatorial wave theory (Yang et al., 2003), use wavelet analysis (e.g. Kikuchi and Wang, 2010; Roundy, 2018), or 3D normal mode functions (Castanheira and Marques, 2015). Nonetheless, the here applied method has been successfully used in previous studies over Africa (e.g. Mounier et al. 2007, 2008; Janicot et al. 2009, 2010; Ventrice and Thorncroft 2013; Mekonnen

Table 4.2: Structure of the study and use of datasets. The table lists the subsections in 5 and outlines which datasets have been used to filter for the tropical waves and which precipitation datasets have been subsequently plotted in the corresponding figures.

Section	Topic	1. Wave filtered dataset	2. Plotted dataset (raw, composite, correlation)	Figs.
5.1	Mean climate	-	TRMM	5.1
5.2	Total variance of wave activity	TRMM	TRMM	5.2
5.3	Modulation patterns	OLR	CHIRPS, KASSD	5.3–5.4
5.4	Modulation intensity	OLR	CHIRPS	5.5
		OLR	KASSD	5.5–5.6
		TRMM	TRMM	5.5
5.5	Relative contribution to precipitation	TRMM	TRMM	5.7–5.9
5.6	The role of orography	TRMM	TRMM	5.7–5.9
5.7	Wave interactions	TRMM	TRMM	5.10
6.1	Circulation patterns and moisture modulation	OLR	CHIRPS, ERA-Interim	6.1–6.5
6.2	Vertical structure and mechanism of rainfall modulation	OLR	ERA-Interim	6.6
		OLR	IGRA	6.7
6.3	Relationship to extra-tropical Rossby waves	OLR	-	6.8
		OLR	RMM	6.9
		OLR	CHIRPS, ERA-Interim	6.10
7.1	Tropical waves as predictable spatio-temporal modes	TRMM	TRMM	7.1–7.3
7.2	Theoretical spatio-temporal properties	-	-	7.4–7.5
7.3	Statistical forecasting using spatio-temporal correlations	-	TRMM	7.6–7.8
7.4	Implications for tropical rainfall forecasting	TRMM	TRMM	7.9
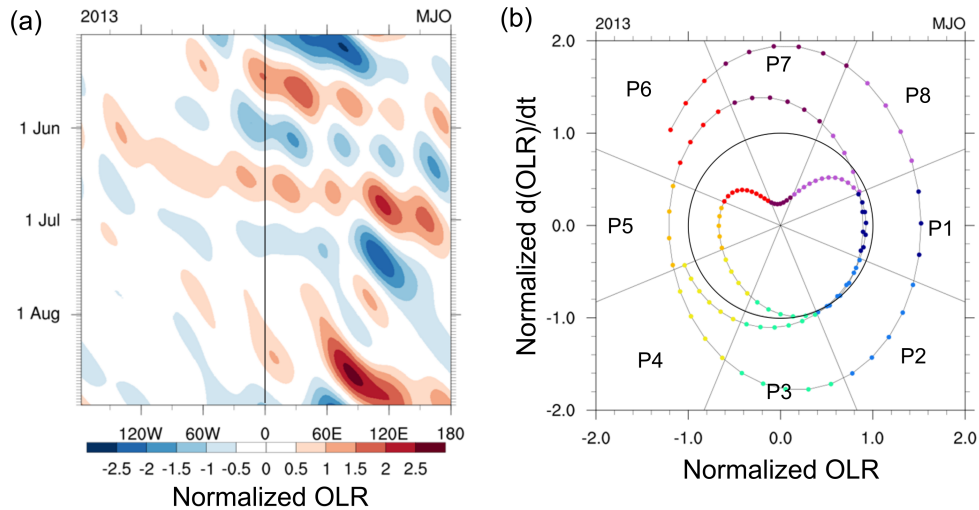
Figure 4.2: Construction of composite plots. (a) Example of a Hovmoeller diagram of an MJO filtered normalized OLR signal. Negative anomalies correspond to wet conditions. (b) Example for the MJO in a phase diagram. Plotting the wave filtered signal at 0°E (black line in (a)) against the time derivative at 0°E, results in a phase diagram of the local wave activity. The phase space is divided into eight phases (coloring); dates when the amplitude is less than one standard deviation are considered to be inactive. Reprinted from Schlueter et al. (2019a). © 2019, American Meteorological Society. Used with permission.

and Thorncroft 2016). Chapter 6 shows that composites of dynamical fields using this method are able to reproduce the circulation patterns that are expected from wave theory.

As pointed out by section 2.1.5, several empirical orthogonal functions based global metrics for the MJO activity have been proposed, such as the RMM (Wheeler and Hendon, 2004) index and the OLR-based MJO index (Kiladis et al. 2014). These indices have the advantage of measuring the global propagation of the MJO and being less affected by background noise. Over Africa conversely, the MJO manifests itself rather as a standing signal (Alaka and Maloney, 2012, 2014, 2017). A local wave filtering, as applied in this study, will thus mainly depict the standing signal over Africa and might miss the global propagative signal as seen over the Indian and Pacific Oceans.

4.4 Composite analysis

Composites of the waves were constructed to investigate the propagation and structure of modulation patterns by averaging rainfall anomalies over all dates during the extended monsoon season when the wave is in a specific phase based on the OLR signal (Fig. 5.3–5.4). A local wave phase and amplitude is defined following the method initially developed by Riley et al. (2011) for the MJO.

The filtered wave signal and its corresponding time-derivative are calculated for a reference location in West Africa at 0°E and 5°–15°N (Fig. 4.2a). Both fields are standardized by dividing by the standard deviation of the respective field. The phase diagram is then split in eight equal phases (Fig. 4.2b). Phase 1 refers to a local dry phase over the reference location, phase 5 to the wet phase; during phase 3 and 7 the wave is in its neutral phase, while the rest of the phases are transition phases. During dates when the amplitude of the wave activity is less than one standard deviation, the wave is considered to be inactive. For a more detailed description of the calculation of wave phases, the reader is referred to Yasunaga and Mapes (2012) and van der Linden et al. (2016), where this approach is also applied to study the local influence of tropical waves. For all waves about 400–450 days are available in each phase. Additional maps showing the anomalies based on TRMM filtered waves instead of OLR are available in the supplementary material (Figs. A.1.7–A.1.12). These maps are not as smooth as the plots obtained from CHIRPS, because the sample size is smaller due to the shorter period from 1998–2013; they have, however, the advantages that the wave signal is directly filtered from precipitation instead of OLR and that they include rainfall anomalies over the ocean. As a side remark, it was tested whether OLR-filtered TRMM composites are less noisy. However, the noisiness was not removed and the general patterns did not change significantly (not shown). Statistical significance of the anomalies in the composite analysis (Figs. 5.3–5.4) is calculated using non-parametric bootstrapping. Significance was tested at a 5 % level using a sample of 1000 repetitions. The compositing method mostly removes the background noise and the resultant patterns reflect at least to first order the linear relationship to the analyzed wave.

To investigate the involved mechanisms, composites of several dynamic and thermodynamic fields were calculated for all days when the respective wave is in each phase (Figs. 6.1–6.3). Lower-tropospheric wind and upper-level divergence fields are used to portray the dynamic structure. The moisture transport is analyzed using anomalies of moisture flux, moisture flux convergence, precipitable water (PW), and CHIRPS precipitation during all phases. A spatial smoothing of 2° and 5°, respectively, was applied to wind and moisture flux divergence fields. The position of the ITD gives an estimate of the northward extent of the monsoon layer. The ITD is commonly indicated by the isoline of 14 °C dew point temperature at 2 m (Buckle, 1996). Exemplarily, plots of the waves in a neutral and wet phase are presented (Figs. 6.1-6.3). Composites of all eight phases can be found in the supplementary material (Figs. A.2.1–A.2.12)

The influence of tropical waves on the organization of MCSs was analyzed using three variables that are known to be key ingredients for MCSs (Nicholls and Mohr, 2010; Maranan et al., 2018). CAPE is a general measure for atmospheric instability and the strength of convective updrafts (Moncrieff and Miller, 1976). Secondly, dry mid-levels intensify evaporative downdrafts in MCSs (Raymond and Jiang, 1990; Brown and Zhang, 1997). These downdrafts induce cold pools, which reinforce the MCS (Zipser, 1977; Corfidi, 2003). The strength of downdrafts was estimated using relative humidity in $500\,\mathrm{hPa}$ (RH_{500}) following Roca et al. (2005). Finally, low-level wind shear is necessary for MCSs to separate up- and downdrafts and support longevity of the system (Browning and Ludlam, 1962; Rotunno et al., 1988). Here, we use the total wind difference between 600 and $925\,\mathrm{hPa}$ ($Shear_{600\text{-}925}$). Mean CAPE, RH_{500}, and $Shear_{600\text{-}925}$ anomalies were calculated for each phase in the Guinea Coast and West Sahel boxes.

Mean anomalies of all (thermo-) dynamical fields were calculated with respect to the climatology from 1979 to 2016. Significance in Figs. 6.1–6.6 and 6.10 was tested at the 5 %-level using non-parametric bootstrapping and $n = 1000$ repetitions. Wind anomalies are considered significant when either the zonal or meridional anomaly was significantly different from zero.

4.5 Normalization of precipitation

The composite maps of rainfall require a prior normalization. Northern tropical and subtropical Africa features a wide range of different climates. Annual precipitation ranges from more than 2500 mm yr^{-1} in coastal perhumid areas of western and central Africa to less than 100 mm yr^{-1} in the hyperarid areas in the Saharan desert (Fink et al., 2017). In order to make the effect of tropical waves on precipitation anomaly patterns comparable for these very diverse climates, precipitation values need to be normalized. Using total rainfall anomalies, the modulation in drier regions would not be visible. Indices like the Standardized Precipitation Index (McKee et al., 1993) cannot be calculated on the daily timescale. Here, we propose to use a quantile based approach instead, in order to derive normalized daily precipitation anomalies against a climatological reference. An adjusted definition of quantiles was used to account correctly for identical values and, in particular, the many zero observations in hyperarid regions. We define the quantile q for an observation y and set of climatological observations O of size N as

$$q(y) := \frac{|\{a \in O | a < y\}| + \frac{1}{2}|\{b \in O | b = y\}|}{N}. \tag{4.1}$$

In other words, q gives the percentage of observations a that are smaller than y plus half the percentage of observations b that are equal to y, both relative to the total number of observations. The later part is done to equally weigh observations with the same value. By definition, the median of the climatology equals to $\tilde{q} = 50\%$. Anomalies are then calculated as deviations from the median, resulting in quantile anomalies as measured in percentiles $a = (100q - 50)\%$. This approach allows to compare precipitation anomalies of different climates.

To derive a reasonable sample for the reference climatology, the concept of an extended probabilistic climatology is used (see Vogel et al. 2018 for a more detailed discussion). To increase the sample size and reduce the sampling error, the climatology was defined as a set of observations $\pm$ 7 days around the respective day of the year. A sample of $\pm$ 7 days reasonably minimizes the sampling error and bias (Vogel et al. 2018, Fig. S1 in their supplementary material). Larger windows increase the bias due to different climatological settings at the beginning and end of the window.

4.6 Modulation intensity

Daily rainfall anomalies were computed for the period from 1981 to 2013 for CHIRPS and KASS-D and for the period from 1998 to 2013 for TRMM. Then, the average anomaly during each phase was plotted. For the two focus regions in West Africa, the modulation intensity was measured for all three precipitation datasets. 112 stations are located in the Guinea Coast, whereas the West Sahel box includes 129 stations (Fig. 4.1). The wave activity in both regions was calculated from OLR for the Guinean (5°–10°N) and Sahelian (10°–15°N) zones, respectively, at 0°E. Most of the stations measure from 06 to 06 UTC+1d. In order to remove the time lag of six hours, we shifted the curve for KASS-D by the estimated length of six hours measured in wave phases:

$$\Delta P = \frac{6\,\text{h}}{T/8},$$ (4.2)

where T equals to the mean period of the filtered wave signal as determined by the MATLAB function *meanfreq()*.

The distribution of modulation intensity as seen by different stations was also calculated for both seasons. The mean modulation intensity for each station was calculated by subtracting the mean precipitation in the wettest and driest phase of the eight phases defined above. Due to potential shift between OLR and the

observed station precipitation, the wettest phase is allowed to fall into phases 4–6, whereas the driest phase can lie in phases 8–2.

Kernel density estimation (KDE) has been used to visualize how the modulation intensities vary for the different stations. Commonly, histograms are used to visualize discrete sample of observations. Yet, histograms have disadvantages when visualizing probability density functions (PDFs) of finite samples: They are discontinuous and their shape highly depends on the choice of bin width; additionally, the interpretation of several overlying histograms is rather difficult. A non-parametric alternative to histograms is KDE. In order to create a smooth and, continuous PDF, each observation is weighted with a kernel function. As kernel function we chose a normal distribution. Results did not differ significantly with a different choice of kernel. The bandwidth h of the kernel was calculated following the rule-of-thumb by Freedman and Diaconis (1981):

$$h = \frac{2 \cdot IQR}{N^{\frac{1}{3}}},\tag{4.3}$$

where IQR is the inter-quartile range and N the sample size. An illustrative review explaining KDE and describing the advantages of this method can be found in Gonzales-Fuentes et al. (2015).

4.7 Correlation analysis

The influence of the different tropical waves is expected to depend on the timescale. For example, daily rainfall variability will be mainly driven by waves with a high frequency such as TDs, whereas weekly accumulated rainfall will be mainly determined by low-frequency waves such as the MJO. In order to test how much of the rainfall variability on different timescales can be explained by the modulation of tropical waves the linear correlation coefficient between the rainfall variability on the specific timescale and the wave filtered signal is calculated. In a first step, the variability on different timescales was calculated, applying a running mean of one, three, seven, and 20 days as well as 1° in longitude on the mean TRMM precipitation in the Guinean and Sahelian bands for the transition and full monsoon seasons from 1998 to 2016. This way, the variability on the respective shorter timescales is removed and only the variability on longer timescales is retained. The data are then correlated at each longitude with the wave filtered TRMM signal in the same band. The squared correlation coefficients estimate the explained variance of the rainfall by each wave in this band and during the respective season.

In order to visualize how the correlation varies within the Guinean and Sahelian bands, the correlations of all waves at each longitude were stacked on top of each other for all timescales (Figs. 5.7–5.9). The sum of all correlations should be considered as a maximum percentage that can be explained by tropical waves, as some of the wave bands have small overlaps, and no wave interactions are taken into account. Random noise does not systematically affect the linear correlation, so the correlation shows to first order how much the wave modes contribute to total rainfall variability.

Statistical significance of the correlation coefficients was calculated using a one-sided t-test at a significance level of $p < 0.05$. As both time series are autocorrelated in time, the significance test requires a reduced number of degrees of freedom. For two Gaussian distributed, autocorrelated timeseries x and y of a length N, the reduced degree of freedom DF_{eff} is calculated using

$$DF_{eff} = \frac{N}{1 + 2\sum_{l=0}^{N-1} \frac{N-l}{N} K_x^*(l) K_y^*(l)} + 1, \tag{4.4}$$

where $K_x^*(l)$ and $K_y^*(l)$ are the autocorrelation functions of both time series (Taubenheim 1974, cited by Fink and Speth 1997).

4.8 Wave interactions

The interactions between different types of tropical waves were tested. The mean filtered TRMM precipitation was calculated for the Guinea Coast (5°–10°N, 0°E) and the West Sahel (10°–15°N, 0°E) for the extended monsoon season. Dates when the filtered precipitation exceeded ±1 standard deviation were defined as wet and dry phases of the wave. On average, about 4000 observations fall in each phase for all waves. The average wave-filtered signal in the wet and dry phases is called the primary modulation.

Next, it was analyzed how much a second wave modifies the primary modulation. Therefore, the mean wave-filtered signal of the primary wave was calculated under the condition that a second wave was either in a positive or negative phase. For each possible wave superposition, the sample size was about 500–800 cases. The difference of the mean wave signal during the passage of the second wave to the mean modulation by the primary wave is called the secondary modulation. It should be noted that these values are to be interpreted as the activity in the specific wave spectrum rather than as physical rainfall anomalies. Significant

differences were tested using a t-test for samples of different variances with a significance level of 5 %.

4.9 Radiosonde analysis

Most radiosonde ascents lack measurements above 300 hPa, and thus only relative humidity (RH) below 300 hPa was analyzed. The raw data were read with the python-package *IGRA2reader* and interpolated to every 5 hPa and then composites of all ascents during all eight wave phases were constructed. In order to capture the local wave signal over the station, the wave phases were determined for a narrower Guinean and Sahelian zonal wave band. In Abidjan, wave phases were calculated based on 5°–10°N, 4°W, in Niamey based on 10°–15°N, 2°E. The absolute difference of the wind vector at 600 and 925 hPa was calculated for each profile and averaged for each phase.

To analyze the thermodynamic conditions during the passage of the waves, mixed layer parcel buoyancy of the mean profile during all phases was calculated following Schrage et al. (2006). The parcel buoyancy at a pressure level with the environmental temperature T_e is defined as

$$B = T_p - T_e, \tag{4.5}$$

where T_p is the parcel profile ascending dry adiabatically until the lifting condensation level and moist adiabatically above this level. The parcel profile was determined based on the mean temperature and humidity of the mixed layer between 15 and 65 hPa above ground (approximately 400 m). The lowest 10 hPa were removed before the parcel profile was calculated due to contamination from inconsistent surface measurements that stem from radiosonde initialization. Parcel buoyancy can be used to analyze the vertical stability. By definition $B = 0$ at the level of free convection (LFC) and at the equilibrium level (EL). The integral of B between the surface and LFC is proportional to convective inhibition (CIN), and the area between the LFC and EL to CAPE.

The rainfall signal was plotted using rain gauge data from the stations, where the radiosondes were launched. Rain gauges report daily rainfall from 06 to 06 UTC+1d, whereas radiosonde are launched at 12 UTC. The shift of six hours was eliminated using the method as presented in 4.6.

4.10 Time-lagged analysis

The MJO and ER waves trigger rainfall anomalies up to the Mediterranean Sea (as will be discussed in 5). To test, whether and how the waves couple with the extratropical circulation, geopotential and wind in 300 hPa were analyzed. The influence on lower-tropospheric thickness was analyzed between 600 and 925 hPa. The origin and development of the wave signal were traced using a time-lag analysis. The tropical plumes were observed in the local phase 4 for the MJO and in phase 6 for ER waves. Composites of significant anomalies of precipitation, geopotential, and wind in 300 hPa were calculated for 25 days to 5 days after the MJO wave was in phase 4 and 15 to 3 days after the ER was in phase 6.

4.11 Spatio-temporal autcorrelation

To investigate the spatio-temporal nature of tropical waves, the 2D-autocorrelation of each wave filtered TRMM band in longitude and time was calculated using the MATLAB function *normxcorr2()*. The resulting matrix contains the autocorrelation of the wave signal given a shift of the wave by Δt in time and Δx in longitude (Fig. 7.1–7.3). Thus, the autocorrelation is a measure of the statistical properties of the wave propagating in space (longitude) and time. The phase velocity v_p can be inferred by following the lines of max correlation. v_p was estimated with a linear fit of the angle, in which the correlation maxima are ordered along the time axis within a subjectively chosen range away from $\Delta t = 0$ to visually match the observed wave pattern. Due to the strong dampening of the wave signal in space and time, the group velocity v_g can only be roughly assessed by visual inspection of the angle, in which the entire wave packet is arranged in space-time. The temporal autocorrelation of the wave signal is obtained from the autocorrelation matrix as a cross-section at $\Delta x = 0$. The period T of each wave type was estimated from the distance between the two neighboring minima in the temporal autocorrelation. The wavelength was not clearly evident in the spatial autocorrelation ($\Delta t = 0$) of dispersive MRG and EIG waves. Therefore, the wavelength λ of all wave types was estimated from the relationship $\lambda = v_p \cdot T$, instead. Due to damping of the signal in space and time, the method does not allow the exact measurement of the wave properties. The velocities, period, and wavelength should, thus, be understood as rough estimates and not exact measurements.

5 | Variability

This chapter investigates the influence of tropical waves on synoptic to intraseasonal rainfall variability over Africa. First, the mean climate during the study period is briefly described in 5.1. Then, Section 5.2 assesses the variance of rainfall in the wave bands during the transition season and full monsoon. Section 5.3 discusses the modulation patterns associated with tropical waves. As examples for the modulation of tropical waves, the intensity of rainfall modulation in the Guinea Coast and West Sahel is quantified in 5.4. The relative contribution to precipitation and the role of orography will be discussed in Sections 5.5 and 5.6. The chapter is concluded with the analysis of interactions between different wave types in 5.7.

5.1 Mean climate

The African monsoon system dominates the circulation and distribution of rainfall over northern tropical Africa. During the transition season (Apr.–Jun.; Oct.), when the monsoon has not yet fully started or already ended, rainfall is concentrated over the coastal regions around 5°N (Fig. 5.1a). 49 % of the annual precipitation or a total of ca. 600 mm falls in the Guinea Coast box during this season as outlined in Fig. 5.1. In contrast, the West Sahel box receives 28 % of the annual precipitation or 230 mm in the same season. With the start of the African monsoon, the main rainfall band moves northwards to about 10°N during the full monsoon season from July to September (Fig. 5.1b). Then, 71 % of the annual precipitation or 530 mm falls in the West Sahel; the coastal regions of West Africa experience the little dry season. Only 37 % of the annual precipiation or 450 mm falls during this season in the Guinea Coast. Due to the West African Monsoon, the northward shift is stronger over the land than over the ocean. Rainfall over elevated regions is generally higher than in the lowlands. Prominent orographic include the Guinea Highlands, the Jos Plateau, the Cameroon Line, the Bongo Massif, the Darfur Mountains, and the Ethiopian Highlands as shown in Fig. 4.1. It will be demonstrated in Section 5.5 that these
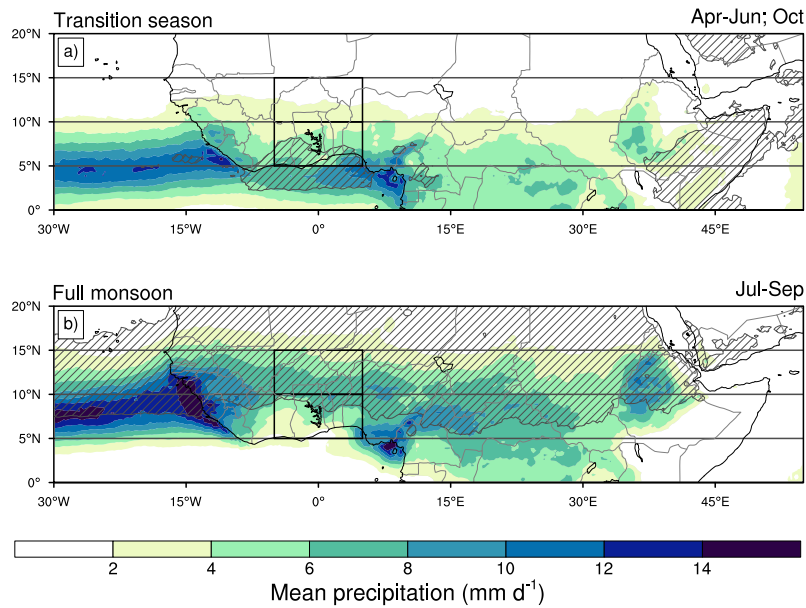
Figure 5.1: Mean seasonal precipitation from TRMM observations (1998-2016) during (a) transition season (April - June; October) and (b) the full monsoon (July - September). Areas with more than 50 % of annual rainfall during the respective season are hatched. Black lines denote the boxes and bands as used in subsequent analyses. Reprinted from Schlueter et al. (2019a). © 2019, American Meteorological Society. Used with permission.

orographic features also play a role for how precipitation is modulated by tropical waves.

5.2 Total variance of wave activity

In a first step, it was analyzed where and how much rainfall variability falls into the specific wave spectra during the transition and full monsoon seasons. For this purpose, Fig. 5.2 shows the standard deviation of wave filtered TRMM precipitation signals during the period from 1998 to 2016. The magnitude of rainfall variability differs in the analyzed wave spectra. CCEW do not show highest variability at the equator as might be expected from the shallow-water equations. Rather, the highest contribution of tropical waves to rainfall variability is directly linked to the mean precipitation patterns and lies where the seasonal rainfall maximum is located. It has to be noted that the background noise significantly contributes to the variance within the different bands and therefore bands with more variance in the raw red spectrum naturally exhibit higher variance in the filtered data as well (cf. Figs. 1 and 2 in Wheeler and Kiladis 1999). The highest variability can be observed for TD and Kelvin waves. During the transition season, TD and Kelvin waves have a comparable variability with a standard deviation of about 3–4 mm d^{-1} at the Guinea Coast. MJO, ER, and MRG are of similar variability with a maximum standard

56
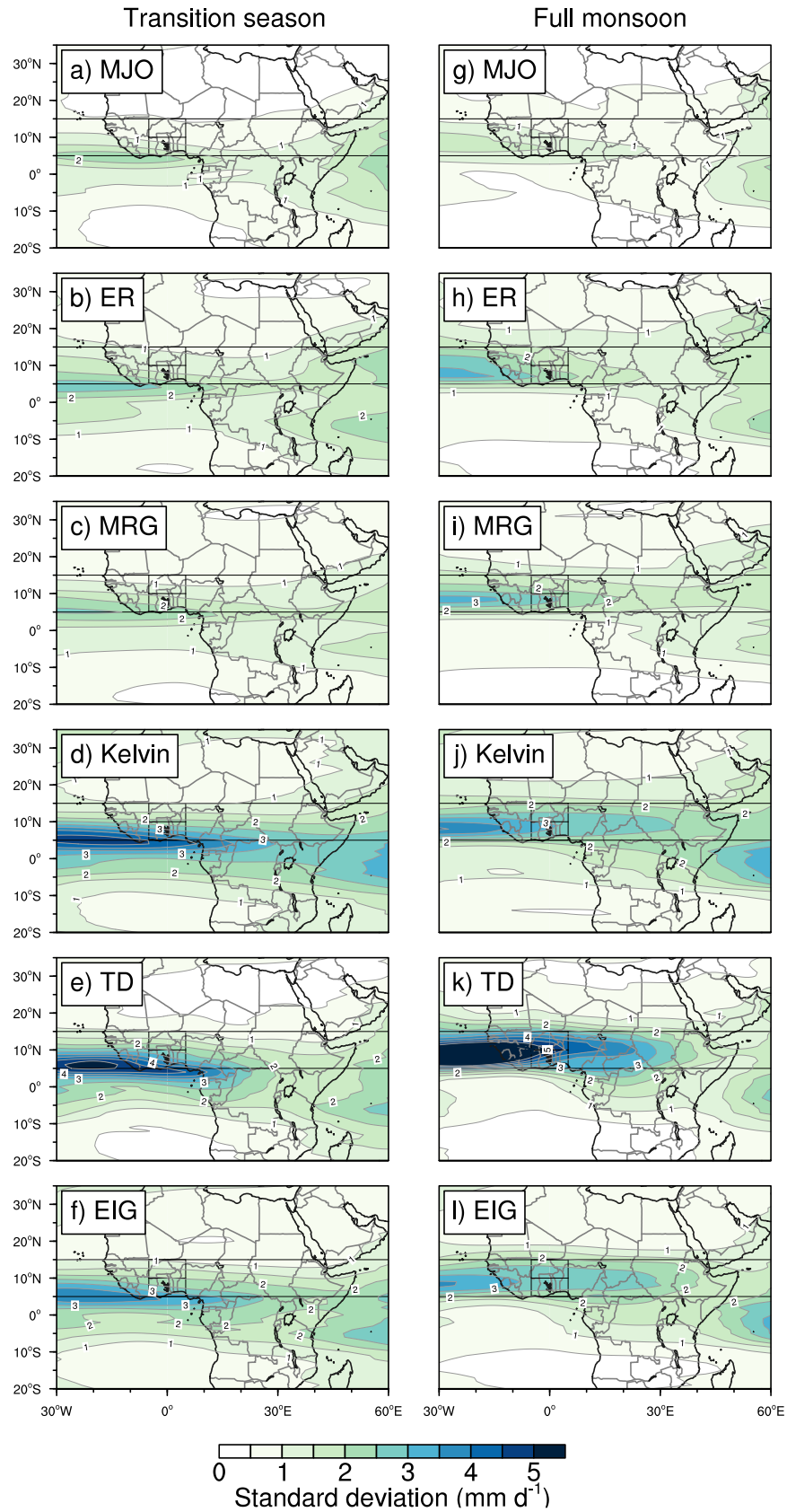
Figure 5.2: Standard deviation of TRMM precipitation (1998–2016) within the specific wave domains for the transition season (a–f) and full monsoon (g–l). Black lines denote the boxes and bands as used in subsequent analyses. For abbreviations of wave names, see Table 4.1. Reprinted from Schlueter et al. (2019a). © 2019, American Meteorological Society. Used with permission.

deviation of about $2\,\mathrm{mm\,d}^{-1}$. The variability in the EIG band is slightly stronger with a maximum standard deviation of about $3\,\mathrm{mm\,d}^{-1}$.

During the full monsoon in contrast, the TD signal is by far the most dominant source of rainfall variability. The intensity in the TD band increases from the Ethiopian highlands towards maximum standard deviation of more than $6\,\mathrm{mm\,d}^{-1}$ over the west coast of Africa. The variability for the other waves is comparable with a maximum standard deviation of about 2–$3\,\mathrm{mm\,d}^{-1}$. During this season, ER and MRG waves exhibit slightly more variability, whereas the MJO and Kelvin waves are slightly less active.

Several authors have compared the different waves on a global scale (Wheeler and Kiladis, 1999; Roundy and Frank, 2004; Kiladis et al., 2009; Huang and Huang, 2011; Schreck et al., 2013; Lubis and Jacobi, 2015). Some of these only provide results for the entire year (Wheeler and Kiladis, 1999; Kiladis et al., 2009). The global maps for the summer and spring season in Roundy and Frank (2004) using OLR roughly agree with the results in Fig. 5.2. The drawback of the studies that filter the waves from OLR or brightness temperature as indicators for deep convection is the low correlation of OLR with daily precipitation over Africa, which is generally less than 0.3 (Fig. A.1.1). Huang and Huang (2011), and Lubis and Jacobi (2015) show the seasonal cycle of different waves demonstrating that the maximum of TD and MRG-activity is during the boreal summer, ER peak during fall and winter, whereas Kelvin waves show the highest activity during boreal spring. Lubis and Jacobi (2015) filter the waves from TRMM precipitation. Their results of the activity of different waves during the extended monsoon season are comparable with the presented results. Skinner and Diffenbaugh (2013) compare in their Fig. 8 the variance of precipitation in different tropical wave spectra over West Africa during June to October in different general circulation models and observations from the Global Precipitation Climatology Project (GPCP). The overall picture is similar: the wave type explaining most variance is TD followed by ER and Kelvin waves. It should be noted that there is considerable inconsistency between the different models and observations, stressing the need for improved representation of the waves in NWP models.

5.3 Modulation patterns

The discussion of Fig. 5.2 already indicated that different wave types modulate rainfall amounts to a different degree. In a next step, the effect of tropical waves on precipitation patterns and modulation intensity during the extended monsoon
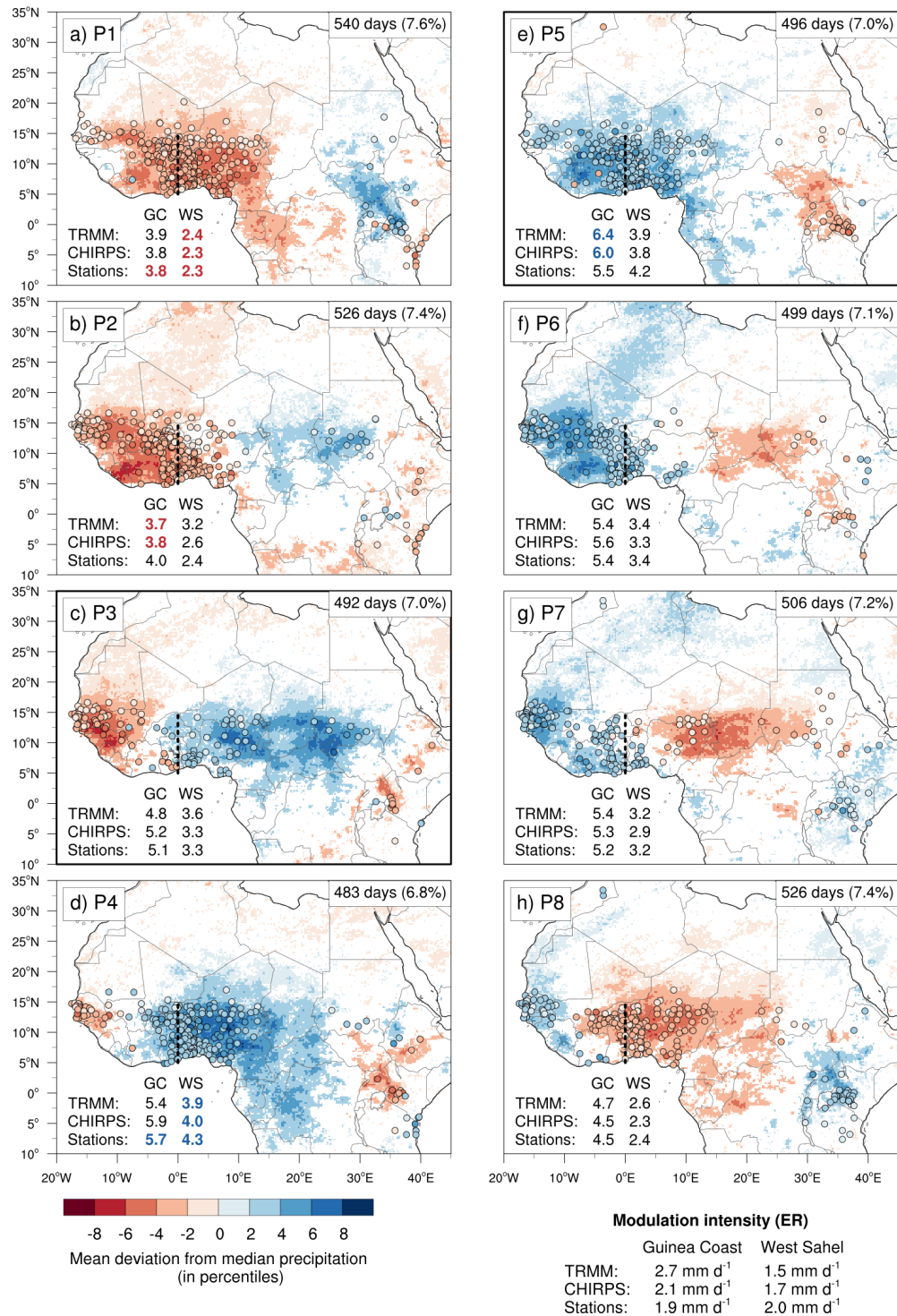
Figure 5.3: Rainfall composite for days with significant ER wave signal, based on OLR anomalies over 5°-15°N, 0°E (dashed line), for CHIRPS (shading) and KASS-D (circles, both 1981–2013) during the extended monsoon season (April - October). As calculated with a bootstrap test, non-significant anomalies ($p > 0.05$) are left white for the CHIRPS data, KASS-D stations that are non-significant are not shown. The number of days used for the composites and the fraction of days per season during each phase is given in the upper right of the plot. The numbers in the lower left part of the subpanels states the mean observed rainfall in all three rainfall datasets for the given phases (TRMM period: 1998–2013) within the Guinea Coast and West Sahel (black boxes). The modulation intensity, measured as the difference between the mean rainfall amount in the wettest (blue number) and driest phase (red number), is summarized at the right bottom. Reprinted from Schlueter et al. (2019a). © 2019, American Meteorological Society. Used with permission.

is analyzed. The modulation patterns of the ER wave are shown for all eight phases and will be discussed in detail because of the notable influence far into the subtropics (Fig. 5.3). For the remaining waves only the wet phase (P5) and one neutral phase (P3) will be shown; the full figures showing all phases and maps with precipitation anomalies as measured and filtered by TRMM can be found in the appendix (Figs. A.1.2–A.1.12).

Although the composites are based on a local wave filtering for a reference location at 0°E, 5°-15°N, the ER wave shows significant and spatially coherent modulation patterns over most of northern tropical Africa. The eight phases give a clear picture of the propagation of the ER wave. As an largely independent dataset, rain gauges measurements confirm the significant influence over the entire continent. The wave exhibits significant modulation patterns that reach up to the Mediterranean Sea and to East Africa. The approximate wave length is 8000 km; thus, it is dry over Central/East Africa when wet anomalies persists over West Africa and vice versa. The modulation patterns as measured by TRMM are very similar to CHIRPS but more noisy and not as pronounced (Fig. A.1.7); as expected from theory, weak symmetric signals at 10°S can be seen in several phases over the Atlantic Ocean. The modulation patterns of ER waves in Janicot et al. (2010, 2011) and Thiawa et al. (2017) are remarkably similar to the results of this composite study. The slightly eastwards tilted precipitation pattern resembles tropical plumes regularly observed during the dry winter season (Knippertz and Martin, 2005; Fröhlich et al., 2013). An analysis of the dynamical fields is needed to verify whether such a relation between tropical plumes and ER waves does in fact exist.

The remaining waves also show modulation patterns influencing entire northern tropical Africa (Figs. 5.4). The MJO modulates the precipitation over the entire African continent far into the subtropics up to the Mediterranean Sea and to East Africa (Figs. 5.4a, f, A.1.2, and A.1.8). Over the west coast, South Sudan, and Central Africa, the modulation is weak. Over the complex East African terrain, the MJO seems to be out of phase. For the transition phases, a weak zonal dipole exists, with wet (dry) conditions over the tropical band and dry (wet) conditions over the Sahara. Weak anticorrelated wave patterns south of 5°N can be seen over the Atlantic Ocean (Fig. A.1.8). The tilted precipitation anomalies over the Sahara as seen for the ER, can also be observed for MJO waves, although this pattern is not as pronounced (P2 and P4, see Fig. A.1.2). Over the Atlas Mountains, precipitation is enhanced during the wet phases and reduced during the dry phases (cf. also Fig. A.1.8). The TRMM-filtered composites suggest that the signal over the Gulf of Guinea precedes the signal over the continent.
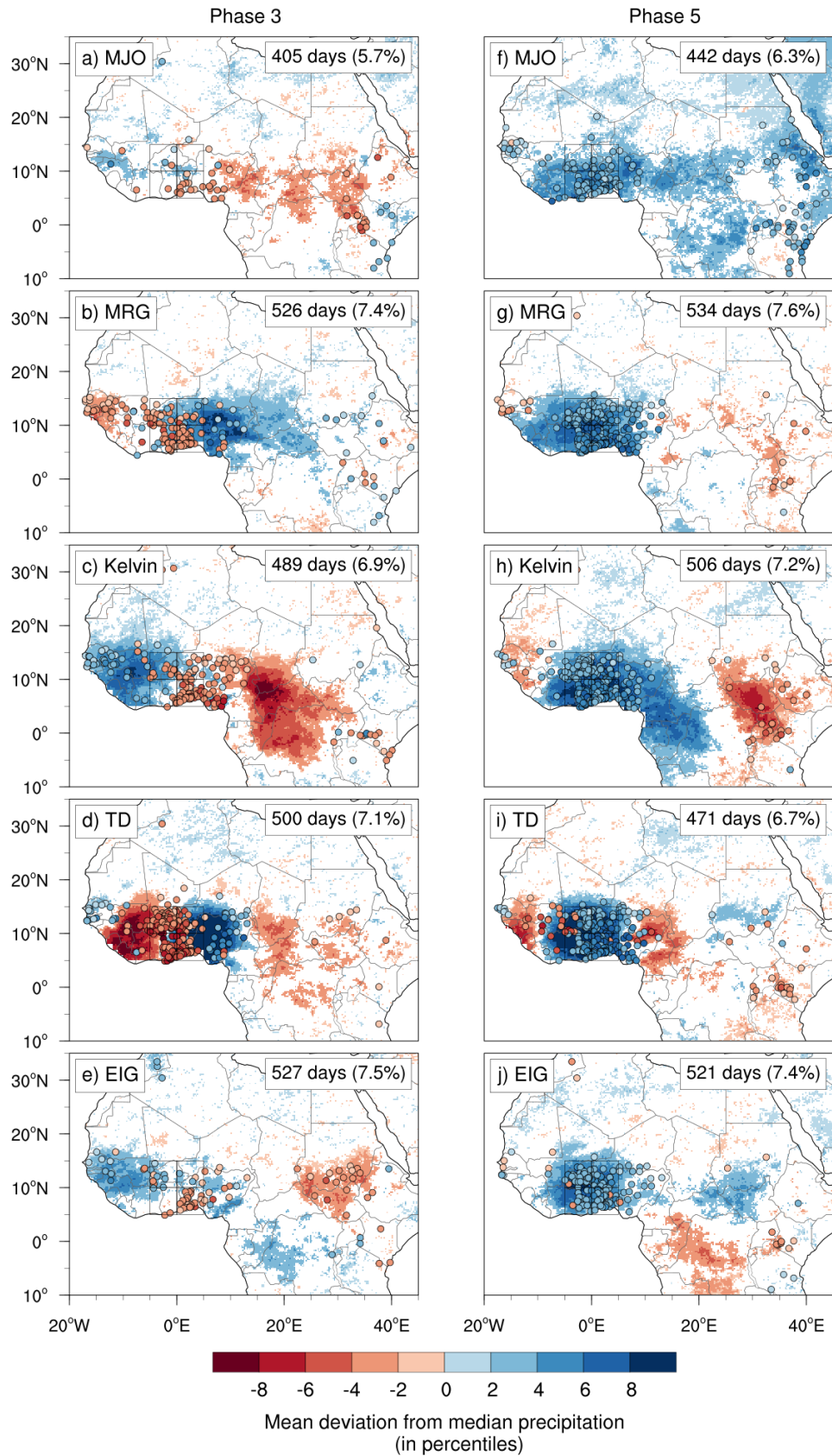
Figure 5.4: Same as Fig. 5.3, but for all waves and phase 3 (neutral phase, a–e) and phase 5 (wet phase, f–j). Plots showing all phases are provided in the appendix (Figs. A.1.2–A.1.6). For abbreviations of wave names, see Table 4.1. Reprinted from Schlueter et al. (2019a). © 2019, American Meteorological Society. Used with permission.

MRG waves are rather confined to the filtered band between 5°-15°N and lose their clear pattern over East Africa (Figs. 5.4b, g, A.1.3, and A.1.9). In the subtropics, only weak significant signals can be observed over the Maghreb region (P7, see Fig. A.1.3). The approximate wave length is > 9000 km. An antisymmetric pattern in the Southern Hemisphere, as expected from theory, is observable with TRMM (Fig. A.1.9) but not with CHIRPS due to the lack of data over oceans. Over Central and East Africa, the antisymmetric pattern is weak.

Kelvin waves are an equatorial phenomenon. This is the reason, why the modulation also extends to 10°S but not to the north of the filtered band at 15°N (Figs. 5.4c, h, A.1.4, and A.1.10). The precipitation patterns are well-defined and blur out over the eastern part of the continent. As a side remark, Kelvin waves might also locally modulate the land-sea breeze as indicated by a modulation which is out of phase at several coastal stations (P4 and P8, Fig. A.1.4).

TD are most dominant over West Africa (Figs. 5.4d, i, A.1.5, and A.1.11). The wave signal weakens east of 10°E. The influence is also mostly confined to the filtered area between 5°–15°N. A weak anticorrelation with precipitation in the Sahara can be observed. Over the Atlantic the precipitation pattern tilts in a northeast-southwest direction (Fig. A.1.11). The average wave length is about 2500 km.

EIG waves show a weaker and more complex modulation pattern compared with the previous waves (Figs. 5.4e, j, A.1.6, and A.1.12). The modulation is strongest over West Africa, equatorial Central Africa and South Sudan. Consistent with theory, antisymmetric rainfall patterns are evident in the Southern Hemisphere, although the anticorrelated rainfall regions are shifted northwards and centered around 5°S. Very weak, significant anticorrelated precipitation anomalies further in the north could be an indication of a contamination by higher order (e.g., n=1, n=2) EIG waves. Further investigations are needed to better understand the involved mechanisms of triggering, propagation, and coupling of EIG waves to precipitation. Rain gauge observations do not match the CHIRPS dataset well due to a phase shift between both datasets, which will be discussed in the following section.

5.4 Modulation intensity

The modulation intensity was measured in absolute rainfall. Figure 5.5 shows the mean precipitation in the Guinea Coast and West Sahel boxes during the eight phases as measured by CHIRPS, TRMM, and KASS-D. Rainfall varies considerably between the different phases of all waves. Additionally, it can be seen
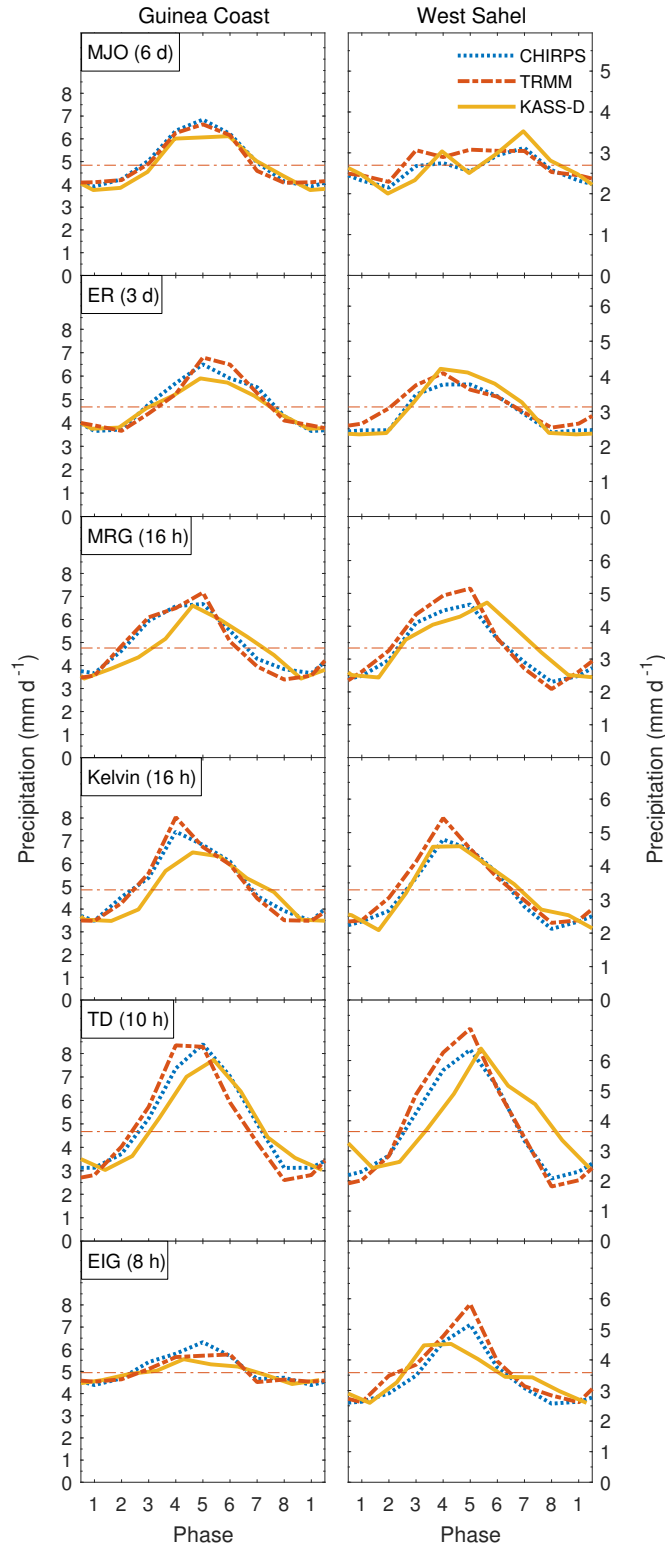
Figure 5.5: Mean precipitation in the eight phases in the Guinea Coast box (left side), and West Sahel box (right side) in CHIRPS (1981–2013, blue dotted line), TRMM (1998–2013, red dashed line), and KASS-D (1981-2013, yellow solid line) during the extended monsoon season (April - October). Because KASS-D lags the other datasets by 6 h, the curve has been shifted using the mean duration of one phase (in brackets). See Section 5.4 for more detail. Note that the y-axis has been scaled with the mean TRMM precipitation during all days with an active wave, which is indicated by the horizontal red line. Reprinted from Schlueter et al. (2019a). © 2019, American Meteorological Society. Used with permission.

that TDs and Kelvin waves have the strongest impact on absolute rainfall anomalies, followed by MRG and ER waves. Despite the known deficiencies of the datasets (Funk et al., 2015; Maggioni et al., 2016), the observed amplitudes agree well for all three datasets.

In a more detailed analysis, gauge observations will be analyzed for the transition season and the full monsoon season. Figure 5.6 shows the distribution of mean modulation for all stations in the West Sahel and Guinea Coast box as the difference of modulation intensities during wet and dry phases of the waves. As a side-remark, it can be noted that negative modulation intensities can be observed, which means that less rain at single stations falls during the wet phase and vice versa. These cases are likely related local factors such as orography (cf. Figs. 5.3–5.4 and Section 5.6) and random errors. The corresponding plot in quantile anomalies can be found in the appendix (Fig. A.1.13).

During the transition season, rainfall at the Guinea Coast is strongly modulated by tropical waves (Fig. 5.6a). Descending in order, the mean modulation intensities are 5.7 (TD), 4.2 (Kelvin), 3.6 (MRG), 3.1 (ER), 3.0 (MJO), and $2.0 \, \mathrm{mm \, d^{-1}}$ (EIG). The standard deviations lie between $0.8 \, \mathrm{mm \, d^{-1}}$ for ER and $1.7 \, \mathrm{mm \, d^{-1}}$ for TD. The West Sahel is still relatively dry during the transition season (Fig. 5.1a). Therefore, the influence of tropical waves is weak, amounting to only 1.3–$2.6 \, \mathrm{mm \, d^{-1}}$ for all waves (Fig. 5.6b).

In the full monsoon season, the modulation at the Guinea Coast is similar to the transition season (Fig. 5.6c). The mean modulation intensities amount to 5.9 (TD), 4.6 (MJO), 4.1 (MRG), 3.7 (Kelvin), 3.2 (ER), and $2.1 \, \mathrm{mm \, d^{-1}}$ (EIG). A noteworthy difference to the transition season is a stronger modulation by the MJO, although the MJO activity itself is weaker during the full monsoon (Fig. 5.2). The standard deviations are higher than during the transition season due to the high gradient of rainfall at the Guinea Coast during the monsoon season (Fig. 5.1). Surprisingly, all CCEWs are as strong or even stronger in the West Sahel (Fig. 5.6d) than over the Guinea Coast (Fig. 5.6c), although the strongest influence of equatorial waves would be expected near the equator from theory. The mean modulation intensities are 6.0 (TD), 5.0 (Kelvin), 4.4 (ER), 4.3 (MRG), 3.5 (EIG), and $2.0 \, \mathrm{mm \, d^{-1}}$ (MJO). For both regions, the largest standard deviation is seen in the modulation intensity for TD. Several stations record a modulation intensity of more than 8 mm/d.
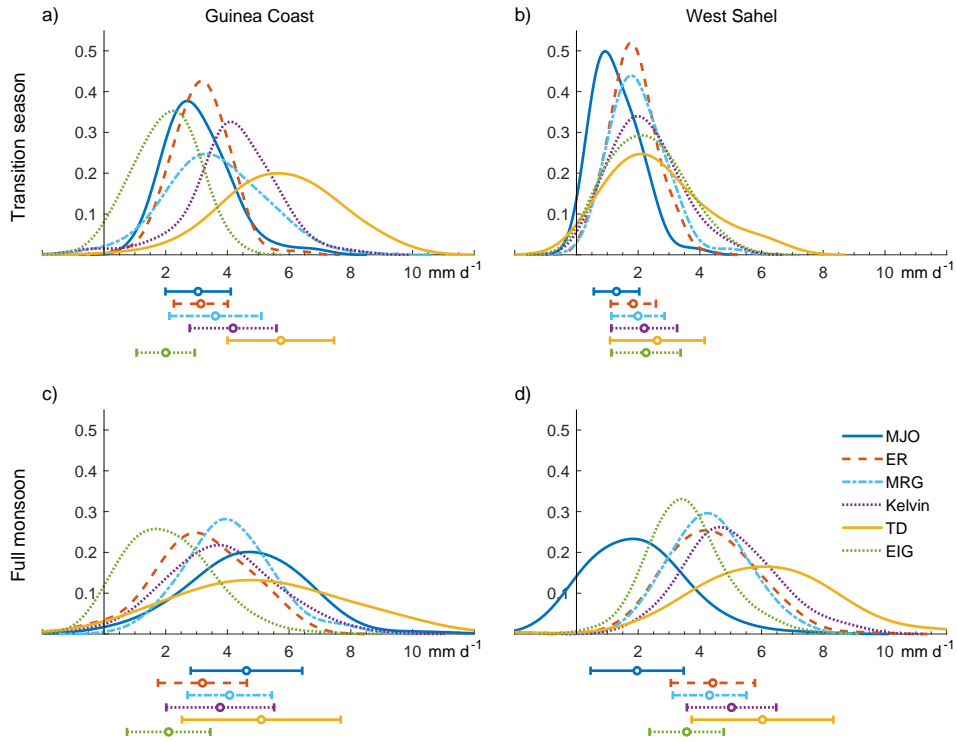
Figure 5.6: Modulation of rainfall by tropical waves in the Guinea Coast (5°W-5°E, 5°-10°N) and the West Sahel (5°W-5°E, 10°-15°N) during the transition season (Apr.–Jun.; Oct., top) and the full monsoon season (Jul.–Sep., bottom) as measured by rain gauges in KASS-D. Dates in wet and dry phases of the tropical waves were obtained by filtering OLR in a Guinean (5°-10°N) and Sahelian band (10°-15°N) from 1979-2013. As a metric for the modulation intensity, the difference of the mean precipitation during wet phases and dry phases was calculated for all stations (Guinea n=112, Sahel n=129). From these stations an empirical probability density function was derived using kernel density estimation. Lines below the axis show mean and standard deviation of the corresponding modulation intensity for each wave. For abbreviations of wave names, see Table 4.1. Reprinted from Schlueter et al. (2019a). © 2019, American Meteorological Society. Used with permission.

## 5.5 Relative contributions to precipitation

To understand the relative contribution of the tropical waves to rainfall variability on different timescales, the wave filtered precipitation was correlated with temporally aggregated raw precipitation (Figs. 5.7–5.9). The squared correlation is calculated as an estimation of the explained variance of raw precipitation by the tropical waves. All waves significantly modulate precipitation over the Sahel and Guinean bands. Using this correlation analysis, we can obtain a more detailed overview over the longitudinally varying modulation strength as well as the relative contribution to rainfall variability on different timescales. Interactions between different waves are not taken into account, so the sum can be seen as the maximum that can be explained by the six tropical waves combined. During the transition season, the Sahel band receives very little rainfall (Fig. 5.1) and the influence of tropical waves

is comparatively weak (Figs. 5.2 and 5.6b). Thus, a figure for the Sahel band during the transition is not discussed here, but is available in the appendix (Fig. A.1.14).

For both seasons and both bands, we can observe that the influence of tropical waves depends on the timescale and varies substantially with location and season. As expected, waves in shorter period bands generally dominate the rainfall variability on shorter timescales, whereas the longer timescales are governed by slower waves. It should be noted that a specific wave modulates precipitation at the accumulation period less or equal to half the wave period. At accumulation times of equal to one period (and longer), the enhanced and suppressed phase cancel each other out and thus no correlation can be seen anymore at this time scale.

The Guinea band exhibits the strongest modulation on the daily timescale during the transition season (Fig. 5.7). Here, the TD and Kelvin waves have the strongest impact. Between the Cameroon Line (12°E) and Ethiopian Highlands (38°E), rainfall variability is dominated by Kelvin waves. On the timescale of three days, MJO, ER, and Kelvin waves are approximately equally important. The influence of TDs is not evident any more on this timescale. On the weekly timescale, ER and MJO remain as the only contributors to rainfall variability. On the short subseasonal timescale (20 days), the MJO is the remnant major source of rainfall variability locally explaining 10–20 % of rainfall variability over West Africa and up to 20–30 % over the Horn of Africa. A stronger influence of the MJO on Central African precipitation during the spring season was documented by Berhane et al. (2015).

During the full monsoon, the TDs gain importance for rainfall variability in the Guinea band. On the daily timescale, they explain up to 30 % of the variability over West Africa (Fig. 5.8). This is consistent with Dickinson and Molinari (2000) and Lavaysse et al. (2006), who found numbers of the same order for AEWs. The importance of AEWs on daily precipitation increases westwards, which might be attributed to the barotropic-baroclinic growth they experience on the way towards the Atlantic (Charney and Stern, 1962; Thorncroft and Hoskins, 1994; Hsieh and Cook, 2005). The influence of Kelvin waves is reduced compared to the transition season, but still explains up to 10 % over Central Africa, slightly less than what is recorded by Mekonnen and Thorncroft (2016). EIG and MRG waves gain importance west of 10°W on the timescale of one to three days. On the synoptic timescale (3–7 days), ER contribute about 10–20 % to rainfall variability. The main influence of the MJO on the short subseasonal timescale (7–20 days) lies within the West African monsoon region, explaining locally more than one third of rainfall
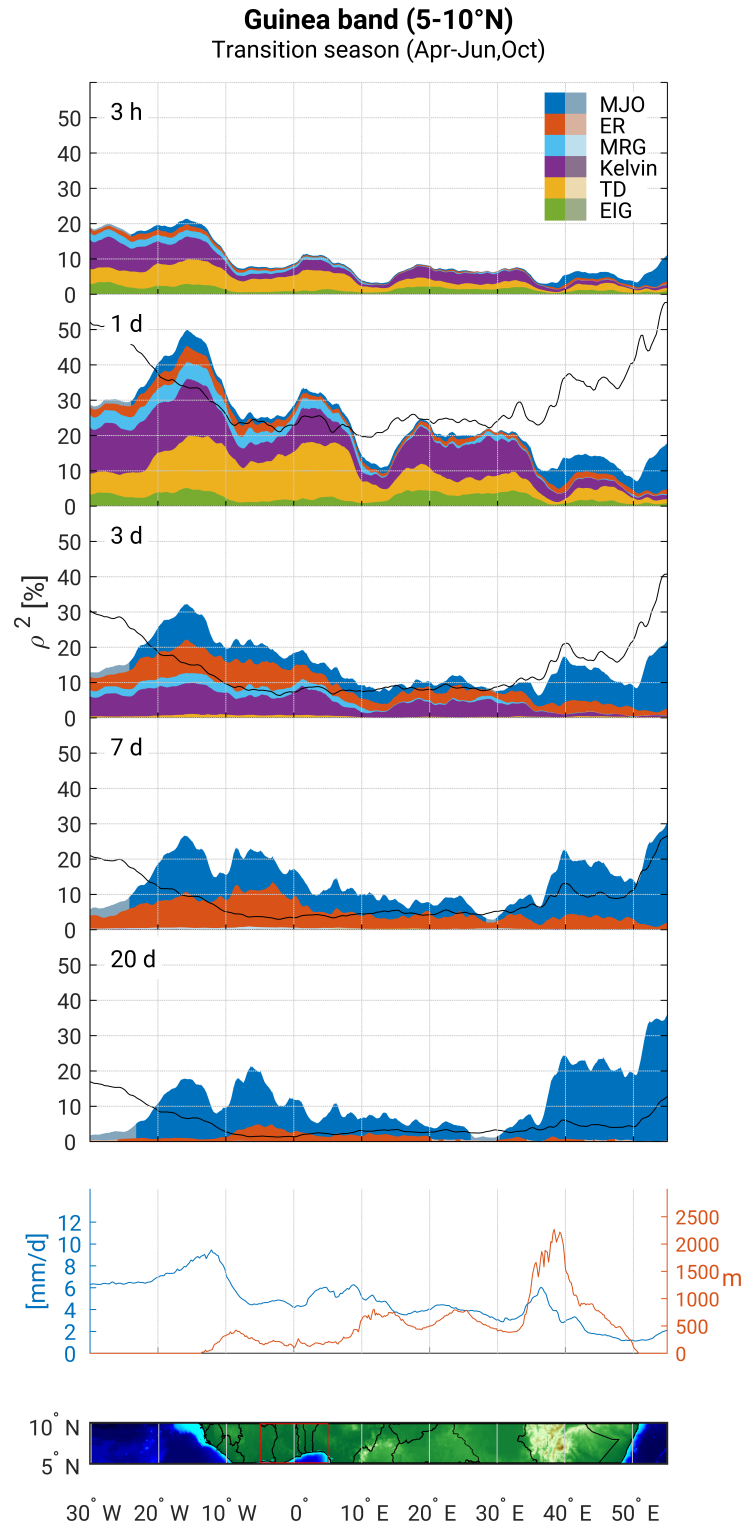
Figure 5.7: (Top) Relative importance of tropical wave signals for TRMM precipitation (1998-2016) on different timescales over (bottom) the Guinean band (5°-10°N) during the transition season (April to June and October). Explained variance is estimated by the squared correlations of the wave signal with raw precipitation. Lines are stacked on top of each other, such that the sum of all lines can be understood as the maximum variance explained by all wave types. Significant correlations ($p < 0.05$) are indicated with saturated colors. The black solid line shows the variance of precipitation at the specific timescale as percentage of the total variance in the raw data (3h). Band-averaged daily precipitation and surface height is given in the second lowest panel. Reprinted from Schlueter et al. (2019a). © 2019, American Meteorological Society. Used with permission.
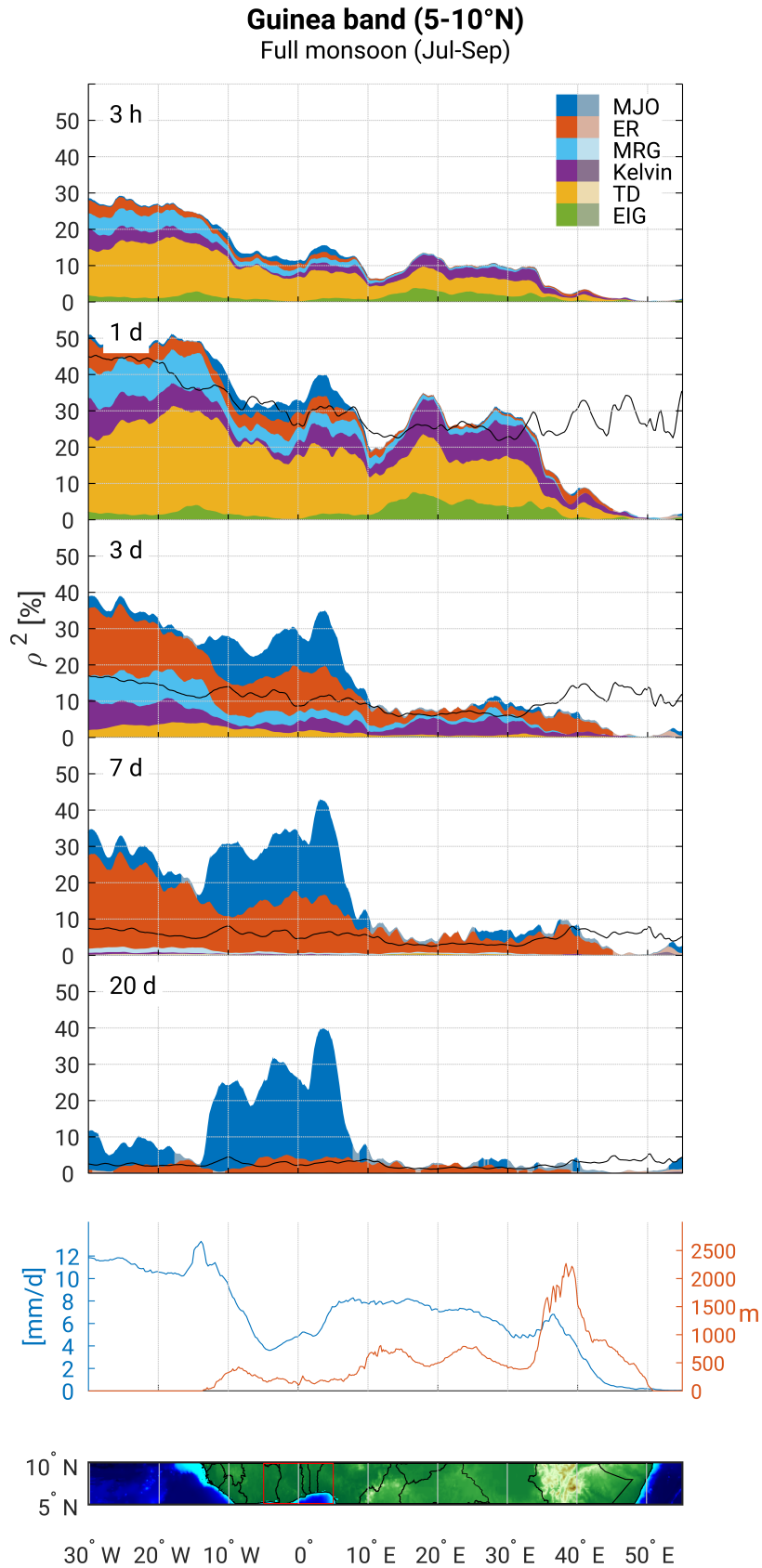
Figure 5.8: Same as Fig. 5.7, but during the full monsoon season (July to September). Reprinted from Schlueter et al. (2019a). © 2019, American Meteorological Society. Used with permission.

variability. There is no significant influence of the MJO on Central and East African rainfall.

In the Sahel band, TD are the dominant wave on the 3-hourly to daily timescale, explaining up to 20 % of the rainfall variability during the full monsoon (Fig. 5.9). A large portion of rainfall variability is concentrated on timescales longer than three days off the West Coast of Africa (black line). From three to seven days, ER waves are a large contributor to rainfall variability in this region, explaining up to one third of rainfall variability. On longer timescales (20 days), only the MJO signal contributes to rainfall variability over the Atlantic Ocean and parts of East Africa. A more pronounced modulation of the MJO in the Guinea band than in the Sahel band was also found by Gu (2009) and Pohl et al. (2009b).

The QBZD and the 'Sahel' mode operate on the timescale of 10–25 days. Mounier et al. (2008) showed that the QBZD has a stationary component and suggested Kelvin waves as triggers for the QBZD (see Section 2.2.2). The present correlation analysis suggests that Kelvin waves do not explain rainfall variability on timescales longer than seven days. It has to be noted though, that the correlation analysis cannot take into account cases when Kelvin waves trigger the QBZD, which then affects longer timescales. The 'Sahel mode' is mainly associated with ER waves (Janicot et al., 2010). ER explain a substantial portion on the weekly timescale; yet, the present analysis suggest, that 'pure' ER waves, as derived from the shallow water equations, are barely relevant on the timescale of 20 days (Figs. 5.7–5.9). The correlation analysis again might not capture cases when on a longer timescale, MJO events over the Indian ocean trigger single ER and Kelvin waves that meet over the African continent as suggested by Matthews (2000, 2004). The present analysis should be understood as an account of how much variability can be explained by the respective wavenumber-frequency bands, independent of more complex wave interactions.

5.6 The role of orography

The effect of orography on the propagation of the MJO and the diurnal cycle of precipitation over the Maritime Continent has been widely discussed (e.g. Inness and Slingo 2006; Peatman et al. 2014; Tseng et al. 2017; Sakaeda et al. 2017; Tan et al. 2018). Over northern tropical Africa, several tropical waves also appear to be influenced by the presence of orography. Both latidunal bands show a reduced influence of tropical waves over orography (Figs. 5.7-5.9). In the Guinea band, Kelvin wave and EIG are reduced after the passage of the Guinea Highlands
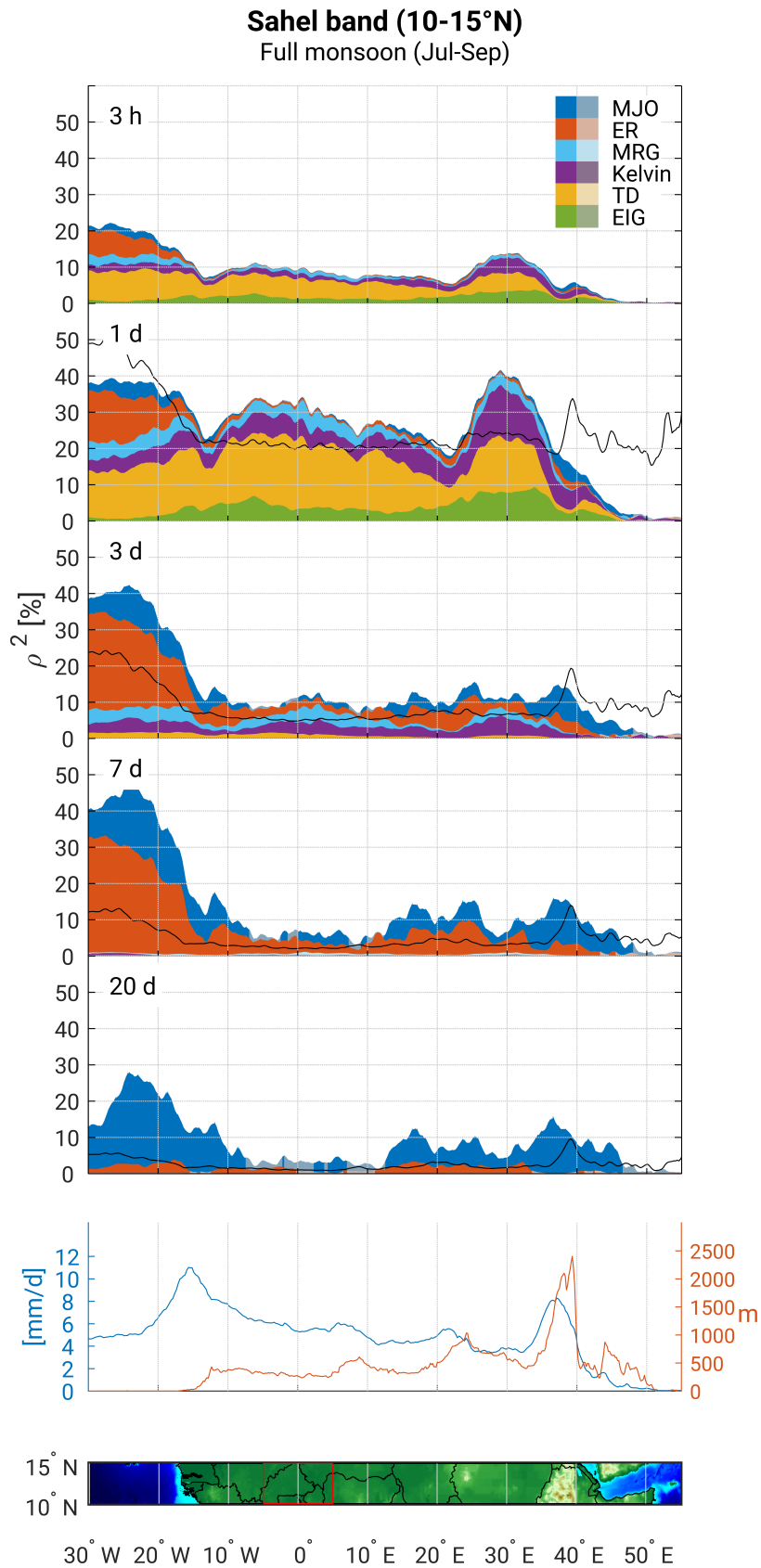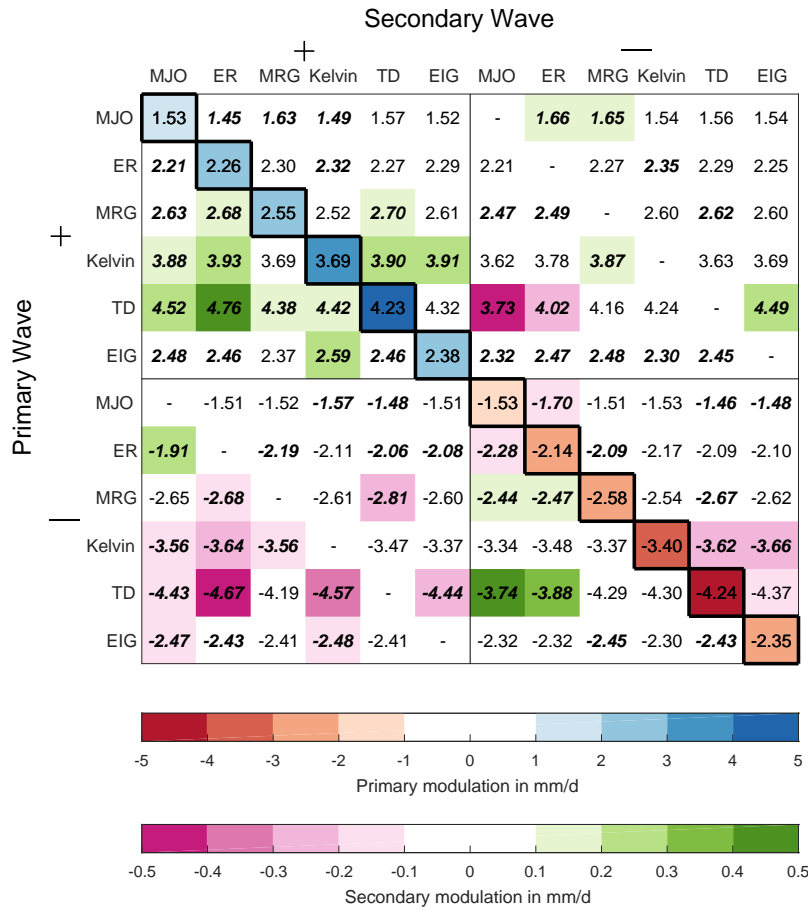
Figure 5.9: Same as Fig. 5.7, but over the Sahelian band (10°-15°N) and during the full monsoon season (July to September). Reprinted from Schlueter et al. (2019a). © 2019, American Meteorological Society. Used with permission.

(12°W), over the Cameroon Line (12°E), and the Ethiopian Highlands (38°E). The reduced modulation of TD is evident over the Guinea Highlands (12°W), Cameroon Line (12°E), the Bongo Massif (25°E), and the Ethiopian Highlands (38°E). In the Sahel band, the influence of tropical waves is reduced over the Guinea Highlands (12°W), the Jos Plateau (8°E), the Darfur Mountains (23°E), and the Ethiopian Highlands (38°E). A reduced modulation over the Cameroon Line can also be seen in Figs. 5.3, 5.4, A.1.4, A.1.5 for the ER, Kelvin waves, and TD. In general, the reduced effect of tropical waves over orography is more pronounced on the daily and subdaily timescale, where the waves compete directly with diurnal circulations, and is of the order of 50 %. The effect of orography, and the Ethiopian Highlands in particular, on Kelvin waves has been documented by Matthews (2000). Kelvin waves encountering orography can be deflected away from the equator similar to coastal Kelvin waves in the ocean (Gill, 1977; Hsu and Lee, 2005). Additionally the orographic lifting and frictionally induced lower-tropospheric convergence create a phase shift (Hsu and Lee, 2005). Figure A.1.4 also suggests that convection over the Cameroon Line is shifted by one phase. AEW preferably form in the lee of mountain ranges, where vorticity is increased (Mozer and Zehnder, 1996), and in consequence of mesoscale convective systems that have been triggered over the mountains (Mekonnen et al., 2006; Thorncroft et al., 2008). The present study illustrates how orography significantly reduces the modulation of tropical waves over northern tropical Africa.

5.7 Wave interactions

Finally, interactions between different types of tropical waves over the two case study regions Guinea Coast and West Sahel are examined. Only the results for the Guinea Coast are presented here because the results are very similar for both regions. Figure 5.10 shows the interaction between a primary wave and a secondary wave for all analyzed wave types in the Guinea Coast. The primary modulation in the Guinea Coast (shown on the diagonal) reflects the pattern already seen in Fig. 5.2. The modulation by a second wave is seen in the entries off the diagonal of the matrix. The magnitude of the secondary modulation depends on the magnitude of the primary modulation and is strongest for TD. In many cases, waves superimpose constructively. The wave activity is generally further enhanced when a primary wave in its positive phase is modulated by a second wave in a positive phase (upper left quarter). Similarly, primary waves in a negative phase modulated by a negative second wave result in a further suppression (lower right quarter). Two interesting exceptions of this wave superpositions can be seen for TD and MRG.

Secondary Wave

Primary Wave		MJO	ER	MRG	Kelvin	TD	EIG	MJO	ER	MRG	Kelvin	TD	EIG
+	MJO	1.53	*1.45*	*1.63*	*1.49*	1.57	1.52	-	*1.66*	*1.65*	1.54	1.56	1.54
	ER	*2.21*	2.26	2.30	*2.32*	2.27	2.29	2.21	-	2.27	*2.35*	2.29	2.25
	MRG	*2.63*	*2.68*	2.55	2.52	*2.70*	2.61	*2.47*	*2.49*	-	2.60	*2.62*	2.60
	Kelvin	*3.88*	*3.93*	3.69	3.69	*3.90*	*3.91*	3.62	3.78	*3.87*	-	3.63	3.69
	TD	*4.52*	*4.76*	*4.38*	*4.42*	4.23	4.32	*3.73*	*4.02*	4.16	4.24	-	*4.49*
	EIG	*2.48*	*2.46*	2.37	*2.59*	*2.46*	2.38	*2.32*	*2.47*	2.48	2.30	2.45	-
−	MJO	-	-1.51	-1.52	*-1.57*	*-1.48*	-1.51	-1.53	*-1.70*	-1.51	-1.53	*-1.46*	*-1.48*
	ER	*-1.91*	-	*-2.19*	-2.11	*-2.06*	*-2.08*	*-2.28*	*-2.14*	*-2.09*	-2.17	-2.09	-2.10
	MRG	-2.65	*-2.68*	-	-2.61	*-2.81*	-2.60	*-2.44*	*-2.47*	*-2.58*	-2.54	*-2.67*	-2.62
	Kelvin	*-3.56*	*-3.64*	*-3.56*	-	-3.47	-3.37	-3.34	-3.48	-3.37	*-3.40*	*-3.62*	*-3.66*
	TD	*-4.43*	*-4.67*	-4.19	*-4.57*	-	*-4.44*	*-3.74*	*-3.88*	-4.29	-4.30	*-4.24*	-4.37
	EIG	*-2.47*	*-2.43*	-2.41	*-2.48*	-2.41	-	-2.32	-2.32	*-2.45*	-2.30	*-2.43*	*-2.35*

Primary modulation in mm/d: -5 -4 -3 -2 -1 0 1 2 3 4 5

Secondary modulation in mm/d: -0.5 -0.4 -0.3 -0.2 -0.1 0 0.1 0.2 0.3 0.4 0.5

Figure 5.10: Interaction of different wave types in the Guinea Coast box. The mean or primary modulation of each wave measured as the mean wave filtered TRMM precipitation is given on the diagonal. Cases with a wave activity exceeding $\pm 1\sigma$ are defined as wet (-) and dry (+) phases. The superposition of a secondary wave is measured as the primary wave signal conditional on the occurrence of a secondary wave. Significant deviations from mean modulation are marked bold and italics ($p < 5\%$). See Section 4.8 for more details. Reprinted from Schlueter et al. (2019a). © 2019, American Meteorological Society. Used with permission.

Here, a modulation of the negative primary wave by a negative ER or MJO result in a more moderate modulation. Similarly, non-linear wave superpositions are evident when a positive wave is superimposed with a negative wave (lower left and upper right quarters). This means that both low-frequency waves in their wet phases amplify the high-frequency waves and suppress them in the dry phase. The analysis for the West Sahel reveals similar patterns (Fig. A.1.15). A dominant difference is a missing modulation of TD by the dry phases of ER and MJO waves.

According to theory, equatorial waves behave as linear or independent solutions of the shallow-water system (Matsuno, 1966). This is, of course, an idealized view; the basic analysis of wave interactions presented here suggest that also the dry phase of TD during the passage of the suppressed phase of MJO and ER events are significantly weaker. The superposition of AEWs and MJO events

was also analyzed by Ventrice et al. (2011). Decreased AEW activity was found when the MJO is active over the western Pacific and Atlantic, AEW activity was enhanced in phases where the MJO is active over Africa and the Indian Ocean. The superposition of MJO, Kelvin and ER waves over Vietnam was analyzed in detail by van der Linden et al. (2016). The presented results suggest complex superpositions that require to be analyzed in more detail.

6 | Mechanisms

This chapter will describe first the circulation patterns of the different wave types and their influence on the moisture distribution. Then, their vertical structure will be examined and differences in mechanisms of rainfall modulation will be shown. The last part of this chapter will analyze how rainfall over the Sahara is triggered by the MJO and ER waves and discuss how these waves interact with the extratropical circulation during such rainfall events.

6.1 Circulation patterns and moisture modulation

The MJO strongly modulates zonal winds and features vortices off the equator (Figs. 6.1, A.2.1, and A.2.7). Hence, it shares dynamical properties of Kelvin waves, also impacting zonal winds, and ER waves with their off-equatorial vortices (Matsuno, 1966). This is consistent with the suggestion that the MJO over Africa is a result of Kelvin and Rossby wave responses to enhanced convection over the warm pool (Matthews, 2004; Janicot et al., 2009; Alaka and Maloney, 2012). Matching results over oceanic regions (Wheeler and Hendon, 2004), the wet phase over northern tropical Africa lies in a region of enhanced westerlies. The observed MJO pattern over Africa has a more standing component (see Fig. A.2.1 and Pohl et al. 2009b). Upper-level divergence and weak low-level convergence are associated with lifting of air parcels and, thus, moistening of the air and increased precipitation (Fig. 6.1b,d). The MJO has a large-scale influence on PW (Fig. 6.1d) as shown previously (Matthews, 2004; Alaka and Maloney, 2012). Lavender and Matthews (2009) argue though that the increased boundary layer moisture is rather a result of enhanced convection than a cause, which is consistent with the lag between precipitation and PW observed in Fig. A.2.7. The monsoonal flow intensifies during wet phases and reduces during dry phases. In central and eastern Africa, the ITD moves southward by 100-200 km during the dry phases and northward during the wet phases (Fig. 6.1d, A.2.1). West of 5°E, the modulation of the ITD is weaker. The SHL is ventilated by monsoonal and Atlantic air masses. Significant moisture
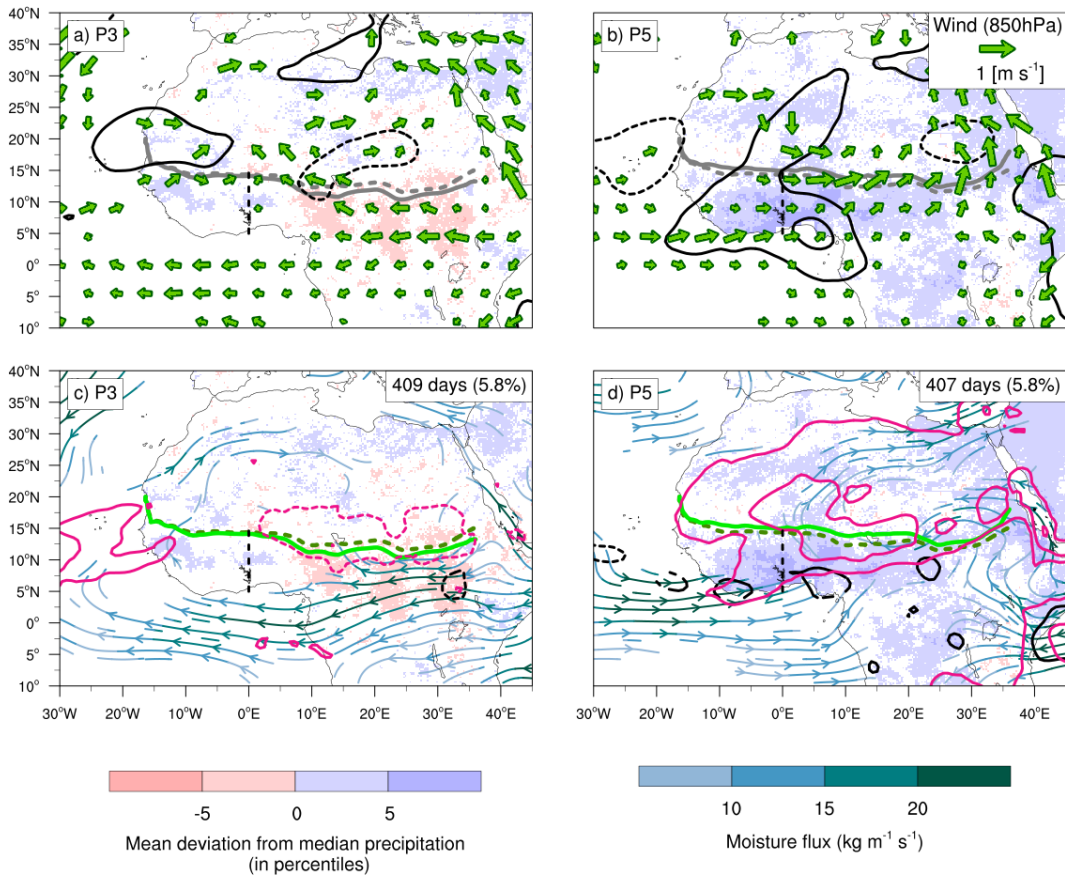
Figure 6.1: Composites of days with significant Madden-Julian Oscillation signal in phase 3 (neutral phase, a+c) and phase 5 (wet phase, b+d) over 5°-15°N, 0°E (dashed vertical line) during the extended monsoon season (March–October). Top panels (a,b) show composites of significant anomalies of 850 hPa wind (green arrows) and divergence at 200 hPa (thick contours, at $-3 \times 10^{-6}\,\text{s}^{-1}$ to $3 \times 10^{-6}\,\text{s}^{-1}$ in $0.5 \times 10^{-6}\,\text{s}^{-1}$ steps, convergence dashed). Bottom panels (c,d) show significant anomalies of moisture flux (streamlines, magnitude in turquoise colors), moisture flux convergence (black lines, at ± 1 and $2 \times 10^{-5}\,\text{kg}\,\text{m}^{-2}\,\text{s}^{-1}$, divergence dashed), and PW (pink lines, at ± 1, 2 and 3 mm, negative dashed). Significant precipitation anomalies are shaded. The mean position of the ITD in each phase is depicted with a gray (top) and green (bottom) line. The dashed gray (top) and dark green line (bottom) shows the mean position in all phases. The number of days and the fraction of days per season during each phase is indicated in the top right corner of panels. Reprinted from (Schlueter et al., 2019b). © 2019, American Meteorological Society. Used with permission.
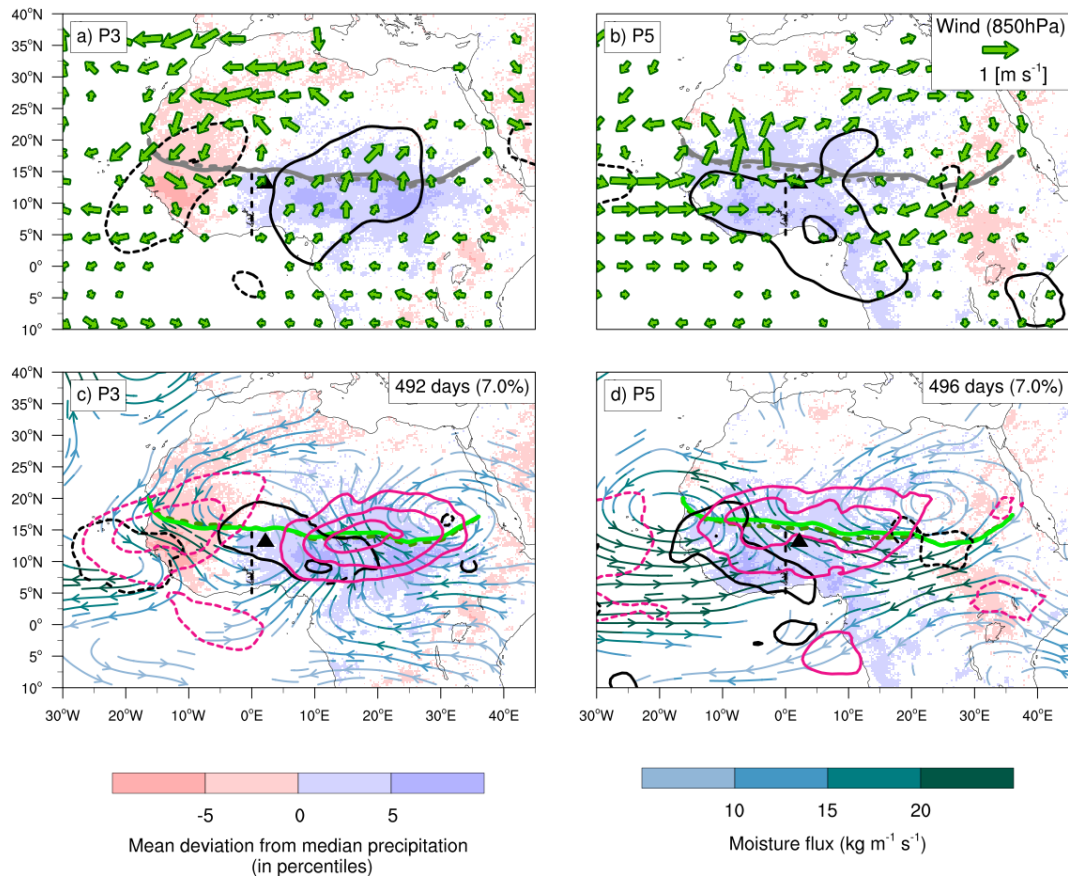
Figure 6.2: Same as Fig. 6.1, but for equatorial Rossby wave. The triangle shows the location of the radiosonde station in Niamey used in Fig. 6.7a. Reprinted from Schlueter et al. (2019b). © 2019, American Meteorological Society. Used with permission.

anomalies can be found far into the subtropics (>30°N). The relationship with the extratropics will be discussed in Section 6.3. Due to the low frequency of the MJO, the total moisture convergence is small compared to the other wave types. As a side remark, the enhanced westerlies during the wet phase lead to increased cyclonic shear vorticity at the southern flank of the AEJ (Matthews, 2004; Ventrice et al., 2011). This affects the stability of the AEJ and thus the AEW occurrence is modified (Alaka and Maloney, 2012, 2014).

The more rotational ER waves show westward propagating vortices with centers off the equator at around 20°N (Figs. 6.2, A.2.2, and A.2.8). Sustained moderate moisture convergence during the passage of the slow-moving ER waves result in a strong modulation of PW and precipitation is mainly aligned with these anomalies. Moist air masses from the Gulf of Guinea and Congo Basin are transported towards tropical West and Central Africa during the wet phase. In the Sahel, wet conditions are related to enhanced monsoonal flow and dry conditions with decreased monsoonal inflow. The mean position of the ITD is roughly 100 km further north in the wet sector of the wave and further south in the dry sector.
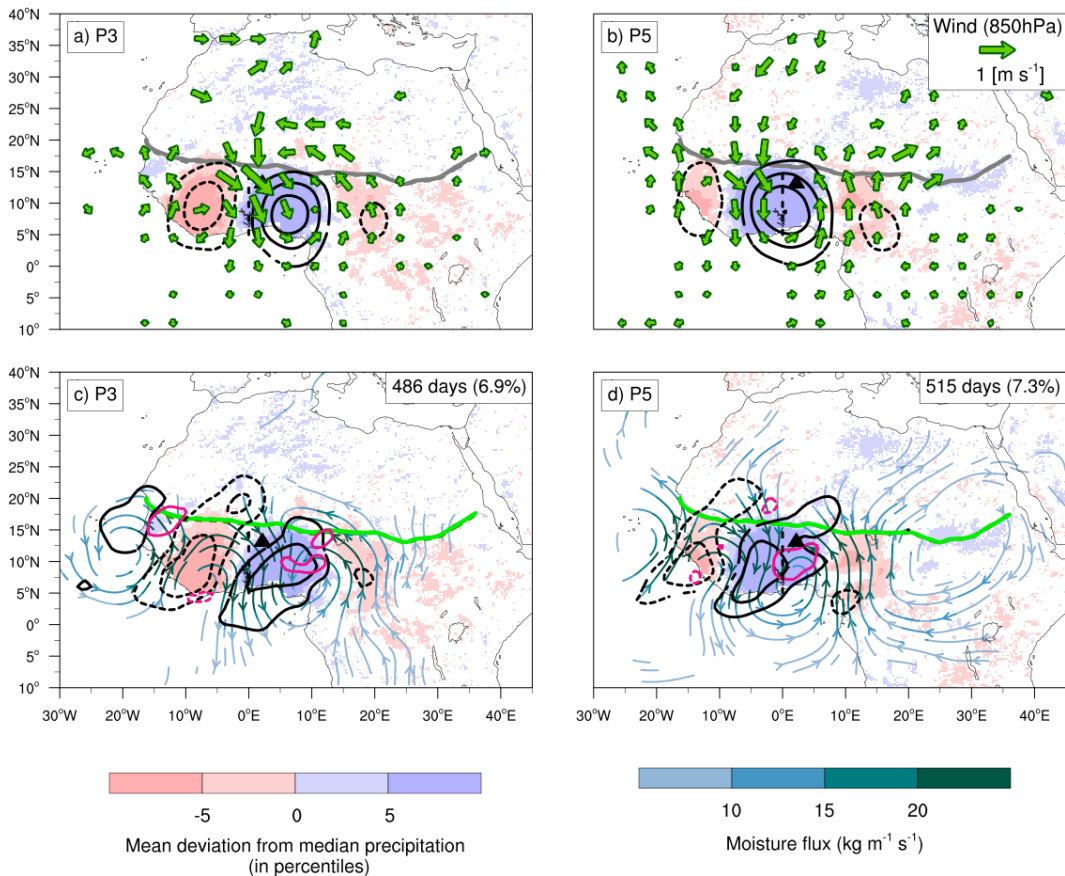
Figure 6.3: Same as Fig. 6.1, but for tropical depression (African Easterly Wave). The triangle shows the location of the radiosonde station in Niamey used in Fig. 6.7a. Reprinted from Schlueter et al. (2019b). © 2019, American Meteorological Society. Used with permission.

The SHL is ventilated by southerlies during phases 5–7 (Figs. 6.2d and A.2.2). These southerlies result in moisture and precipitation anomalies reaching up to the Mediterranean. As discussed in Chapter 5, a tropical-plume like rainfall pattern is observed over the Sahara during phase 6 (Fig. A.2.8f). The triggering of this plume and the relationship to the extratropics will be discussed in Section 6.3. The circulation patterns presented here are comparable with results in previous studies (Janicot et al., 2010; Thiawa et al., 2017). It should be noted that the ER waves are likely related to the so called "Sahel-mode" of intraseasonal rainfall variability (Sultan et al., 2003; Janicot et al., 2010).

TDs have a strong influence on the upper-level divergence field (Figs. 6.3a,b and A.2.5) due to their strong coupling with convection. The flow is modulated up to roughly 25°N. TDs correspond mainly to AEWs over Africa (Roundy and Frank, 2004). Thus, the circulation patterns of TDs presented here match well with the typical structure of AEWs. In the trough of the AEW and ahead of it in the region of northerlies, precipitation is enhanced (Duvel, 1990; Fink and Reiner, 2003; Janiga and Thorncroft, 2016). A secondary maximum, which can be found in the region
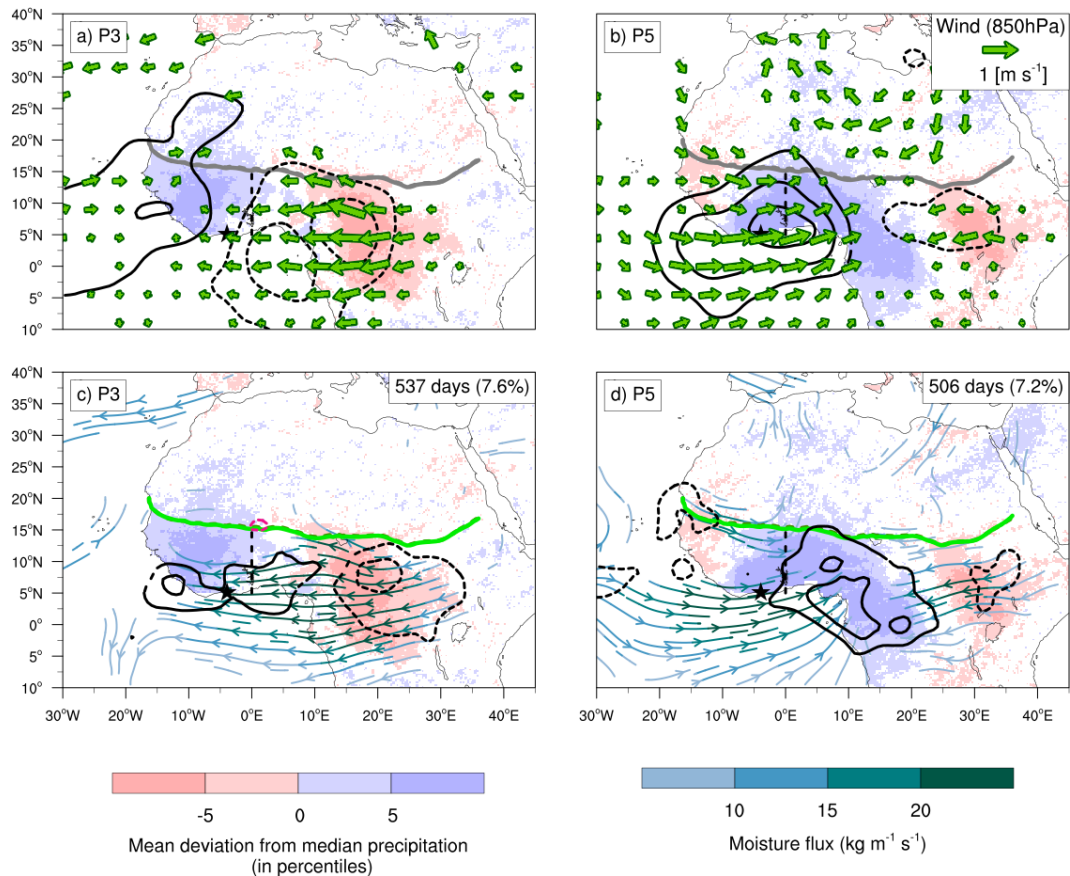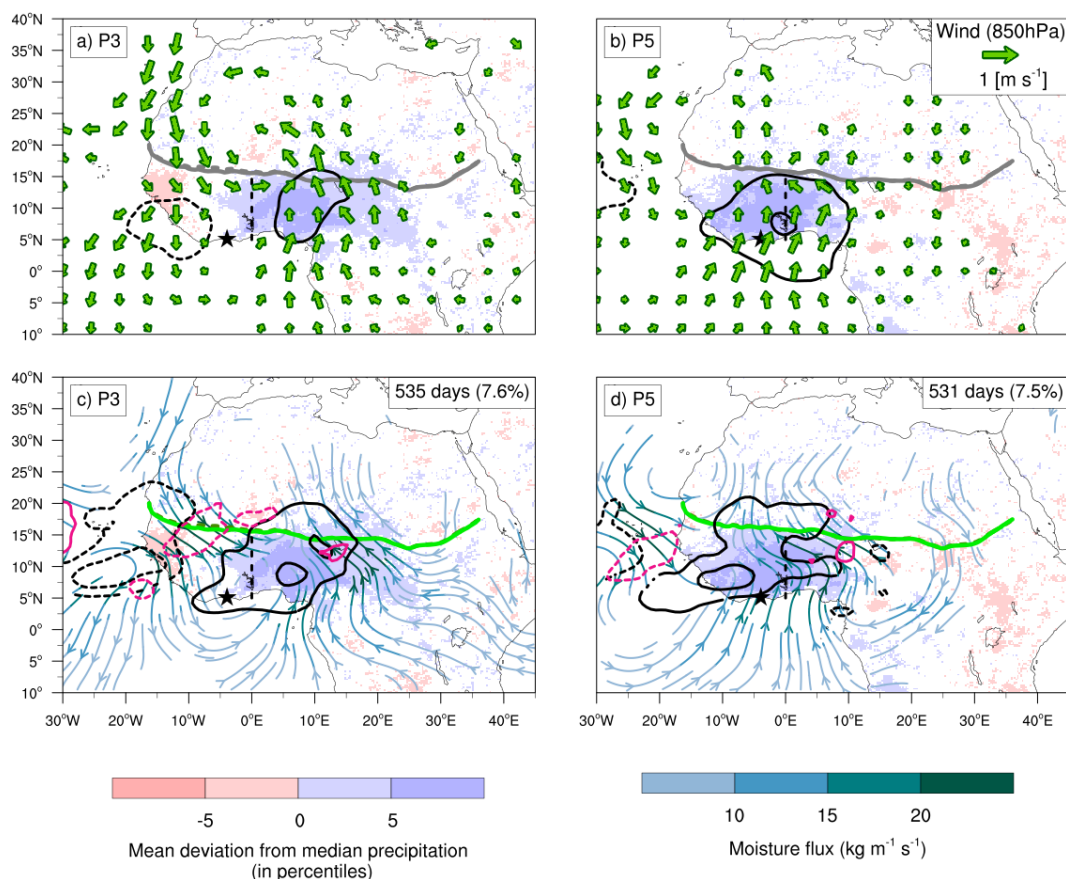
Figure 6.4: Same as Fig. 6.1, but for Kelvin wave. The star shows the location of the radiosonde station in Abidjan used in Fig. 6.7c. Reprinted from Schlueter et al. (2019b). © 2019, American Meteorological Society. Used with permission.

of southerlies, is not resolved by the filtering method applied here. It should be noted that the position of precipitation and dynamical forcing has been described to change substantially when the wave moves offshore (Kiladis et al., 2006), which is not visible in Fig. 6.3. The vortices related to the modulation of the AEJ, result in moisture flux convergence and divergence (Fig. 6.3c,d and A.2.11). The zonal gradient of moisture at the boundary of the monsoon layer (not shown) lead to a tilt of the moisture flux convergence fields. This tilt can also be seen in composites of TRMM precipitation (Fig. A.1.11). In the wake of the precipitation maxima and minima, PW is slightly reduced and enhanced, respectively. Associated with the northerlies in the dry sector and southerlies in the wet sector, the mean position of the ITD modulates by about 50 to 100 km. A weak cross-equatorial flow might stem from contamination by MRG waves, which have a partial overlap in the filter bands with TDs (Cheng et al. 2019).

Kelvin waves show a pronounced influence on the zonal flow patterns symmetric about the equator (Figs. 6.4, A.2.4, and A.2.10) as predicted by theory (Matsuno, 1966). Although the flow pattern is primarily zonal, an enhanced

southerly component is evident in the wet phase (Fig. 6.4b) and a northerly component in the dry phase over West Africa (Fig. A.2.4a). Theoretical studies predict this additional meridional circulation, if the forcing lies off the equator (Gill, 1980; Dias and Pauluis, 2009). The observed circulation patterns are consistent with previous studies over Africa (Mounier et al., 2007; Mekonnen et al., 2008; Nguyen and Duvel, 2008; Sinclaire et al., 2015; Thiawa et al., 2017). The wet phases are associated with regions of enhanced low-level westerlies and vice versa. This deviates from dry inviscid linear theory which would predict precipitation in quadrature with the zonal wind. As convectively coupled Kelvin waves are vertically tilted, the lower-level convergence center leads the precipitation anomalies, with upper-level divergence lagging by approximately $1/8$ of the wavelength (compare top panels of Fig. 6.4 with bottom panels). The vertical structure will be discussed in detail in the following subsection. Similar to the MJO, westerlies during the wet phase lead to increased horizontal shear on the southern flank of the AEJ. Kelvin waves facilitate precipitation mainly due to moisture flux convergence (Fig. 6.4d). Because moisture has a low gradient meridionally (not shown), the moisture flux convergence is predominantly generated due to convergence of zonal winds. The mean ITD position does not shift significantly. The influence on precipitation and circulation reaches into the Sahel to about 15°N. As Kelvin waves quickly move over Africa and moisture is removed by precipitation, PW is not strongly affected.

MRG waves over the African continent are not well studied. They are a more rotational wave type and feature deep westward moving vortices reaching from 850–300 hPa and centered at around 25–30°N (Figs. 6.5, A.2.3, and A.2.9). Consistent with shallow water theory, they modulate the cross-equatorial meridional flow. Precipitation is mainly related to moisture flux convergence. Similar to the faster moving TDs and Kelvin waves, the modulation of PW is weaker compared with the MJO and ER waves. As MRG waves have a strong meridional component at the equator, moist air masses are transported northward originating from the Gulf of Guinea and Congo Basin. These moisture anomalies reach up to 20°N. The mean ITD position, however, is not significantly affected. Moisture flux convergence directly at the Guinea Coast leads the anomalies further inland. In the subtropics, a westward propagating signal can be observed at 300 hPa (Fig. A.2.3). MRG waves share several similarities with TDs. As their spectral bands partially overlap, both modes can project onto each other. Over the Pacific, MRG waves can transition to off-equatorial TDs (Takayabu and Nitta, 1993). Both wave modes closely interact over Africa (Cheng et al., 2019). Despite the spectral overlap, the clearly different

Figure 6.5: Same as Fig. 6.1, but for mixed Rossby gravity wave. The star shows the location of the radiosonde station in Abidjan used in Fig. 6.7b. Reprinted from Schlueter et al. (2019b). © 2019, American Meteorological Society. Used with permission.

circulation patterns of MRGs (Fig. 6.5) and TDs (Fig. 6.3) indicate that MRG waves are in fact a distinct wave mode over Africa and should be treated individually. The most notable difference is that enhanced precipitation in MRG waves is found in the low-level southerlies, whereas TDs feature enhanced precipitation in the region of northerlies.

The influence of EIG waves on the circulation and moisture fields is weak and, thus, the corresponding plots are only shown in the supplementary material (Figs. A.2.6, and A.2.12). As predicted by shallow-water theory, regions of upper-level divergence and positive precipitation anomalies in the northern hemisphere are related with northerlies, and vice versa (Fig. A.2.6a,d). The moisture distribution and ITD position are hardly influenced. The role of EIG waves on the WAM has not been studied so far. This study shows that the influence of EIG waves on the dynamics and thermodynamics of the WAM is minor. EIG waves are more difficult to capture due to their weak influence on circulation (Kiladis et al., 2016). A drawback of the applied methods is that the filtering, which is based on daily OLR measurements, might miss the sub-daily EIG signal. Additionally, reanalysis

might not adequately capture these imbalanced modes, which are to a large extent not assimilated by current NWP models (Žagar et al., 2016).

6.2 Vertical structure and mechanism of rainfall modulation

The mechanisms of rainfall modulation depend on the vertical profile of the tropical waves. Figure 6.6 shows the modulation of three key ingredients for MCS organization in two boxes in West Africa as measured by reanalysis data. To give a more detailed picture of the vertical structure of ER waves, TDs, Kelvin, and MRG waves, radiosonde data are also analyzed (Fig. 6.7). No consistent modulation of radiosonde data was found for the MJO and EIG wave and, thus, their composites are not shown here.

The MJO indicates facilitated conditions for organization of MCSs in the reanalysis data. CAPE in the Guinea Coast leads the convective maximum by two phases and is in phase with convection in the West Sahel (Fig. 6.6a). Before the wet peak, absolute wind shear increases and decreases sharply after the peak. Convective down-drafts are likely weaker during wet phases, as mid-level moisture is enhanced. Conditions for MCSs are favorable before and during the wet peak of rainfall and slightly unfavorable after the peak in rainfall.

ER waves (Fig. 6.6b) demonstrate a unique modulation of thermodynamic conditions with unfavorable conditions for MCSs during the wet phases. In contrast to the other wave types, CAPE and wind shear are reduced during wet phases and enhanced during dry phases, although the CAPE anomaly is weak. Mid-level moisture is strongly enhanced during the wet phases of ER waves and decreased during dry phases. Radiosonde data at Niamey gives a more detailed view on the vertical structure of ER waves (Fig. 6.7a). In contrast to the following waves, ER waves are not tilted vertically and suggest instead a deep barotropic structure. During the passage of ER waves, the entire troposphere moistens and then dries. In the mid-troposphere, absolute RH increases and decreases by more than 10 %. Consistent with reanalysis data, the effect on parcel buoyancy is weak. LFC and CIN are slightly lowered during the wet phase. Winds turn cyclonically with time consistent with Fig. A.2.2. The AEJ is weaker before the wet phase and stronger afterwards. Upper-level wind divergence leads the rainfall maximum. This indicates that precipitation is mainly generated by large-scale lifting and moistening.

The influence of TDs (Fig. 6.6c) on organization of convection resembles the modulation by Kelvin waves. The phasing and magnitude of CAPE, mid-level
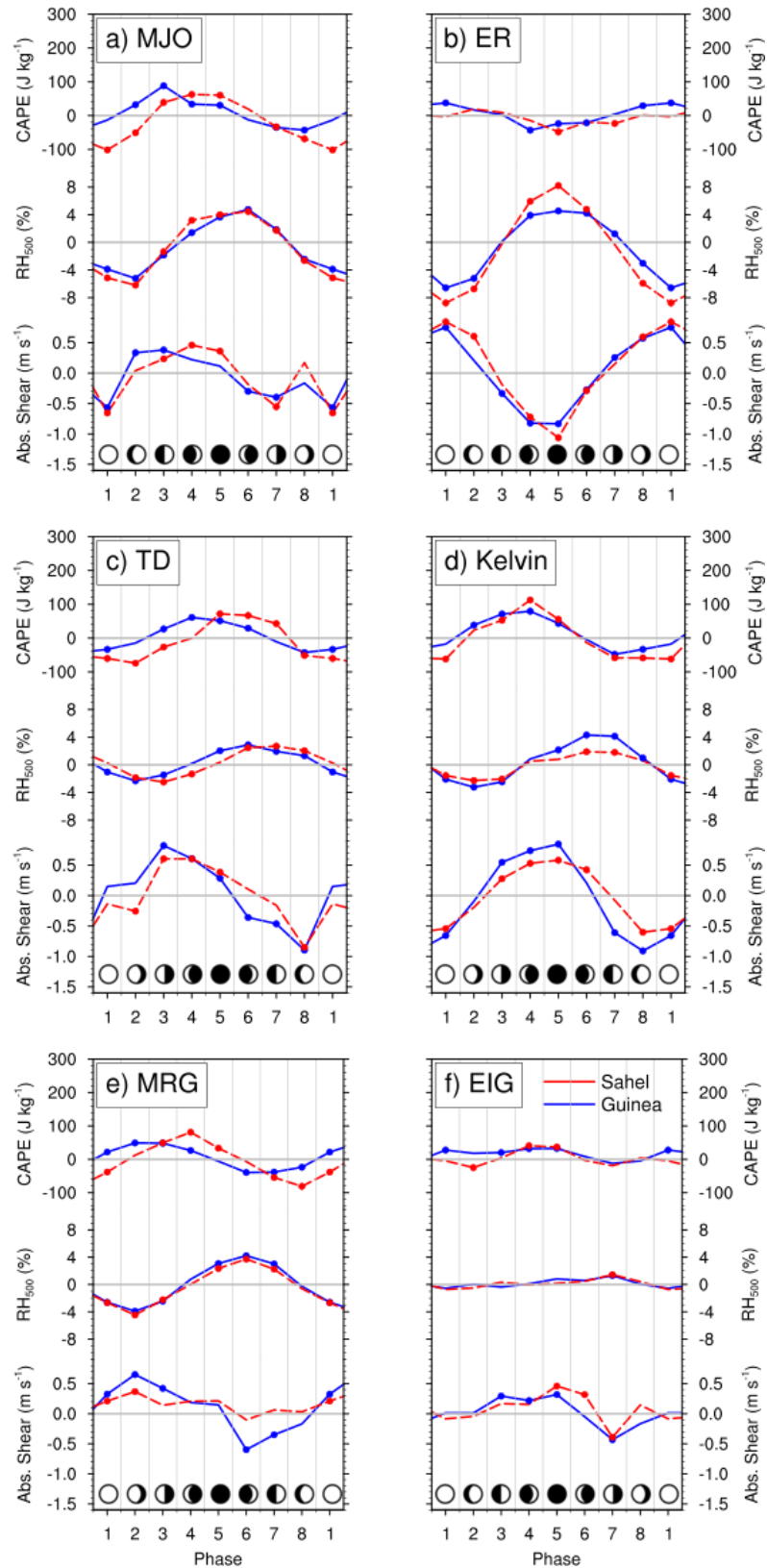
Figure 6.6: Modulation of CAPE, relative humdity in 500 hPa (RH$_{500}$), and the low-level wind shear between 600 and 925 hPa in the Sahel box (dashed red line) and Guinea box (solid blue line) during all 8 phases for six tropical waves (a-f). Significant anomalies are marked with a solid circle. Small moon symbols indicate the phase of the wave, with dry anomalies in white and wet anomalies in black (see Figs. A.2.1–A.2.12). Reprinted from Schlueter et al. (2019b). © 2019, American Meteorological Society. Used with permission.
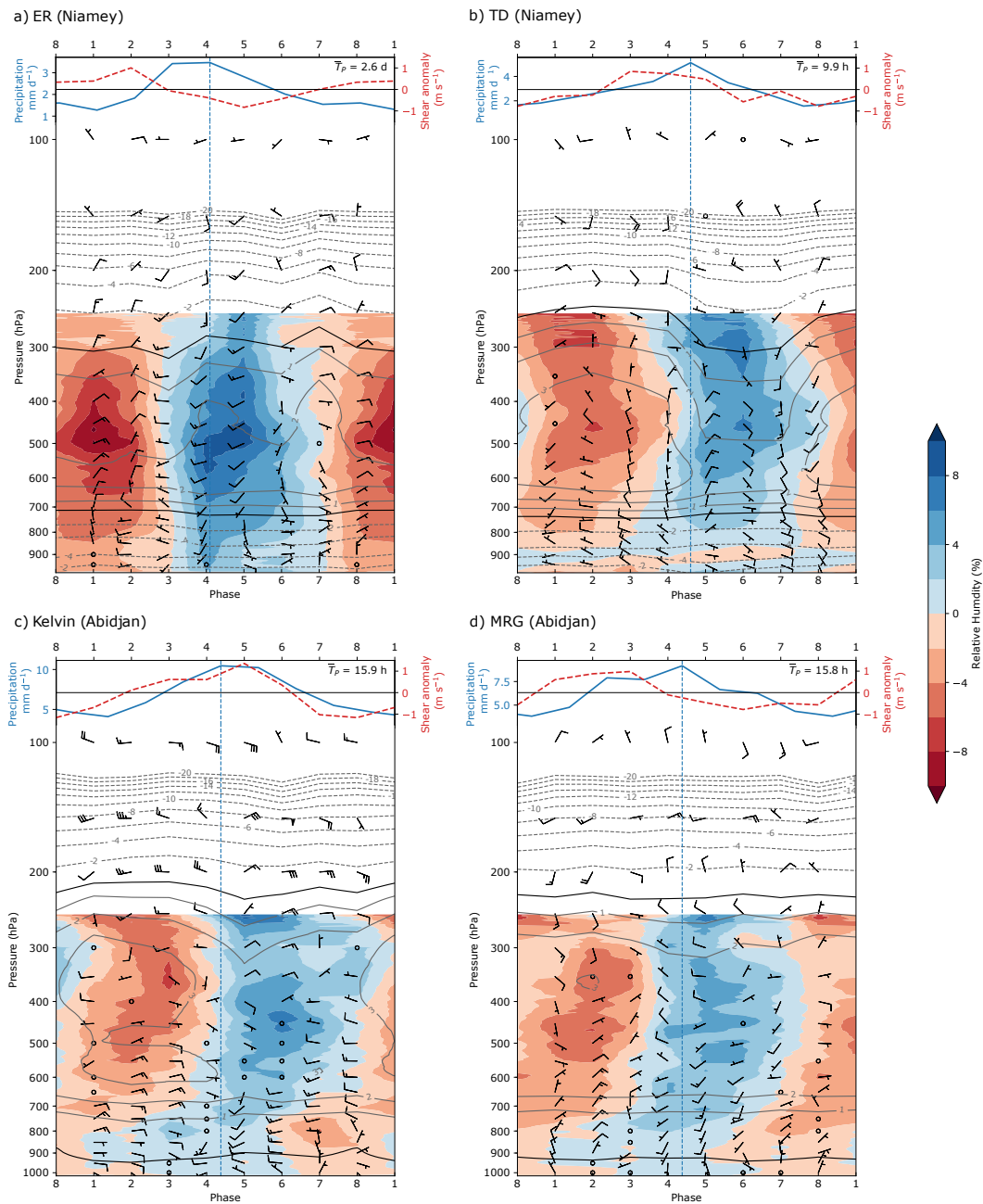
Figure 6.7: Radiosonde composite for all phases of (a) ER waves and (b) TDs over Niamey, as well as (c) Kelvin and (d) MRG waves over Abidjan during April to October. Filtering was done at 2°E and 10°–15°N for Niamey 2°E and 5°–10°N for Abidjan. Top of panels shows absolute wind shear anomaly between 600 and 925 hPa (red dashed line) and precipitation anomaly (blue line) as recorded by the rain gauge at the respective location. The precipitation is shifted by 6h to account for the time difference between radiosonde and rain gauge measurement (converted by average phase length $\overline{T}_P$, see method Section 4.9 for more detail). The blue dashed vertical line indicates peak of rainfall. Lower parts of panels show relative humidity anomaly (shading), parcel buoyancy anomaly (contours, negative dashed), and horizontal wind anomaly (wind barbs, half barbs equal to $0.5\,\mathrm{m\,s^{-1}}$, full barbs to $1\,\mathrm{m\,s^{-1}}$, and triangles to $5\,\mathrm{m\,s^{-1}}$). Bottom thick black contour line represents the LFC, and top thick line the EL. Reprinted from Schlueter et al. (2019b). © 2019, American Meteorological Society. Used with permission.

moisture, and wind shear anomalies are remarkably similar. Wind shear anomalies, however, are slightly weaker and do not change as abruptly compared to Kelvin waves. TDs are also tilted vertically, as the profile over Niamey shows (Fig. 6.7b). A very shallow region of positive humidity anomalies exists at 900 hPa during the dry phase. During phases 3–4, the troposphere moistens relatively rapidly, starting from the lower and the upper troposphere. By phase 5, the entire troposphere is moistened. Moist anomalies remain at 500–350 hPa after the passage of rain. Parcel buoyancy is strongly modulated with CAPE notably enhanced and CIN reduced before the wet peak, which is quickly diminished and increased, respectively, when deep convection occurs. After the peak of rainfall, the LFC is lifted and the EL is lowered. Consistent westerly (easterly) anomalies are evident in the lower troposphere during the dry (wet) phase. The AEJ is modulated and turns anti-cyclonically with time, whereas upper-level winds turn cyclonically. Wind shear increases before and during the rainfall peak. It can be concluded that rainfall is embedded in an environment that facilitates the formation of MCSs.

Kelvin waves (Fig. 6.6d) have similar modulation signatures as the MJO but on a shorter timescale. CAPE leads precipitation by about one phase. Mid-level moisture is reduced prior to the peak of rainfall and enhanced after the peak of rainfall. As Kelvin waves modulate zonal winds (Figs. 6.4 and A.2.4), low-level wind shear is strongly modulated, which leads the wet peak by half a phase. The radiosonde measurements at Abidjan reveal a vertical tilt (Fig. 6.7c). Moisture anomalies build up at 900–800 hPa three phases before the peak in rainfall, rise, and finally the entire troposphere is moistened after the peak of rainfall. Upper- and mid-level moisture anomalies persist after the wet peak, while lower levels start to dry again (phases 7–8). Parcel buoyancy is strongly modulated. CAPE is enhanced before the peak of rainfall and reduces with the onset of rain. During the deep convection, CIN increases, the LFC shifts upwards, and the EL is lowered. The vertical tilt of the Kelvin wave is also evident in zonal wind anomalies, which move upward with time. Meridional winds are only weakly modulated. Low-level wind shear is enhanced during the wet phase. The AEJ is strengthened during and after the dry phase, and reduces after the peak of rainfall. Upper-level winds are strongly modulated. The tropical easterly jet is enhanced during phases 5-7 and weakened during the phases 8–2. Upper-level winds diverge during the peak of rainfall facilitating deep convection. In summary, the radiosonde data suggest a build-up of low-level clouds before the rainfall peak, followed by deep and well organized convection, and finally a stratiform outflow region.

The influence of MRG waves (Fig. 6.6e) on the thermodynamic environment is in between the MJO and ER. CAPE anomalies lead precipitation anomalies by three phases in the Guinea Coast and by one phase in the West Sahel. Mid-level moisture is enhanced after the peak of the wet phase and suppressed after the dry phase. Wind shear anomalies lead precipitation anomalies by about two phases with a weaker modulation in the West Sahel. Radiosonde ascents at Abidjan reveal a vertical tilt (Fig. 6.7d). Moisture builds up at low levels (900–800 hPa) two to three phases before the peak in rainfall. The moisture anomaly shifts upward and, eventually, the entire troposphere is moistened during the rainfall peak. Upper- and mid-level moisture anomalies persist after the wet peak, while dry anomalies build up at lower levels (phases 5–7). MRG waves only weakly modulate parcel buoyancy with enhanced CAPE before the build-up of deep convection and reduced CAPE during it. The AEJ is stronger during the dry phase and weakened during the wet phase. Upper-level winds converge before the wet peak and diverge after the wet peak indicating that deep convection is first suppressed but then emerges during the wet peak. As low-level wind shear is enhanced before the wet peak and reduces after the rainfall peak, good conditions for MCS organization persist only during the wet peak. The build-up of rainfall by MRG waves is gradual over Abidjan until deep convection develops followed by a stratiform outflow region (Fig. 6.7d).

EIG waves (Fig. 6.6f) only weakly modulate CAPE, mid-level moisture, and wind shear. Wind shear is weakly enhanced before and during, and reduced after the wet phase. This study suggests that EIG waves have at most a minor influence on mesoscale organization of precipitation.

All tropical waves, except ER waves, have a similar vertical structure although they act on different timescales (Mapes et al., 2006; Kiladis et al., 2009). CCEWs are tilted vertically. Ahead of the region of enhanced rainfall, winds converge and moisture is increased at low levels. Mid levels moisten during the progression of the wave until the entire troposphere is moist during the deep convective phase. Furthermore, the Boussinesq model theoretically predicts such a behavior for imbalanced waves (Roundy and Janiga, 2012). This model is an alternative theory to the shallow-water model, which additionally takes buoyancy into account. In balanced waves, buoyancy does not act as a restoring force and thus they do not possess such a vertical tilt. The radiosonde analysis are consistent with these results. The more imbalanced modes (TDs, Kelvin, and partially the MRG waves) show a tilted vertical structure, whereas the balanced, equivalent barotropic ER wave lacks such a tilt (Kiladis and Wheeler, 1995; Yang and Hoskins, 2017; Yang et al., 2018). The tilt of ER waves depends on longitude. As the waves grow baroclinically, their

tilt decreases when moving over Africa towards the Atlantic Ocean (Yang et al., 2018). To test this was beyond the scope of this study. The vertical structure of the MJO, which was not analyzed in this study, is similar to that of a Kelvin wave (Mapes et al., 2006; Tian et al., 2006; Roundy, 2012; Jiang et al., 2015).

Rainfall anomalies in the more balanced ER wave are mostly related to large-scale moistening and quasi-geostropic lifting. Stratiform rain is thus facilitated. The rainfall anomaly in predominantly imbalanced waves (MJO, Kelvin, and partially MRG) is of convective nature. Increased CAPE and low-level shear as well as decreased mid-level humidity favor vigorous and organized convection during the wet phase. TDs show the same effects. As MRGs have imbalanced characteristics at low wavenumbers and transition to a quasigeostrophic behavior at higher wavenumbers (Delayen and Yano, 2009), the organization of MCSs is not as strongly modulated, compared with the MJO, TDs, and Kelvin waves. Several studies have documented that favorable conditions for MCSs exist over Africa during the passage of AEWs (e.g. Duvel, 1990; Fink and Reiner, 2003; Janiga and Thorncroft, 2016; Maranan et al., 2018) and Kelvin waves (e.g. Mounier et al., 2007; Nguyen and Duvel, 2008; Laing et al., 2011; Sinclaire et al., 2015). Kelvin and MRG waves are also known to modulate MCSs (Holder et al., 2008). Although EIG waves are by nature imbalanced modes, this study could only reveal a minor influence on vertical profiles. Yet, it could be speculated that the applied methods could either not measure this adequately due to the high speed of EIG waves or that they are too fast to affect the timescale of convective organization.

6.3 Relationship to extra-tropical Rossby waves

The MJO and ER waves can trigger tropical plume-like precipitation anomalies over the Sahara. These structures appear during the local phase 4 of the MJO (Fig. A.2.7d) and phase 6 of ER (Fig. A.2.8f; 3D-visualization of the plume in Fig. A.2.13). Between April and July, 73 % of cases with MJO in phase 4 occur and 74 % of cases with ER in phase 6 (Fig. 6.8). The preference of tropical plumes during spring is even more evident when only looking at strong cases in phase 4 and 6, respectively, where the local wave amplitude is greater than 2. 90 % of the 97 strong MJO cases during the extended monsoon season and 76 % of the 106 strong ER cases take place during April and May (not shown). During the pre-monsoon, when most of the cases happen, extratropical Rossby wave trains can penetrate far south. The breaking of these Rossby waves leads to a tilted trough near the Atlas mountains and subsequently triggers a tropical plume (Knippertz, 2003; Knippertz and Martin, 2005; Fröhlich et al., 2013).
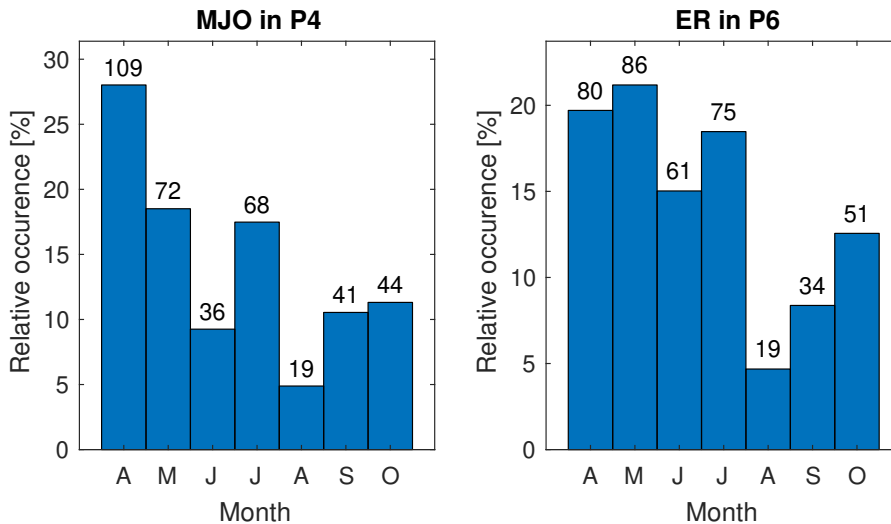
Figure 6.8: Relative occurrence of months during which local (a) MJO is significant in phase 4 and (b) ER in phase 6 at 0°E. Numbers over the bars show total count of days during each month. Reprinted from Schlueter et al. (2019b). © 2019, American Meteorological Society. Used with permission.

This study uses a local wave filtering. This way the local "flavor" of the MJO is captured more adequately. To allow comparison with the widely used real-time multivariate MJO index (RMM, Wheeler and Hendon 2004), Fig. 6.9 shows the RMM during the local phase 4, when the plume is observed. The MJO as a global mode is over the western hemisphere and Africa (RMM Phases 1 and 8). It has to be noted also that the observed MJO pattern over Africa has a more standing component (see Fig. 6.10 and Pohl et al. 2009b). Roughly 40 % of significant local MJO events over Africa are missed by the global RMM index (Fig. 6.9). Thus, a direct comparison with global MJO studies is limited.

The MJO couples with extra-tropical Rossby waves as the associated precipitation and circulation patterns suggest, which resemble tropical plumes (Figs. 6.1d and A.2.1d). The relationship between the tropical and extratropical regime on the intraseasonal timescale is complex. One mechanism of how the MJO influences remote areas are through the excitation of Rossby wave trains (Opsteegh and van den Dool, 1980; Hoskins and Karoly, 1981; Seo and Lee, 2017). During phase 4, precipitation is enhanced south of a trough located over the Atlas mountains. The time lag composites prior to the tropical plume show that positive geopotential height anomalies are evident in the upper troposphere one month prior to rainfall events (Fig. 6.10a). In the Northern Hemisphere, a quasi-stationary Rossby wave train exists. The composites suggest that the MJO band rather reflects a standing than an eastward propagating mode. A dry anomaly persists over Africa for several weeks and vanishes as soon as the geopotential

RMM during P4
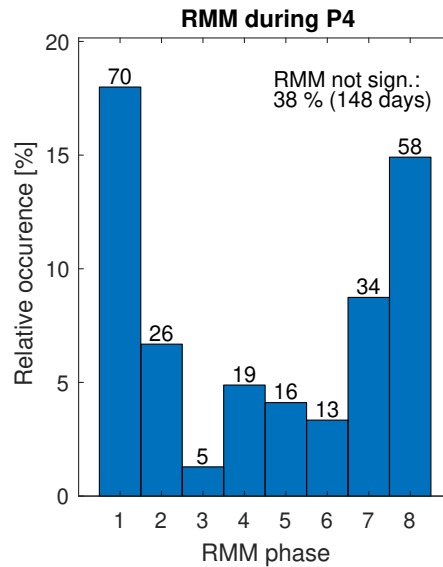
Figure 6.9: Real-time multivariate MJO index (RMM) when local MJO is significant in phase 4. The histogram depicts the relative occurrence in each phase. Numbers over the bars show total count of days during each RMM phase. The index was obtained from http://www.bom.gov.au/climate/mjo/. Reprinted from Schlueter et al. (2019b). © 2019, American Meteorological Society. Used with permission.

anomaly vanishes. Related to the Rossby wave train over the Atlantic Ocean, the SHL is strengthened ahead of a rigde over Central Europe (Figs. 6.10a-c). The blocking frequency over the Atlantic Ocean and Europe has been shown to be modulated by the MJO (Henderson et al., 2016). Following this rigde, a trough amplifies over Central Europe ten days later, which merges with a trough over the Atlas mountains (Figs. 6.10e-f). The related south-westerlies over the Sahara transport moisture northwards and facilitate the generation of rainfall over the region (Fig. 6.1d). Additionally to the geopotential anomalies over the Atlantic Ocean and Europe, a cyclonic and anti-cyclonic vortex pair exists over the Indian subcontinent 25–15 days before the event (Figs. 6.10a-c). This indicates a potential influence of the Indian monsoon system on the WAM on the intraseasonal timescale. The Indian Monsoon system can influence the MJO signal over Africa during the monsoon season (Leroux et al., 2010; Berhane et al., 2015). Active and break phases of the Indian monsoon also project onto the intraseasonal signal of rainfall over West Africa 15–20 days later (Janicot et al., 2009). The quasi-stationarity of the signal in the extratropics suggests a possible link to other intraseasonal modes. The geopotential patterns at day -25 resemble a positive NAO pattern that reverses until day 0. Although, the AO is weak during boreal summer, a positive AO precedes the event, as negative geopotential anomalies in polar and positive anomalies in subtropical regions suggest. Time lag analysis of the NAO, AO, and PNA indices reveal that positive NAO and AO phases are more likely 40 to 20 days before the
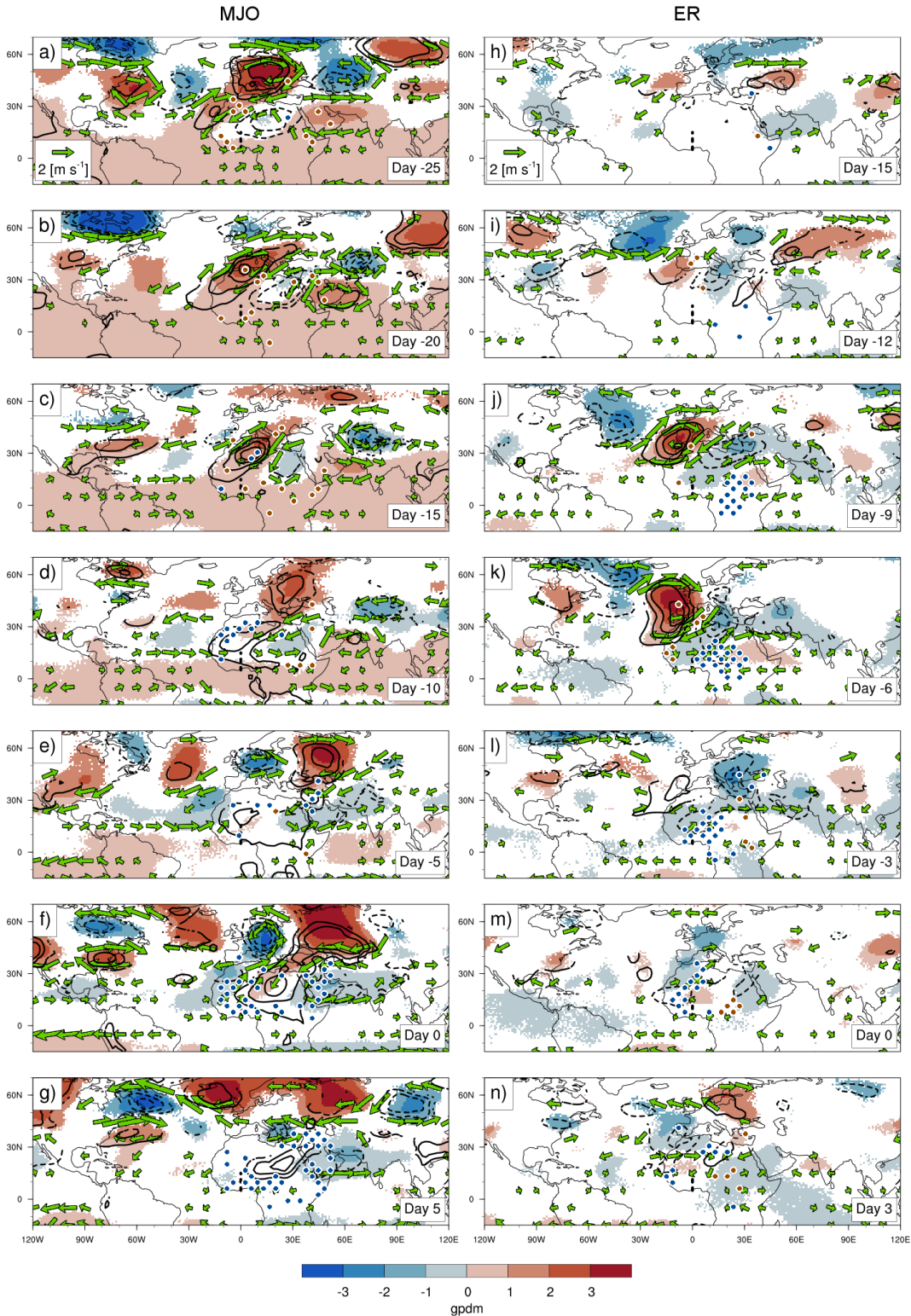
Figure 6.10: Time lag composites of significant anomalies of wind (vector) and geopotential (shading) in 300 hPa and geopotential thickness between 925 and 600 hPa (contours, from -1 to 1 gpdm in 0.25 steps, negative dashed) for days before the occurrence of a tropical plume-like MJO signal during phase 4 (a-g) and an ER signal during phase 6 (h-n). Significant precipitation anomalies over Africa are shown with blue (positive) and red (negative) dots. The wave signal was filtered for 5°–15°N, 0°E (dashed line). The analyzed time period spans from 1979 to 2013 for the extended monsoon season (March–October). Reprinted from Schlueter et al. (2019b). © 2019, American Meteorological Society. Used with permission.
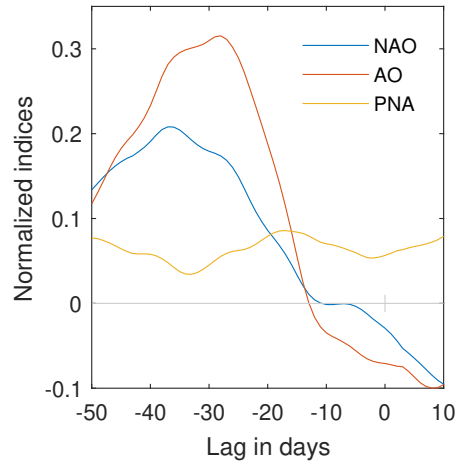
Figure 6.11: Time lag analysis of mean NAO, AO, and PNA indices before significant MJO signals in local phase 4 at 0°E. A 15-day running mean was applied to the timeseries in order to highlight the intraseasonal variability. Reprinted from Schlueter et al. (2019b). © 2019, American Meteorological Society. Used with permission.

plume (Fig. 6.11). The NAO is related to intraseasonal variability over West Africa (Alaka and Maloney, 2014) and the global MJO (Cassou, 2008; Lin et al., 2009). The AO, which is correlated with the NAO, has been also associated with the MJO (Zhou and Miller, 2005; L'Heureux and Higgins, 2008). A connection with the PNA could not be found in this study, as has been noted for the global MJO previously (Ferranti et al., 1990; Mori and Watanabe, 2008; Lukens et al., 2017), albeit for the boreal winter, whereas this study focuses on the pre-monsoon in late boreal spring.

ER waves, which act on a shorter timescale than the MJO, also show a precipitation pattern over the Sahara reminiscent of tropical plumes. The involved mechanism is likely different. Upper-level geopotential height patterns suggests that the westward propagating ER signal interacts with the eastward movement of extratropical Rossby waves, triggering a wave breaking and leading to a tropical plume in phase 6 (not shown). Enhanced precipitation can then be found south and south-east of a trough over the Atlas mountains. A similar pattern has been documented previously (Janicot et al., 2010; Thiawa et al., 2017). Twelve days before the event, weak geopotential anomaly patterns reach from the Atlantic Ocean to the Indian subcontinent, forming a Rossby wave train (Fig. 6.10i). As it intensifies, a ridge over western Europe triggers cold south-easterlies over northern Africa, which ventilate the northern part of the SHL. Over northern India, significant geopotential and thickness anomalies are evident at day -15 (Fig. 6.10h). These anomalies travel westwards and intensify over Central and East Africa (Figs. 6.10j-k). A trough, which stretches from the Atlas mountains to Central Europe, strengthens and triggers north-westerly wind anomalies that subsequently lead to

the formation of the tropical plume (Figs. 6.10l-m). Based on the time-lagged composites we hypothesize that breaking extratropical Rossby wave can project onto the ER band. From the time-lag analysis, it is not clear, however, to what portion ER waves can be attributed, i.e. to an extratropical wave train or to tropical origin. Further research is needed here. Separating both regimes would help to answer this question. As a final side remark, mid-latitude wave trains originating over the Atlantic influence the intraseasonal variability of the WAM (Vizy and Cook, 2009, 2014; Chauvin et al., 2010; Leroux et al., 2011). The SHL serves as a link between the extratropics and tropics (Chauvin et al., 2010; Leroux et al., 2011; Roehrig et al., 2011). Consequently, the strength and location of the SHL affects the activity of AEWs and intraseasonal variability of rainfall over northern tropical Africa. These studies and the results presented here emphasize the relevance of extratropical forcing for the intraseasonal rainfall variability in the study region.

7 | Potential for forecasting

Numerical methods lack useful skill in prediction of rainfall variability over Africa (see Section 2.3). This stresses the need for new forecasting methods. This chapter presents a novel approach to forecast tropical rainfall. First, Section 7.1 presents how tropical waves carry predictability on the synoptic to intraseasonal timescale as systematic spatio-temporal correlation patterns. The observed wave properties are compared with theoretical values in 7.2. Together with colleagues from the Department of Mathematics, we developed a statistical forecast method, which exploits such spatio-temporal correlation patterns. This concept for a statistical forecast of African rainfall will be presented in 7.3. Finally, Section 7.4 concludes this chapter with final remarks on the potential of tropical waves for forecasting rainfall in the entire tropics.

7.1 Tropical waves as predictable spatio-temporal modes

Atmospheric modes explain a large portion of synoptic to intraseasonal rainfall variability over Africa, as Chapter 5 has corroborated. In the equatorial shallow water theory, waves are assumed to conserve their energy and damping by, e.g., friction or non-linear effects is not considered (Matsuno, 1966). In reality however, all tropical wave types can be described as wavelets. Due to damping and dispersion, they have a limited lifetime and, maybe except for the planetary-scale MJO, a spatially confined influence. The spatio-temporal autocorrelation of a wave signal reveals qualitatively the stability of the wave in time and space. A statistical model can exploit the correlation patterns of current observations with observations at lead time Δt. The maximum absolute autocorrelation at lead time Δt and distance Δx is a rough estimate for the predictability in a statistical sense associated with each wave type. Furthermore, the autocorrelation allows an estimation of the group and phase velocities, which have both implications for predictability. The group velocity is the speed, at which the entire wave packet travels. It can be interpreted as the speed of wave energy or information (Nettel, 2003). Therefore, the group
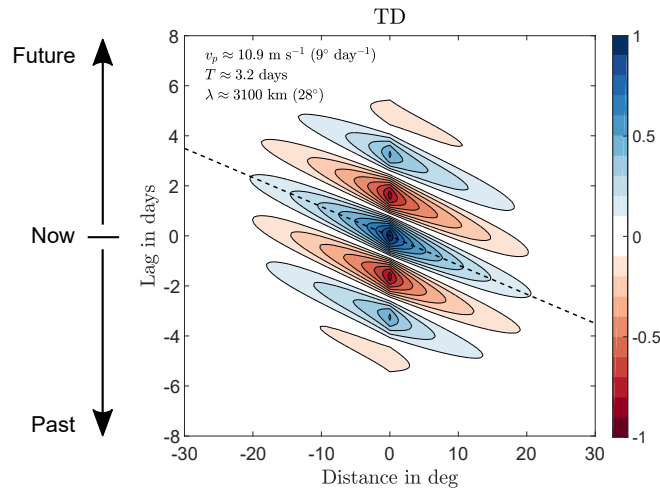
Figure 7.1: Tempo-spatial crosscorrelation of the TD signal in TRMM rainfall (1998-2016) over northern tropical Africa (30°W–50°E, 5°–15°N) during July to September. The dashed vertical line shows the extrapolated estimated fit for the phase velocity v_p. The upper left corner states the estimated phase velocity v_p, period T, and wavelength λ. See Section 4.11 for further details on the applied methods.

velocity is most important for the prediction of where variability associated with the wave can be expected in general. This could be relevant when, e.g., the probability of tropical cyclones activity in a basin (but not their occurrence) is the aim of the prediction (Frank and Roundy, 2006; Schreck et al., 2011). Of secondary interest is the correct prediction of the phase velocity. The phase velocity determines the phase of the wave within the wave packet. In the context of the present study, this would be relevant, e.g., in forecasting whether the passing wave packets results in a dry or wet anomaly.

To investigate spatio-temporal properties of each wave type, their autocorrelation patterns are described in the following and the implications for predictability are discussed. This study analyzes the autocorrelation of TRMM filtered bands, which highlights the nature of convectively coupled waves. A different picture might result from an analysis of, e.g., upper-level divergence, which is also modulated by the passage of dry equatorial waves. As the aim of this study is to investigate the effect of tropical waves on rainfall variability, the present analysis is restricted to filtered TRMM rainfall.

At the synoptic scale, TDs are the dominating wave type over West Africa, which explain up to one quarter of daily rainfall variability (see Section 5.5). The autocorrelation of the TD signal over Africa reveals the spatio-temporal pattern of AEWs (Fig. 7.1). The figure shows how strongly the wave activity in the analyzed region (30°W–50°E) is correlated on average with wave activity at a spatial distance of Δx and with a temporal lead/lag of Δt. The propagation of the wave phase
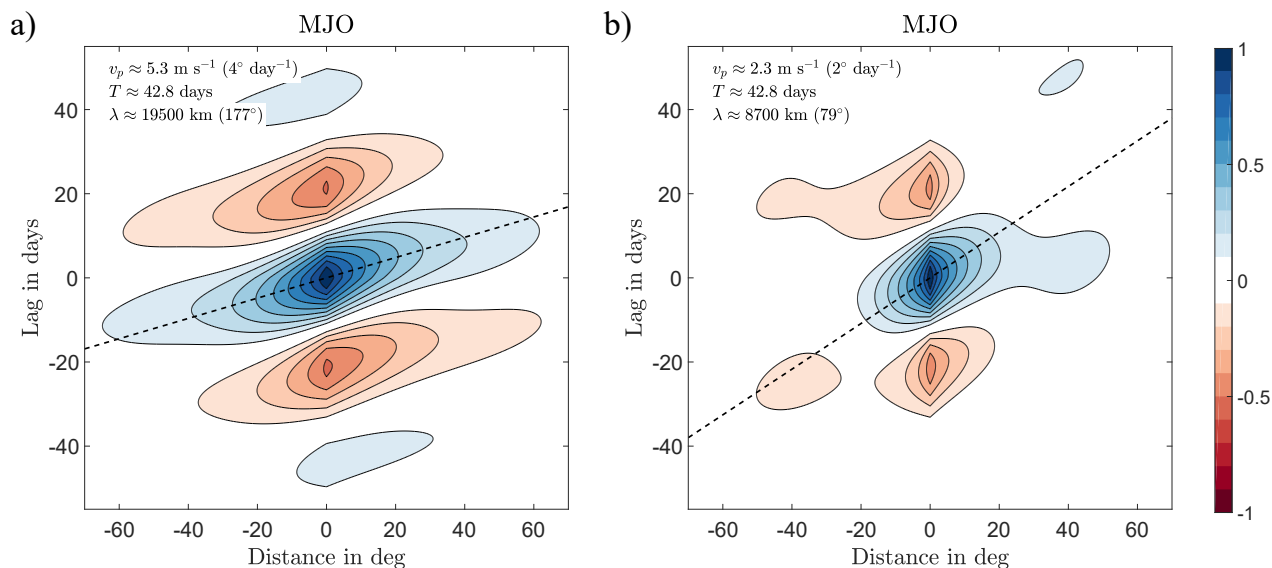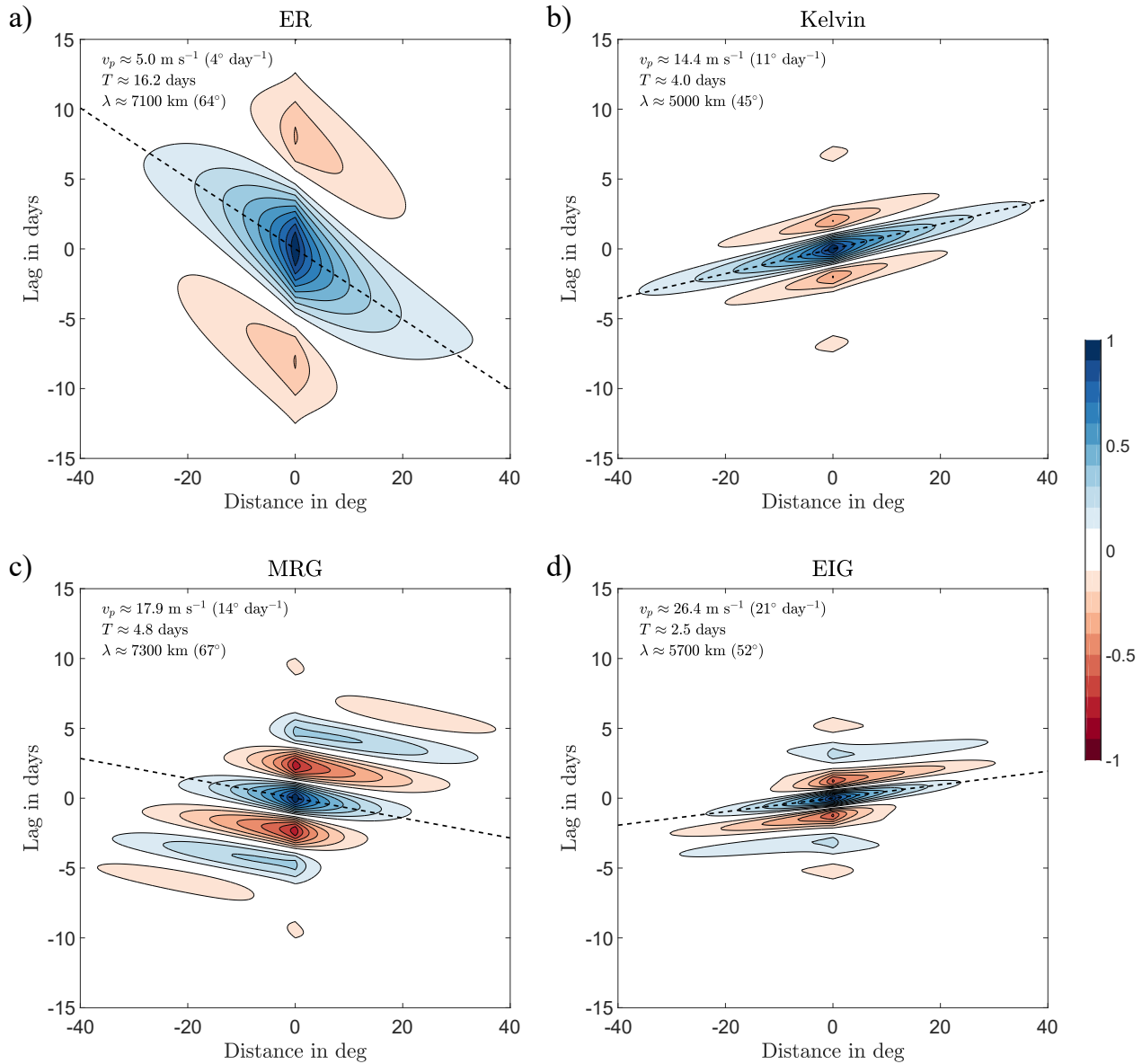
Figure 7.2: Same as 7.1, but for the MJO in the northern tropical band (5°–15°N) over (a) the entire tropics (180°W–180°E) and (b) Africa (30°W–50°E).

in space and time can be clearly seen in the areas of connected positive and negative correlations. With an estimated period of $T = 3.2$ days and phase velocity $v_p = 10.9\,\mathrm{m\,s^{-1}}$, the AEW is slightly faster than in previous studies (e.g. Reed et al. 1977). One reason for slightly faster v_p could be that using TRMM to filter for TDs might overemphasize rainfall associated with MCSs, which travel with a faster phase speed of approximately 10–20 $\mathrm{m\,s^{-1}}$ (Aspliden et al., 1976; Mathon et al., 2002; Fink and Reiner, 2003; Laing et al., 2008) The varying response to a passing wave in space (see Section 5.6) might be the reason that the temporal correlation at $\Delta x = 0$ is more pronounced than the correlation in space at $\Delta t = 0$. The estimated wavelength of 3100 km is also consistent with previous studies (Diedhiou et al., 1999; Kiladis et al., 2006). The mean predictability, which could be exploited by statistical models, can be estimated from Fig. 7.1. The maximum correlation after one period still exceeds 0.5 at $\Delta x = 0$ suggesting, that the modulating effect of AEWs can be exploited by statistical models on the synoptic timescale.

The MJO is a planetary wave mode affecting precipitation at the intraseasonal timescale. The MJO on a global scale shows a strong intraseasonal signal with a mean period of $T \approx 43$ days propagating with an estimated phase velocity of $v_p = 5.3\,\mathrm{m\,s^{-1}}$ (Fig. 7.2a) consistent with previous estimates (Weickmann et al., 1985; Adames and Kim, 2016). The mean planetary zonal wave number is approximately $k = 2$. The autocorrelation pattern over the African continent presents a different picture compared with the global autocorrelation pattern (Fig. 7.2b). Consistent with previous studies, the MJO has a more standing component (Matthews, 2004; Janicot et al., 2009; Alaka and Maloney, 2012). The spatial correlation pattern

a) **ER**

$v_p \approx 5.0$ m s^{-1} ($4°$ day^{-1})
$T \approx 16.2$ days
$\lambda \approx 7100$ km ($64°$)

b) **Kelvin**

$v_p \approx 14.4$ m s^{-1} ($11°$ day^{-1})
$T \approx 4.0$ days
$\lambda \approx 5000$ km ($45°$)

c) **MRG**

$v_p \approx 17.9$ m s^{-1} ($14°$ day^{-1})
$T \approx 4.8$ days
$\lambda \approx 7300$ km ($67°$)

d) **EIG**

$v_p \approx 26.4$ m s^{-1} ($21°$ day^{-1})
$T \approx 2.5$ days
$\lambda \approx 5700$ km ($52°$)

Figure 7.3: Same as 7.1, but for (a) ER, (b) Kelvin, (c) MRG, and (d) EIG waves

are confined to approximately $40°$, where the estimated phase velocity is with $v_p = 2.3\,\text{m s}^{-1}$ twice as slow. Having the same period, the estimated planetary wavenumber is $k = 4.5$. The absolute correlation with the MJO signal after 22 days is about 0.4. This highlights the potential of the MJO signal as a predictor for the intraseasonal timescale.

The autocorrelation patterns of all CCEWs are shown in Fig. 7.3. The estimated spatial scales are in a similar range between $\lambda = 5000$ and $7300\,\text{km}$ ($k = 5.5$–8). As largest CCEW, ER waves have a period of $T = 16.2$ days and a phase velocity of $v_p = 5.0\,\text{m s}^{-1}$ (Fig. 7.3a). The numbers are similar to Janicot et al. (2010) who found a wavelength of $7500\,\text{km}$ for ER waves over Africa and

a wave speed of $6\,\mathrm{m\,s^{-1}}$. The autocorrelation suggests that ER waves are useful predictors in statistical forecasts up to about eight days, after which the maximum absolute correlation drops below 0.3.

Kelvin waves have a phase velocity of $v_p = 14.4\,\mathrm{m\,s^{-1}}$ (Fig. 7.3b) consistent with previous estimates of $v_p = 12 - 15\,\mathrm{m\,s^{-1}}$ (Nguyen and Duvel, 2008; Mounier et al., 2007; Mekonnen et al., 2008). Their period is relatively short with $T = 4.0$ days and after two days, the maximum absolute correlation drops below 0.4, suggesting that Kelvin waves are useful as predictors in statistical forecasts for up to two days.

MRG and EIG waves show a stronger wave dispersion in comparison to ER and Kelvin waves. In MRG waves, the phase propagates westwards with an estimated phase velocity of $v_p = 18\,\mathrm{m\,s^{-1}}$ (Fig. 7.3c). Estimates of the phase speed of MRG waves range from $9\,\mathrm{m\,s^{-1}}$ (Chang, 1970; Yang et al., 2007a) to $20\,\mathrm{m\,s^{-1}}$ (Hendon and Liebmann, 1991; Wheeler et al., 2000; Dias and Kiladis, 2016). The entire MRG wave packet, however, travels eastward, resulting in dispersion of the wave (Yang et al., 2007a). A rough visual estimate of the velocity of the wave packet yields an estimated group velocity for the MRG waves of $v_g = 3\text{–}5\,\mathrm{m\,s^{-1}}$. With a period of $T = 4.8$ days, MRG waves have a slightly shorter period than Kelvin waves.

EIG waves are with $v_p = 26\,\mathrm{m\,s^{-1}}$ the fastest analyzed CCEW (Fig. 7.3d), equivalent to estimates by Dias and Kiladis (2016). With a period of $T = 2.5$ days, they are also the waves with the highest frequency. The autocorrelation pattern reveals that the entire wave packet travels slower than individual phases. Therefore, EIG waves are also dispersive. Due to the strong autocorrelation at $\Delta x = 0$ the group velocity is difficult to assess. Visually estimated, their group velocity lies between 3 and $7\,\mathrm{m\,s^{-1}}$.

This analysis gave first insights into the predictability of single tropical wave modes over Africa. The presented results are largely also valid for the rest of the tropics, as the spatio-temporal autocorrelation of tropical waves on the entire globe are very similar to results over Africa (Figs. A.3.1–A.3.2). The global autocorrelation patterns are stronger and smoother than those over Africa. All patterns resemble 2D Gabor wavelets, which were originally developed for a spectral analysis of the visual cortex (Daugman, 1980, 1988; Lee, 1996). These functions can also be understood as Gaussian-windowed plane waves. Reconciling the observations with these (or similar functions) could provide a useful way to represent and better understand the spatio-temporal characteristics of atmospheric waves. Further research is needed in this respect.

7.2 Theoretical spatio-temporal properties
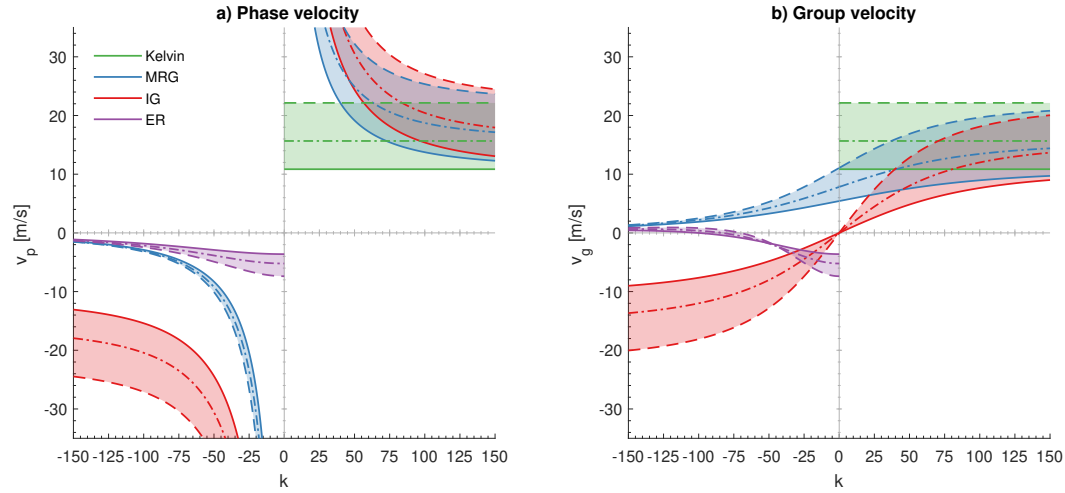
Figure 7.4: Theoretical (a) phase and (b) group velocities of Kelvin ($n = -1$), MRG ($n = 0$), IG ($n = 1$), and ER ($n = 1$) waves for planetary zonal wavenumbers -400 to 400 and equivalent depths h_e of 12 m (solid line), 25 m (dash-dot line), and 50 m (dotted line). Negative wavenumbers refer to waves with westward propagating phase and positive wavenumbers to an eastward propagation. Derivatives for v_g were obtained using www.wolframalpha.com.

Matsuno's set of equations for motions at the equator yields theoretical dispersion curves for CCEWs. The observed correlation patterns can be compared with predicted properties of CCEWs. As the MJO and TDs are not covered in the equatorial shallow-water theory, in the following only ER, Kelvin, MRG and EIG will be considered. This section will treat theoretical considerations on the predictability of phase and energy of CCEWs as predicted by their dispersion relations given by Eq. (2.5)–(2.8).

The phase velocity v_p and the group velocity v_g of a wave with frequency ω and zonal wavenumber k are defined by

$$v_p = \frac{\omega}{k}, \tag{7.1}$$

$$v_g = \frac{\partial \omega}{\partial k}. \tag{7.2}$$

Figure 7.4 shows the theoretical phase and group velocities of Kelvin ($n = -1$), ER ($n = 1$), westward and eastward MRG ($n = 0$), IG ($n = 1$) waves[1] obtained from Eq. (2.5)–(2.8). A detailed discussion of the wave properties can be found in the

---

[1] To avoid confusion, the reader should be reminded that this study refers to the eastward propagating MRG waves ($n = 0$) as EIG ($n = 0$) following established nomenclature. As pointed out in Section 5.3, the filtered EIG ($n = 0$) signal might, nevertheless, contain some higher meridional modes (EIG $n \geq 1$). Results in this study relating to EIG waves should, therefore, be compared to both dispersion lines of (eastward) MRG ($n = 0$) and (eastward) IG ($n = 1$) in Figs. 7.4–7.5.
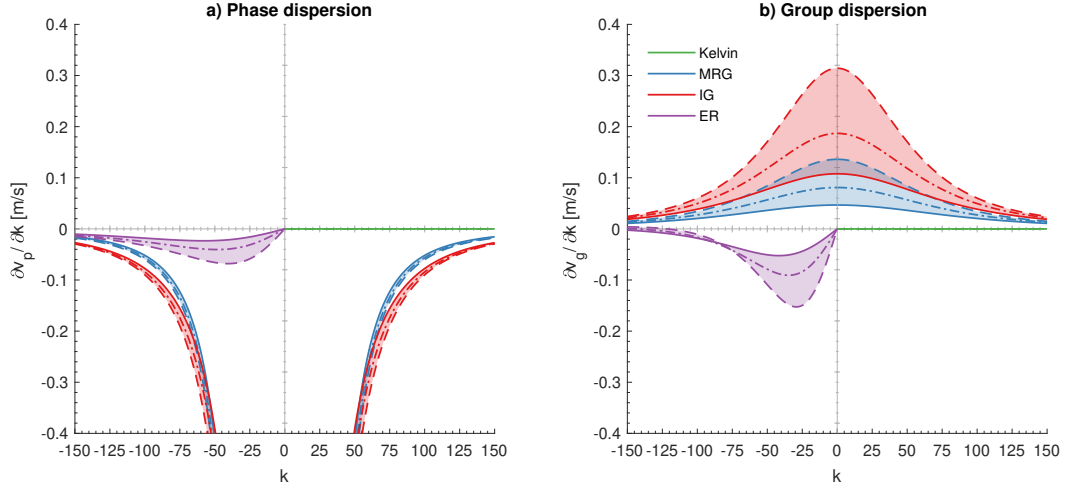
Figure 7.5: (a) Phase dispersion $\partial v_p / \partial k$ and (b) group dispersion $\partial v_g / \partial k$ (see Fig. 7.4) of equatorial waves as function of planetary wavenumber k. Derivatives were obtained using www.wolframalpha.com.

pertinent literature (e.g. Matsuno 1966; Kiladis et al. 2009; Wheeler and Nguyen 2015). Thus, this section will focus on the aspect relevant for predictability aspects.

Kelvin waves have a constant v_p and v_g, which is equal to the internal gravity wave speed as $c = \sqrt{gh_e}$, which merely depends on the equivalent depth h_e (Matsuno, 1966; Kiladis et al., 2009). With increasing wavenumber k, v_p and v_g of IG and eastward MRG ($n = 0$) waves approach this internal gravity wave speed, whereas v_p and v_g (westward) in MRG and ER approach 0. For all waves, a lower equivalent depth, which occurs at stronger convective coupling (Haertel and Kiladis, 2004), generally results in a slower v_p and v_g. The estimated v_p for ER and Kelvin waves at their respective wavenumber in Section 7.1 correspond well with theory and yield an equivalent depth of $h_e \approx 12$–50 m, which are common values for CCEWs (see Fig. 2.4, Wheeler and Kiladis 1999). The rough estimates of v_g for MRG and EIG waves match theory. Conversely, the estimated v_p for MRG and EIG waves do not match theoretical values and one would expect a wave at much smaller scales ($|k < 30|$). One possible explanation is the strong dispersion of v_p at small $|k|$, which will be treated in the next paragraph.

Wave dispersion leads to a loss of the signal with time. The phase dispersion d_p and the group dispersion d_g are defined as

$$d_p = \frac{\partial v_p}{\partial k}, \tag{7.3}$$

$$d_g = \frac{\partial v_g}{\partial k} \tag{7.4}$$

and can be understood as measures of how strongly v_p and v_g are affected by a changing k (Kneubühl, 1997). For non dispersive waves both, d_p and d_p, equal zero. The theoretical phase and group dispersions reveal the differences in dispersion for the individual wave types (Fig. 7.5). Kelvin waves are not dispersive for all k. ER waves have a maximum of phase and group dispersion between $k = -20$ to -50. At wavenumbers near zero, ER waves are barely dispersive. At low wavenumbers, MRG and EIG waves, however, have a maximum in d_g and d_p approaches infinity. From a theoretical point of view, the strong phase dispersion at low wavenumbers render it difficult to estimate v_p from wave autocorrelation plots as done in the previous section. This raises the question of how accurate the estimated phase velocities (and the corresponding wavelengths) are for these highly dispersive wave types. As this was not the main aim of the present study, this question remains open and should be studied in a subsequent analysis.

The theoretical velocity and dispersion curves have implications for the predictability of each wave. The phase speed of some CCEW approaches infinity for low wave numbers. However, the speed in which the information or energy travels is limited by the group velocity v_g. All wave types have a group velocity smaller than the internal gravity wave speed $v_g \leq \sqrt{gh_e}$. This speed is the maximum speed, in which energy can be transmitted to remote locations via pressure gradient and gravity forces. As a calculation example, CCEWs, which are triggered by a convective burst over the West Pacific (180°E), can affect West Africa (0°E) after 14.8 days at the earliest, assuming an internal gravity wave speed of $15.6\,\mathrm{m\,s}^{-1}$ ($h_e = 25\,\mathrm{m}$)[2]. Furthermore, the predictability of CCEW depends on the dispersion of v_g in time. Even without the presence of wave damping, as is assumed in shallow-water theory, dispersion results in a smearing of the signal with time. It was shown, that the dispersion increases with the scale of MRG and IG waves. The presented autocorrelation patterns and the theoretical considerations highlighted how tropical waves behave as systematic correlation patterns traveling in space and time. The next section will present how a statistical model can use such systematic spatio-temporal correlations for forecasting rainfall.

7.3 Statistical forecasting using spatio-temporal correlations

The lack of skill in current global EPS and the existing spatio-temporal correlation of rainfall motivated the development of a forecasting method, which has the aim

---

[2] Dry waves with an equivalent depth of $h_e = 200\,\mathrm{m}$ are considerably faster and travel with $v_g \leq 44.3\,\mathrm{m\,s}^{-1}$. These waves would reach West Africa already after 5.2 days.
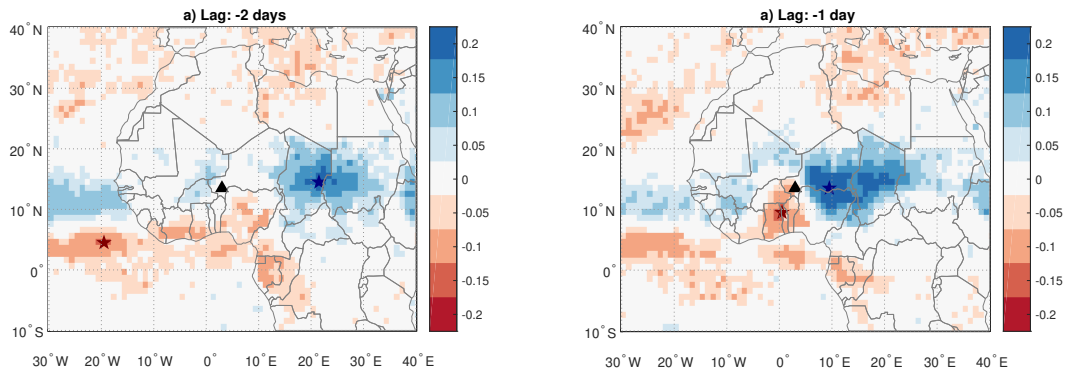
Figure 7.6: Example of spatio-temporal correlation patterns over West Africa in TRMM rainfall. This map shows the Spearman's rank correlation coefficient between rainfall over Niamey (black triangle) and rainfall over Africa (a) two days and (b) one day before. The analyzed period ranges from July to September during 1998–2016. Only significant correlations ($p < 0.05$) are shown. The blue and red stars mark the grid point with highest and lowest correlation, respectively.

to provide skillful rainfall predictions over Africa using existing correlations. In collaboration with colleagues from Mathematics, we[3] devised a novel statistical rainfall forecasting method for the tropics. The method has been described in more detail in Klar (2017) and Vogel (2019) and, thus, only the core ideas will be presented here.

The modulating influence of atmospheric modes organizes rainfall in space and time. The resulting spatio-temporal correlation patterns for rainfall at a given location depend on the importance of individual atmospheric modes and their respective superposition. As an example for such spatio-temporal correlations, Figure 7.6 shows how daily-accumulated rainfall over Niamey, the capital of Niger, is correlated with daily rainfall over West Africa one and two days before. Two days prior to rainfall over Niamey, an area of highly correlated pixels lies over the East Sahel with negative correlations to its west (Fig. 7.6a). The pixel with maximum correlation is located at the eastern border of Chad to the Sudan. On the next day, the blob of maximum correlation has propagated westward with an approximate speed of $16 \, \text{m s}^{-1}$ and reaches south-western Niger (Fig. 7.6b). The correlation pattern matches well with AEWs (see Section 7.1), however the higher speed is more in the range of MCSs, which travel with an average speed of $10–20 \, \text{m s}^{-1}$ (Aspliden et al., 1976; Mathon et al., 2002; Fink and Reiner, 2003; Laing et al., 2008). The sharp edge at the western side of the correlation cloud at day -1 also suggests the imprint of squall lines in the correlation pattern. A second correlation dipole pattern is evident over the East Atlantic. This pattern can be associated with the position

---

[3] Peter Vogel[*†], Andreas Schlueter[†], Manuel Klar[*], Tilmann Gneiting[*‡], Peter Knippertz[†], and Andreas Fink[†]. [*]Institute for Stochastics, [†]Institute of Meteorology and Climate Research, Karlsruhe Institute of Technology, Germany. [‡]Heidelberg Institute for Theoretical Studies, Heidelberg, Germany.
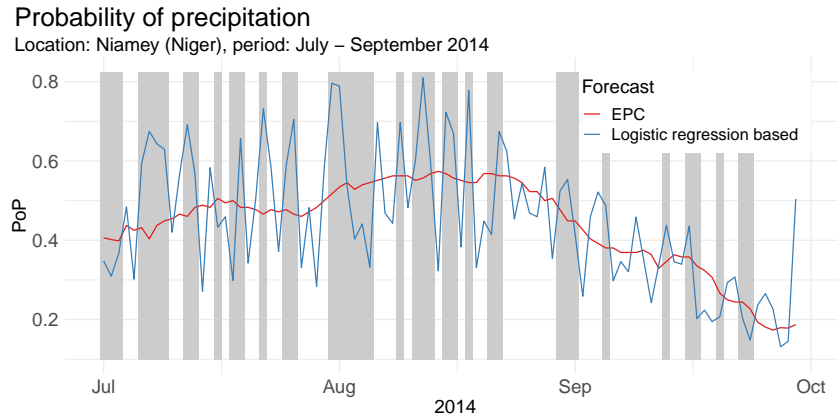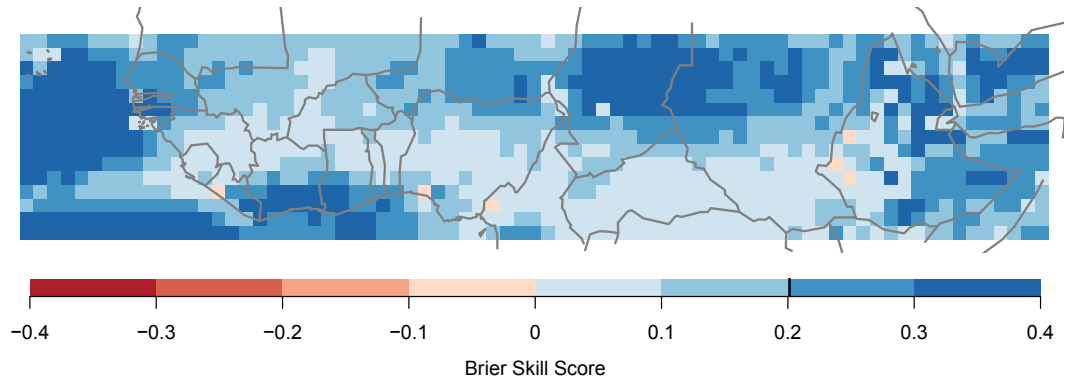
Figure 7.7: Example of the statistical forecast (blue) of rainfall probability over Niamey compared to the ensemble probabilistic climatology (EPC, red) and observation of rainfall over Niamey (gray areas). Reprinted with permission from Vogel (2019). © 2019, Peter Vogel.

of the tropical rainbelt or the state of the West African monsoon. If the rainbelt is further to the south, Niamey experiences on average less rainfall, than during a northern position of the rainbelt. The maximum negative correlation two days prior lies in the southern branch of this dipole. At day -1 the correlation pattern over the West Atlantic has weakened and rainfall is mainly determined by the AEW-like structure to the east and west of Niamey. Additional anticorrelation at day -2 and -1 exists with rainfall over northern Africa and the Mediterranean suggesting a weak influence from the extratropics (see review in Section 2.2.3) and from convection in the equatorial region, which might be related to passing equatorial Kelvin waves or the MJO. To summarize, the correlation patterns in Fig. 7.6 are consistent with the expected result by the superposition of several atmospheric wave modes and other phenomena such as the position of the tropical rainbelt. As a final remark, it is noted that the presented figure differs slightly from Klar (2017) and Vogel (2019), who analyzed a smaller domain and used station data for Niamey. For consistency, with the statistical method, which will be presented next, TRMM rainfall was used in this study.

We propose a simple statistical model that is able to exploit the spatio-temporal correlation patterns found in the TRMM rainfall data, which are exemplarily demonstrated in Fig 7.6. As the climatology has approximately the skill of post-processed global EPS forecasts over northern tropical Africa (Vogel et al., 2018), the proposed statistical method builds on the climatology and incorporates additional predictors derived from the spatio-temporal correlation fields as shown in Fig 7.6. In a nutshell, the probability of rainfall p at a given location is predicted using the local climatology $s(d)$ at day d of the year and the rainfall at the location of minimum and maximum correlations one and two days prior (indicated by a star

Figure 7.8: Brier skill score of the statistical forecast method over northern tropical Africa relative to the EPC for July to September 1998 to 2014. Reprinted with permission from Vogel (2019). © 2019, Peter Vogel.

in Fig 7.6). For each pixel, a logistic regression model estimates the probability of rainfall occurrence p as

$$\text{logit}\, p|d, o_{1+}, o_{2+}, o_{1-}, o_{2-} = \tag{7.5}$$
$$s(d) + a_{1+}f(o_{1+}) + a_{2+}f(o_{2+}) + a_{1-}f(o_{1-}) + a_{2-}f(o_{2-}),$$

where f is a transformation function of rainfall amounts observed at the location of maximum and minimum correlation one and two days prior (denoted with $o_{1+}, o_{2+}, o_{1-}, o_{2-}$). The mathematical details of the model are discussed in more detail in Klar (2017) and Vogel (2019).

An example for the performance of this statistical model at the grid point in Niamey is shown in 7.7. As a benchmark forecast, the ensemble probabilistic climatology (EPC, red line) can by construction capture well the mean distribution of rainfall over the course of the season. The statistical model follows the EPC, but predicts at times values considerably lower and higher than the EPC. As discussed in Vogel (2019), both the EPC and the statistical model are reliable, meaning that they lack systematic biases and the forecasted probabilities equal observed probabilities on average. The proposed method, however, has increased resolution compared to the EPC. The statistical model covers a wider range in forecasted rainfall probabilities, which allows a better discrimination between wet and dry days. The statistical model can capture part of the observed variability (gray shading). The predictive performance of the model will be evaluated against the EPC for the Sahel region in the next paragraph.

The model shows a positive Brier Skill Score (BSS) (Gneiting and Raftery, 2007) relative to the EPC for almost all pixels shown in Fig. 7.8. The BSS is a measure for forecast improvement compared to a reference (here the EPC). The

BSS is positive for an improved forecast and negative for a less skillful forecast. It can lie between -1 and 1 and can be understood as the relative improvement compared to the reference forecast. The mean BSS in the study is 0.2. This means that the proposes statistical model outperforms a simple climatological forecast by 20 %. This is especially striking, remembering that raw global EPS do not skillfully forecast 1-day accumulated rainfall compared to the EPC and even post-processed EPS forecasts have only an BSS slightly above zero (Vogel, 2019). The statistical model performs well in the northern Sahel and at the Guinean Coast, where the BSS exceeds 0.3 in large areas. Figures 7.8 and 7.6 suggest that the limited predictability in the region between the Guinea Coast and the Sahel might be linked to a dipole mode related to the position of the tropical rainbelt (Nicholson and Grist, 2001; Nicholson, 2008). The physical reasons for the geographically varying correlation pattern and the potential for skillful statistical forecasts remain somewhat speculative and needs to studied in more detail in future. As a final remark, the statistical model was also tested using TD and Kelvin wave activity one and two days prior as predictors but was not followed further as the skill was lower than the proposed logistic regression model, which uses the entire correlation fields of rainfall (Fig. A.3.3). The setup of the proposed model in Eq. (7.5) is superior to a linear model with several individual wave types, as the former allows the adaptive representation of several superimposed waves and local effects.

Besides the striking improvement in skill compared to standard NWP models, the method has also practical advantages in its application to the forecasting of tropical rainfall in the real-world. The method is mathematically relatively simple and computationally very cheap. Only real-time satellite information is needed as input data. At the time of writing, the used TRMM data are still available as real-time data. Prospectively, the TRMM dataset will be replaced by the Integrated Multi-satelliE Retrievals for GPM (IMERG) V6 during the course of 2019 (NASA Precipitation Processing Center, 2019, personal communication). The proposed statistical model was tested for rainfall probabilities with a lead time of one day. It is left open to future research to test how the model can also exploit predictability of rainfall on longer timescales, which stems, e.g., from ER waves or the MJO. Furthermore, the model could be designed in a way to allow a seamless prediction on several timescales. So far, the model only uses the minimum and maximum correlation at two days. The statistical model will likely be more skillful if it can capture the entire spatio-temporal correlation pattern. One very promising alternative to a linear statistical model are neural networks. In recent years, a wide variety of machine learning approaches has been developed. Specifically, 2D and
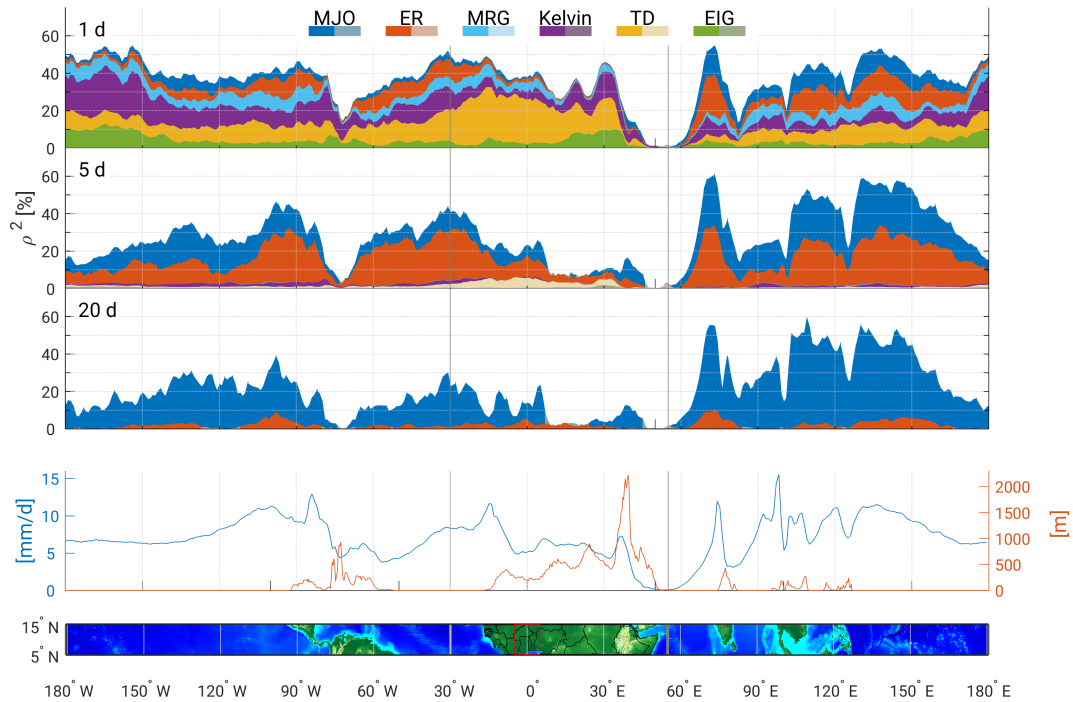
Figure 7.9: Same as Fig. 5.7, but over the northern tropical band (5°-15°N) and during the full monsoon season (July to September). The study region of this thesis is shown in gray vertical lines. Focus regions in Chapters 5–6 are indicated by red boxes.

3D convolutional neural networks are able to capture spatio-temporal correlation patterns well (e.g. Shi et al. 2017; Hou et al. 2017). Furthermore, neural networks can also represent non-linear wave interactions, which were not analyzed in this study. Finally, a possible extension of the model could be the inclusion of further predictors such as moisture fields or dynamical fields from NWP predictions.

7.4 Implications for tropical rainfall forecasting

The previous section has proposed a novel statistical forecast method of African rainfall, which exploits physically interpretable spatio-temporal correlation patterns. This thesis has focused on the importance of tropical waves for rainfall variability over Africa. In principle however, the proposed forecasting method can be also transferred to other regions of the tropics affected by atmospheric modes. Figure 7.9 shows how the portion of explained variance by tropical waves varies in the entire northern tropical band during July to September. Tropical waves are a major driver of rainfall variability in almost the entire band. All analyzed wave types affect rainfall on the daily timescale. While TDs are most prominent on the daily timescale over Africa, Kelvin and EIG waves have a maximum over the Central Pacific Ocean explaining about 20 % and 10 %, respectively. On the timescale of five days, ER waves contribute up to 30 % to rainfall variability over

the Indian, West and East Pacific, and Atlantic Ocean. Over the Indian and West Pacific Ocean, the MJO explains more than 50 % of rainfall variability locally on the intraseasonal timescale (20 days). Based on Fig. 7.9, we hypothesize that statistical predictability exist in other regions of the tropics, which could be exploited by the proposed model. As discussed in Section 5.6, tropical waves are less important over orography or in very dry regions such as the region of the Somali jet. There, local stochastic processes are likely dominant, which do not follow any spatio-temporal signal, and thus, the proposed statistical method will likely have little or no skill. The potential of the method for different regions in the tropics should be verified in future research.

8 | Conclusions

Synoptic to intraseasonal rainfall variability is of high socio-economic importance for African societies. Nonetheless, current NWP largely fail to deliver skillful forecasts for tropical Africa, partially due to a lack of fundamental research in this region. This dissertation had the overarching aim to quantify the influence of tropical waves on rainfall variability over Africa, to investigate the involved mechanisms and to test their potential for forecasting rainfall. This aim was addressed in a comprehensive review in Chapter 2 and analyses of the influence of tropical waves on rainfall variability in Chapter 5, of the involved mechanisms in Chapter 6, and of the potential of tropical waves for forecasting rainfall over Africa in Chapter 7. While Chapter 2 reviewed the literature for entire Africa, Chapters 5 to 7 focused on northern tropical Africa during the extended monsoon season. The following provides conclusions from these Chapters, refers to the respective research questions raised in Chapter 3 and elucidates, how this dissertation adds to the current body of knowledge.

Chapter 2 presented a comprehensive review of existing literature about the influence of several synoptic to intraseasonal atmospheric modes on rainfall variability over Africa. It first examined the pioneering developments in theoretical understanding of atmospheric modes and the increase of observational coverage of the atmosphere, which both laid the foundation to a better understanding of rainfall variability over Africa. Next, it delineated how several tropical and extratropical wave modes influence rainfall variability on different spatial and temporal scales over various parts of Africa. Finally, the review laid out the progress in forecasting synoptic to intraseasonal rainfall variability over Africa made until the early 21st century and discussed some of the challenges for accurate rainfall prediction.

As outlined in the literature review, the impact of tropical waves on rainfall variability over northern tropical Africa has long been known. The relative influence of the different tropical wave types, however, has never been quantified for this region. As previous studies applied different methodologies and datasets, a systematic comparison of the results was hitherto impossible. Chapter 5 closes

this gap and gives a first comprehensive and systematic account of the influence of all major tropical wave types for daily to intraseasonal rainfall variability over northern tropical Africa. A consistent method was applied to all waves, and modulation intensities were quantified comparing two satellite datasets and data from a relatively dense rain gauge network. The quantification of rainfall anomalies using quantiles made it possible for the first time to systematically compare the influence on precipitation in different climatic zones and revealed influences deep into the subtropics. All analyzed waves were found to significantly modulate rainfall variability in northern tropical Africa on different temporal scales. The main findings of Chapter 5 with respect to research questions 1a–d are:

RQ 1a Equatorial waves contribute most to rainfall variability over northern tropical Africa in the area of the seasonal rainfall maximum. TD and Kelvin waves explain the overall highest variability followed equally by MRG and ER waves.

RQ 1b Precipitation patterns of tropical waves are mainly confined to the tropics, but the influence of MJO and ER wave reaches deep into the subtropics and their modulation patterns resemble tropical plumes (Knippertz and Martin, 2005; Fröhlich et al., 2013). The different datasets show comparable modulation intensities varying from less than 2 to above $7 \, \mathrm{mm \, d^{-1}}$ depending on the wave type.

RQ 1c Tropical waves modulate precipitation on different timescales. The influence varies with location and season. On the 3-hourly to daily timescale, TD and Kelvin waves are dominant. On longer timescales (7–20d), only MJO and ER remain as modulating factors for rainfall variability. For the first time, this study analyzed the influence of EIG on northern Africa. Over Central and East Africa, EIG waves explain 5–10 % of rainfall variability on the daily timescale. The rainfall modulation is reduced generally over orography.

RQ 1d When tropical waves superimpose, they can interact with each other in a non-linear way. During their wet phases, the low-frequency waves (MJO and ER) amplify the high-frequency TD and MRG waves and suppress them in their dry phase.

The necessary dynamic and thermodynamic conditions creating tropical rainfall variability are known to vary systematically in space and time. Tropical waves are the main factor determining the atmospheric environmental conditions

that facilitate or suppress precipitation on daily to monthly timescales. So far no systematic comparison has been performed to analyze these waves and their influence on rainfall, dynamics, and thermodynamics over the region of northern tropical Africa. Chapter 6 systematically investigated the effect of all major wave types on the dynamics and thermodynamics in the WAM region. The key results with respect to research questions 2a–c are:

> **RQ 2a** Tropical waves show specific circulation patterns that are largely consistent with theoretical predictions. The slow modes, MJO and ER waves, have a strong impact on PW, whereas moisture convergence is the dominant factor for rainfall generation in the faster TDs, Kelvin, and MRG waves. Monsoonal inflow is increased during wet phases of the MJO, and ER and MRG waves. Due to the slow speed of the MJO and ER waves and their influence on PW, they are the only wave types significantly modulating the zonal position of the ITD by up to 100–200 km. MRGs are a distinct wave mode over Africa that is significantly different from AEWs with respects to its dynamics. The modulation by EIG waves is very weak.
>
> **RQ 2b** Radiosonde data reveal the vertical tilt of imbalanced wave modes (TDs, Kelvin, and partially the MRG waves). The balanced ER waves are not vertically tilted. Organization of MCSs is facilitated during the wet phases of the imbalanced modes, MJO, TDs, and Kelvin waves. Slightly favorable conditions occur during the passage of MRG waves. MCS formation is hampered during the passage of the balanced ER mode. Rainfall triggered by ER waves is more likely generated by large-scale moistening and stratiform lifting.
>
> **RQ 2c** The MJO and ER waves interact with the extratropics. In both cases an extratropical Rossby wave train causes a trough over the Atlas mountains, which then triggers rainfall over the Sahara. An additional factor is the intraseasonal variability of the Indian monsoon. The extratropical Rossby wave signal is likely caused by the MJO in the tropics, whereas the ER signal is partially triggered by a related extratropical Rossby wave train over the Atlantic and partially has tropical origin. The MJO event is likely preceded by a positive NAO and AO signals.

As current global NWP forecasts lack skill over tropical Africa, novel rainfall forecasting methods need to be developed. Chapter 7 evaluated the potential of tropical waves for rainfall forecasting over Africa using the autocorrelation of the wave signals as a novel visualization for the spatio-temporal wave properties. Statistical models that exploit existing spatio-temporal correlation patterns have useful skill. To our knowledge, we are the first to propose such a statistical models for African rainfall. The key findings of Chapter 7 with respect to research questions 3a–c are:

> **RQ 3a** Observed tropical waves can be described as wavelets of spatio-temporal correlation, which have a specific period, zonal wavelength, phase and group speed. As rough estimates for predictability, these correlation patterns highlight the potential for synoptic rainfall forecasting. The observed properties agree with values predicted by equatorial shallow-water theory. Exceptions are MRG and EIG waves, which have a strong phase dispersion at low wavenumbers.
>
> **RQ 3b** Precipitation is correlated in space and time. These correlations patterns are physically explainable by tropical waves and other atmospheric phenomena such as the position of the tropical rainbelt. A logistic regression model, which uses the local climatology and spatio-temporal correlations as predictors, can successfully predict rainfall occurrence over Africa with a lead time of one day. The statistical model is calibrated and outperforms the climatological forecast and current NWP models by about 20 %.
>
> **RQ 3c** Tropical waves explain large portions of synoptic to intraseasonal rainfall variability in almost the entire tropics. Therefore, the statistical model, we proposed for Africa, has also potential in forecasting rainfall variability for most regions of the tropics. However, the model will likely fail over, e.g., orography or in very dry regions where tropical waves are less important.

The novelty of this dissertation lies in the use of a variety of observational data, the developments of new methods and, most importantly, the achieved advances of scientific understanding. The strength of the study is the application of established filtering and compositing methods (Wheeler and Kiladis, 1999; Yasunaga and Mapes, 2012) to a comprehensive collection of three rainfall datasets from satellite and rain gauge observations, model reanalysis and radiosonde observations (see Section 4.2). Instead of comparing absolute rainfall anomalies, this studies is

the first to measure the modulation of tropical waves in quantiles such that their effect in different climatic zones can be observed. New visualization methods were developed to measure the relative importance of waves in longitudinal bands (Section 4.7 and Figs. 5.7–5.9), wave interactions (Section 4.8 and Fig. 5.7), and spatio-temporal correlation properties of waves (Section 4.11 and Figs. 7.1–7.3). Together with Klar (2017) and Vogel (2019), work in this thesis has contributed to the development of a novel statistical forecasting method of tropical rainfall, which unexpectedly has more skill than existing NWP models over Africa, even after sophisticated ensemble postprocessing. This dissertation confirmed individual studies on the influence of tropical waves on rainfall variability and (thermo-)dynamics over Africa (see references cited in the literature review). It is the first comprehensive study of all major wave types and their relative contribution. Moreover, this dissertation investigates first the tropical-extratropical interaction triggered by the MJO and ER waves leading to rainfall over the Sahara, which were indicated by Pohl et al. (2009b) and Janicot et al. (2010). Moreover, this study underlines that atmospheric motions, including tropical waves, affecting rainfall variability can be interpreted as separate quasi-geostrophically balanced motions and unbalanced inertio-gravity motions, which behave fundamentally different. This was already highlighted by theoretical studies dating back to the 18th century (Laplace 1778 – 1825, reprinted Laplace 2017; Hough 1897, 1898; Longuet-Higgins 1968). In the author's opinion this differentiation is a useful diagnostic framework, which seems not to be sufficiently regarded in the literature of recent decades. This study showed that the mechanism affecting rainfall differ crucially over Africa. Balanced waves suppress the organization of rainfall and trigger rainfall through large-scale quasi-geostrophic lifting, whereas unbalanced modes facilitate the organization of mesoscale convection. Finally, this dissertation showed the great potential of tropical waves and spatio-temporal correlations in general as predictors in statistical models of synoptic rainfall variability over Africa and most of the tropics.

9 | Outlook

This thesis presented the role of tropical waves for rainfall variability over Africa, analyzed the involved mechanisms and demonstrated their potential for tropical rainfall forecasting. Despite the comprehensive analysis, several issues were beyond the scope of this work. These open question and possible next steps are discussed in the following.

Several aspects of tropical waves over Africa could not be dealt with in this dissertation. Chapter 5 and 6 were restricted to an observational account of rainfall modulation and mechanisms of tropical waves over northern tropical Africa. Similar comprehensive studies are needed for equatorial and southern Africa. First results in this direction were already achieved by the author and will likely be pursued in the near future. This study only analyzed thermodynamic variables and did not explicitly consider individual diabatic processes such as radiation and latent heat release, which is left for further research. Finally, this study did not specifically consider faster WIG and higher order ($n \geq 1$) EIG waves and it remains largely unknown how these waves couple with convection. High temporal and spatial resolutions are needed for future studies of these wave types.

Tropical-extratropical interaction, such as the analyzed teleconnection patterns for the MJO and ER waves, are potential predictors on the intraseasonal timescale and should be analyzed in more detail. The BSc dissertation by Benjamin Körner, which was supervised by the author, about the extratropical influences in form of so-called "Cold Air Surges" (see Section 2.2.3) is a first step in this direction. Over northern Africa, cold surges have been studied so far only by Vizy and Cook (2009, 2014) and the exact mechanisms remain unclear. Our analysis of a strong cold air surge case during July 2005 indicated that the extratropics affect the West African monsoon mainly due to the very dry characteristics of the arriving air mass, and not due to the cold air as has been previously suggested. Further research of these tropical-extratropical interactions is needed due to their relevance for predictability of rainfall over Africa at longer lead times.

Despite the considerable progress obtained during the 20th and early 21st century, several major questions on theoretical properties of tropical waves remain open, which were beyond the scope of this dissertation. Answering these questions will likely improve our understanding and predictions of African rainfall. Although linear wave solutions such as the equatorial waves are considered to be independent and not to interact in shallow-water theory, in reality, different wave modes can interact in a non-linear way. As an example, slower wave modes impact also on the intensity of fast waves (see Section 5.7). Furthermore, several wave modes such as the MJO and other (sub-)tropical modes (AEW, QBZD, Sahel mode) manifest themselves in a superposition of different diabatically coupled balanced and unbalanced transients acting on multiple scales (Žagar and Franzke 2015; Yang et al. 2018, Mounier et al. 2008, Janicot et al. 2010). The specific "taste" of individual cases in reality likely depends on the contribution of the different superimposed transients. A unified theoretical framework for the (thermo-)dynamics of these non-canonical wave modes is still missing. Such a unified theory linking tropical, subtropical and extratropical modes would likely help to understand their nature better and would, ultimately, lead to improved prediction of rainfall variability in the tropics and Africa, in particular.

This study emphasizes the need of an adequate representation of tropical waves in NWP models for weather prediction over northern tropical Africa. Chapter 6 highlighted the differences between the effect of imbalanced modes in the WAM region compared to balanced modes and unveiled which dynamical processes need to be modeled realistically to represent the coupling between tropical waves and rainfall. Operational NWP forecasts are improving in the representation of tropical waves (Dias et al., 2018; Janiga et al., 2018). In particular, the large-scale modulation of winds and moisture by the MJO, the quasi-geostrophic equatorial (and related extratropical) Rossby waves are predicted reasonably well on a timescale of two to three weeks (Grazzini and Vitart, 2015; Li and Robertson, 2015; Janiga et al., 2018; Tseng et al., 2018). However, current NWP models struggle to assimilate and accurately forecast in particular smaller scale imbalanced modes (Ying and Zhang, 2017). This stresses the need of new schemes such as those proposed by Žagar et al. (2005; 2012; 2016) and, in particular over Africa, convection-permitting models to improve the representation of mesoscale convective systems.

Along with Klar (2017) and Vogel (2019), this study provides a paradigm shift for forecasting of tropical rainfall. These studies showed unexpectedly that even simple statistical models using spatio-temporal correlations patterns have more skill

than current NWP models over Africa. Given the strong relevance of tropical waves for rainfall in most of the tropics, this novel method is expected to be skillful also in other tropical regions. The statistical models, briefly presented here, are rather simple and can be improved in several ways such as extension to longer lead times, expansion to the entire tropics, and the application of more sophisticated machine learning approaches to also capture non-linear effects. Finally, dynamical-statistical models that incorporate real-time filtered wave information from NWP models and observations (Wheeler and Weickmann 2001; Wheeler and Hendon 2004; Roundy et al. 2009; Janiga et al. 2018) are a promising pathway, in the author's opinion, in order to combine the advantages of NWP and statistical approaches. The author has initiated the development of a web application, called "Statistical Equatorial RAinfall Forecast (SERAF)" providing real-time wave analyses for the entire tropics, which will also incorporate the proposed statistical model and should be made public in the near future. Provided that funding is secured, the Waves to Weather project will pursue these propositions in its second phase.

This thesis has shown that tropical waves are key predictors of African rainfall and should be thus considered, specifically. Operational forecasters in Africa make limited use of analysis of CCEWs. The presented new visualization showing the contribution of tropical waves on precipitation variability on different timescales is useful for weather forecasters to determine the relevance of different waves for their region depending on the analyzed timescale. Further research and collaboration with national and pan-African weather agencies should be encouraged to foster the knowledge transfer to local societies. The vulnerability of societies in Africa to synoptic and intraseasonal rainfall variability calls for developments of more skillful forecast systems. Given the complexity of the probabilistic information, these forecasts need to be effectively communicated to decision makers and the general public and should be designed to protect societies and enhance resilience against drought or heavy rainfall.
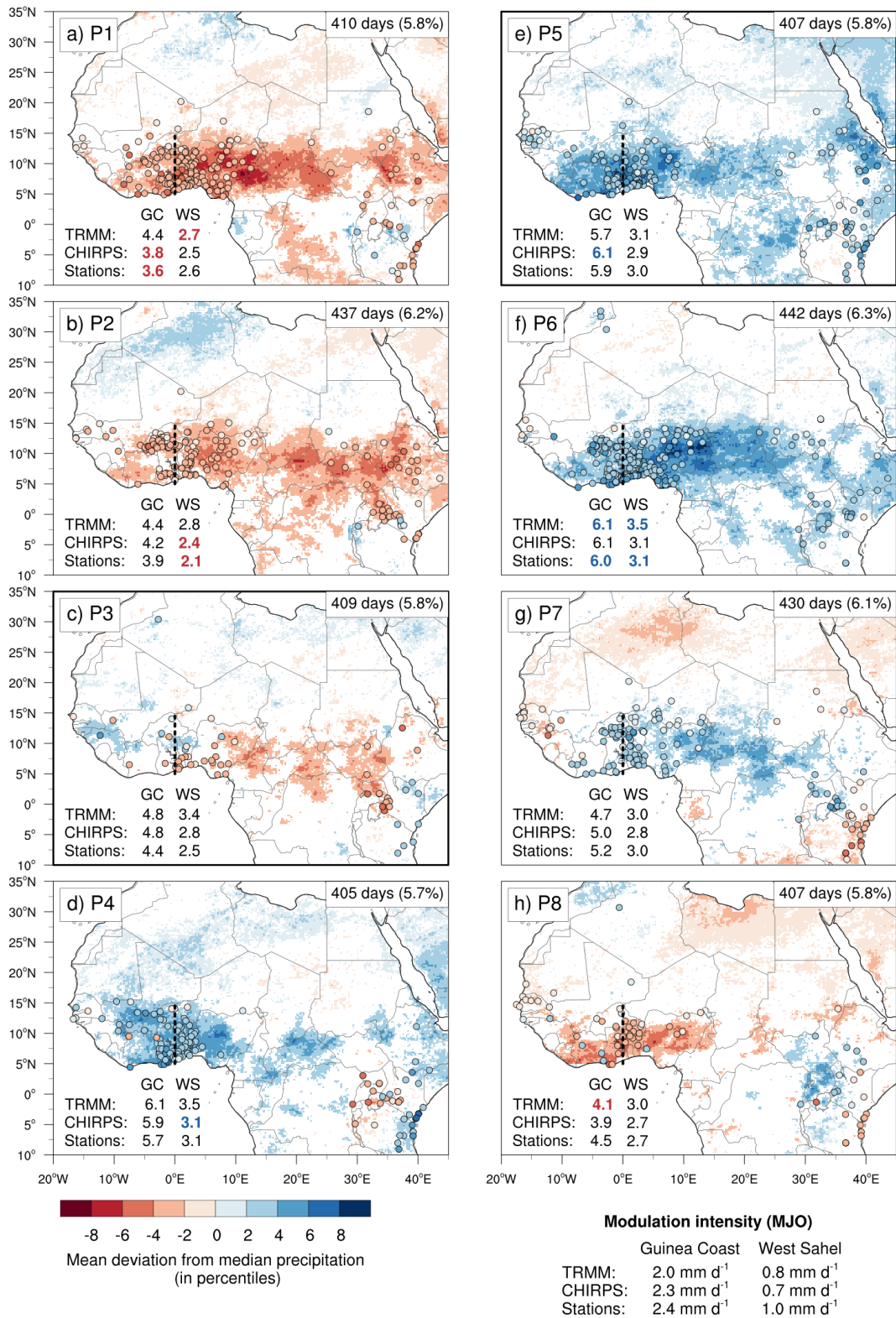
# A │ Appendix

A.1 Rainfall modulation
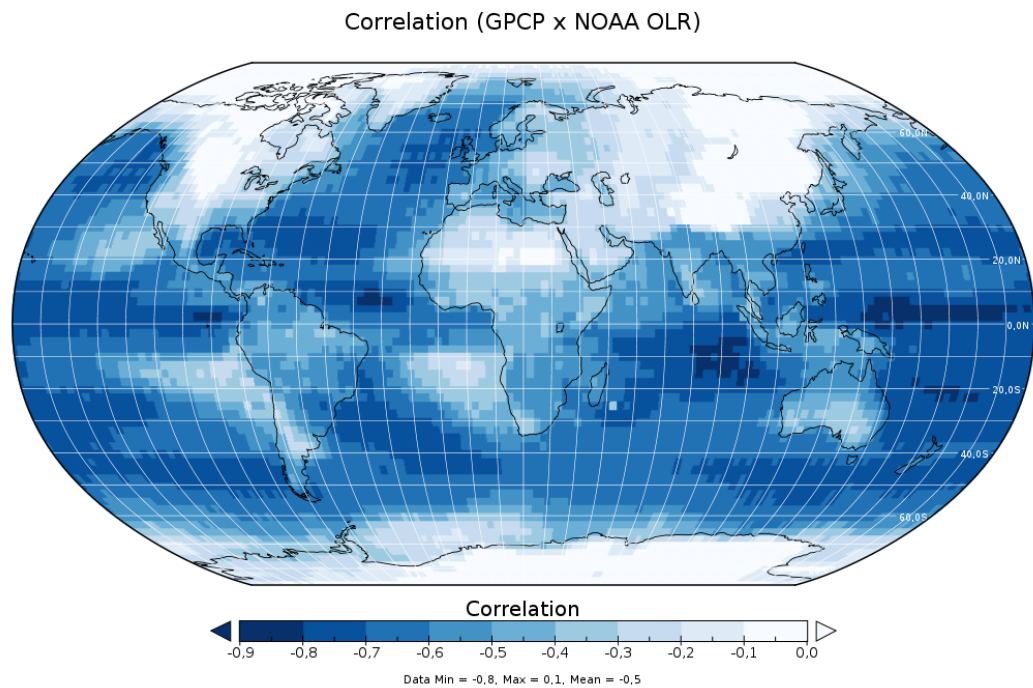
Figure A.1.1: Correlation of daily precipitation from the Global Precipitation Climatology Project (GPCP) and NOAA OLR. Note the low correlations in the extratropics, the subtropics, and over West Africa. Reprinted from Schlueter et al. (2019a), supplementary material. © 2019, American Meteorological Society. Used with permission.
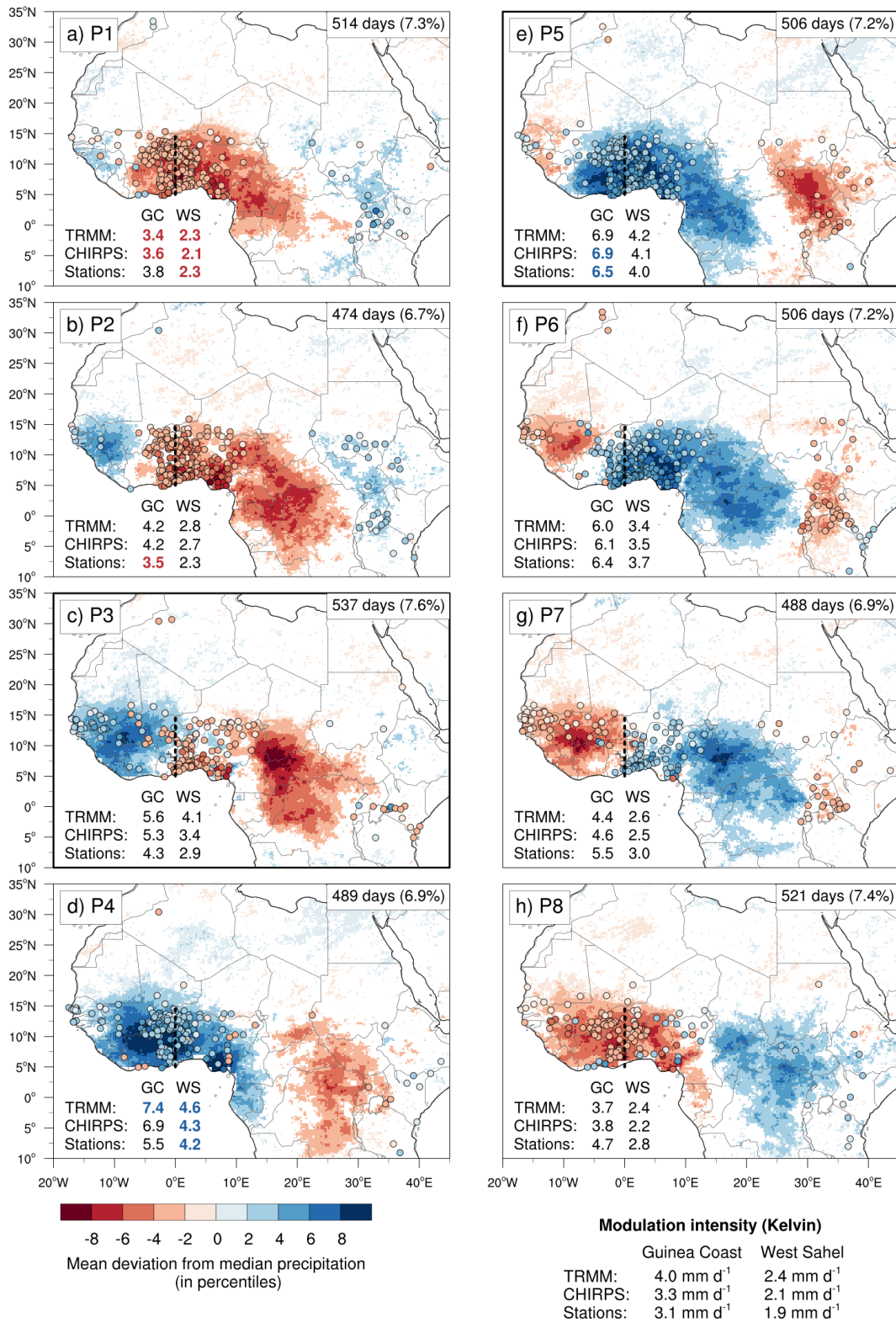
Figure A.1.2: Same as Fig 5.3, but for Madden-Julian Oscillation. Reprinted from Schlueter et al. (2019a), supplementary material. © 2019, American Meteorological Society. Used with permission.
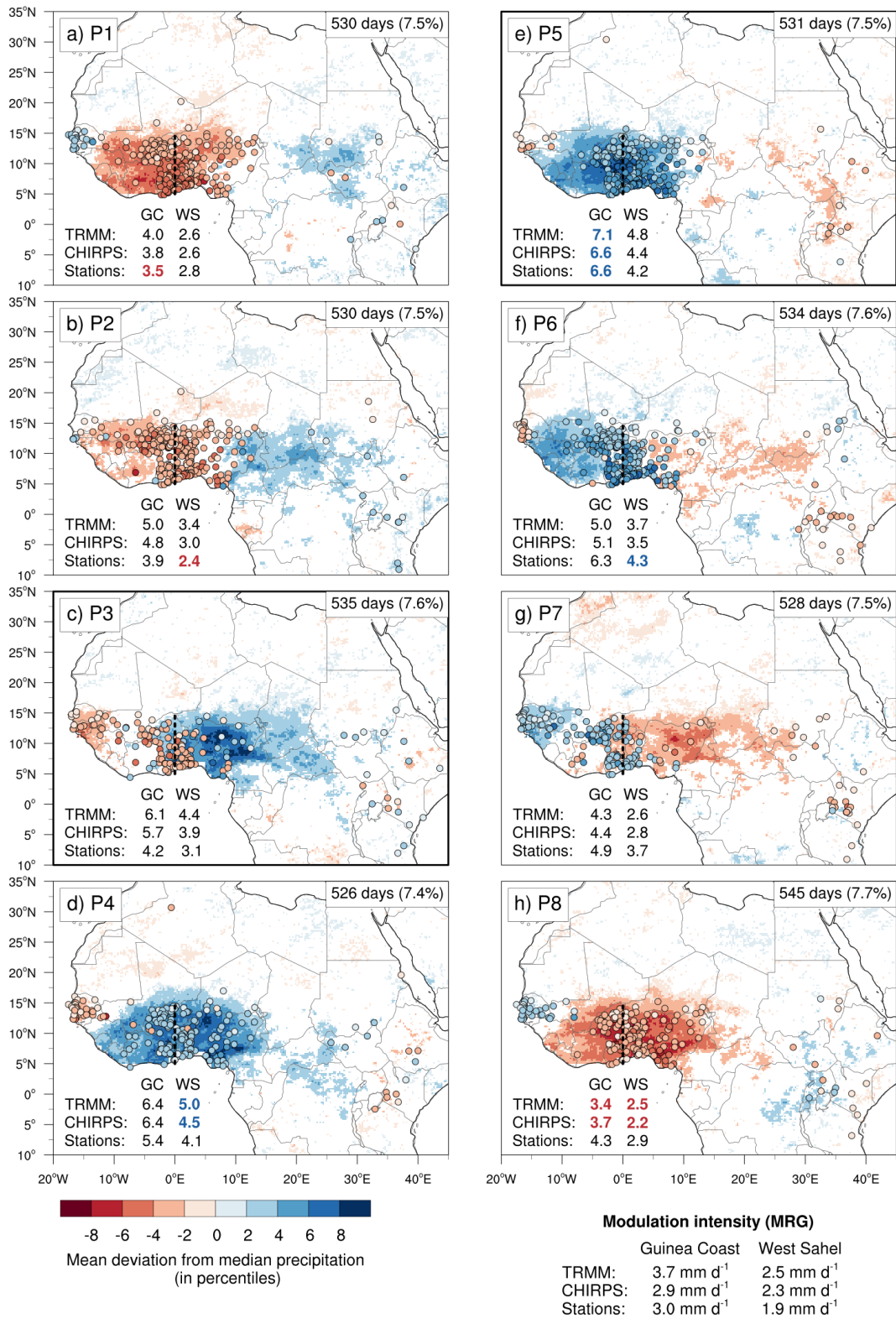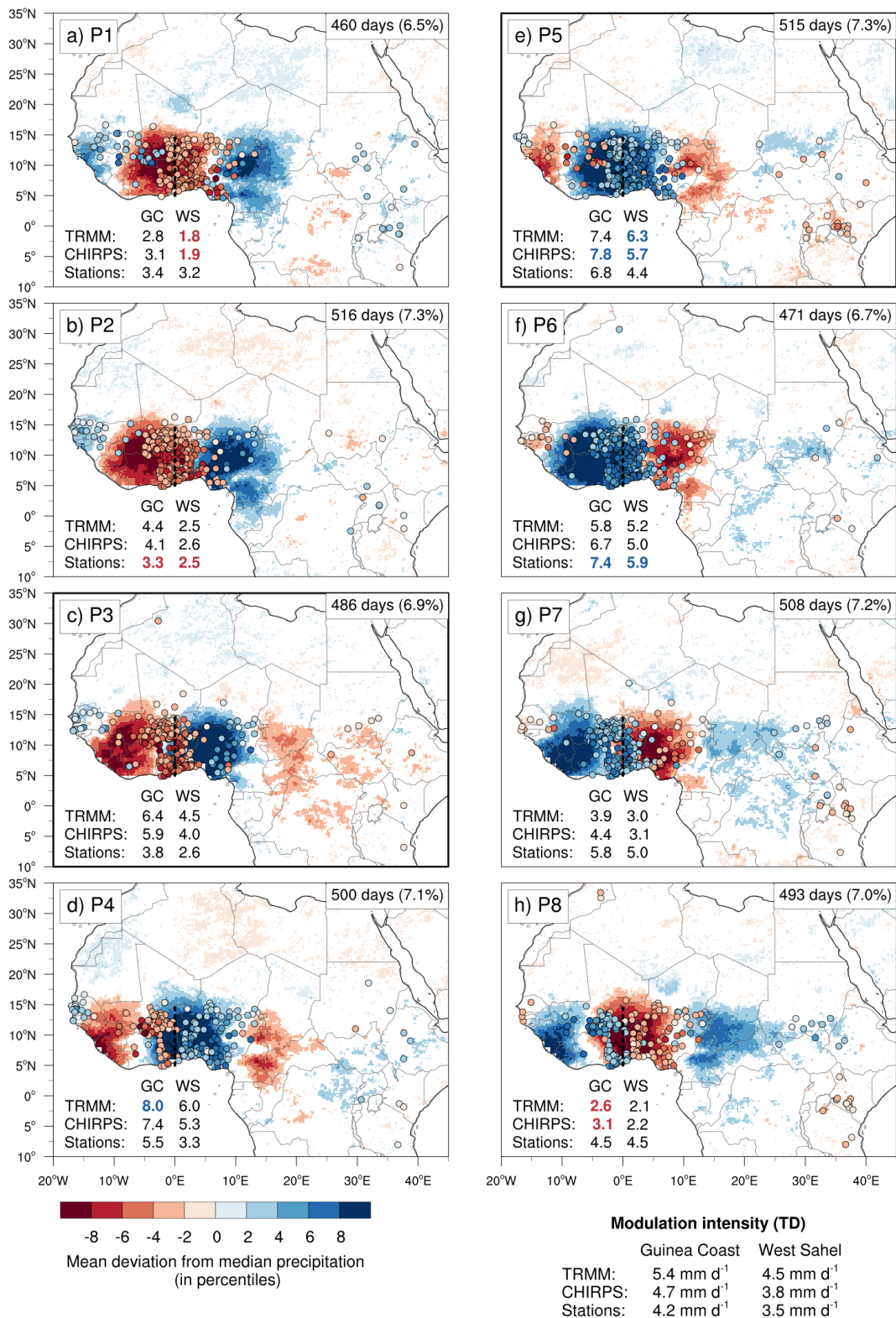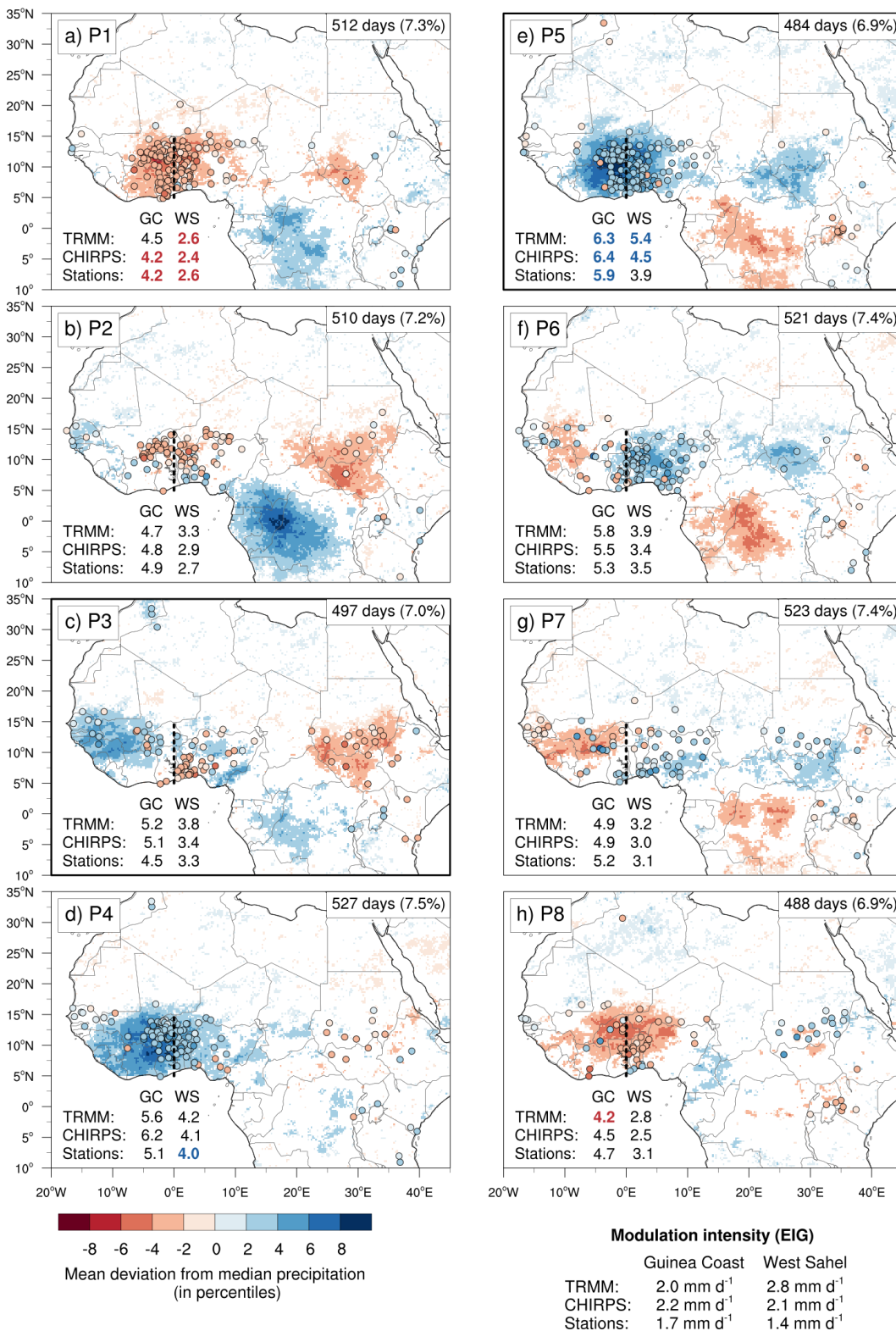
Figure A.1.3: Same as Fig 5.3, but for mixed Rossby gravity waves. Reprinted from Schlueter et al. (2019a), supplementary material. © 2019, American Meteorological Society. Used with permission.
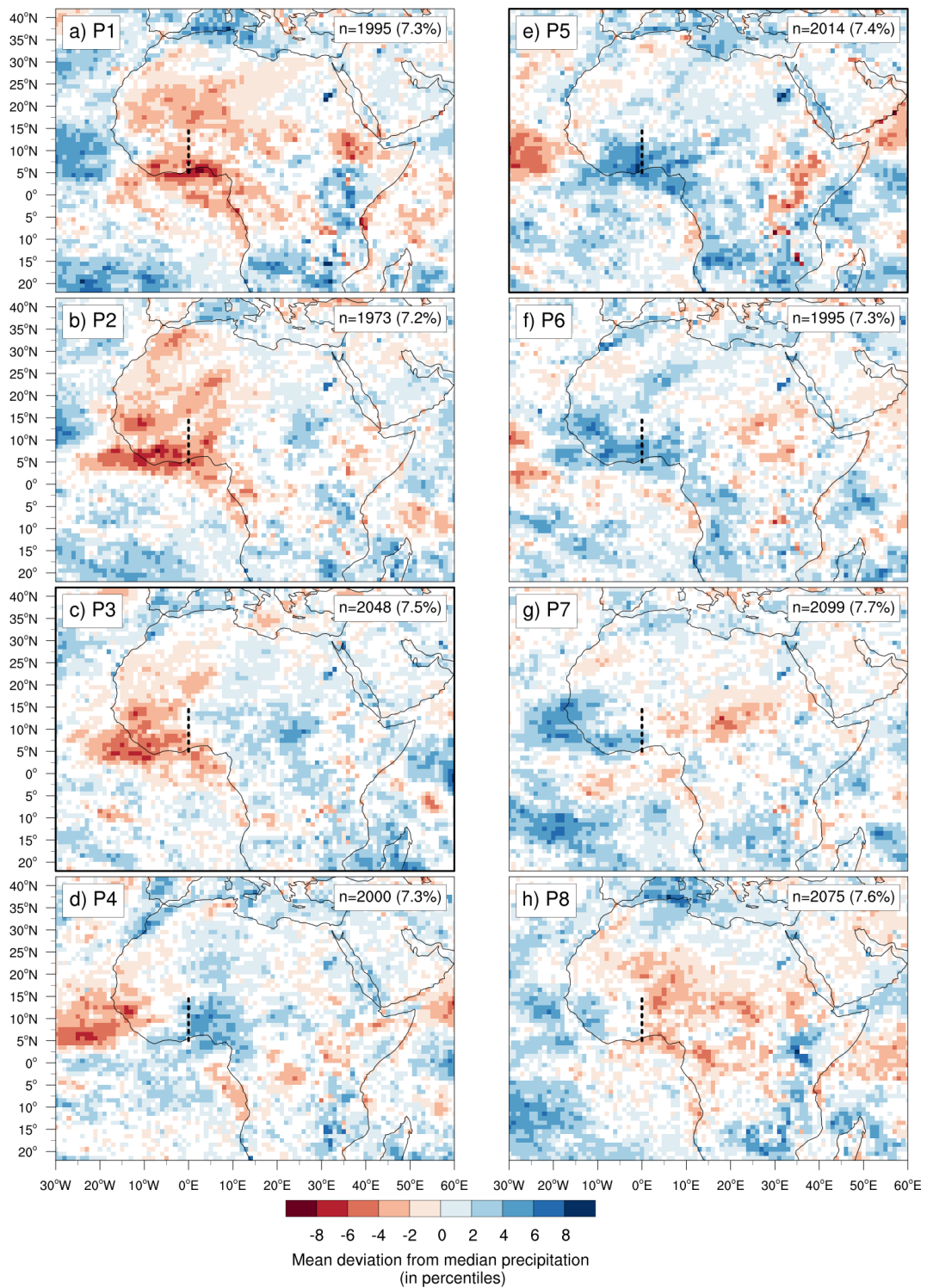
Figure A.1.4: Same as Fig 5.3, but for Kelvin waves. Reprinted from Schlueter et al. (2019a), supplementary material. © 2019, American Meteorological Society. Used with permission.
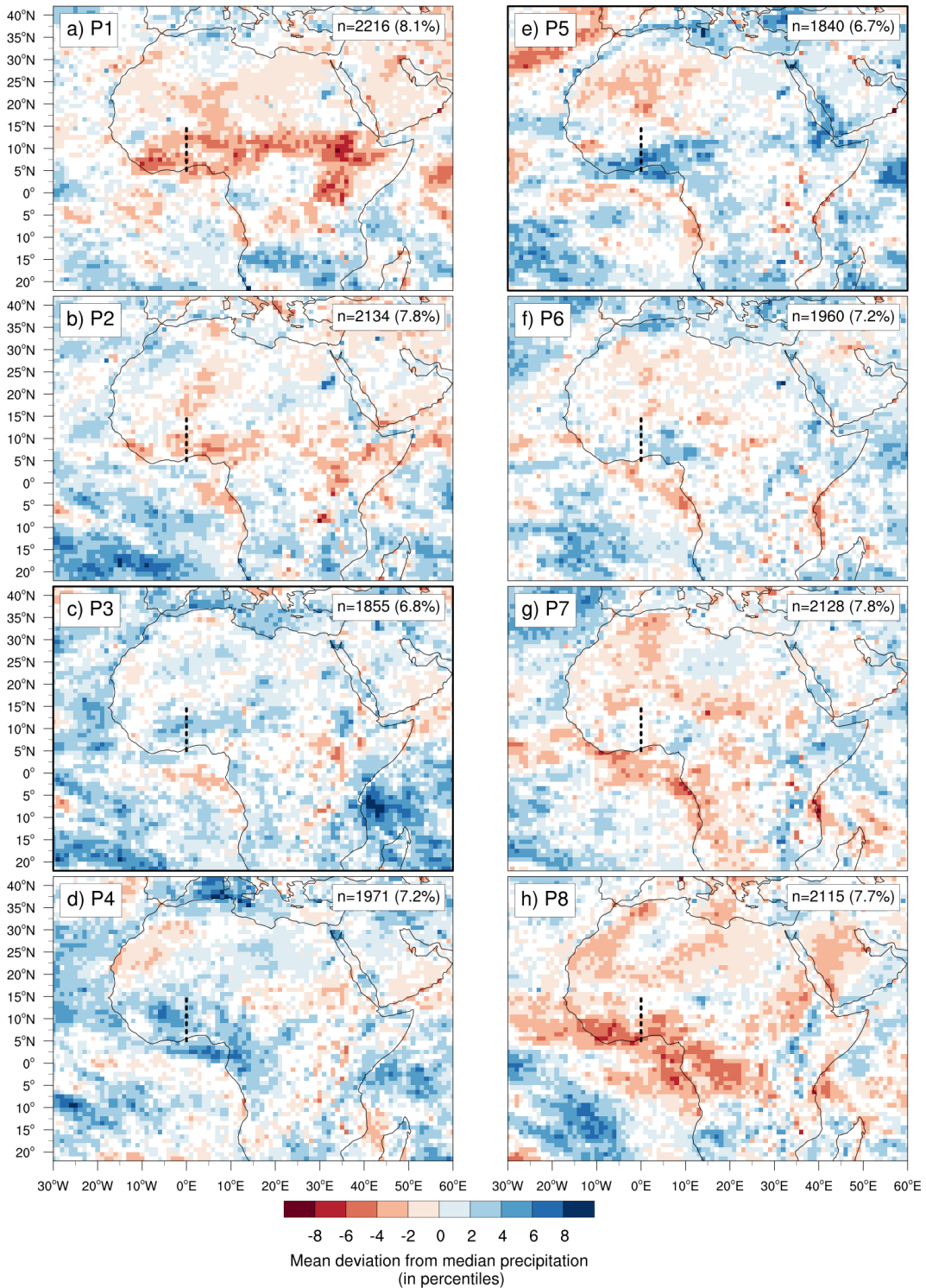
Figure A.1.5: Same as Fig 5.3, but for tropical disturbances (mostly African Easterly Waves). Reprinted from Schlueter et al. (2019a), supplementary material. © 2019, American Meteorological Society. Used with permission.
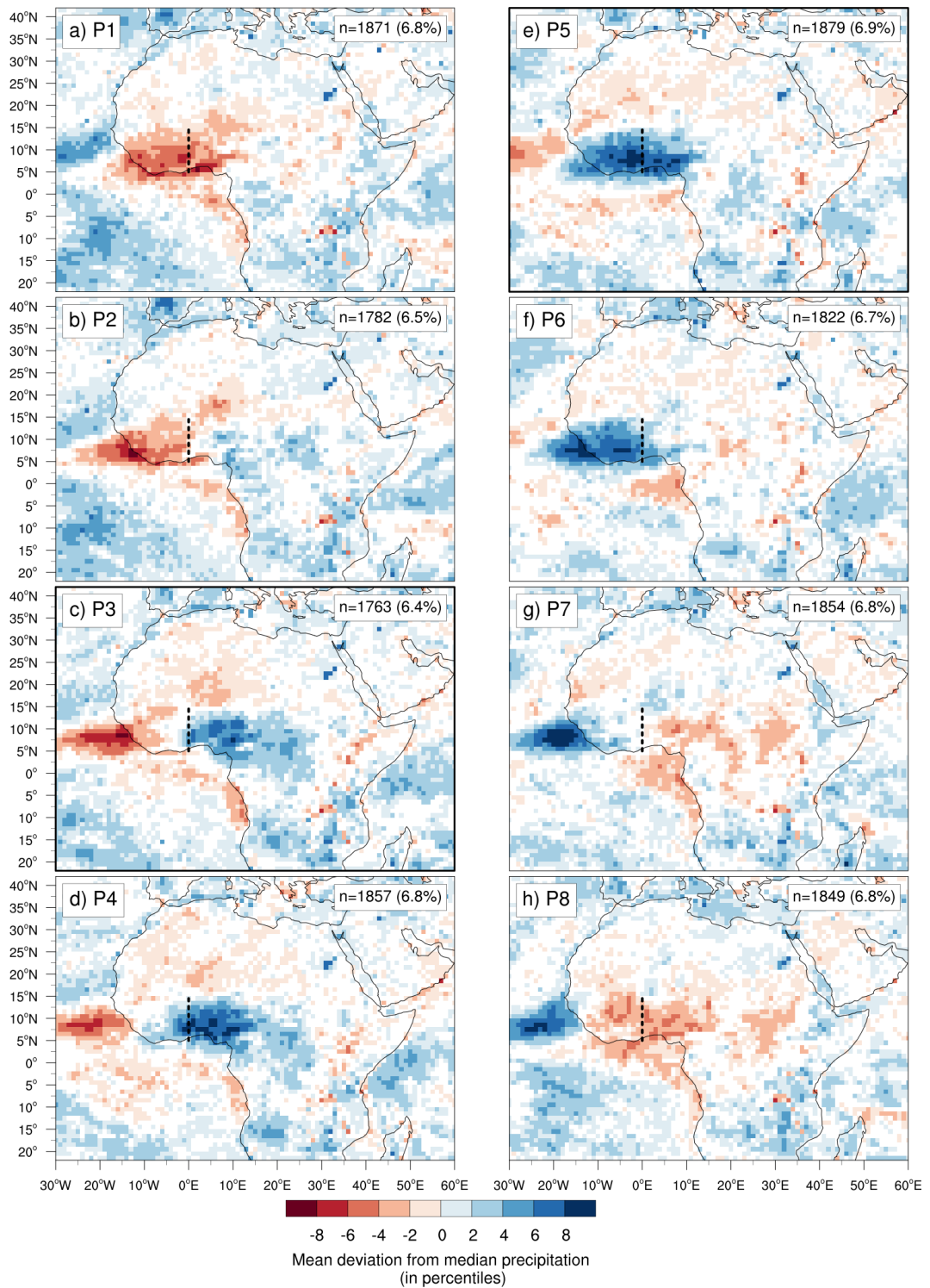
Figure A.1.6: Same as Fig 5.3, but for eastward inertio-gravity waves. Reprinted from Schlueter et al. (2019a), supplementary material. © 2019, American Meteorological Society. Used with permission.

Figure A.1.7: Same as Fig 5.3 showing a composite of the equatorial Rossby wave, but filtering based on 3h-TRMM precipitation instead of NOAA OLR and showing TRMM rainfall anomalies. TRMM has been spatially aggregated to a 1°x1°-grid and temporally aggregated to daily values before the calculation of quantiles at each grid point. This helps to obtain smoother results, because random errors are reduced by increasing the sample size. The filtering period ranges from 1998–2013. Reprinted from Schlueter et al. (2019a), supplementary material. © 2019, American Meteorological Society. Used with permission.

Figure A.1.8: Same as Fig. A.1.7, but for Madden-Julian Oscillation. Reprinted from Schlueter et al. (2019a), supplementary material. © 2019, American Meteorological Society. Used with permission.
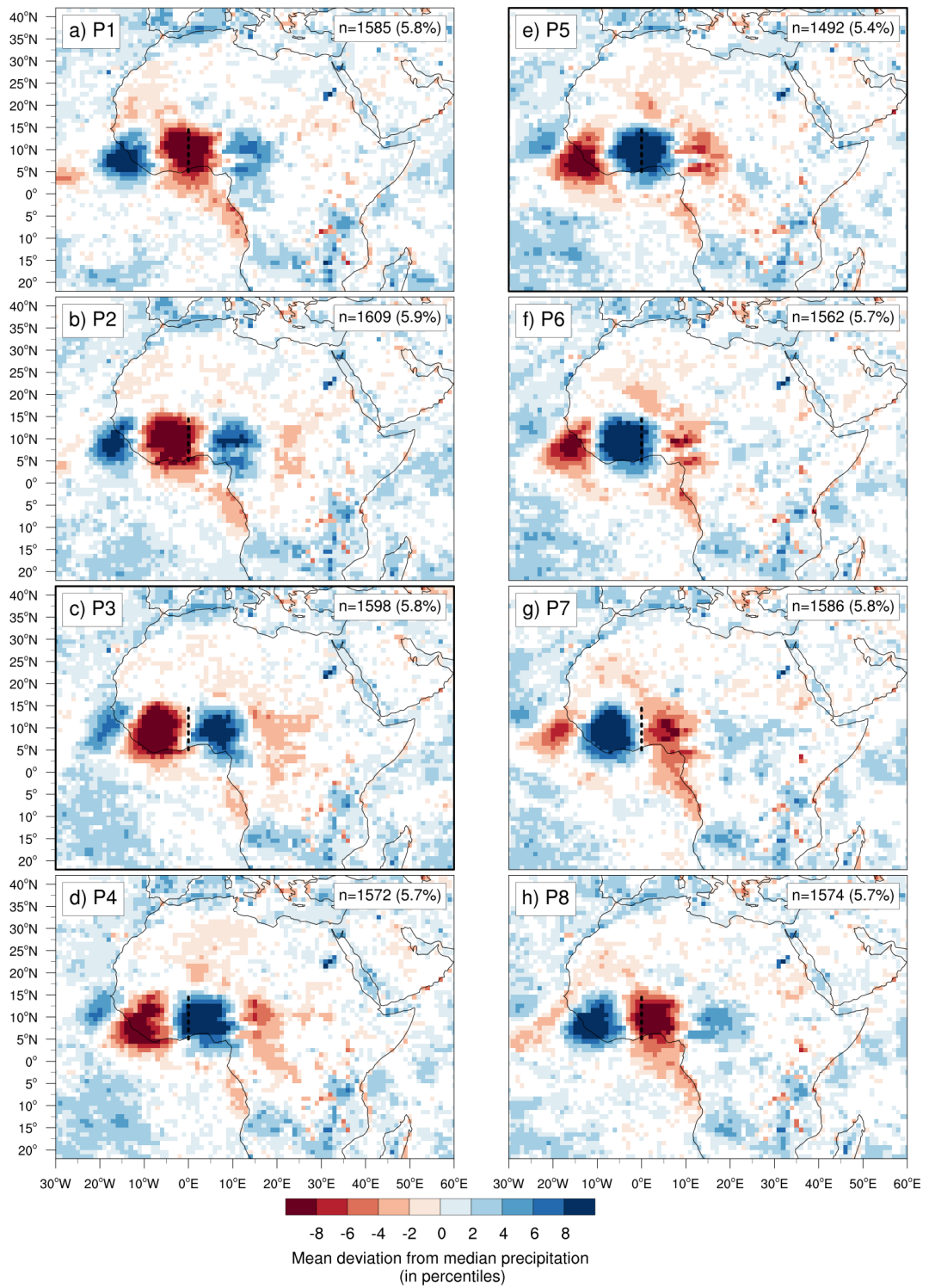
Figure A.1.9: Same as Fig. A.1.7, but for mixed Rossby gravity waves. Reprinted from Schlueter et al. (2019a), supplementary material. © 2019, American Meteorological Society. Used with permission.
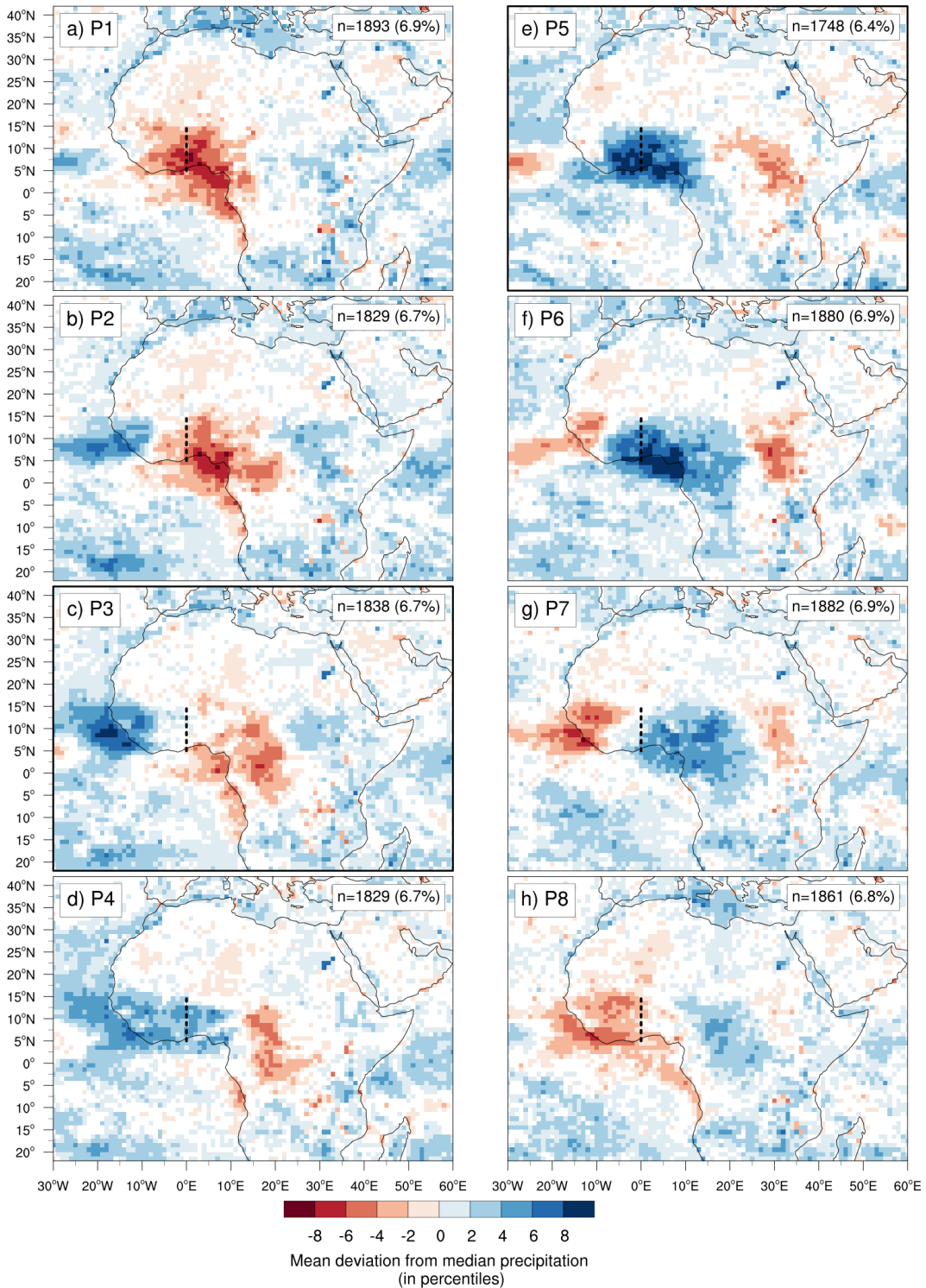
Figure A.1.10: Same as Fig. A.1.7, but for Kelvin waves. Reprinted from Schlueter et al. (2019a), supplementary material. © 2019, American Meteorological Society. Used with permission.

Figure A.1.11: Same as Fig. A.1.7, but for tropical disturbances (mostly African Easterly Waves). Reprinted from Schlueter et al. (2019a), supplementary material. © 2019, American Meteorological Society. Used with permission.

Figure A.1.12: Same as Fig. A.1.7, but for eastward inertio-gravity waves. Reprinted from Schlueter et al. (2019a), supplementary material. © 2019, American Meteorological Society. Used with permission.
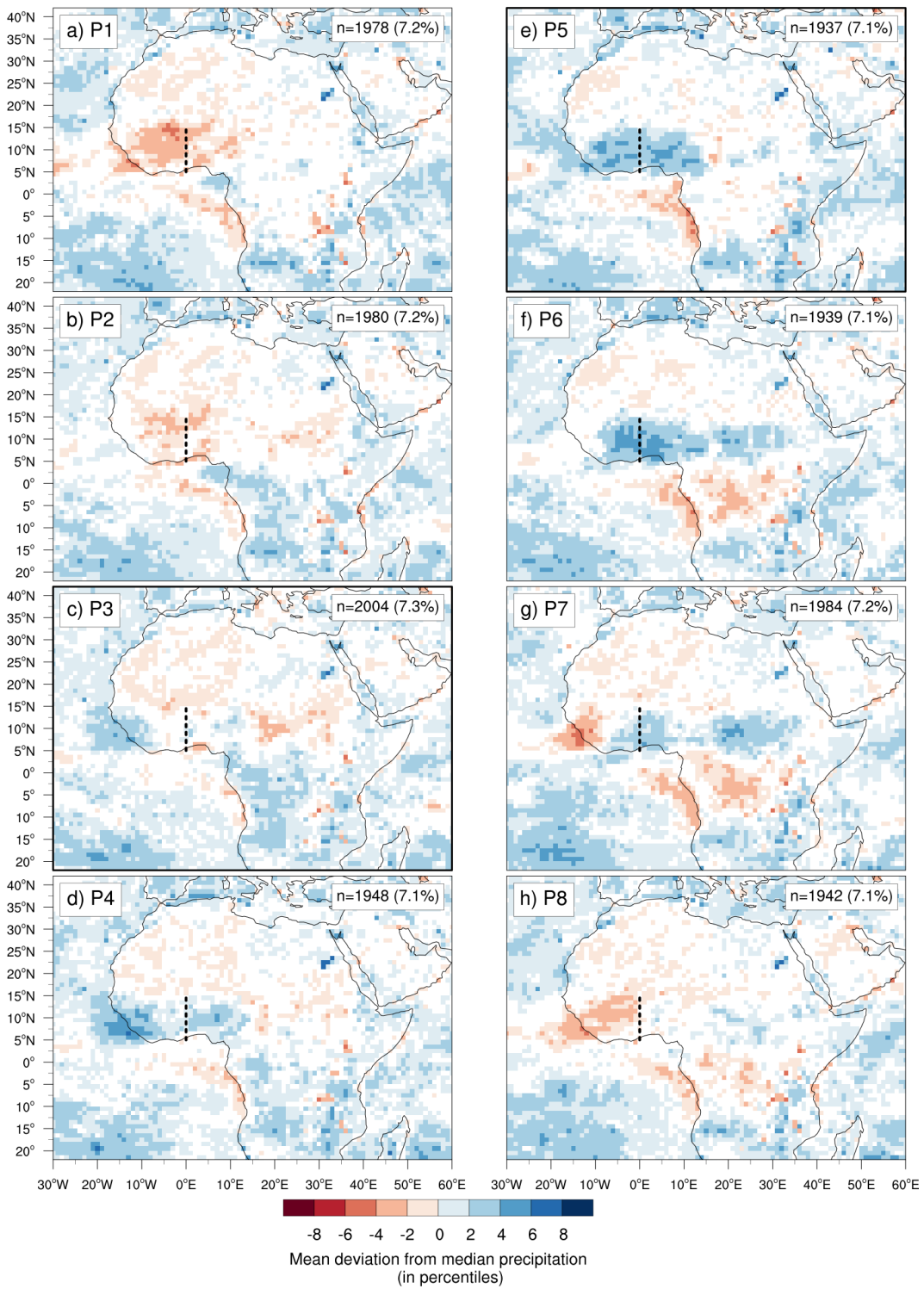
Figure A.1.13: Same as Fig. 5.6, but measured in quantile anomalies (for more details see subsection e in methods section). Reprinted from Schlueter et al. (2019a), supplementary material. © 2019, American Meteorological Society. Used with permission.

Figure A.1.14: Same as Fig. 5.7, but over the Sahelian band (10°-15°N) and during the transition season (April to June and October). Reprinted from Schlueter et al. (2019a), supplementary material. © 2019, American Meteorological Society. Used with permission.
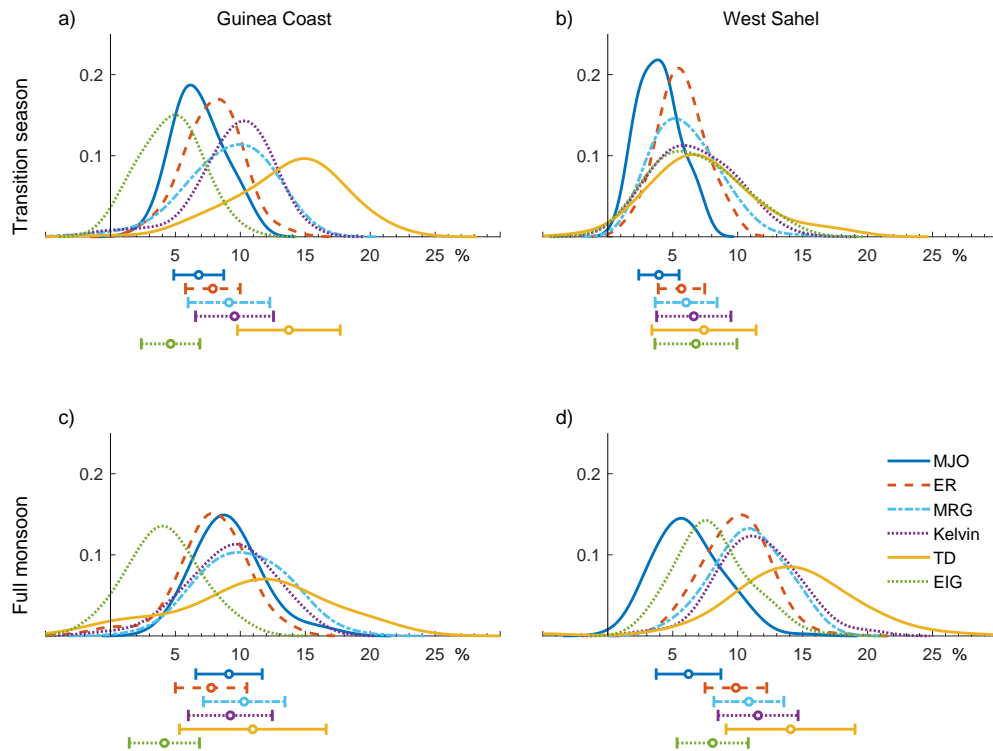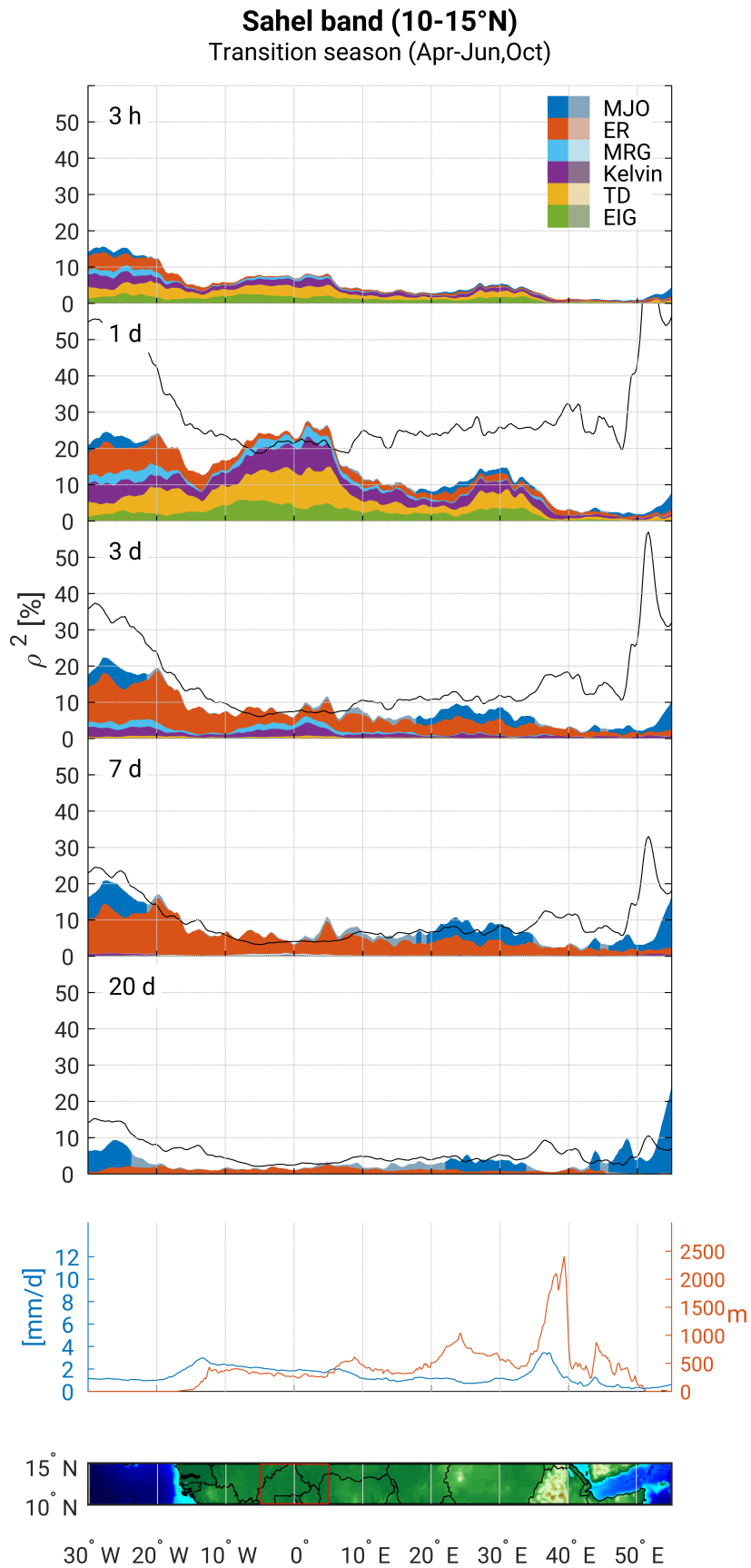
Figure A.1.15: Same as Fig 5.10, but for the West Sahel box (5°W–5°E, 10°–15°N). Reprinted from Schlueter et al. (2019a), supplementary material. © 2019, American Meteorological Society. Used with permission.

A.2 Mechanisms

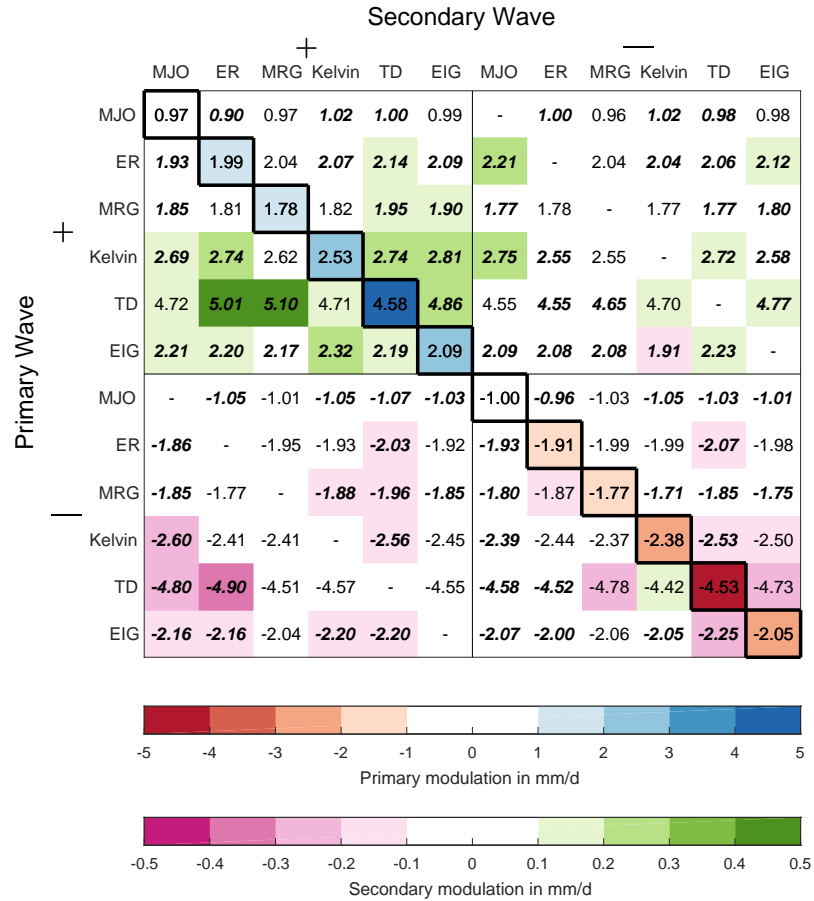

Figure A.2.1: Same composite of the Madden-Julian Oscillation as Fig. 1a,b in the main paper, but showing all wave phases. Reprinted from Schlueter et al. (2019b), supplementary material. © 2019, American Meteorological Society. Used with permission.

Figure A.2.2: Same composite of the equatorial Rossby waves as Fig. 2a,b in the main paper, but showing all wave phases. Reprinted from Schlueter et al. (2019b), supplementary material. © 2019, American Meteorological Society. Used with permission.

Figure A.2.3: Same composite of the mixed Rossby gravity waves as Fig. 3a,b in the main paper, but showing all wave phases. Reprinted from Schlueter et al. (2019b), supplementary material. © 2019, American Meteorological Society. Used with permission.

Figure A.2.4: Same composite of the Kelvin waves as Fig. 4a,b in the main paper, but showing all wave phases. Reprinted from Schlueter et al. (2019b), supplementary material. © 2019, American Meteorological Society. Used with permission.
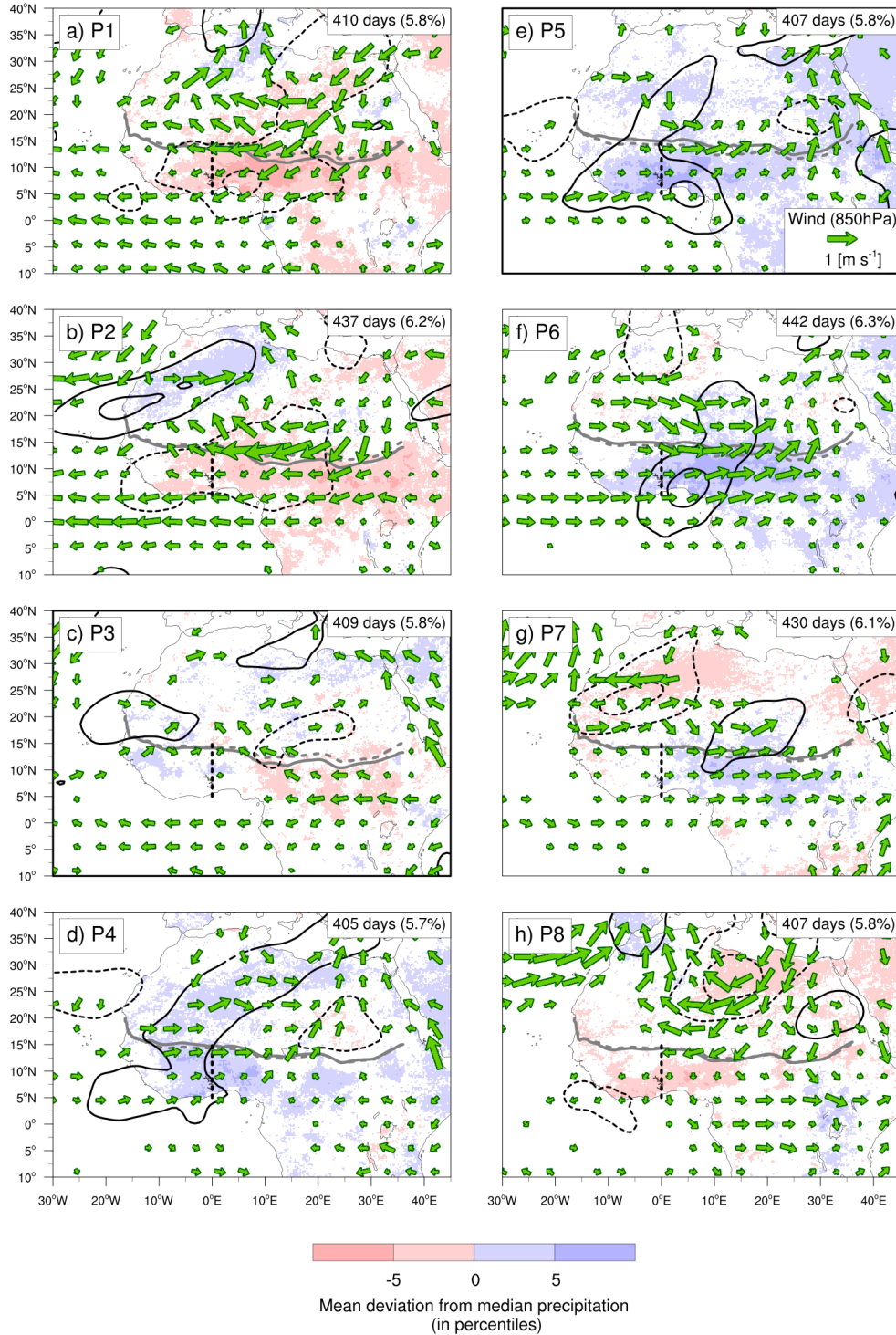
Figure A.2.5: Same composite of the tropical disturbances (mostly African Easterly Waves) as Fig. 5a,b in the main paper, but showing all wave phases. Reprinted from Schlueter et al. (2019b), supplementary material. © 2019, American Meteorological Society. Used with permission.

137

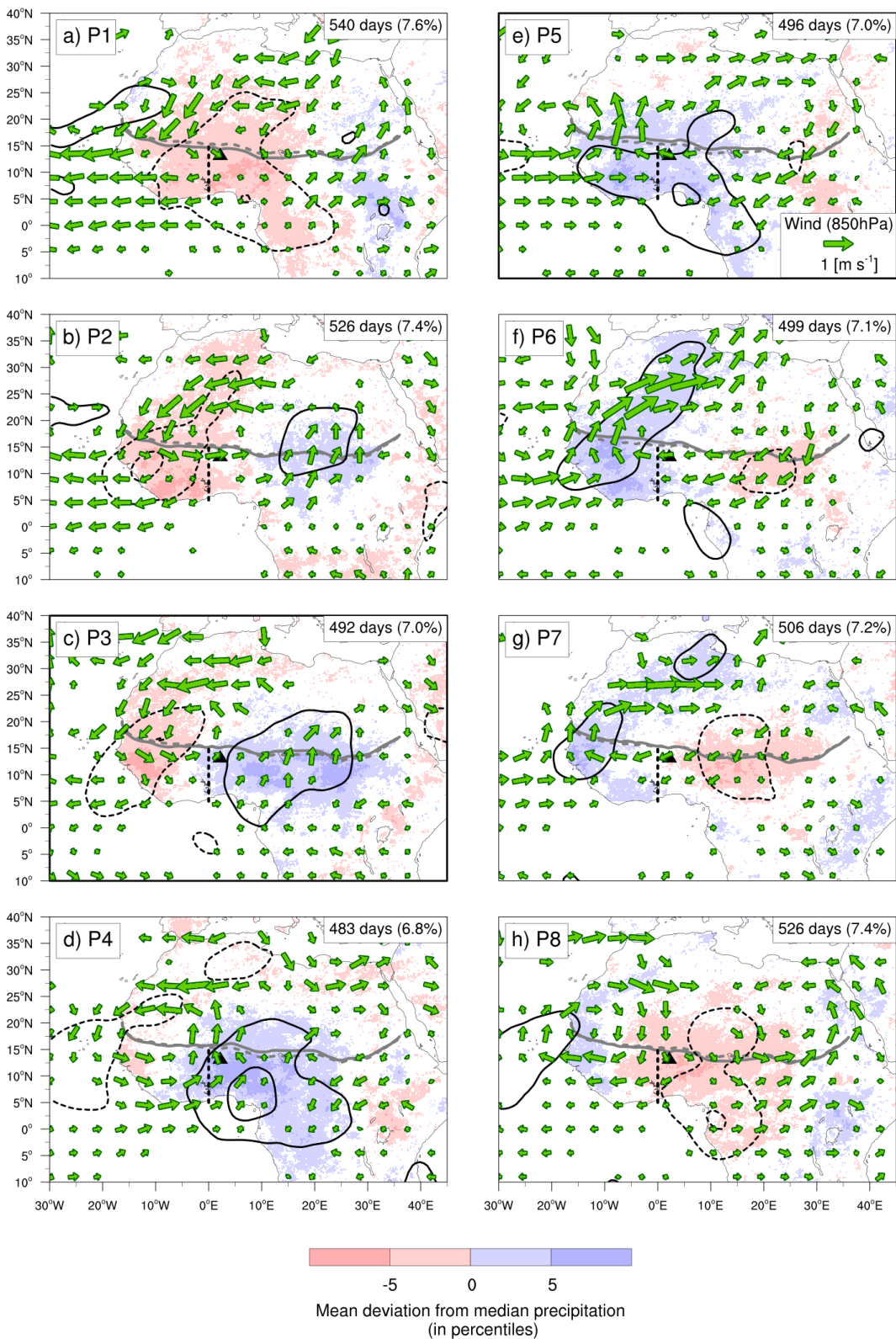**Figure A.2.6:** Same composite as Fig. 1a,b in the main paper, but showing all wave phases of the eastward inertio-gravity waves. Reprinted from Schlueter et al. (2019b), supplementary material. © 2019, American Meteorological Society. Used with permission.
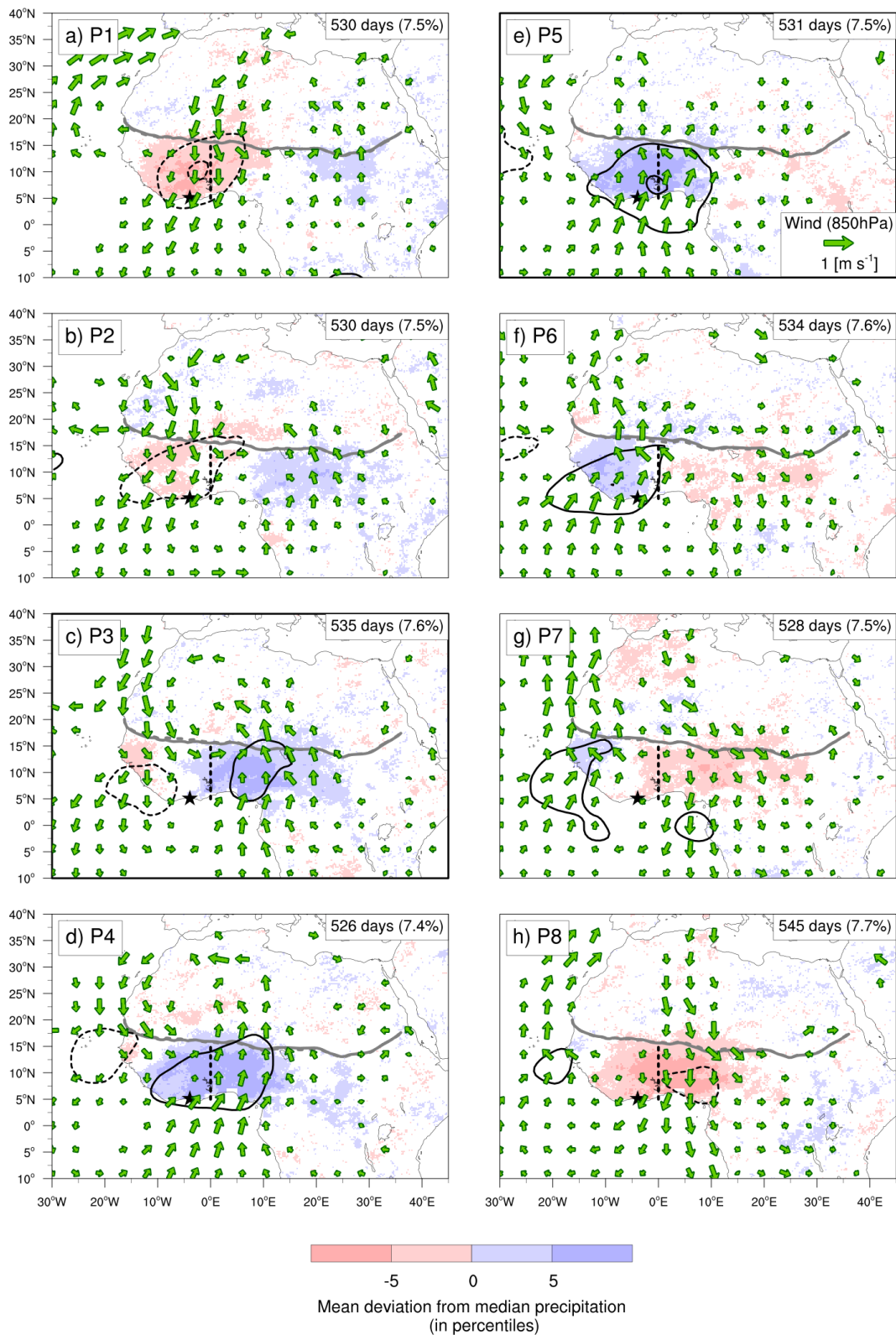
Figure A.2.7: Same composite of the Madden-Julian Oscillation as Fig. 1c,d in the main paper, but showing all wave phases. Reprinted from Schlueter et al. (2019b), supplementary material. © 2019, American Meteorological Society. Used with permission.
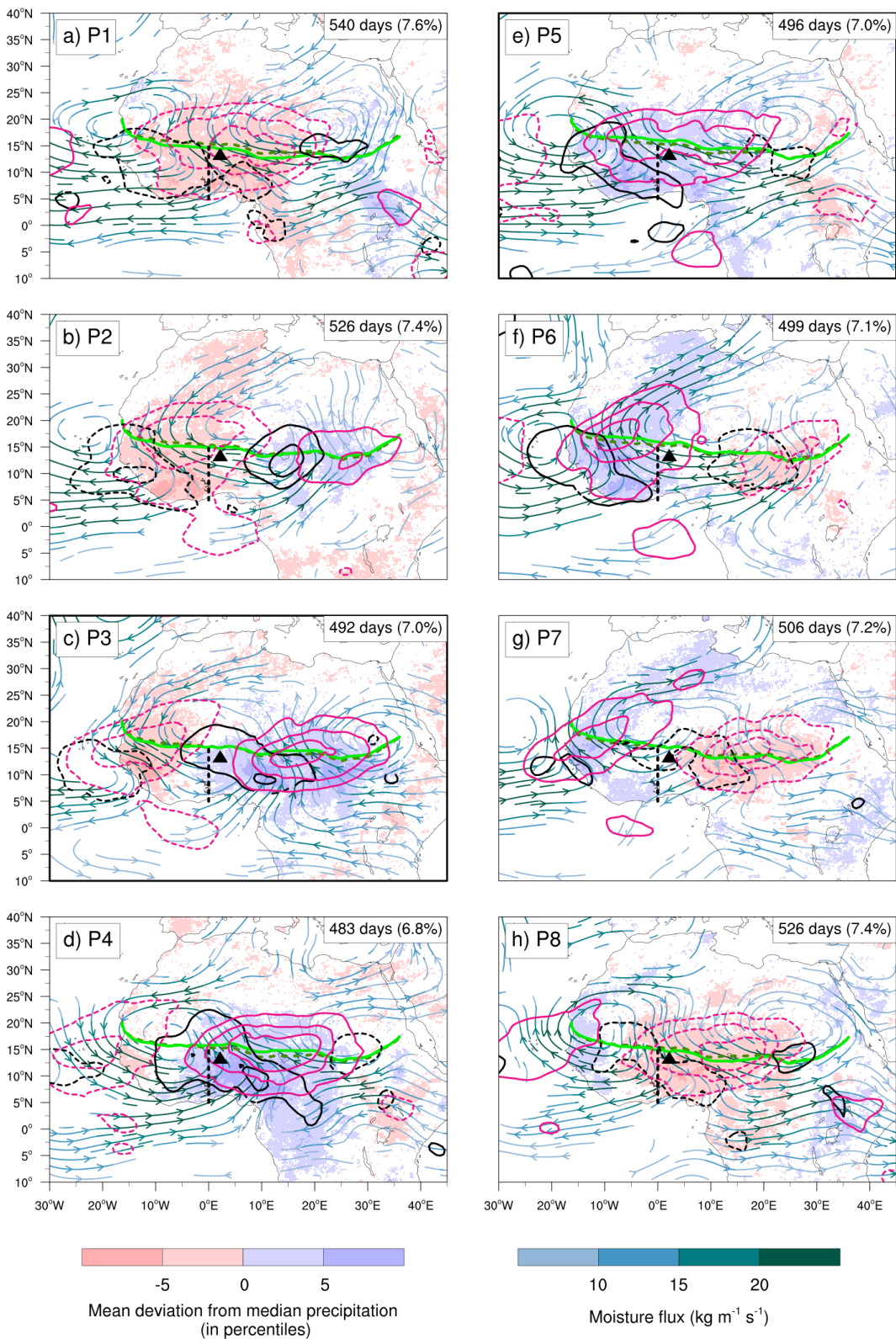
Figure A.2.8: Same composite of the equatorial Rossby waves as Fig. 2c,d in the main paper, but showing all wave phases. Reprinted from Schlueter et al. (2019b), supplementary material. © 2019, American Meteorological Society. Used with permission.
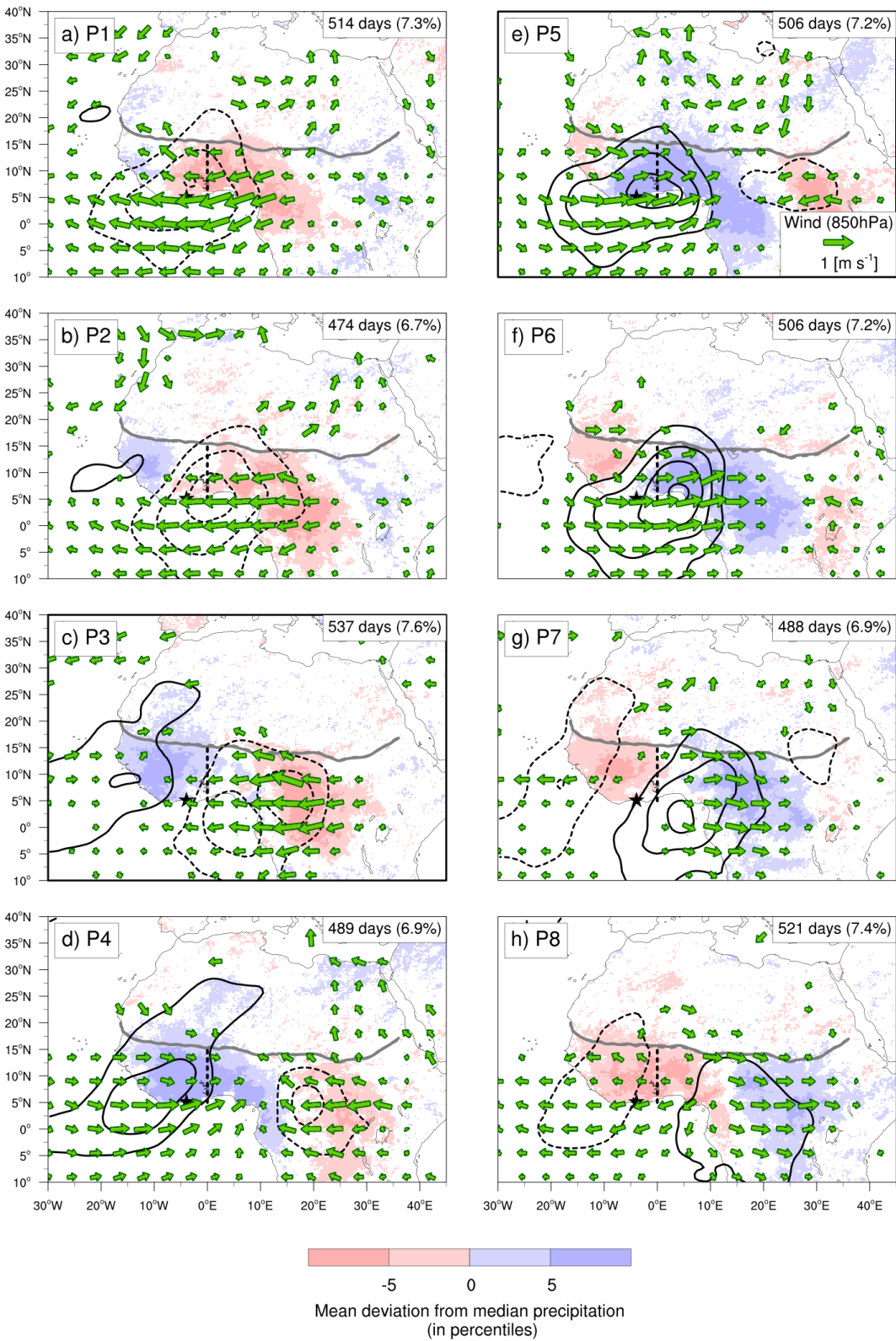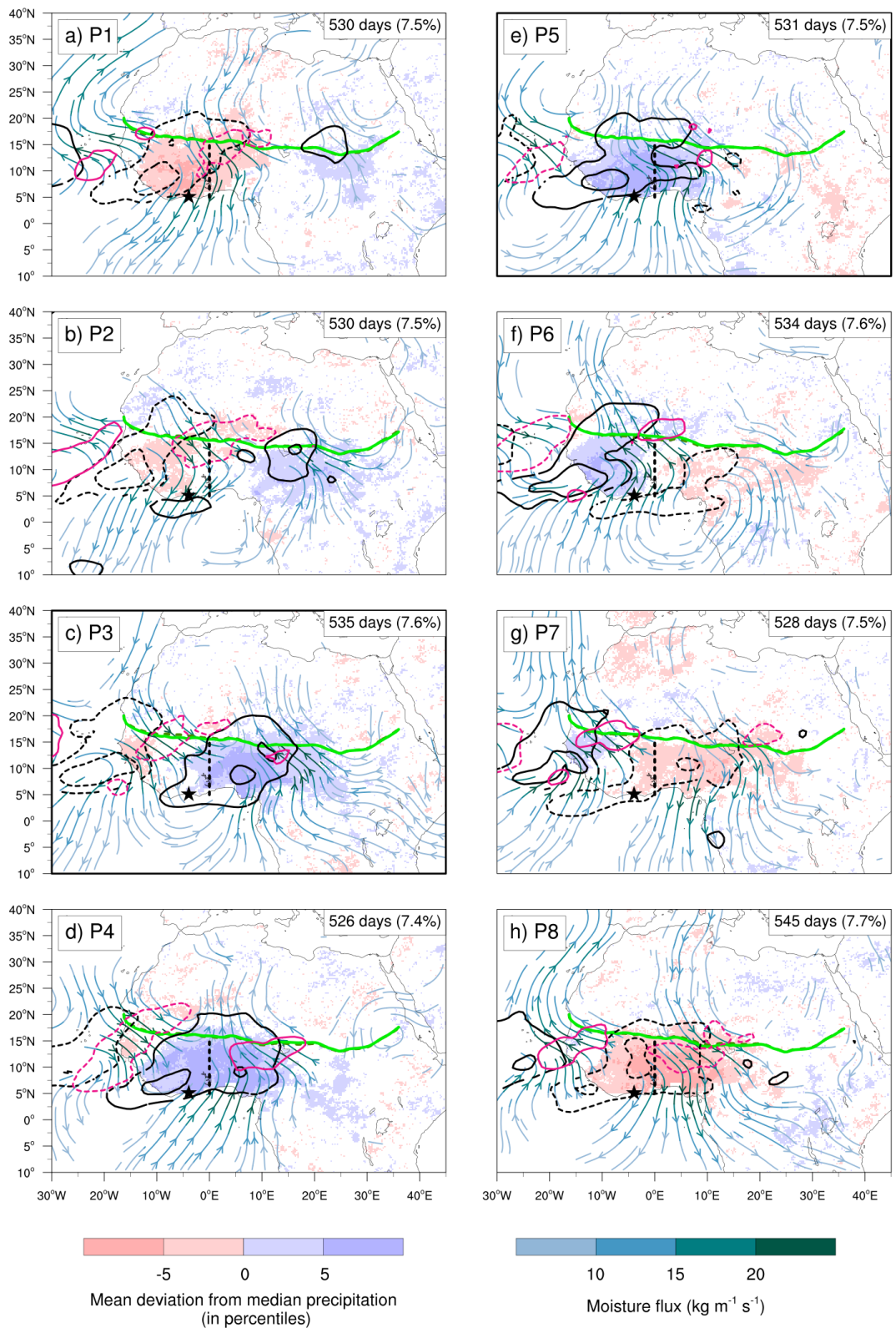
Figure A.2.9: Same composite of the mixed Rossby gravity waves as Fig. 3c,d in the main paper, but showing all wave phases. Reprinted from Schlueter et al. (2019b), supplementary material. © 2019, American Meteorological Society. Used with permission.
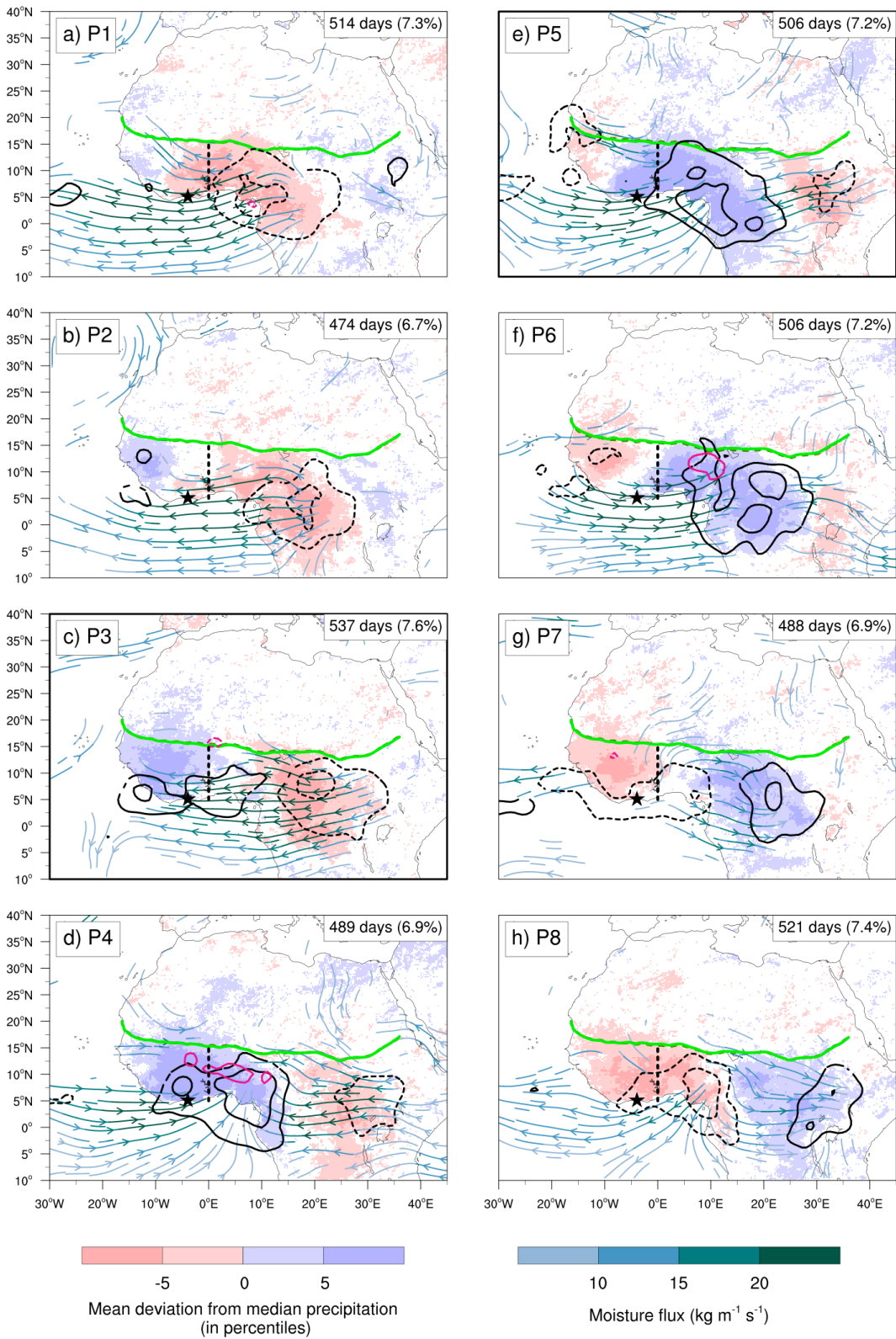
Figure A.2.10: Same composite of the Kelvin waves as Fig. 4c,d in the main paper, but showing all wave phases. Reprinted from Schlueter et al. (2019b), supplementary material. © 2019, American Meteorological Society. Used with permission.
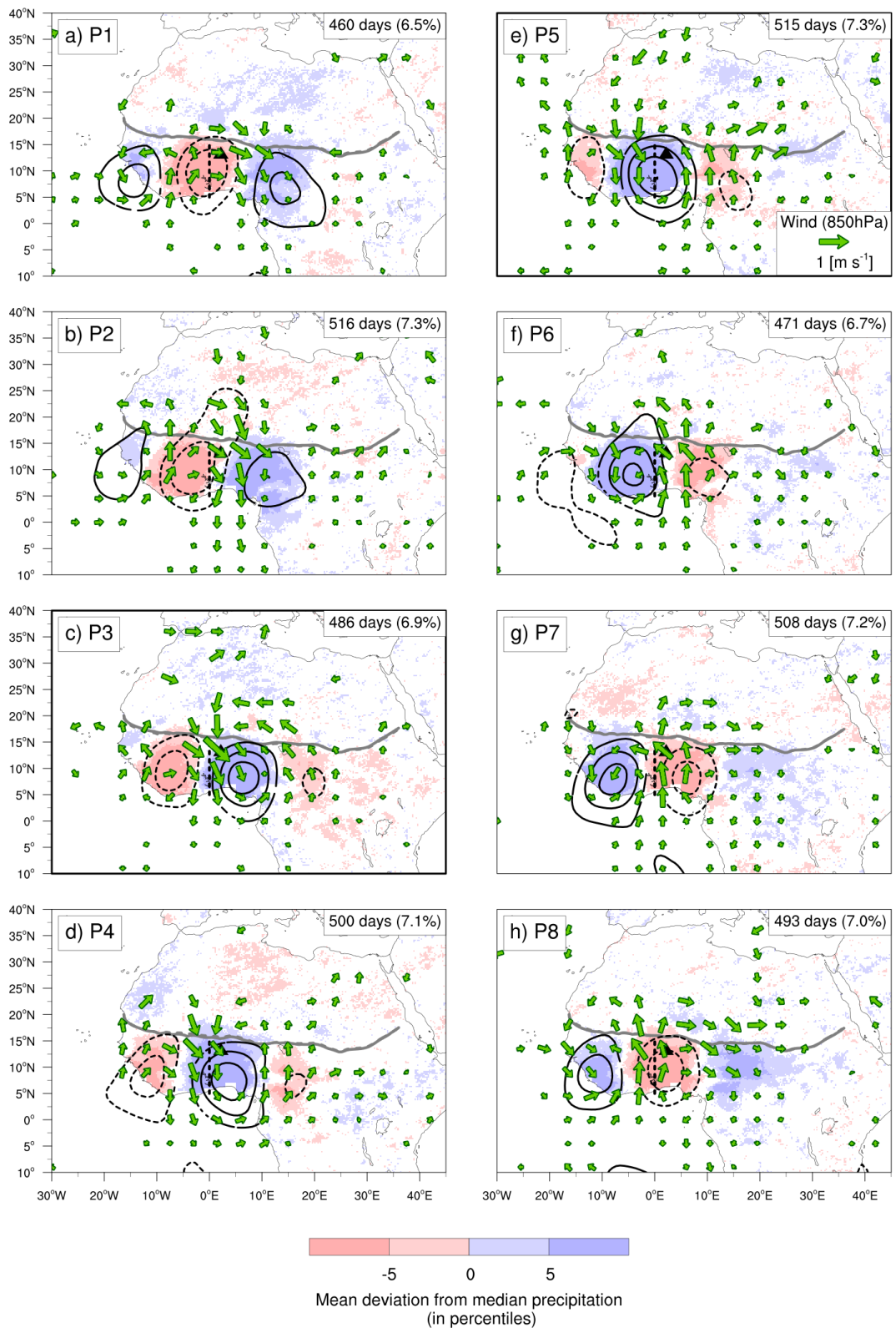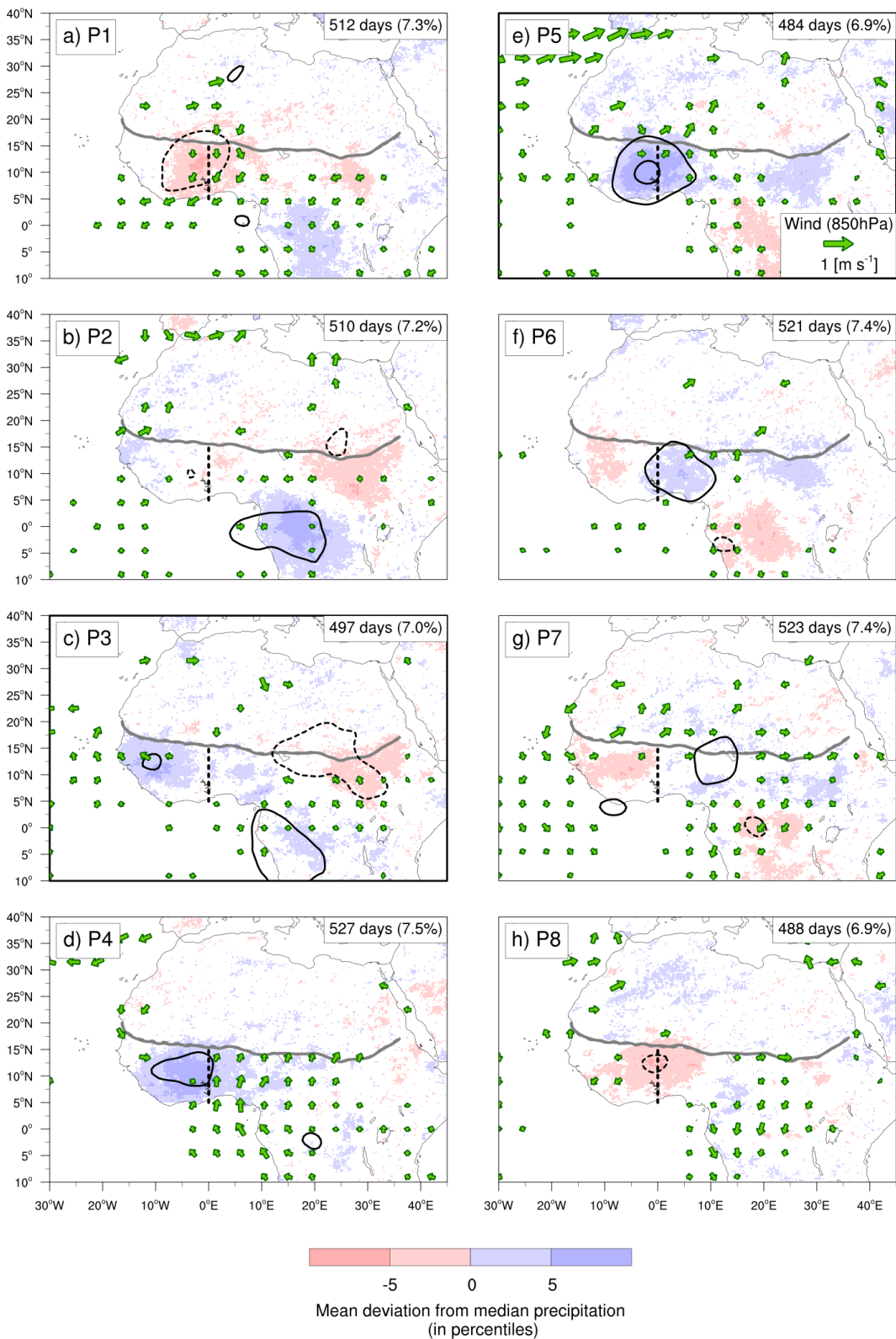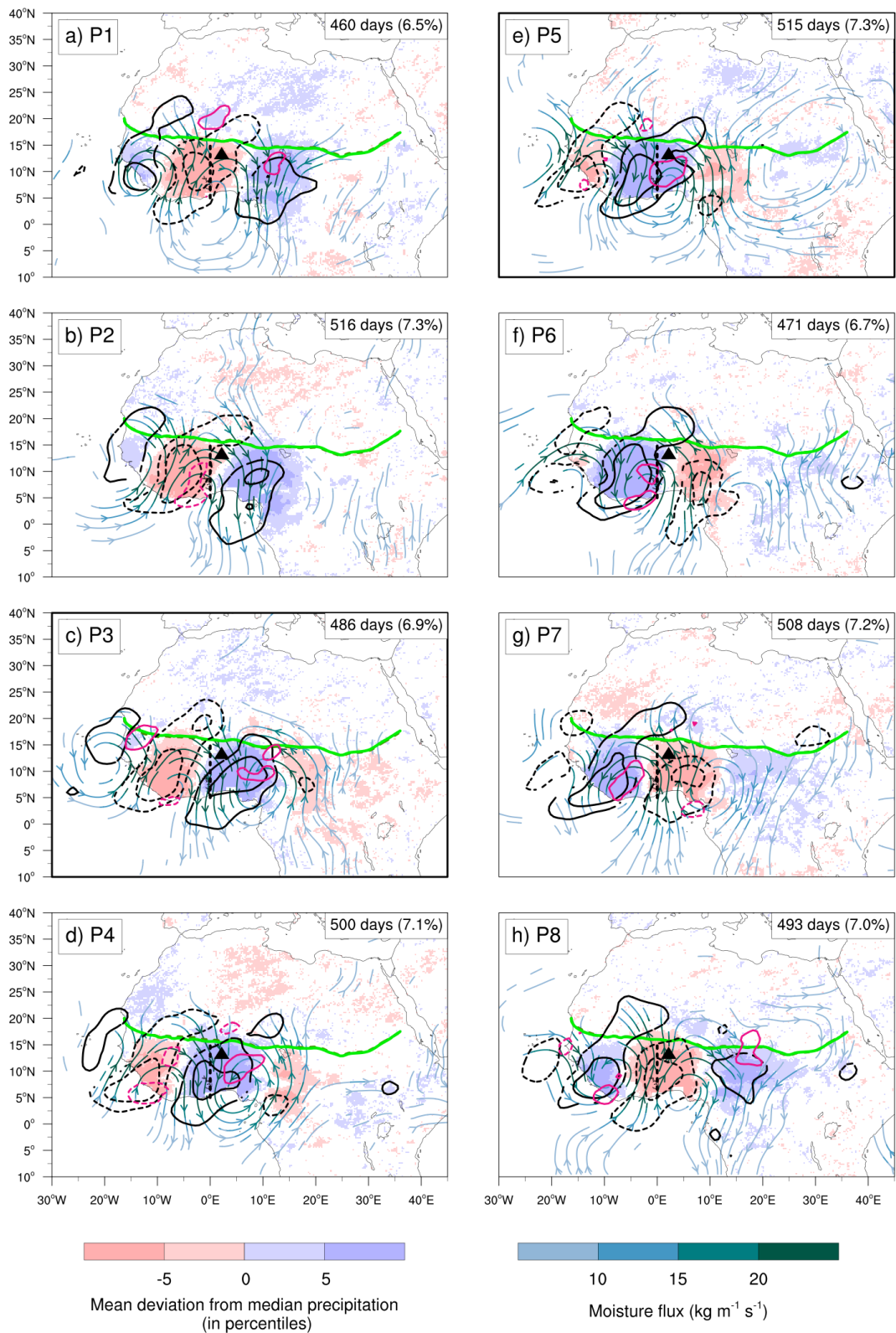
Figure A.2.11: Same composite of the tropical disturbances (mostly African Easterly Waves) as Fig. 5c,d in the main paper, but showing all wave phases. Reprinted from Schlueter et al. (2019b), supplementary material. © 2019, American Meteorological Society. Used with permission.
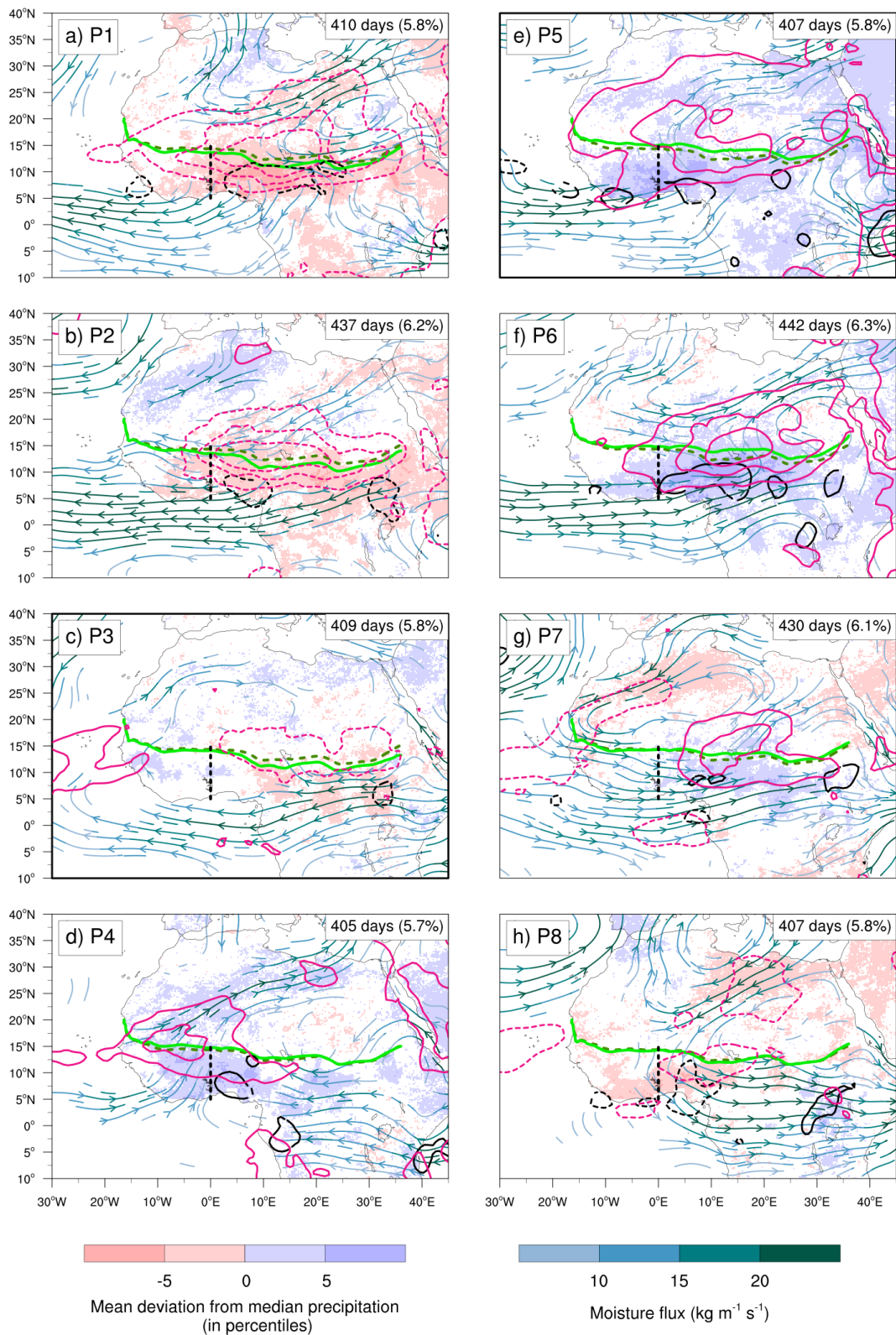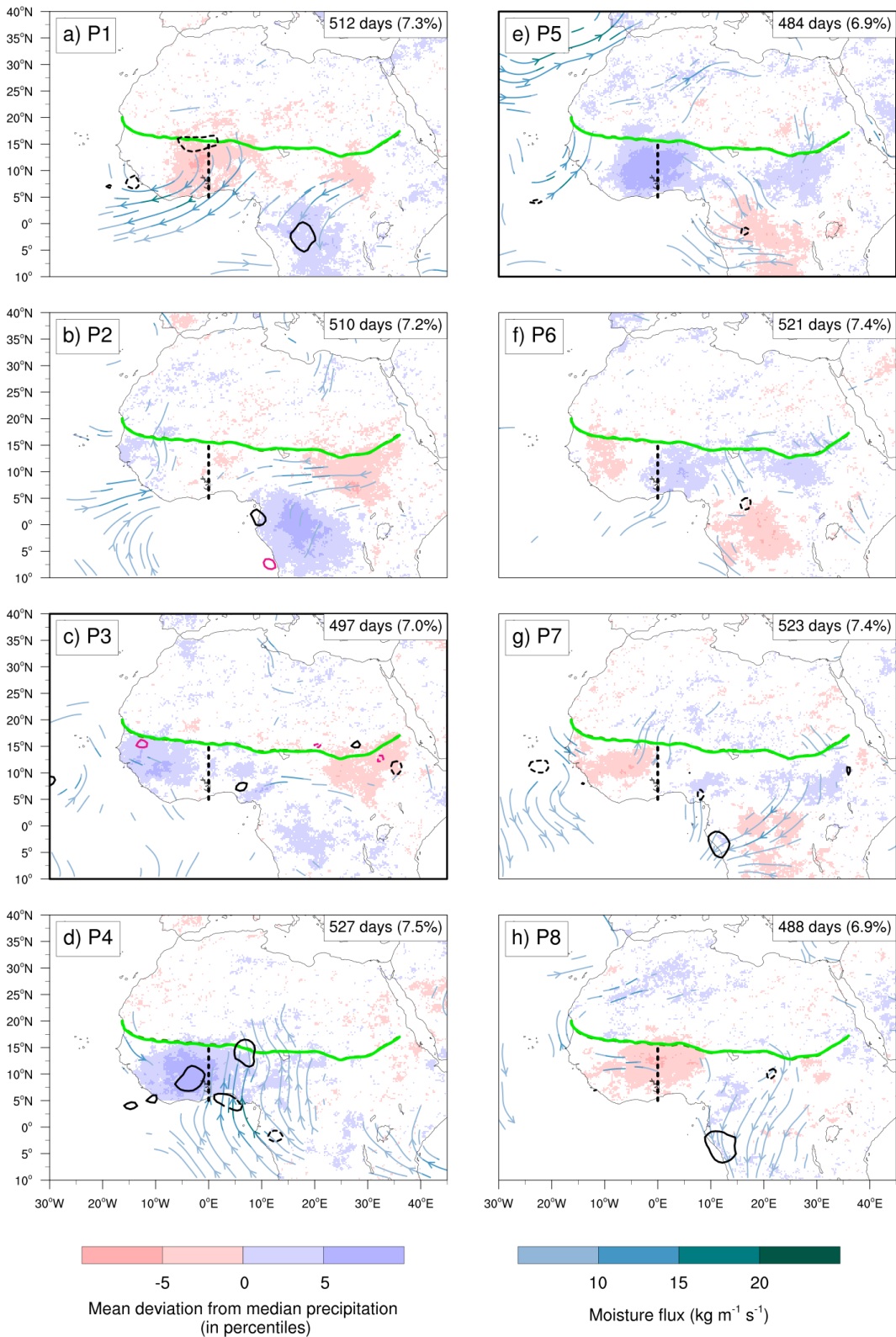
Figure A.2.12: Same composite as Fig. 1c,d in the main paper, but showing all wave phases of the eastward inertio-gravity waves. Reprinted from Schlueter et al. (2019b), supplementary material. © 2019, American Meteorological Society. Used with permission.
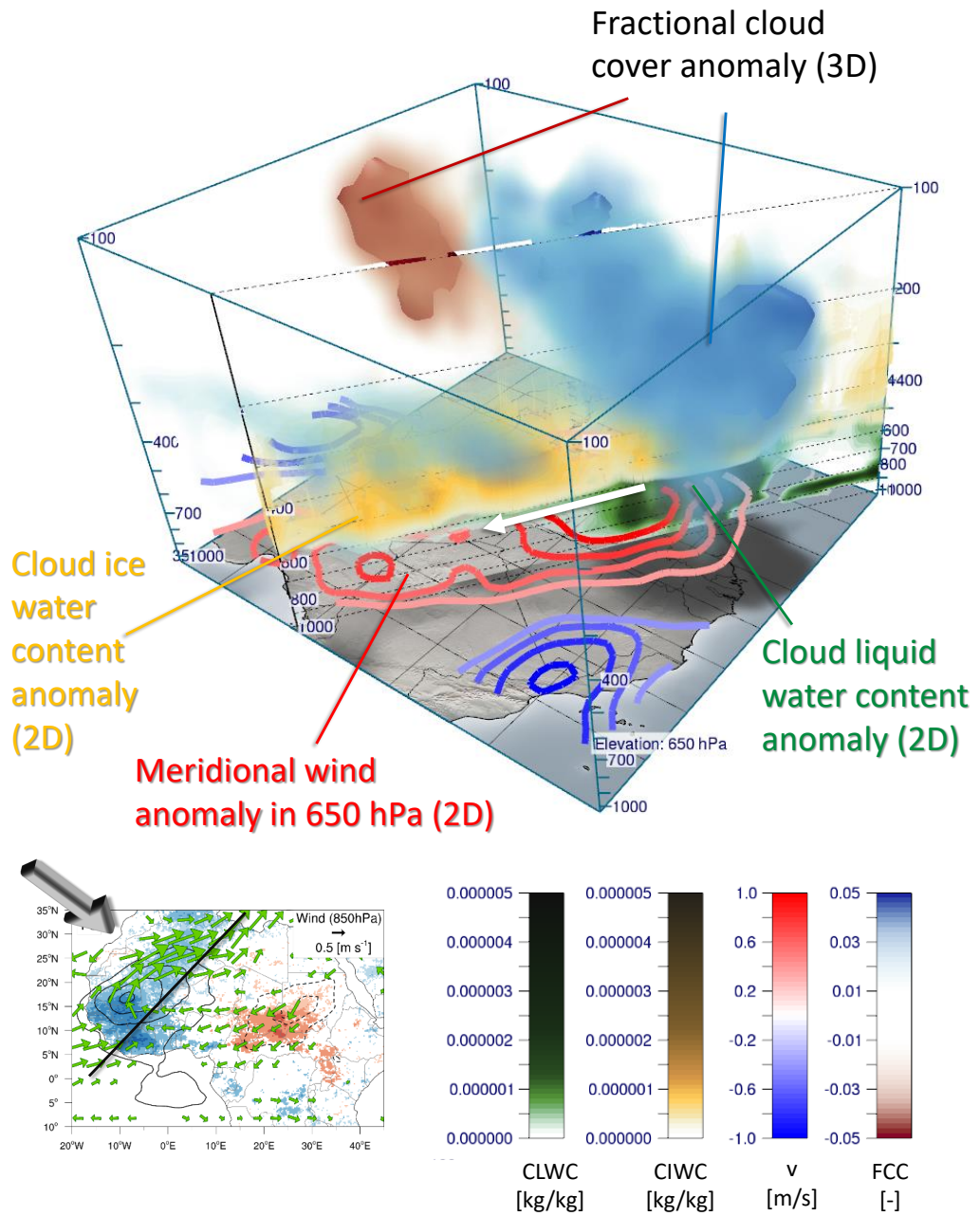
Figure A.2.13: 3D-composite of the tropical plume triggered by the ER wave in phase 6 viewed from north-west. The dark red and blue 3D feature shows the fractional cloud cover anomaly. In a vertical 2D cross-section along the plume (black line in map, bottom left), the cloud ice water content anomaly and cloud liquid water content anomaly are shown. The horizontal cross-section displays the meridional wind anomaly in 650 hPa. The visualization uses composites of the variables at 50 hPa steps from 1000 to 100 hPa and was created with Met.3D (Rautenhaus et al., 2015).

A.3 Potential for forecasting
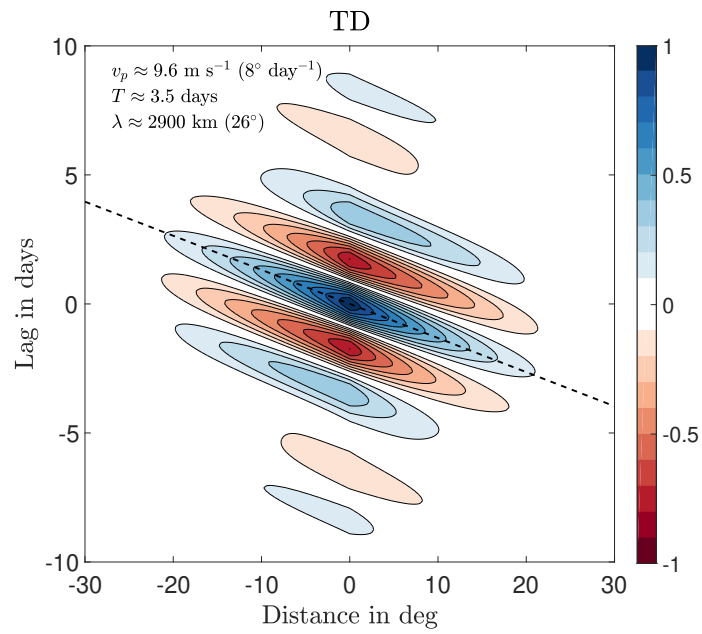
Figure A.3.1: Same as 7.1, but for the entire tropics (180°W–180°E).
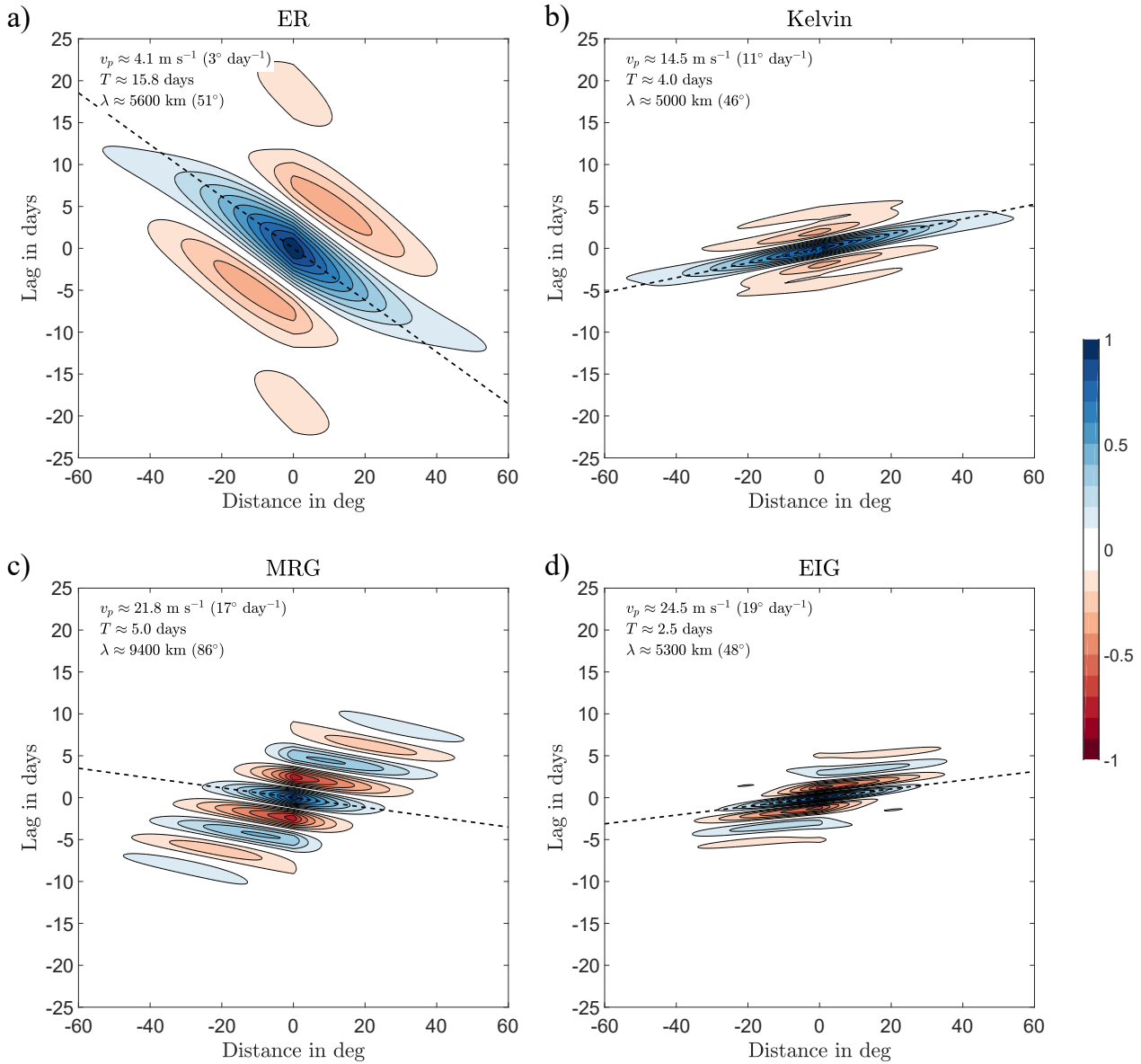
Figure A.3.2: Same as 7.3, but for the entire tropics (180°W–180°E).
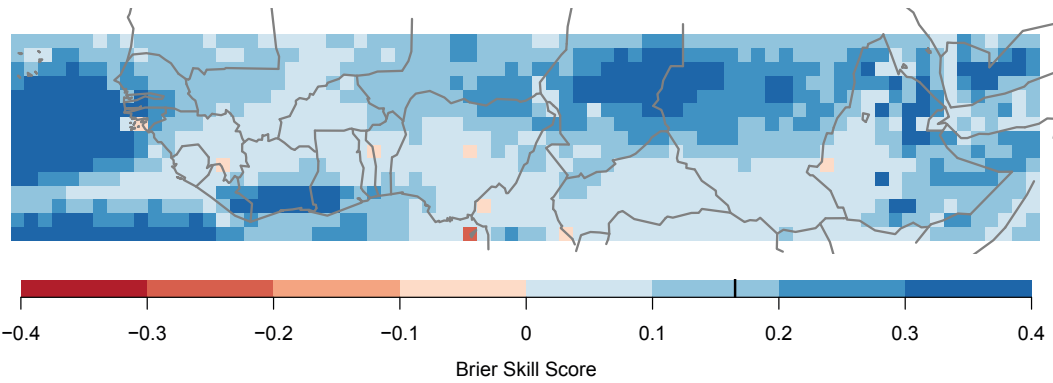
Figure A.3.3: Same as Fig. 7.8, but for a statistical model using TD and Kelvin waves as predictors instead of rainfall. © 2019, Peter Vogel. Used with permission.

Bibliography

Adames, Á. F., and D. Kim, 2016: The MJO as a Dispersive, Convectively Coupled Moisture Wave: Theory and Observations. *Journal of the Atmospheric Sciences*, **73 (3)**, 913–941, doi: 10.1175/JAS-D-15-0170.1.

Agustí-Panareda, A., A. C. M. Beljaars, C. Cardinali, I. Genkova, and C. D. Thorncroft, 2010a: Impacts of Assimilating AMMA Soundings on ECMWF Analyses and Forecasts. *Weather and Forecasting*, **25 (4)**, 1142–1160, doi: 10.1175/2010WAF2222370.1.

Agustí-Panareda, A., and Coauthors, 2010b: The ECMWF re-analysis for the AMMA observational campaign. *Quarterly Journal of the Royal Meteorological Society*, **136 (651)**, 1457–1472, doi: 10.1002/qj.662.

Alaka, G. J., and E. D. Maloney, 2012: The Influence of the MJO on Upstream Precursors to African Easterly Waves. *Journal of Climate*, **25 (9)**, 3219–3236, doi: 10.1175/JCLI-D-11-00232.1.

Alaka, G. J., and E. D. Maloney, 2014: The Intraseasonal Variability of African Easterly Wave Energetics. *Journal of Climate*, **27 (17)**, 6559–6580, doi: 10.1175/JCLI-D-14-00146.1.

Alaka, G. J., and E. D. Maloney, 2017: Internal Intraseasonal Variability of the West African Monsoon in WRF. *Journal of Climate*, **30 (15)**, 5815–5833, doi: 10.1175/JCLI-D-16-0750.1.

Albignat, J. P., and R. J. Reed, 1980: The Origin of African Wave Disturbances during Phase III of GATE. *Monthly Weather Review*, **108 (11)**, 1827–1839, doi: 10.1175/1520-0493(1980)108<1827:TOOAWD>2.0.CO;2.

Alfieri, L., P. Burek, E. Dutra, B. Krzeminski, D. Muraro, J. Thielen, and F. Pappenberger, 2013: GloFAS - global ensemble streamflow forecasting and flood early warning. *Hydrology and Earth System Sciences*, **17 (3)**, 1161–1175, doi: 10.5194/hess-17-1161-2013.

Arakawa, A., and W. H. Schubert, 1974: Interaction of a Cumulus Cloud Ensemble with the Large-Scale Environment, Part I. *Journal of the Atmospheric Sciences*, **31 (3)**, 674–701, doi: 10.1175/1520-0469(1974)031<0674:IOACCE>2.0.CO;2.

Arkin, P. A., and P. E. Ardanuy, 1989: Estimating Climatic-Scale Precipitation from Space: A Review. *Journal of Climate*, **2 (11)**, 1229–1238, doi: 10.1175/1520-0442(1989)002<1229:ECSPFS>2.0.CO;2.

Aspliden, C. I., Y. Tourre, and J. B. Sabine, 1976: Some Climatological Aspects of West African Disturbance Lines During GATE. *Monthly Weather Review*, **104 (8)**, 1029–1035, doi: 10.1175/1520-0493(1976)104<1029:SCAOWA>2.0.CO;2.

Bahaga, T. K., A. H. Fink, and P. Knippertz, 2019: Revisiting interannual to decadal teleconnections influencing seasonal rainfall in the Greater Horn of Africa during the 20th century. *International Journal of Climatology*, **18 (12)**, 302, doi: 10.1002/joc.5986.

Bandyopadhyay, S., S. Kanji, and L. Wang, 2012: The impact of rainfall and temperature variation on diarrheal prevalence in Sub-Saharan Africa. *Applied Geography*, **33**, 63–72, doi: 10.1016/j.apgeog.2011.07.017.

Barnett, B. J., and O. Mahul, 2007: Weather Index Insurance for Agriculture and Rural Areas in Lower-Income Countries. *American Journal of Agricultural Economics*, **89 (5)**, 1241–1247, doi: 10.1111/j.1467-8276.2007.01091.x.

Barrios, S., L. Bertinelli, and E. Strobl, 2010: Trends in Rainfall and Economic Growth in Africa: A Neglected Cause of the African Growth Tragedy. *Review of Economics and Statistics*, **92 (2)**, 350–366, doi: 10.1162/rest.2010.11212.

Basher, R., 2006: Global early warning systems for natural hazards: systematic and people-centred. *Philosophical Transactions of the Royal Society A: Mathematical, Physical and Engineering Sciences*, **364 (1845)**, 2167–2182, doi: 10.1098/rsta.2006.1819.

Benson, C., and E. J. Clay, 2004: *Understanding the economic and financial impacts of natural disasters*, Disaster risk management series, Vol. 4. World Bank, Washington, DC, ISBN: 0821356852.

Berhane, F., B. F. Zaitchik, and H. S. Badr, 2015: The Madden–Julian Oscillation's Influence on Spring Rainy Season Precipitation over Equatorial West Africa. *Journal of Climate*, **28 (22)**, 8653–8672, doi: 10.1175/JCLI-D-14-00510.1.

Bjerknes, J., 1919: On the structure of moving cyclones. *Monthly Weather Review*, **47 (2)**, 95–99, doi: 10.1175/1520-0493(1919)47<95:OTSOMC>2.0.CO;2.

Borgogno, F., P. D'Odorico, F. Laio, and L. Ridolfi, 2007: Effect of rainfall interannual variability on the stability and resilience of dryland plant ecosystems. *Water Resources Research*, **43 (6)**, 31,613, doi: 10.1029/2006WR005314.

Brown, R. G., and C. Zhang, 1997: Variability of Midtropospheric Moisture and Its Effect on Cloud-Top Height Distribution during TOGA COARE. *Journal of the Atmospheric Sciences*, **54 (23)**, 2760–2774, doi: 10.1175/1520-0469(1997) 054<2760:VOMMAI>2.0.CO;2.

Browning, K. A., and F. H. Ludlam, 1962: Airflow in convective storms. *Quarterly Journal of the Royal Meteorological Society*, **88 (376)**, 117–135, doi: 10.1002/ qj.49708837602.

Buckle, C., 1996: *Weather and Climate in Africa*. Longman, Harlow, ISBN: 0582093333.

Buizza, R., and M. Leutbecher, 2015: The forecast skill horizon. *Quarterly Journal of the Royal Meteorological Society*, **141 (693)**, 3366–3382, doi: 10.1002/qj. 2619.

Burpee, R. W., 1972: The Origin and Structure of Easterly Waves in the Lower Troposphere of North Africa. *Journal of the Atmospheric Sciences*, **29 (1)**, 77–90, doi: 10.1175/1520-0469(1972)029<0077:TOASOE>2.0.CO;2.

Burpee, R. W., 1975: Some Features of Synoptic–Scale Waves Based on a Compositing Analysis of GATE Data. *Monthly Weather Review*, **103 (10)**, 921–925, doi: 10.1175/1520-0493(1975)103<0921:SFOSWB>2.0.CO;2.

Caine, A., P. Dorward, G. Clarkson, N. Evans, C. Canales, and D. Stern, 2015: *Review of Mobile Applications that Involve the Use of Weather and Climate Information: their use and potential for Smallholder Farmers*, CCAFS Working Paper, Vol. 150. CGIAR Research Program on Climate Change, Agriculture and Food Security (CCAFS), Copenhagen, Denmark, URL https://hdl.handle.net/ 10568/69496.

Camberlin, P., 2018: Climate of Eastern Africa. *Oxford Research Encyclopedia of Climate Science: Climate of Africa*, doi: 10.1093/acrefore/9780190228620. 013.512.

Caminade, C., and Coauthors, 2011: Mapping Rift Valley fever and malaria risk over West Africa using climatic indicators. *Atmospheric Science Letters*, **12 (1)**, 96–103, doi: 10.1002/asl.296.

Cassou, C., 2008: Intraseasonal interaction between the Madden-Julian Oscillation and the North Atlantic Oscillation. *Nature*, **455 (7212)**, 523–527, doi: 10.1038/ nature07286.

Castanheira, J. M., and C. A. F. Marques, 2015: Convectively coupled equatorial-wave diagnosis using three-dimensional normal modes. *Quarterly Journal of the Royal Meteorological Society*, **141 (692)**, 2776–2792, doi: 10.1002/qj.2563.

Chang, C.-P., 1970: Westward Propagating Cloud Patterns in the Tropical Pacific as seen from Time-Composite Satellite Photographs. *Journal of the Atmospheric Sciences*, **27 (1)**, 133–138, doi: 10.1175/1520-0469(1970)027<0133: WPCPIT>2.0.CO;2.

Chang, C.-P., 1977: Viscous Internal Gravity Waves and Low–Frequency Oscillations in the Tropics. *Journal of the Atmospheric Sciences*, **34 (6)**, 901–910, doi: 10.1175/1520-0469(1977)034<0901:VIGWAL>2.0.CO;2.

Chang, C.-P., V. F. Morris, and J. M. Wallace, 1970: A Statistical Study of Easterly Waves in the Western Pacific: July–December 1964. *Journal of the Atmospheric Sciences*, **27 (2)**, 195–201, doi: 10.1175/1520-0469(1970) 027<0195:ASSOEW>2.0.CO;2.

Chang, C.-W. J., W.-L. Tseng, H.-H. Hsu, N. Keenlyside, and B.-J. Tsuang, 2015: The Madden-Julian Oscillation in a warmer world. *Geophysical Research Letters*, **42 (14)**, 6034–6042, doi: 10.1002/2015GL065095.

Charney, J. G., and M. E. Stern, 1962: On the Stability of Internal Baroclinic Jets in a Rotating Atmosphere. *Journal of the Atmospheric Sciences*, **19 (2)**, 159–172, doi: 10.1175/1520-0469(1962)019<0159:OTSOIB>2.0.CO;2.

Chauvin, F., R. Roehrig, and J.-P. Lafore, 2010: Intraseasonal Variability of the Saharan Heat Low and Its Link with Midlatitudes. *Journal of Climate*, **23 (10)**, 2544–2561, doi: 10.1175/2010JCLI3093.1.

Cheng, Y. M., C. D. Thorncroft, and G. N. Kiladis, 2019: Two contrasting African easterly wave behaviors. *J. Atmos. Sci. (in revision)*.

CIA, 2019: The World Factbook (accessed 25 March 2019). Central Intelligence Agency, U. S.A., URL https://www.cia.gov/library/publications/the-world-factbook/.

Cook, K. H., 2000: The South Indian Convergence Zone and Interannual Rainfall Variability over Southern Africa. *Journal of Climate*, **13 (21)**, 3789–3804, doi: 10.1175/1520-0442(2000)013<3789:TSICZA>2.0.CO;2.

Corfidi, S. F., 2003: Cold Pools and MCS Propagation: Forecasting the Motion of Downwind-Developing MCSs. *Weather and Forecasting*, **18 (6)**, 997–1017, doi: 10.1175/1520-0434(2003)018<0997:CPAMPF>2.0.CO;2.

Coriolis, G., 1835: Mémoire sur les équations du mouvement relatif des Systèmes de corps. *J. De l'Ecole Royale Polytechnique*, **(15)**, 144–154.

Coughlan de Perez, E., and S. J. Mason, 2014: Climate information for humanitarian agencies: some basic principles. *Earth Perspectives*, **1 (1)**, 11, doi: 10.1186/2194-6434-1-11.

Cox, J., and T. A. Abeku, 2007: Early warning systems for malaria in Africa: from blueprint to practice. *Trends in Parasitology*, **23 (6)**, 243–246, doi: 10.1016/j.pt.2007.03.008.

Crimp, S. J., J. R. E. Lutjeharms, and S. J. Mason, 1998: Sensitivity of a tropical-temperate trough to sea-surface temperature anomalies in the Agulhas retroflection region. *Water SA*, **24**, 93–100.

Daugman, J. G., 1980: Two-dimensional spectral analysis of cortical receptive field profiles. *Vision Research*, **20 (10)**, 847–856, doi: 10.1016/0042-6989(80)90065-6.

Daugman, J. G., 1988: Complete discrete 2-D Gabor transforms by neural networks for image analysis and compression. *IEEE Transactions on Acoustics, Speech, and Signal Processing*, **36 (7)**, 1169–1179, doi: 10.1109/29.1644.

Davis, G., 2007: History of the NOAA satellite program. *Journal of Applied Remote Sensing*, **1 (1)**, 012 504, doi: 10.1117/1.2642347.

Dee, D. P., and Coauthors, 2011: The ERA-Interim reanalysis: configuration and performance of the data assimilation system. *Quarterly Journal of the Royal Meteorological Society*, **137 (656)**, 553–597, doi: 10.1002/qj.828.

Delayen, K., and J.-I. Yano, 2009: Is asymptotic non-divergence of the large-scale tropical atmosphere consistent with equatorial wave theories? *Tellus A: Dynamic Meteorology and Oceanography*, **61 (4)**, 491–497, doi: 10.1111/j.1600-0870. 2009.00404.x.

Desbureaux, S., and R. Damania, 2018: Rain, forests and farmers: Evidence of drought induced deforestation in Madagascar and its consequences for biodiversity conservation. *Biological Conservation*, **221**, 357–364, doi: 10. 1016/j.biocon.2018.03.005.

Dezfuli, A. K., 2017: Climate of Western and Central Equatorial Africa. *Oxford Research Encyclopedia of Climate Science: Climate of Africa*, doi: 10.1093/ acrefore/9780190228620.013.511.

Dias, J., M. Gehne, G. N. Kiladis, N. Sakaeda, P. Bechtold, and T. Haiden, 2018: Equatorial Waves and the Skill of NCEP and ECMWF Numerical Weather Prediction Systems. *Monthly Weather Review*, **146 (6)**, 1763–1784, doi: 10. 1175/MWR-D-17-0362.1.

Dias, J., and G. N. Kiladis, 2016: The Relationship between Equatorial Mixed Rossby–Gravity and Eastward Inertio-Gravity Waves. Part II. *Journal of the Atmospheric Sciences*, **73 (5)**, 2147–2163, doi: 10.1175/JAS-D-15-0231.1.

Dias, J., and O. Pauluis, 2009: Convectively Coupled Waves Propagating along an Equatorial ITCZ. *Journal of the Atmospheric Sciences*, **66 (8)**, 2237–2255, doi: 10.1175/2009JAS3020.1.

Dias, J., and O. Pauluis, 2011: Modulations of the Phase Speed of Convectively Coupled Kelvin Waves by the ITCZ. *Journal of the Atmospheric Sciences*, **68 (7)**, 1446–1459, doi: 10.1175/2011JAS3630.1.

Dickinson, M., and J. Molinari, 2000: Climatology of Sign Reversals of the Meridional Potential Vorticity Gradient over Africa and Australia. *Monthly Weather Review*, **128 (11)**, 3890–3900, doi: 10.1175/1520-0493(2001) 129<3890:COSROT>2.0.CO;2.

Diedhiou, A., S. Janicot, A. Viltard, P. de Felice, and H. Laurent, 1999: Easterly wave regimes and associated convection over West Africa and tropical Atlantic: results from the NCEP/NCAR and ECMWF reanalyses. *Climate Dynamics*, **15 (11)**, 795–822, doi: 10.1007/s003820050316.

Durre, I., R. S. Vose, X. Yin, S. Applequist, and J. Arnfield, 2016: Integrated Global Radiosonde Archive (IGRA) Version 2. *NOAA National Centers for Environmental Information*, doi: 10.7289/V5X63K0Q.

Duvel, J.-P., 1990: Convection over Tropical Africa and the Atlantic Ocean during Northern Summer. Part II: Modulation by Easterly Waves. *Monthly Weather Review*, **118 (9)**, 1855–1868, doi: 10.1175/1520-0493(1990)118<1855: COTAAT>2.0.CO;2.

Ebert, E., and Coauthors, 2013: Progress and challenges in forecast verification. *Meteorological Applications*, **20 (2)**, 130–139, doi: 10.1002/met.1392.

Ebhuoma, E. E., and D. M. Simatele, 2017: 'We know our Terrain': indigenous knowledge preferred to scientific systems of weather forecasting in the Delta State of Nigeria. *Climate and Development*, **5 (2)**, 1–12, doi: 10.1080/ 17565529.2017.1374239.

Eldridge, R. H., 1957: A synoptic study of west african disturbance lines. *Quarterly Journal of the Royal Meteorological Society*, **83 (357)**, 303–314, doi: 10.1002/ qj.49708335704.

Elless, T. J., and R. D. Torn, 2018: African Easterly Wave Forecast Verification and Its Relation to Convective Errors within the ECMWF Ensemble Prediction System. *Weather and Forecasting*, **33 (2)**, 461–477, doi: 10.1175/ WAF-D-17-0130.1.

Emanuel, K. A., 1987: An Air-Sea Interaction Model of Intraseasonal Oscillations in the Tropics. *Journal of the Atmospheric Sciences*, **44 (16)**, 2324–2340, doi: 10.1175/1520-0469(1987)044<2324:AASIMO>2.0.CO;2.

Enfield, D. B., A. M. Mestas-Nuñez, D. A. Mayer, and L. Cid-Serrano, 1999: How ubiquitous is the dipole relationship in tropical Atlantic sea surface temperatures? *Journal of Geophysical Research*, **104 (C4)**, 7841–7848, doi: 10.1029/1998JC900109.

Engel, T., A. H. Fink, P. Knippertz, G. Pante, and J. Bliefernicht, 2017: Extreme Precipitation in the West African Cities of Dakar and Ouagadougou: Atmospheric Dynamics and Implications for Flood Risk Assessments. *Journal of Hydrometeorology*, **18 (11)**, 2937–2957, doi: 10.1175/JHM-D-16-0218.1.

Ertel, H., 1942: Ein neuer hydrodynamischer Wirbelsatz. *Meteorologische Zeitschrift*, **(59)**, 277–281.

FAO, 2016a: AQUASTAT website (accessed 7 January 2019). Food and Agriculture Organization of the United Nations (FAO), Rome, Italy, URL http://www.fao.org/nr/aquastat.

FAO, 2016b: FAOSTAT website (accessed 7 January 2019). Food and Agriculture Organization of the United Nations (FAO), Rome, Italy, URL http://www.fao.org/faostat/.

FAO, 2017: *Africa regional overview of food security and nutrition 2017: The food security and nutrition-conflict nexus : building resilience for food security, nutrition and peace*. Food and Agriculture Organization of the United Nations, Accra, ISBN: 978-92-5-109981-0.

Fauchereau, N., B. Pohl, C. J. C. Reason, M. Rouault, and Y. Richard, 2009: Recurrent daily OLR patterns in the Southern Africa/Southwest Indian Ocean region, implications for South African rainfall and teleconnections. *Climate Dynamics*, **32 (4)**, 575–591, doi: 10.1007/s00382-008-0426-2.

Ferranti, L., T. N. Palmer, F. Molteni, and E. Klinker, 1990: Tropical-Extratropical Interaction Associated with the 30–60 Day Oscillation and Its Impact on Medium and Extended Range Prediction. *Journal of the Atmospheric Sciences*, **47 (18)**, 2177–2199, doi: 10.1175/1520-0469(1990)047<2177:TEIAWT>2.0.CO;2.

Fink, A. H., 2012: To the 75th anniversary of the discovery of african easterly waves. *30th Conference on Hurricanes and Tropical Meteorology*, Vol. 15.

Fink, A. H., and A. Reiner, 2003: Spatiotemporal variability of the relation between African Easterly Waves and West African Squall Lines in 1998 and 1999. *Journal of Geophysical Research*, **108 (D11)**, 199, doi: 10.1029/2002JD002816.

Fink, A. H., and P. Speth, 1997: Some potential forcing mechanisms of the year-to-year variability of the tropical convection and its intraseasonal (25–70-day) variability. *International Journal of Climatology*, **17 (14)**, 1513–1534, doi: 10.1002/(SICI)1097-0088(19971130)17:14<1513::AID-JOC210>3.0.CO;2-U.

Fink, A. H., and Coauthors, 2017: Mean Climate and Seasonal Cycle. *Meteorology of Tropical West Africa*, D. J. Parker, and M. Diop-Kane, Eds., John Wiley & Sons, Ltd, ISBN: 9781118391297, Chichester, UK, 1–39, doi: 10.1002/9781118391297.ch1.

Fontaine, B., S. Louvet, and P. Roucou, 2008: Definition and predictability of an OLR-based West African monsoon onset. *International Journal of Climatology*, **28 (13)**, 1787–1798, doi: 10.1002/joc.1674.

Frank, W. M., and P. E. Roundy, 2006: The Role of Tropical Waves in Tropical Cyclogenesis. *Monthly Weather Review*, **134 (9)**, 2397–2417, doi: 10.1175/MWR3204.1.

Freedman, D., and P. Diaconis, 1981: On the histogram as a density estimator: L 2 theory. *Zeitschrift für Wahrscheinlichkeitstheorie und Verwandte Gebiete*, **57 (4)**, 453–476, doi: 10.1007/BF01025868.

Frierson, D. M. W., D. Kim, I.-S. Kang, M.-I. Lee, and J.-L. Lin, 2011: Structure of AGCM-Simulated Convectively Coupled Kelvin Waves and Sensitivity to Convective Parameterization. *Journal of the Atmospheric Sciences*, **68 (1)**, 26–45, doi: 10.1175/2010JAS3356.1.

Fröhlich, L., P. Knippertz, A. H. Fink, and E. Hohberger, 2013: An Objective Climatology of Tropical Plumes. *Journal of Climate*, **26 (14)**, 5044–5060, doi: 10.1175/JCLI-D-12-00351.1.

Froude, L. S. R., L. Bengtsson, and K. I. Hodges, 2013: Atmospheric predictability revisited. *Tellus A: Dynamic Meteorology and Oceanography*, **65 (1)**, 19 022, doi: 10.3402/tellusa.v65i0.19022.

Funk, C., and Coauthors, 2015: The climate hazards infrared precipitation with stations–a new environmental record for monitoring extremes. *Scientific data*, **2**, 150 066, doi: 10.1038/sdata.2015.66.

García-Herrera, R., and D. Barriopedro, 2018: Climate of the Mediterranean Region. *Oxford Research Encyclopedia of Climate Science: Climate of Africa*, doi: 10.1093/acrefore/9780190228620.013.509.

Garreaud, R. D., 2001: Subtropical cold surges: regional aspects and global distribution. *International Journal of Climatology*, **21 (10)**, 1181–1197, doi: 10.1002/joc.687.

Gill, A. E., 1977: Coastally trapped waves in the atmosphere. *Quarterly Journal of the Royal Meteorological Society*, **103 (437)**, 431–440, doi: 10.1002/qj.49710343704.

Gill, A. E., 1980: Some simple solutions for heat-induced tropical circulation. *Quarterly Journal of the Royal Meteorological Society*, **106 (449)**, 447–462, doi: 10.1002/qj.49710644905.

Gneiting, T., and A. E. Raftery, 2007: Strictly Proper Scoring Rules, Prediction, and Estimation. *Journal of the American Statistical Association*, **102 (477)**, 359–378, doi: 10.1198/016214506000001437.

Gonzales-Fuentes, L., K. Barbé, L. Barford, L. Lauwers, and L. Philips, 2015: A qualitative study of probability density visualization techniques in measurements. *Measurement*, **65**, 94–111, doi: 10.1016/j.measurement.2014.12.022.

Goudie, A., and M. Seely, 2011: *World Heritage Desert Landscapes: Potential Priorities for the Recognition of Desert Landscapes and Geomorphological sites on the World Heritage List*, Vol. 9. International Union for Conservation of Nature (IUCN), Gland, Switzerland.

Grazzini, F., and F. Vitart, 2015: Atmospheric predictability and Rossby wave packets. *Quarterly Journal of the Royal Meteorological Society*, **141 (692)**, 2793–2802, doi: 10.1002/qj.2564.

Gu, G., 2009: Intraseasonal variability in the equatorial Atlantic-West Africa during March–June. *Climate Dynamics*, **32 (4)**, 457–471, doi: 10.1007/s00382-008-0428-0.

Haertel, P. T., and G. N. Kiladis, 2004: Dynamics of 2-Day Equatorial Waves. *Journal of the Atmospheric Sciences*, **61 (22)**, 2707–2721, doi: 10.1175/JAS3352.1.

Haiden, T., M. J. Rodwell, D. S. Richardson, A. Okagaki, T. Robinson, and T. Hewson, 2012: Intercomparison of Global Model Precipitation Forecast Skill in 2010/11 Using the SEEPS Score. *Monthly Weather Review*, **140 (8)**, 2720–2733, doi: 10.1175/MWR-D-11-00301.1.

Harlim, J., and A. J. Majda, 2013: Test models for filtering and prediction of moisture-coupled tropical waves. *Quarterly Journal of the Royal Meteorological Society*, **139 (670)**, 119–136, doi: 10.1002/qj.1956.

Harrison, M. S. J., 1984: A generalized classification of South African summer rain-bearing synoptic systems. *Journal of Climatology*, **4 (5)**, 547–560, doi: 10.1002/joc.3370040510.

Hart, N. C. G., C. J. C. Reason, and N. Fauchereau, 2010: Tropical–Extratropical Interactions over Southern Africa: Three Cases of Heavy Summer Season Rainfall. *Monthly Weather Review*, **138 (7)**, 2608–2623, doi: 10.1175/2010MWR3070.1.

Hayashi, Y., 1970: A Theory of Large-Scale Equatorial Waves Generated by Condensation Heat and Accelerating. *Journal of the Meteorological Society of Japan. Ser. II*, **48 (2)**, 140–160, doi: 10.2151/jmsj1965.48.2_140.

Henderson, S. A., E. D. Maloney, and E. A. Barnes, 2016: The Influence of the Madden–Julian Oscillation on Northern Hemisphere Winter Blocking. *Journal of Climate*, **29 (12)**, 4597–4616, doi: 10.1175/JCLI-D-15-0502.1.

Hendon, H. H., and B. Liebmann, 1991: The Structure and Annual Variation of Antisymmetric Fluctuations of Tropical Convection and Their Association with Rossby–Gravity Waves. *Journal of the Atmospheric Sciences*, **48 (19)**, 2127–2140, doi: 10.1175/1520-0469(1991)048<2127:TSAAVO>2.0.CO;2.

Hendon, H. H., C. Zhang, and J. D. Glick, 1999: Interannual Variation of the Madden–Julian Oscillation during Austral Summer. *Journal of Climate*, **12 (8)**, 2538–2550, doi: 10.1175/1520-0442(1999)012<2538:IVOTMJ>2.0.CO;2.

Holder, C. T., S. E. Yuter, A. H. Sobel, and A. R. Aiyyer, 2008: The Mesoscale Characteristics of Tropical Oceanic Precipitation during Kelvin and Mixed Rossby–Gravity Wave Events. *Monthly Weather Review*, **136 (9)**, 3446–3464, doi: 10.1175/2008MWR2350.1.

Holton, J. R., and G. J. Hakim, 2013: *An introduction to dynamic meteorology*. 5th ed., Academic Press, Amsterdam, ISBN: 9780123848666.

Hoskins, B. J., and D. J. Karoly, 1981: The Steady Linear Response of a Spherical Atmosphere to Thermal and Orographic Forcing. *Journal of the Atmospheric Sciences*, **38 (6)**, 1179–1196, doi: 10.1175/1520-0469(1981)038<1179:TSLROA>2.0.CO;2.

Hoskins, B. J., M. E. McIntyre, and A. W. Robertson, 1985: On the use and significance of isentropic potential vorticity maps. *Quarterly Journal of the Royal Meteorological Society*, **111 (470)**, 877–946, doi: 10.1002/qj.49711147002.

Hoskins, B. J., and G.-Y. Yang, 2000: The Equatorial Response to Higher-Latitude Forcing. *Journal of the Atmospheric Sciences*, **57 (9)**, 1197–1213, doi: 10.1175/1520-0469(2000)057<1197:TERTHL>2.0.CO;2.

Hou, R., C. Chen, and M. Shah, 2017: An End-to-end 3D Convolutional Neural Network for Action Detection and Segmentation in Videos. URL http://arxiv. org/pdf/1712.01111v1.

Houérou, H. N., 2009: *Bioclimatology and Biogeography of Africa*. Springer Berlin Heidelberg, Berlin, Heidelberg, ISBN: 978-3-540-85192-9, doi: 10. 1007/978-3-540-85192-9.

Hough, S. S., 1897: On the Application of Harmonic Analysis to the Dynamical Theory of the Tides. Part I. On Laplace's Oscillations of the First Species, and on the Dynamics of Ocean Currents. *Philosophical Transactions of the Royal Society A: Mathematical, Physical and Engineering Sciences*, **189**, 201–257, doi: 10.1098/rsta.1897.0009.

Hough, S. S., 1898: On the Application of Harmonic Analysis to the Dynamical Theory of the Tides. Part II: On the General Integration of Laplace's Dynamical Equations. *Philosophical Transactions of the Royal Society A: Mathematical, Physical and Engineering Sciences*, **191**, 139–185, doi: 10.1098/rsta.1898. 0005.

House, F. B., A. Gruber, G. E. Hunt, and A. T. Mecherikunnel, 1986: History of satellite missions and measurements of the Earth Radiation Budget (1957–1984). *Reviews of Geophysics*, **24 (2)**, 357, doi: 10.1029/RG024i002p00357.

Houze, R. A., 2004: Mesoscale convective systems. *Reviews of Geophysics*, **42 (4)**, 86, doi: 10.1029/2004RG000150.

Hsieh, J.-S., and K. H. Cook, 2005: Generation of African Easterly Wave Disturbances: Relationship to the African Easterly Jet. *Monthly Weather Review*, **133 (5)**, 1311–1327, doi: 10.1175/MWR2916.1.

Hsu, H.-H., 1996: Global View of the intraseasonal Oscillation during Northern Winter. *Journal of Climate*, **9 (10)**, 2386–2406, doi: 10.1175/ 1520-0442(1996)009<2386:GVOTIO>2.0.CO;2.

Hsu, H.-H., and M.-Y. Lee, 2005: Topographic Effects on the Eastward Propagation and Initiation of the Madden–Julian Oscillation. *Journal of Climate*, **18 (6)**, 795–809, doi: 10.1175/JCLI-3292.1.

Huang, P., and R. Huang, 2011: Climatology and Interannual Variability of Convectively Coupled Equatorial Waves Activity. *Journal of Climate*, **24 (16)**, 4451–4465, doi: 10.1175/2011JCLI4021.1.

Hubert, H., 1939: Origine africaine d'un cyclone tropical atlantique. *Ann. Phys. France d'Outre-Mer*, **6**, 97–115.

Huffman, G. J., and Coauthors, 2007: The TRMM Multisatellite Precipitation Analysis (TMPA): Quasi-Global, Multiyear, Combined-Sensor Precipitation Estimates at Fine Scales. *Journal of Hydrometeorology*, **8 (1)**, 38–55, doi: 10.1175/JHM560.1.

Ichiye, T., 1959: On long waves in a stratified, equatorial ocean caused by a travelling disturbance. *Deep Sea Research (1953)*, **6**, 16–37, doi: 10.1016/0146-6313(59)90054-1.

ILO, 2019: ILOSTAT website (accessed 22 March 2019). International Labour Organization (ILO), URL https://www.ilo.org/ilostat.

Inness, P. M., and J. M. Slingo, 2006: The interaction of the Madden–Julian Oscillation with the Maritime Continent in a GCM. *Quarterly Journal of the Royal Meteorological Society*, **132 (618)**, 1645–1667, doi: 10.1256/qj.05.102.

Jalloh, A., Ed., 2013: *West African agriculture and climate change: A comprehensive analysis*, IFPRI research monograph, Vol. 178. 1st ed., International Food Policy Research Institute (IFPRI), Washington, DC, 9780896292048.

Janicot, S., F. Mounier, S. Gervois, B. Sultan, and G. N. Kiladis, 2010: The Dynamics of the West African Monsoon. Part V: The Detection and Role of the Dominant Modes of Convectively Coupled Equatorial Rossby Waves. *Journal of Climate*, **23 (14)**, 4005–4024, doi: 10.1175/2010JCLI3221.1.

Janicot, S., F. Mounier, N. M. J. Hall, S. Leroux, B. Sultan, and G. N. Kiladis, 2009: Dynamics of the West African Monsoon. Part IV: Analysis of 25–90-Day Variability of Convection and the Role of the Indian Monsoon. *Journal of Climate*, **22 (6)**, 1541–1565, doi: 10.1175/2008JCLI2314.1.

Janicot, S., and Coauthors, 2011: Intraseasonal variability of the West African monsoon. *Atmospheric Science Letters*, **12 (1)**, 58–66, doi: 10.1002/asl.280.

Janiga, M. A., C. J. Schreck, J. A. Ridout, M. Flatau, N. P. Barton, E. J. Metzger, and C. A. Reynolds, 2018: Subseasonal Forecasts of Convectively Coupled Equatorial Waves and the MJO: Activity and Predictive Skill. *Monthly Weather Review*, **146 (8)**, 2337–2360, doi: 10.1175/MWR-D-17-0261.1.

Janiga, M. A., and C. D. Thorncroft, 2016: The Influence of African Easterly Waves on Convection over Tropical Africa and the East Atlantic. *Monthly Weather Review*, **144 (1)**, 171–192, doi: 10.1175/MWR-D-14-00419.1.

Jensen, N., and C. Barrett, 2016: Agricultural Index Insurance for Development. *Applied Economic Perspectives and Policy*, **97 (2)**, 199–219, doi: 10.1093/aepp/ppw022.

Jiang, X., and Coauthors, 2015: Vertical structure and physical processes of the Madden-Julian oscillation: Exploring key model physics in climate simulations. *Journal of Geophysical Research: Atmospheres*, **120 (10)**, 4718–4748, doi: 10.1002/2014JD022375.

Jiri, O., P. L. Mafongoya, and P. Chivenge, 2015: Indigenous knowledge systems, seasonal 'quality' and climate change adaptation in Zimbabwe. *Climate Research*, **66 (2)**, 103–111, doi: 10.3354/cr01334.

Kadomura, H., 2005: Climate anomalies and extreme events in Africa in 2003, including heavy rains and floods that occured during Northern Hemisphere summer. *African study monographs. Supplementary issue.*, **(30)**, 165–181, doi: 10.14989/68453.

Kaitho, R. J., A. A. Jama, J. W. Stuth, G. Kariuki, A. Abdirahman, L. MacOpiyo, and J. Ndung'u, 2007: Livestock Early Warning Information Resource in the Horn of Africa. *Outlook on Agriculture*, **36 (4)**, 267–272, doi: 10.5367/000000007783418525.

Kasahara, A., and K. Puri, 1981: Spectral Representation of Three-Dimensional Global Data by Expansion in Normal Mode Functions. *Monthly Weather Review*, **109 (1)**, 37–51, doi: 10.1175/1520-0493(1981)109<0037:SROTDG>2.0.CO;2.

Keen, R. A., 1982: The Role of Cross-Equatorial Tropical Cyclone Pairs in the Southern Oscillation. *Monthly Weather Review*, **110 (10)**, 1405–1416, doi: 10.1175/1520-0493(1982)110<1405:TROCET>2.0.CO;2.

Kelley, O. A., 2014: Where the Least Rainfall Occurs in the Sahara Desert, the TRMM Radar Reveals a Different Pattern of Rainfall Each Season. *Journal of Climate*, **27 (18)**, 6919–6939, doi: 10.1175/JCLI-D-14-00145.1.

Kijazi, A. L., L. B. Chang'a, E. T. Liwenga, A. Kanemba, and S. J. Nindi, 2013: The use of indigenous knowledge in weather and climate prediction in Mahenge

and Ismani wards, Tanzania. *Journal of Geography and Regional Planning*, **6 (7)**, 274–279, doi: 10.5897/JGRP2013.0386.

Kikuchi, K., and B. Wang, 2010: Spatiotemporal Wavelet Transform and the Multiscale Behavior of the Madden–Julian Oscillation. *Journal of Climate*, **23 (14)**, 3814–3834, doi: 10.1175/2010JCLI2693.1.

Kiladis, G. N., J. Dias, and M. Gehne, 2016: The Relationship between Equatorial Mixed Rossby–Gravity and Eastward Inertio-Gravity Waves. Part I. *Journal of the Atmospheric Sciences*, **73 (5)**, 2123–2145, doi: 10.1175/JAS-D-15-0230.1.

Kiladis, G. N., J. Dias, K. H. Straub, M. C. Wheeler, S. N. Tulich, K. Kikuchi, K. M. Weickmann, and M. J. Ventrice, 2014: A Comparison of OLR and Circulation-Based Indices for Tracking the MJO. *Monthly Weather Review*, **142 (5)**, 1697–1715, doi: 10.1175/MWR-D-13-00301.1.

Kiladis, G. N., C. D. Thorncroft, and N. M. J. Hall, 2006: Three-Dimensional Structure and Dynamics of African Easterly Waves. Part I: Observations. *Journal of the Atmospheric Sciences*, **63 (9)**, 2212–2230, doi: 10.1175/JAS3741.1.

Kiladis, G. N., and K. M. Weickmann, 1997: Horizontal Structure and Seasonality of Large-Scale Circulations Associated with Submonthly Tropical Convection. *Monthly Weather Review*, **125 (9)**, 1997–2013, doi: 10.1175/ 1520-0493(1997)125<1997:HSASOL>2.0.CO;2.

Kiladis, G. N., and M. C. Wheeler, 1995: Horizontal and vertical structure of observed tropospheric equatorial Rossby waves. *Journal of Geophysical Research*, **100 (D11)**, 22 981, doi: 10.1029/95JD02415.

Kiladis, G. N., M. C. Wheeler, P. T. Haertel, K. H. Straub, and P. E. Roundy, 2009: Convectively coupled equatorial waves. *Reviews of Geophysics*, **47 (2)**, doi: 10.1029/2008RG000266.

Kim, H.-M., 2017: The impact of the mean moisture bias on the key physics of MJO propagation in the ECMWF reforecast. *Journal of Geophysical Research: Atmospheres*, **122 (15)**, 7772–7784, doi: 10.1002/2017JD027005.

Kim, H.-M., D. Kim, F. Vitart, V. E. Toma, J.-S. Kug, and P. J. Webster, 2016: MJO Propagation across the Maritime Continent in the ECMWF Ensemble Prediction System. *Journal of Climate*, **29 (11)**, 3973–3988, doi: 10.1175/ JCLI-D-15-0862.1.

Kim, H.-M., F. Vitart, and D. E. Waliser, 2018: Prediction of the Madden–Julian Oscillation: A Review. *Journal of Climate*, **31 (23)**, 9425–9443, doi: 10.1175/JCLI-D-18-0210.1.

Klar, M., 2017: Statistical forecasts of rain occurrence over West Africa. Master's thesis, Karlsruhe Institute of Technology, Karlsruhe.

Kneubühl, F. K., 1997: *Oscillations and waves: With 16 tables*. Springer, Berlin, ISBN: 3-540-62001-x.

Knippertz, P., 2003: Tropical–Extratropical Interactions Causing Precipitation in Northwest Africa: Statistical Analysis and Seasonal Variations. *Monthly Weather Review*, **131 (12)**, 3069–3076, doi: 10.1175/1520-0493(2003)131<3069:TICPIN>2.0.CO;2.

Knippertz, P., 2007: Tropical–extratropical interactions related to upper-level troughs at low latitudes. *Dynamics of Atmospheres and Oceans*, **43 (1-2)**, 36–62, doi: 10.1016/j.dynatmoce.2006.06.003.

Knippertz, P., A. H. Fink, A. Reiner, and P. Speth, 2003: Three Late Summer/Early Autumn Cases of Tropical–Extratropical Interactions Causing Precipitation in Northwest Africa. *Monthly Weather Review*, **131 (1)**, 116–135, doi: 10.1175/1520-0493(2003)131<0116:TLSEAC>2.0.CO;2.

Knippertz, P., and J. E. Martin, 2005: Tropical plumes and extreme precipitation in subtropical and tropical West Africa. *Quarterly Journal of the Royal Meteorological Society*, **131 (610)**, 2337–2365, doi: 10.1256/qj.04.148.

Knippertz, P., and Coauthors, 2017: A meteorological and chemical overview of the DACCIWA field campaign in West Africa in June–July 2016. *Atmospheric Chemistry and Physics*, **17 (17)**, 10 893–10 918, doi: 10.5194/acp-17-10893-2017.

Knutson, T. R., K. M. Weickmann, and J. E. Kutzbach, 1986: Global-Scale Intraseasonal Oscillations of Outgoing Longwave Radiation and 250 mb Zonal Wind during Northern Hemisphere Summer. *Monthly Weather Review*, **114 (3)**, 605–623, doi: 10.1175/1520-0493(1986)114<0605:GSIOOO>2.0.CO;2.

Kudamatsu, M., T. Persson, and D. Strömberg, 2012: *Weather and infant mortality in Africa*, Discussion paper series / Centre for Economic Policy Research Development economics, Vol. 9222. Centre for Economic Policy Research, London.

Kuettner, J. P., and D. E. Parker, 1976: GARP topics. *Bulletin of the American Meteorological Society*, **57 (1)**, 11–30, doi: 10.1175/1520-0477-57.1.11.

Kundu, P. K., I. M. Cohen, D. R. Dowling, and G. Tryggvason, 2016: *Fluid mechanics*. 6th ed., Elsevier Acad. Press, Amsterdam, ISBN: 9780124059351.

Lafore, J.-P., and Coauthors, 2017: A multi-scale analysis of the extreme rain event of Ouagadougou in 2009. *Quarterly Journal of the Royal Meteorological Society*, **143 (709)**, 3094–3109, doi: 10.1002/qj.3165.

Laing, A. G., R. Carbone, V. Levizzani, and J. Tuttle, 2008: The propagation and diurnal cycles of deep convection in northern tropical Africa. *Quarterly Journal of the Royal Meteorological Society*, **134 (630)**, 93–109, doi: 10.1002/qj.194.

Laing, A. G., R. E. Carbone, and V. Levizzani, 2011: Cycles and Propagation of Deep Convection over Equatorial Africa. *Monthly Weather Review*, **139 (9)**, 2832–2853, doi: 10.1175/2011MWR3500.1.

Laing, A. G., J. M. Fritsch, and A. J. Negri, 1999: Contribution of Mesoscale Convective Complexes to Rainfall in Sahelian Africa: Estimates from Geostationary Infrared and Passive Microwave Data. *Journal of Applied Meteorology*, **38 (7)**, 957–964, doi: 10.1175/1520-0450(1999)038<0957:COMCCT>2.0.CO;2.

Laplace, P. S. d., 2017: *Œuvres Complétes de Laplace: Publiees sous les auspices de l'academie des sciences (classic reprint)*. Forgotten Books, London, United Kingdom, ISBN: 978-0243882083.

Lau, K.-M., and P. H. Chan, 1985: Aspects of the 40–50 Day Oscillation during the Northern Winter as Inferred from Outgoing Longwave Radiation. *Monthly Weather Review*, **113 (11)**, 1889–1909, doi: 10.1175/1520-0493(1985)113<1889:AOTDOD>2.0.CO;2.

Lau, K.-M., and L. Peng, 1987: Origin of Low-Frequency (Intraseasonal) Oscillations in the Tropical Atmosphere. Part I: Basic Theory. *Journal of the Atmospheric Sciences*, **44 (6)**, 950–972, doi: 10.1175/1520-0469(1987)044<0950:OOLFOI>2.0.CO;2.

Lau, W. K.-M., and D. E. Waliser, 2012: *Intraseasonal Variability in the Atmosphere-Ocean Climate System*. Springer Praxis Books, Springer Berlin Heidelberg, Berlin, Heidelberg, ISBN: 978-3-642-13914-7, doi: 10.1007/978-3-642-13914-7.

Lavaysse, C., A. Diedhiou, H. Laurent, and T. Lebel, 2006: African Easterly Waves and convective activity in wet and dry sequences of the West African Monsoon. *Climate Dynamics*, **27 (2-3)**, 319–332, doi: 10.1007/s00382-006-0137-5.

Lavaysse, C., C. Flamant, and S. Janicot, 2010a: Regional-scale convection patterns during strong and weak phases of the Saharan heat low. *Atmospheric Science Letters*, **11 (4)**, 255–264, doi: 10.1002/asl.284.

Lavaysse, C., C. Flamant, S. Janicot, and P. Knippertz, 2010b: Links between African easterly waves, midlatitude circulation and intraseasonal pulsations of the West African heat low. *Quarterly Journal of the Royal Meteorological Society*, **136 (S1)**, 141–158, doi: 10.1002/qj.555.

Lavaysse, C., C. Flamant, S. Janicot, D. J. Parker, J.-P. Lafore, B. Sultan, and J. Pelon, 2009: Seasonal evolution of the West African heat low: a climatological perspective. *Climate Dynamics*, **33 (2-3)**, 313–330, doi: 10.1007/s00382-009-0553-4.

Lavender, S. L., and A. J. Matthews, 2009: Response of the West African Monsoon to the Madden–Julian Oscillation. *Journal of Climate*, **22 (15)**, 4097–4116, doi: 10.1175/2009JCLI2773.1.

Lavender, S. L., C. M. Taylor, and A. J. Matthews, 2010: Coupled Land–Atmosphere Intraseasonal Variability of the West African Monsoon in a GCM. *Journal of Climate*, **23 (21)**, 5557–5571, doi: 10.1175/2010JCLI3419.1.

Lee, T. S., 1996: Image representation using 2D Gabor wavelets. *IEEE Transactions on Pattern Analysis and Machine Intelligence*, **18 (10)**, 959–971, doi: 10.1109/34.541406.

Lélé, I. M., and P. J. Lamb, 2010: Variability of the Intertropical Front (ITF) and Rainfall over the West African Sudan–Sahel Zone. *Journal of Climate*, **23 (14)**, 3984–4004, doi: 10.1175/2010JCLI3277.1.

Lenton, T. M., 2013: What early warning systems are there for environmental shocks? *Environmental Science & Policy*, **27**, S60–S75, doi: 10.1016/j.envsci.2012.06.011.

Leroux, S., N. M. J. Hall, and G. N. Kiladis, 2010: A climatological study of transient-mean-flow interactions over West Africa. *Quarterly Journal of the Royal Meteorological Society*, **136 (S1)**, 397–410, doi: 10.1002/qj.474.

166

Leroux, S., N. M. J. Hall, and G. N. Kiladis, 2011: Intermittent African Easterly Wave Activity in a Dry Atmospheric Model: Influence of the Extratropics. *Journal of Climate*, **24 (20)**, 5378–5396, doi: 10.1175/JCLI-D-11-00049.1.

Lewis, J. M., 2005: Roots of Ensemble Forecasting. *Monthly Weather Review*, **133 (7)**, 1865–1885, doi: 10.1175/MWR2949.1.

L'Heureux, M. L., and R. W. Higgins, 2008: Boreal Winter Links between the Madden–Julian Oscillation and the Arctic Oscillation. *Journal of Climate*, **21 (12)**, 3040–3050, doi: 10.1175/2007JCLI1955.1.

Li, S., and A. W. Robertson, 2015: Evaluation of Submonthly Precipitation Forecast Skill from Global Ensemble Prediction Systems. *Monthly Weather Review*, **143 (7)**, 2871–2889, doi: 10.1175/MWR-D-14-00277.1.

Liebmann, B., and C. A. Smith, 1996: Description of a Complete (Interpolated) Outgoing Longwave Radiation Dataset. *Bulletin of the American Meteorological Society*, **(77)**, 1275–1277.

Lin, H., G. Brunet, and J. Derome, 2009: An Observed Connection between the North Atlantic Oscillation and the Madden–Julian Oscillation. *Journal of Climate*, **22 (2)**, 364–380, doi: 10.1175/2008JCLI2515.1.

Lin, J.-L., M.-I. Lee, D. Kim, I.-S. Kang, and D. M. W. Frierson, 2008: The Impacts of Convective Parameterization and Moisture Triggering on AGCM-Simulated Convectively Coupled Equatorial Waves. *Journal of Climate*, **21 (5)**, 883–909, doi: 10.1175/2007JCLI1790.1.

Littell, J. S., D. L. Peterson, K. L. Riley, Y. Liu, and C. H. Luce, 2016: A review of the relationships between drought and forest fire in the United States. *Global change biology*, **22 (7)**, 2353–2369, doi: 10.1111/gcb.13275.

Liu, P., Q. Zhang, C. Zhang, Y. Zhu, M. Khairoutdinov, H.-M. Kim, C. Schumacher, and M. Zhang, 2016: A Revised Real-Time Multivariate MJO Index. *Monthly Weather Review*, **144 (2)**, 627–642, doi: 10.1175/MWR-D-15-0237.1.

Liu, X., and Coauthors, 2017: MJO prediction using the sub-seasonal to seasonal forecast model of Beijing Climate Center. *Climate Dynamics*, **48 (9-10)**, 3283–3307, doi: 10.1007/s00382-016-3264-7.

Longuet-Higgins, M. S., 1968: The Eigenfunctions of Laplace's Tidal Equations over a Sphere. *Philosophical Transactions of the Royal Society A: Mathematical,*

Physical and Engineering Sciences, **262 (1132)**, 511–607, doi: 10.1098/rsta. 1968.0003.

Lorenz, E. N., 1963: Deterministic Nonperiodic Flow. *Journal of the Atmospheric Sciences*, **20 (2)**, 130–141, doi: 10.1175/1520-0469(1963)020<0130: DNF>2.0.CO;2.

Lorenz, E. N., 1982: Atmospheric predictability experiments with a large numerical model. *Tellus*, **34 (6)**, 505–513, doi: 10.3402/tellusa.v34i6.10836.

Louvet, S., B. Sultan, S. Janicot, P. H. Kamsu-Tamo, and O. Ndiaye, 2016: Evaluation of TIGGE precipitation forecasts over West Africa at intraseasonal timescale. *Climate Dynamics*, **47 (1-2)**, 31–47, doi: 10.1007/ s00382-015-2820-x.

Lubis, S. W., and C. Jacobi, 2015: The modulating influence of convectively coupled equatorial waves (CCEWs) on the variability of tropical precipitation. *International Journal of Climatology*, **35 (7)**, 1465–1483, doi: 10.1002/joc. 4069.

Lukens, K. E., S. B. Feldstein, C. Yoo, and S. Lee, 2017: The dynamics of the extratropical response to Madden-Julian Oscillation convection. *Quarterly Journal of the Royal Meteorological Society*, **143 (703)**, 1095–1106, doi: 10. 1002/qj.2993.

Lyons, S. W., 1991: Origins of Convective Variability over Equatorial Southern Africa during Austral Summer. *Journal of Climate*, **4 (1)**, 23–39, doi: 10.1175/ 1520-0442(1991)004<0023:OOCVOE>2.0.CO;2.

Macdonald, R. B., and F. G. Hall, 1980: Global crop forecasting. *Science*, **208 (4445)**, 670–679, doi: 10.1126/science.208.4445.670.

Macron, C., B. Pohl, Y. Richard, and M. Bessafi, 2014: How do Tropical Temperate Troughs Form and Develop over Southern Africa? *Journal of Climate*, **27 (4)**, 1633–1647, doi: 10.1175/JCLI-D-13-00175.1.

Madden, R. A., and P. R. Julian, 1971: Detection of a 40–50 Day Oscillation in the Zonal Wind in the Tropical Pacific. *Journal of the Atmospheric Sciences*, **28 (5)**, 702–708, doi: 10.1175/1520-0469(1971)028<0702:DOADOI>2.0.CO;2.

Madden, R. A., and P. R. Julian, 1972: Description of Global-Scale Circulation Cells in the Tropics with a 40–50 Day Period. *Journal of the Atmospheric*

Sciences, **29 (6)**, 1109–1123, doi: 10.1175/1520-0469(1972)029<1109: DOGSCC>2.0.CO;2.

Madden, R. A., and P. R. Julian, 1994: Observations of the 40–50-Day Tropical Oscillation—A Review. *Monthly Weather Review*, **122 (5)**, 814–837, doi: 10. 1175/1520-0493(1994)122<0814:OOTDTO>2.0.CO;2.

Magaña, V., and M. Yanai, 1995: Mixed Rossby–Gravity Waves Triggered by Lateral Forcing. *Journal of the Atmospheric Sciences*, **52 (9)**, 1473–1486, doi: 10.1175/1520-0469(1995)052<1473:MRWTBL>2.0.CO;2.

Maggioni, V., P. C. Meyers, and M. D. Robinson, 2016: A Review of Merged High-Resolution Satellite Precipitation Product Accuracy during the Tropical Rainfall Measuring Mission (TRMM) Era. *Journal of Hydrometeorology*, **17 (4)**, 1101–1117, doi: 10.1175/JHM-D-15-0190.1.

Malhi, Y., S. Adu-Bredu, R. A. Asare, S. L. Lewis, and P. Mayaux, 2013: African rainforests: past, present and future. *Philosophical transactions of the Royal Society of London. Series B, Biological sciences*, **368 (1625)**, 20120 312, doi: 10.1098/rstb.2012.0312.

Manhique, A. J., C. J. C. Reason, L. Rydberg, and N. Fauchereau, 2011: ENSO and Indian Ocean sea surface temperatures and their relationships with tropical temperate troughs over Mozambique and the Southwest Indian Ocean. *International Journal of Climatology*, **31 (1)**, 1–13, doi: 10.1002/joc.2050.

Mapes, B. E., 2000: Convective Inhibition, Subgrid-Scale Triggering Energy, and Stratiform Instability in a Toy Tropical Wave Model. *Journal of the Atmospheric Sciences*, **57 (10)**, 1515–1535, doi: 10.1175/1520-0469(2000)057<1515: CISSTE>2.0.CO;2.

Mapes, B. E., S. N. Tulich, J.-L. Lin, and P. Zuidema, 2006: The mesoscale convection life cycle: Building block or prototype for large-scale tropical waves? *Dynamics of Atmospheres and Oceans*, **42 (1-4)**, 3–29, doi: 10.1016/j. dynatmoce.2006.03.003.

Maranan, M., A. H. Fink, and P. Knippertz, 2018: Rainfall types over southern West Africa: Objective identification, climatology and synoptic environment. *Quarterly Journal of the Royal Meteorological Society*, doi: 10.1002/qj.3345.

Mathon, V., H. Laurent, and T. Lebel, 2002: Mesoscale Convective System Rainfall in the Sahel. *Journal of Applied Meteorology*, **41 (11)**, 1081–1092, doi: 10.1175/1520-0450(2002)041<1081:MCSRIT>2.0.CO;2.

Matsuno, T., 1966: Quasi-geostrophic motions in the equatorial area. *Journal of the Meteorological Society of Japan*, **44 (1966)**, 25–44, doi: 10.2151/jmsj1965.44.1_25.

Matthews, A. J., 2000: Propagation mechanisms for the Madden-Julian Oscillation. *Quarterly Journal of the Royal Meteorological Society*, **126 (569)**, 2637–2651, doi: 10.1002/qj.49712656902.

Matthews, A. J., 2004: Intraseasonal Variability over Tropical Africa during Northern Summer. *Journal of Climate*, **17 (12)**, 2427–2440, doi: 10.1175/1520-0442(2004)017<2427:IVOTAD>2.0.CO;2.

Mayr, H. G., J. G. Mengel, E. R. Talaat, H. S. Porter, and K. L. Chan, 2003: Planetary-scale inertio gravity waves in the Mesosphere. *Geophysical Research Letters*, **30 (23)**, 2228, doi: 10.1029/2003GL018376.

Mayr, H. G., J. G. Mengel, E. R. Talaat, H. S. Porter, and K. L. Chan, 2004: Properties of internal planetary-scale inertio gravity waves in the mesosphere. *Annales Geophysicae*, **22 (10)**, 3421–3435, doi: 10.5194/angeo-22-3421-2004.

McGuirk, J. P., and D. J. Ulsh, 1990: Evolution of Tropical Plumes in VAS Water Vapor Imagery. *Monthly Weather Review*, **118 (9)**, 1758–1766, doi: 10.1175/1520-0493(1990)118<1758:EOTPIV>2.0.CO;2.

McKee, T., N. Doesken, and J. Kleist, 1993: The relationship of drought frequency and duration to time scales. *Proceedings of the 8th Conference on Applied Climatology*, Vol. 17, No. 22, American Meteorological Society, Boston, MA, 179–183.

Meinke, H., and R. C. Stone, 2005: Seasonal and Inter-Annual Climate Forecasting: The New Tool for Increasing Preparedness to Climate Variability and Change in Agricultural Planning and Operations. *Increasing Climate Variability and Change: Reducing the Vulnerability of Agriculture and Forestry*, J. Salinger, M. Sivakumar, and R. P. Motha, Eds., Springer Netherlands, Dordrecht, ISBN: 978-1-4020-4166-2, 221–253, doi: 10.1007/1-4020-4166-7_11.

Mekonnen, A., and C. D. Thorncroft, 2016: On mechanisms that determine synoptic time scale convection over East Africa. *International Journal of Climatology*, **36 (12)**, 4045–4057, doi: 10.1002/joc.4614.

Mekonnen, A., C. D. Thorncroft, and A. R. Aiyyer, 2006: Analysis of Convection and Its Association with African Easterly Waves. *Journal of Climate*, **19 (20)**, 5405–5421, doi: 10.1175/JCLI3920.1.

Mekonnen, A., C. D. Thorncroft, A. R. Aiyyer, and G. N. Kiladis, 2008: Convectively Coupled Kelvin Waves over Tropical Africa during the Boreal Summer: Structure and Variability. *Journal of Climate*, **21 (24)**, 6649–6667, doi: 10.1175/2008JCLI2008.1.

Meynadier, R., O. Bock, F. Guichard, A. Boone, P. Roucou, and J.-L. Redelsperger, 2010: West African Monsoon water cycle: 1. A hybrid water budget data set. *Journal of Geophysical Research*, **115 (D19)**, 1705, doi: 10.1029/2010JD013917.

Milliff, R. F., and R. A. Madden, 1996: The Existence and Vertical Structure of Fast, Eastward-Moving Disturbances in the Equatorial Troposphere. *Journal of the Atmospheric Sciences*, **53 (4)**, 586–597, doi: 10.1175/1520-0469(1996) 053<0586:TEAVSO>2.0.CO;2.

Moncrieff, M. W., and M. J. Miller, 1976: The dynamics and simulation of tropical cumulonimbus and squall lines. *Quarterly Journal of the Royal Meteorological Society*, **102 (432)**, 373–394, doi: 10.1002/qj.49710243208.

Moore, S. M., A. Monaghan, K. S. Griffith, T. Apangu, P. S. Mead, and R. J. Eisen, 2012: Improvement of disease prediction and modeling through the use of meteorological ensembles: human plague in Uganda. *PloS one*, **7 (9)**, e44 431, doi: 10.1371/journal.pone.0044431.

Mori, M., and M. Watanabe, 2008: The Growth and Triggering Mechanisms of the PNA: A MJO-PNA Coherence. *Journal of the Meteorological Society of Japan*, **86 (1)**, 213–236, doi: 10.2151/jmsj.86.213.

Mounier, F., 2004: Evidence of two independent modes of convection at intraseasonal timescale in the West African summer monsoon. *Geophysical Research Letters*, **31 (16)**, 245, doi: 10.1029/2004GL020665.

Mounier, F., S. Janicot, and G. N. Kiladis, 2008: The West African Monsoon Dynamics. Part III: The Quasi-Biweekly Zonal Dipole. *Journal of Climate*, **21 (9)**, 1911–1928, doi: 10.1175/2007JCLI1706.1.

Mounier, F., G. N. Kiladis, and S. Janicot, 2007: Analysis of the Dominant Mode of Convectively Coupled Kelvin Waves in the West African Monsoon. *Journal of Climate*, **20 (8)**, 1487–1503, doi: 10.1175/JCLI4059.1.

Mozer, J. B., and J. A. Zehnder, 1996: Lee vorticity Production by Large-Scale Tropical Mountain Ranges. Part II: A Mechanism for the Production of African Waves. *Journal of the Atmospheric Sciences*, **53 (4)**, 539–549, doi: 10.1175/1520-0469(1996)053<0539:LVPBLS>2.0.CO;2.

Murakami, T., L.-X. Chen, A. Xie, and M. L. Shrestha, 1986: Eastward Propagation of 30–60 Day Perturbations as Revealed from Outgoing Longwave Radiation Data. *Journal of the Atmospheric Sciences*, **43 (10)**, 961–971, doi: 10.1175/1520-0469(1986)043<0961:EPODPA>2.0.CO;2.

Neelin, J. D., and I. M. Held, 1987: Modeling Tropical Convergence Based on the Moist Static Energy Budget. *Monthly Weather Review*, **115 (1)**, 3–12, doi: 10.1175/1520-0493(1987)115<0003:MTCBOT>2.0.CO;2.

Neena, J. M., J. Y. Lee, D. E. Waliser, B. Wang, and X. Jiang, 2014: Predictability of the Madden–Julian Oscillation in the Intraseasonal Variability Hindcast Experiment (ISVHE). *Journal of Climate*, **27 (12)**, 4531–4543, doi: 10.1175/JCLI-D-13-00624.1.

Nettel, S., 2003: *Wave physics: Oscillations - solitons - chaos ; with more than 100 problems with hints for solution and numerous examples*. 3rd ed., Physics and astronomy online library, Springer, Berlin, ISBN: 3-540-44314-2.

Nguyen, H., and J.-P. Duvel, 2008: Synoptic Wave Perturbations and Convective Systems over Equatorial Africa. *Journal of Climate*, **21 (23)**, 6372–6388, doi: 10.1175/2008JCLI2409.1.

Nicholls, S. D., and K. I. Mohr, 2010: An Analysis of the Environments of Intense Convective Systems in West Africa in 2003. *Monthly Weather Review*, **138 (10)**, 3721–3739, doi: 10.1175/2010MWR3321.1.

Nicholson, S. E., 2008: The intensity, location and structure of the tropical rainbelt over west Africa as factors in interannual variability. *International Journal of Climatology*, **28 (13)**, 1775–1785, doi: 10.1002/joc.1507.

Nicholson, S. E., 2017: Climatology: Methods. *Oxford Research Encyclopedia of African History*, doi: 10.1093/acrefore/9780190277734.013.27.

Nicholson, S. E., 2018: Climate of the Sahel and West Africa. *Oxford Research Encyclopedia of Climate Science: Climate of Africa*, doi: 10.1093/acrefore/9780190228620.013.510.

Nicholson, S. E., C. Funk, and A. H. Fink, 2018: Rainfall over the African continent from the 19th through the 21st century. *Global and Planetary Change*, **165**, 114–127, doi: 10.1016/j.gloplacha.2017.12.014.

Nicholson, S. E., and J. P. Grist, 2001: A conceptual model for understanding rainfall variability in the West African Sahel on interannual and interdecadal timescales. *International Journal of Climatology*, **21 (14)**, 1733–1757, doi: 10.1002/joc.648.

Nicholson, S. E., D. Klotter, and A. K. Dezfuli, 2012: Spatial reconstruction of semi-quantitative precipitation fields over Africa during the nineteenth century from documentary evidence and gauge data. *Quaternary Research*, **78 (1)**, 13–23, doi: 10.1016/j.yqres.2012.03.012.

NOAA, 1988: 5-minute Gridded Global Relief Data (ETOPO5): National Geophysical Data Center, NOAA. doi: 10.7289/V5D798BF.

Opsteegh, J. D., and H. M. van den Dool, 1980: Seasonal Differences in the Stationary Response of a Linearized Primitive Equation Model: Prospects for Long-Range Weather Forecasting? *Journal of the Atmospheric Sciences*, **37 (10)**, 2169–2185, doi: 10.1175/1520-0469(1980)037<2169:SDITSR>2.0.CO;2.

Palmén, E., 1949: Origin and Structure of High-Level Cyclones South of the: Maximum Westerlies. *Tellus*, **1 (1)**, 22–31, doi: 10.1111/j.2153-3490.1949.tb01925.x.

Palmer, T. N., 2018: The ECMWF ensemble prediction system: Looking back (more than) 25 years and projecting forward 25 years. *Quarterly Journal of the Royal Meteorological Society*, **125 (2188)**, 2333, doi: 10.1002/qj.3383.

Palmer, T. N., F. J. Doblas-Reyes, A. Weisheimer, and M. J. Rodwell, 2008: Toward Seamless Prediction: Calibration of Climate Change Projections Using Seasonal Forecasts. *Bulletin of the American Meteorological Society*, **89 (4)**, 459–470, doi: 10.1175/BAMS-89-4-459.

Parker, D. J., and Coauthors, 2008: The Amma Radiosonde Program and its Implications for the Future of Atmospheric Monitoring Over Africa. *Bulletin of the American Meteorological Society*, **89 (7)**, 1015–1028, doi: 10.1175/2008BAMS2436.1.

Peatman, S. C., A. J. Matthews, and D. P. Stevens, 2014: Propagation of the Madden-Julian Oscillation through the Maritime Continent and scale interaction with the diurnal cycle of precipitation. *Quarterly Journal of the Royal Meteorological Society*, **140 (680)**, 814–825, doi: 10.1002/qj.2161.

Piersig, W., 1936: Schwankungen von Luftdruck und Luftbewegung sowie ein Beitrag zum Wettergeschehen im Passatgebiet des östlichen Nordatlantischen Ozeans. *Archiv der Deutschen Seewarte*, **54 (6)**.

Piersig, W., 1944: The Cyclonic Disturbances of the Sub-Tropical Eastern North Atlantic. *Bulletin of the American Meteorological Society*, **25 (1)**, 2–16, doi: 10.1175/1520-0477-25.1.2.

Plougonven, R., and F. Zhang, 2007: On the Forcing of Inertia–Gravity Waves by Synoptic-Scale Flows. *Journal of the Atmospheric Sciences*, **64 (5)**, 1737–1742, doi: 10.1175/JAS3901.1.

Pohl, B., and P. Camberlin, 2006a: Influence of the Madden–Julian Oscillation on East African rainfall. I: Intraseasonal variability and regional dependency. *Quarterly Journal of the Royal Meteorological Society*, **132 (621)**, 2521–2539, doi: 10.1256/qj.05.104.

Pohl, B., and P. Camberlin, 2006b: Influence of the Madden–Julian Oscillation on East African rainfall: II. March–May season extremes and interannual variability. *Quarterly Journal of the Royal Meteorological Society*, **132 (621)**, 2541–2558, doi: 10.1256/qj.05.223.

Pohl, B., N. Fauchereau, Y. Richard, M. Rouault, and C. J. C. Reason, 2009a: Interactions between synoptic, intraseasonal and interannual convective variability over Southern Africa. *Climate Dynamics*, **33 (7-8)**, 1033–1050, doi: 10.1007/s00382-008-0485-4.

Pohl, B., S. Janicot, B. Fontaine, and R. Marteau, 2009b: Implication of the Madden–Julian Oscillation in the 40-Day Variability of the West African Monsoon. *Journal of Climate*, **22 (13)**, 3769–3785, doi: 10.1175/2009JCLI2805.1.

Pohl, B., Y. Richard, and N. Fauchereau, 2007: Influence of the Madden–Julian Oscillation on Southern African Summer Rainfall. *Journal of Climate*, **20 (16)**, 4227–4242, doi: 10.1175/JCLI4231.1.

Powell, S. W., 2017: Successive MJO propagation in MERRA-2 reanalysis. *Geophysical Research Letters*, **44 (10)**, 5178–5186, doi: 10.1002/2017GL073399.

Precipitation Processing System (PPS) at NASA GSFC, 2018: TRMM (TMPA) Rainfall Estimate L3 3 hour 0.25 degree x 0.25 degree V7. doi: 10.5067/TRMM/TMPA/3H/7.

Pytharoulis, I., and C. D. Thorncroft, 1999: The Low-Level Structure of African Easterly Waves in 1995. *Monthly Weather Review*, **127 (10)**, 2266–2280, doi: 10.1175/1520-0493(1999)127<2266:TLLSOA>2.0.CO;2.

Rautenhaus, M., M. Kern, A. Schäfler, and R. Westermann, 2015: Three-dimensional visualization of ensemble weather forecasts – Part 1: The visualization tool Met.3D (version 1.0). *Geoscientific Model Development*, **8 (7)**, 2329–2353, doi: 10.5194/gmd-8-2329-2015.

Raveh-Rubin, S., 2017: Dry Intrusions: Lagrangian Climatology and Dynamical Impact on the Planetary Boundary Layer. *Journal of Climate*, **30 (17)**, 6661–6682, doi: 10.1175/JCLI-D-16-0782.1.

Raymond, D. J., 2001: A New Model of the Madden–Julian Oscillation. *Journal of the Atmospheric Sciences*, **58 (18)**, 2807–2819, doi: 10.1175/1520-0469(2001)058<2807:ANMOTM>2.0.CO;2.

Raymond, D. J., and H. Jiang, 1990: A Theory for Long-Lived Mesoscale Convective Systems. *Journal of the Atmospheric Sciences*, **47 (24)**, 3067–3077, doi: 10.1175/1520-0469(1990)047<3067:ATFLLM>2.0.CO;2.

Reason, C. J. C., 2017: Climate of Southern Africa. *Oxford Research Encyclopedia of Climate Science: Climate of Africa*, doi: 10.1093/acrefore/9780190228620.013.513.

Redelsperger, J.-L., C. D. Thorncroft, A. Diedhiou, T. Lebel, D. J. Parker, and J. Polcher, 2006: African Monsoon Multidisciplinary Analysis: An International Research Project and Field Campaign. *Bulletin of the American Meteorological Society*, **87 (12)**, 1739–1746, doi: 10.1175/BAMS-87-12-1739.

Reed, R. J., D. C. Norquist, and E. E. Recker, 1977: The Structure and Properties of African Wave Disturbances as Observed During Phase III of GATE. *Monthly Weather Review*, **105 (3)**, 317–333, doi: 10.1175/1520-0493(1977)105<0317:TSAPOA>2.0.CO;2.

Regula, H., 1936: Druckschwankungen und Tornados an der Westküste von Afrika. *Ann. Hydrogr. Maritimem Meteor.*, **64**, 107–111.

Riehl, H., 1945: *Waves in the easterlies and the polar front in the tropics*, Miscellaneous reports / Department of Meteorology of the University of Chicago, Vol. no. 17. 2nd ed., The University of Chicago Press, Chicago, Ill.

Riehl, H., 1950: On the Role of the Tropics in the General Circulation of the Atmosphere. *Tellus*, **2 (1)**, 1–17, doi: 10.3402/tellusa.v2i1.8531.

Riley, E. M., B. E. Mapes, and S. N. Tulich, 2011: Clouds Associated with the Madden–Julian Oscillation: A New Perspective from CloudSat. *Journal of the Atmospheric Sciences*, **68 (12)**, 3032–3051, doi: 10.1175/JAS-D-11-030.1.

Roberts, A. J., J. H. Marsham, and P. Knippertz, 2015: Disagreements in Low-Level Moisture between (Re)Analyses over Summertime West Africa. *Monthly Weather Review*, **143 (4)**, 1193–1211, doi: 10.1175/MWR-D-14-00218.1.

Roca, R., J.-P. Lafore, C. Piriou, and J.-L. Redelsperger, 2005: Extratropical Dry-Air Intrusions into the West African Monsoon Midtroposphere: An Important Factor for the Convective Activity over the Sahel. *Journal of the Atmospheric Sciences*, **62 (2)**, 390–407, doi: 10.1175/JAS-3366.1.

Rodwell, M. J., and B. J. Hoskins, 1996: Monsoons and the dynamics of deserts. *Quarterly Journal of the Royal Meteorological Society*, **122 (534)**, 1385–1404, doi: 10.1002/qj.49712253408.

Roehrig, R., F. Chauvin, and J.-P. Lafore, 2011: 10–25-Day Intraseasonal Variability of Convection over the Sahel: A Role of the Saharan Heat Low and Midlatitudes. *Journal of Climate*, **24 (22)**, 5863–5878, doi: 10.1175/2011JCLI3960.1.

Roncoli, C., K. Ingram, and P. Kirshen, 2002: Reading the Rains: Local Knowledge and Rainfall Forecasting in Burkina Faso. *Society & Natural Resources*, **15 (5)**, 409–427, doi: 10.1080/08941920252866774.

Rosenzweig, M. R., and C. Udry, 2014: Rainfall Forecasts, Weather, and Wages over the Agricultural Production Cycle. *American Economic Review*, **104 (5)**, 278–283, doi: 10.1257/aer.104.5.278.

Rossby, C. G., and collaborators, 1939: Relation between variations in the intensity of zonal circulation of the atmosphere and the displacements of the semi-permanent centers of action. *Journal of Marine Research*, **2 (1)**, 38–55.

Rotunno, R., J. B. Klemp, and M. L. Weisman, 1988: A Theory for Strong, Long-Lived Squall Lines. *Journal of the Atmospheric Sciences*, **45 (3)**, 463–485, doi: 10.1175/1520-0469(1988)045<0463:ATFSLL>2.0.CO;2.

Roundy, P. E., 2012: Observed Structure of Convectively Coupled Waves as a Function of Equivalent Depth: Kelvin Waves and the Madden–Julian Oscillation. *Journal of the Atmospheric Sciences*, **69 (7)**, 2097–2106, doi: 10.1175/ JAS-D-12-03.1.

Roundy, P. E., 2018: A wave-number frequency wavelet analysis of convectively coupled equatorial waves and the MJO over the Indian Ocean. *Quarterly Journal of the Royal Meteorological Society*, **72**, 3755, doi: 10.1002/qj.3207.

Roundy, P. E., and W. M. Frank, 2004: A Climatology of Waves in the Equatorial Region. *Journal of the Atmospheric Sciences*, **61 (17)**, 2105–2132, doi: 10. 1175/1520-0469(2004)061<2105:ACOWIT>2.0.CO;2.

Roundy, P. E., and M. A. Janiga, 2012: Analysis of vertically propagating convectively coupled equatorial waves using observations and a non-hydrostatic Boussinesq model on the equatorial beta-plane. *Quarterly Journal of the Royal Meteorological Society*, **138 (665)**, 1004–1017, doi: 10.1002/qj.983.

Roundy, P. E., C. J. Schreck, and M. A. Janiga, 2009: Contributions of Convectively Coupled Equatorial Rossby Waves and Kelvin Waves to the Real-Time Multivariate MJO Indices. *Monthly Weather Review*, **137 (1)**, 469–478, doi: 10.1175/2008MWR2595.1.

Saji, N. H., B. N. Goswami, P. N. Vinayachandran, and T. Yamagata, 1999: A dipole mode in the tropical Indian Ocean. *Nature*, **401 (6751)**, 360–363, doi: 10.1038/43854.

Sakaeda, N., G. N. Kiladis, and J. Dias, 2017: The Diurnal Cycle of Tropical Cloudiness and Rainfall Associated with the Madden–Julian Oscillation. *Journal of Climate*, **30 (11)**, 3999–4020, doi: 10.1175/JCLI-D-16-0788.1.

Salby, M. L., and R. R. Garcia, 1987: Transient Response to Localized Episodic Heating in the Tropics. Part I: Excitation and Short-Time Near-Field Behavior. *Journal of the Atmospheric Sciences*, **44 (2)**, 458–498, doi: 10.1175/ 1520-0469(1987)044<0458:TRTLEH>2.0.CO;2.

Sanni, S. A., K. O. Oluwasemire, and N. O. Nnoli, 2012: Traditional capacity for weather prediction, variability and coping strategies in the front line states of nigeria. *Agricultural Sciences*, **03 (04)**, 625–630, doi: 10.4236/as.2012.34075.

Scheffer, M., and Coauthors, 2009: Early-warning signals for critical transitions. *Nature*, **461 (7260)**, 53–59, doi: 10.1038/nature08227.

Schlueter, A., 2019: Synoptic to intraseasonal variability of African rainfall (under review). *Oxford Research Encyclopedia of Climate Science: Climate of Africa*.

Schlueter, A., A. H. Fink, and P. Knippertz, 2019b: A Systematic Comparison of Tropical Waves over Northern Africa. Part II: Dynamics and Thermodynamics. *Journal of Climate*, doi: 10.1175/JCLI-D-18-0651.1.

Schlueter, A., A. H. Fink, P. Knippertz, and P. Vogel, 2019a: A Systematic Comparison of Tropical Waves over Northern Africa. Part I: Influence on Rainfall. *Journal of Climate*, **32 (5)**, 1501–1523, doi: 10.1175/ JCLI-D-18-0173.1.

Schrage, J. M., A. H. Fink, V. Ermert, and E. D. Ahlonsou, 2006: Three MCS Cases Occurring in Different Synoptic Environments in the Sub-Sahelian Wet Zone during the 2002 West African Monsoon. *Journal of the Atmospheric Sciences*, **63 (9)**, 2369–2382, doi: 10.1175/JAS3757.1.

Schreck, C. J., J. Molinari, and K. I. Mohr, 2011: Attributing Tropical Cyclogenesis to Equatorial Waves in the Western North Pacific. *Journal of the Atmospheric Sciences*, **68 (2)**, 195–209, doi: 10.1175/2010JAS3396.1.

Schreck, C. J., L. Shi, J. P. Kossin, and J. J. Bates, 2013: Identifying the MJO, Equatorial Waves, and Their Impacts Using 32 Years of HIRS Upper-Tropospheric Water Vapor. *Journal of Climate*, **26 (4)**, 1418–1431, doi: 10. 1175/JCLI-D-12-00034.1.

Schubert, W. H., E. Ruprecht, R. Hertenstein, R. N. Ferreira, R. Taft, C. Rozoff, P. Ciesielski, and H.-C. Kuo, 2004: English translations of twenty-one of Ertel's papers on geophysical fluid dynamics. *Meteorologische Zeitschrift*, **13 (6)**, 527–576, doi: 10.1127/0941-2948/2004/0013-0527.

Semunegus, H., A. Mekonnen, and C. J. Schreck, 2017: Characterization of convective systems and their association with African easterly waves. *International Journal of Climatology*, **37 (12)**, 4486–4492, doi: 10.1002/joc. 5085.

Seo, K.-H., and H.-J. Lee, 2017: Mechanisms for a PNA-Like Teleconnection Pattern in Response to the MJO. *Journal of the Atmospheric Sciences*, **74 (6)**, 1767–1781, doi: 10.1175/JAS-D-16-0343.1.

Shi, X., Z. Gao, L. Lausen, H. Wang, D.-Y. Yeung, W.-k. Wong, and W.-c. Woo, 2017: Deep learning for precipitation nowcasting: A benchmark and a new model. *Advances in Neural Information Processing Systems*, 5617–5627.

Shoko, K., and N. Shoko, 2013: Indigenous Weather Forecasting Systems: A Case Study of the Abiotic Weather Forecasting Indicators for Wards 12 and 13 in Mberengwa District Zimbabwe. *Asian Social Science*, **9 (5)**, doi: 10.5539/ass.v9n5p285.

Sinclaire, Z., A. Lenouo, C. Tchawoua, and S. Janicot, 2015: Synoptic Kelvin type perturbation waves over Congo basin over the period 1979–2010. *Journal of Atmospheric and Solar-Terrestrial Physics*, **130-131**, 43–56, doi: 10.1016/j.jastp.2015.04.015.

Skinner, C. B., and N. S. Diffenbaugh, 2013: The contribution of African easterly waves to monsoon precipitation in the CMIP3 ensemble. *Journal of Geophysical Research: Atmospheres*, **118 (9)**, 3590–3609, doi: 10.1002/jgrd.50363.

Skofronick-Jackson, G., and Coauthors, 2017: The Global Precipitation Measurement (GPM) Mission for Science and Society. *Bulletin of the American Meteorological Society*, **98 (8)**, 1679–1695, doi: 10.1175/BAMS-D-15-00306.1.

Staal, A., S. C. Dekker, M. Hirota, and E. H. van Nes, 2015: Synergistic effects of drought and deforestation on the resilience of the south-eastern Amazon rainforest. *Ecological Complexity*, **22**, 65–75, doi: 10.1016/j.ecocom.2015.01.003.

Stan, C., D. M. Straus, J. S. Frederiksen, H. Lin, E. D. Maloney, and C. Schumacher, 2017: Review of Tropical-Extratropical Teleconnections on Intraseasonal Time Scales. *Reviews of Geophysics*, **55 (4)**, 902–937, doi: 10.1002/2016RG000538.

Stephens, E. M., T. L. Edwards, and D. Demeritt, 2012: Communicating probabilistic information from climate model ensembles-lessons from numerical weather prediction. *Wiley Interdisciplinary Reviews: Climate Change*, **3 (5)**, 409–426, doi: 10.1002/wcc.187.

Stern, M. E., 1963: Trapping of Low Frequency Oscillations in an Equatorial "Boundary Layer". *Tellus*, **15 (3)**, 246–250, doi: 10.1111/j.2153-3490.1963.tb01384.x.

Straub, K. H., and G. N. Kiladis, 2003: Extratropical Forcing of Convectively Coupled Kelvin Waves during Austral Winter. *Journal of the Atmospheric Sciences*, **60 (3)**, 526–543, doi: 10.1175/1520-0469(2003)060<0526: EFOCCK>2.0.CO;2.

Sultan, B., S. Janicot, and C. Correia, 2009: Medium Lead-Time Predictability of Intraseasonal Variability of Rainfall in West Africa. *Weather and Forecasting*, **24 (3)**, 767–784, doi: 10.1175/2008WAF2222155.1.

Sultan, B., S. Janicot, and A. Diedhiou, 2003: The West African Monsoon Dynamics. Part I: Documentation of Intraseasonal Variability. *Journal of Climate*, **16 (21)**, 3389–3406, doi: 10.1175/1520-0442(2003)016<3389: TWAMDP>2.0.CO;2.

Sun, Y. Q., and F. Zhang, 2016: Intrinsic versus Practical Limits of Atmospheric Predictability and the Significance of the Butterfly Effect. *Journal of the Atmospheric Sciences*, **73 (3)**, 1419–1438, doi: 10.1175/JAS-D-15-0142.1.

Takayabu, Y. N., and T. Nitta, 1993: 3-5 Day-Period Disturbances Coupled with Convection over the Tropical Pacific Ocean. *Journal of the Meteorological Society of Japan. Ser. II*, **71 (2)**, 221–246, doi: 10.2151/jmsj1965.71.2_221.

Tan, H., P. Ray, B. S. Barrett, M. Tewari, and M. W. Moncrieff, 2018: Role of topography on the MJO in the maritime continent: a numerical case study. *Climate Dynamics*, **40 (2)**, 6252, doi: 10.1007/s00382-018-4275-3.

Taubenheim, J., 1974: Zur Berücksichtigung der Autokorrelation bei der statistischen Signifikanzprüfung von Korrelation zwischen zwei Zeitreihen. *Gerlands Beiträge zur Geophysik*, **83 (2)**, 121–128.

Taye, A., D. H. Mariam, and V. Murray, 2010: Interim report: review of evidence of the health impact of famine in Ethiopia. *Perspectives in public health*, **130 (5)**, 222–226, doi: 10.1177/1757913910379197.

Taylor, C. M., 2008: Intraseasonal Land–Atmosphere Coupling in the West African Monsoon. *Journal of Climate*, **21 (24)**, 6636–6648, doi: 10.1175/ 2008JCLI2475.1.

Taylor, C. M., and Coauthors, 2011: New perspectives on land-atmosphere feedbacks from the African Monsoon Multidisciplinary Analysis. *Atmospheric Science Letters*, **12 (1)**, 38–44, doi: 10.1002/asl.336.

Thiawa, W. M., S. Janicot, K. H. Cook, B. Fontaine, A. Mekonnen, O. Ndiaye, Tamo, Pierre-Honoré, K., and E. K. Vizy, 2017: Subseasonal Forecasting. *Meteorology of Tropical West Africa*, D. J. Parker, and M. Diop-Kane, Eds., John Wiley & Sons, Ltd, ISBN: 9781118391297, Chichester, UK, 255–288, doi: 10.1002/9781118391297.ch7.

Thiawa, W. M., and V. B. Kumar, 2015: NOAA's African Desk: Twenty Years of Developing Capacity in Weather and Climate Forecasting in Africa. *Bulletin of the American Meteorological Society*, **96 (5)**, 737–753, doi: 10.1175/BAMS-D-13-00274.1.

Thompson, D. W. J., and J. M. Wallace, 1998: The Arctic oscillation signature in the wintertime geopotential height and temperature fields. *Geophysical Research Letters*, **25 (9)**, 1297–1300, doi: 10.1029/98GL00950.

Thomson, M. C., and S. J. Connor, 2001: The development of Malaria Early Warning Systems for Africa. *Trends in Parasitology*, **17 (9)**, 438–445, doi: 10.1016/S1471-4922(01)02077-3.

Thomson, W., 1880: On Gravitational Oscillations of Rotating Water. *Proceedings of the Royal Society of Edinburgh*, **10**, 92–100, doi: 10.1017/S0370164600043467.

Thorncroft, C. D., N. M. J. Hall, and G. N. Kiladis, 2008: Three-Dimensional Structure and Dynamics of African Easterly Waves. Part III: Genesis. *Journal of the Atmospheric Sciences*, **65 (11)**, 3596–3607, doi: 10.1175/2008JAS2575.1.

Thorncroft, C. D., and B. J. Hoskins, 1994: An idealized study of African easterly waves. I: A linear view. *Quarterly Journal of the Royal Meteorological Society*, **120 (518)**, 953–982, doi: 10.1002/qj.49712051809.

Thorncroft, C. D., H. Nguyen, C. Zhang, and P. Peyrillé, 2011: Annual cycle of the West African monsoon: Regional circulations and associated water vapour transport. *Quarterly Journal of the Royal Meteorological Society*, **137 (654)**, 129–147, doi: 10.1002/qj.728.

Tian, B., D. E. Waliser, E. J. Fetzer, B. H. Lambrigtsen, Y. L. Yung, and B. Wang, 2006: Vertical Moist Thermodynamic Structure and Spatial–Temporal Evolution of the MJO in AIRS Observations. *Journal of the Atmospheric Sciences*, **63 (10)**, 2462–2485, doi: 10.1175/JAS3782.1.

Tilman, D., and A. El Haddi, 1992: Drought and biodiversity in Grasslands. *Oecologia*, **89 (2)**, 257–264, doi: 10.1007/BF00317226.

Tindall, J. C., J. Thuburn, and E. J. Highwood, 2006a: Equatorial waves in the lower stratosphere. I: A novel detection method. *Quarterly Journal of the Royal Meteorological Society*, **132 (614)**, 177–194, doi: 10.1256/qj.04.152.

Tindall, J. C., J. Thuburn, and E. J. Highwood, 2006b: Equatorial waves in the lower stratosphere. II: Annual and interannual variability. *Quarterly Journal of the Royal Meteorological Society*, **132 (614)**, 195–212, doi: 10.1256/qj.04.153.

Todd, M. C., and R. Washington, 1999: Circulation anomalies associated with tropical-temperate troughs in southern Africa and the south west Indian Ocean. *Climate Dynamics*, **15 (12)**, 937–951, doi: 10.1007/s003820050323.

Todd, M. C., R. Washington, and P. I. Palmer, 2004: Water vapour transport associated with tropical–temperate trough systems over southern Africa and the southwest Indian Ocean. *International Journal of Climatology*, **24 (5)**, 555–568, doi: 10.1002/joc.1023.

Tseng, K.-C., E. A. Barnes, and E. D. Maloney, 2018: Prediction of the Midlatitude Response to Strong Madden-Julian Oscillation Events on S2S Time Scales. *Geophysical Research Letters*, **45 (1)**, 463–470, doi: 10.1002/2017GL075734.

Tseng, W.-L., H.-H. Hsu, N. Keenlyside, C.-W. June Chang, B.-J. Tsuang, C.-Y. Tu, and L.-C. Jiang, 2017: Effects of Surface Orography and Land–Sea Contrast on the Madden–Julian Oscillation in the Maritime Continent: A Numerical Study Using ECHAM5-SIT. *Journal of Climate*, **30 (23)**, 9725–9741, doi: 10.1175/JCLI-D-17-0051.1.

Tulich, S. N., and G. N. Kiladis, 2012: Squall Lines and Convectively Coupled Gravity Waves in the Tropics: Why Do Most Cloud Systems Propagate Westward? *Journal of the Atmospheric Sciences*, **69 (10)**, 2995–3012, doi: 10.1175/JAS-D-11-0297.1.

van der Linden, R., A. H. Fink, J. G. Pinto, T. Phan-Van, and G. N. Kiladis, 2016: Modulation of Daily Rainfall in Southern Vietnam by the Madden–Julian Oscillation and Convectively Coupled Equatorial Waves. *Journal of Climate*, **29 (16)**, 5801–5820, doi: 10.1175/JCLI-D-15-0911.1.

Vellinga, M., A. Arribas, and R. Graham, 2013: Seasonal forecasts for regional onset of the West African monsoon. *Climate Dynamics*, **40 (11-12)**, 3047–3070, doi: 10.1007/s00382-012-1520-z.

Ventrice, M. J., and C. D. Thorncroft, 2013: The Role of Convectively Coupled Atmospheric Kelvin Waves on African Easterly Wave Activity. *Monthly Weather Review*, **141 (6)**, 1910–1924, doi: 10.1175/MWR-D-12-00147.1.

Ventrice, M. J., C. D. Thorncroft, and P. E. Roundy, 2011: The Madden–Julian Oscillation's Influence on African Easterly Waves and Downstream Tropical Cyclogenesis. *Monthly Weather Review*, **139 (9)**, 2704–2722, doi: 10.1175/ MWR-D-10-05028.1.

Verdin, J., C. Funk, G. Senay, and R. Choularton, 2005: Climate science and famine early warning. *Philosophical transactions of the Royal Society of London. Series B, Biological sciences*, **360 (1463)**, 2155–2168, doi: 10.1098/rstb.2005.1754.

Vicente-Serrano, S. M., and Coauthors, 2012: Challenges for drought mitigation in Africa: The potential use of geospatial data and drought information systems. *Applied Geography*, **34**, 471–486, doi: 10.1016/j.apgeog.2012.02.001.

Vigaud, N., and A. Giannini, 2018: West African convection regimes and their predictability from submonthly forecasts. *Climate Dynamics*, **5**, 14, doi: 10. 1007/s00382-018-4563-y.

Vigaud, N., B. Pohl, and J. Crétat, 2012: Tropical-temperate interactions over southern Africa simulated by a regional climate model. *Climate Dynamics*, **39 (12)**, 2895–2916, doi: 10.1007/s00382-012-1314-3.

Vitart, F., and A. W. Robertson, 2018: The sub-seasonal to seasonal prediction project (S2S) and the prediction of extreme events. *npj Climate and Atmospheric Science*, **1 (1)**, 3549, doi: 10.1038/s41612-018-0013-0.

Vitart, F., S. J. Woolnough, M. A. Balmaseda, and A. M. Tompkins, 2007: Monthly Forecast of the Madden–Julian Oscillation Using a Coupled GCM. *Monthly Weather Review*, **135 (7)**, 2700–2715, doi: 10.1175/MWR3415.1.

Vizy, E. K., and K. H. Cook, 2009: A mechanism for African monsoon breaks: Mediterranean cold air surges. *Journal of Geophysical Research*, **114 (D1)**, doi: 10.1029/2008JD010654.

Vizy, E. K., and K. H. Cook, 2014: Impact of cold air surges on rainfall variability in the Sahel and wet African tropics: a multi-scale analysis. *Climate Dynamics*, **43 (3)**, 1057–1081, doi: 10.1007/s00382-013-1953-z.

Vogel, P., 2019: Assessing Predictive Performance: From Precipitation Forecasts over the Tropics to Receiver Operating Characteristic Curves and Back. PhD thesis, Karlsruhe Institute of Technology, Karlsruhe, doi: 10.5445/IR/ 1000091649.

Vogel, P., P. Knippertz, A. H. Fink, A. Schlueter, and T. Gneiting, 2018: Skill of Global Raw and Postprocessed Ensemble Predictions of Rainfall over Northern Tropical Africa. *Weather and Forecasting*, **33 (2)**, 369–388, doi: 10.1175/ WAF-D-17-0127.1.

Waliser, D. E., K.-M. Lau, W. Stern, and C. Jones, 2003: Potential Predictability of the Madden–Julian Oscillation. *Bulletin of the American Meteorological Society*, **84 (1)**, 33–50, doi: 10.1175/BAMS-84-1-33.

Walker, G., and E. Bliss, 1932: World weather V. *Royal Meteorological Socieaty*, **36 (4)**, 53–84.

Wallace, J. M., and D. S. Gutzler, 1981: Teleconnections in the Geopotential Height Field during the Northern Hemisphere Winter. *Monthly Weather Review*, **109 (4)**, 784–812, doi: 10.1175/1520-0493(1981)109<0784:TITGHF>2.0.CO;2.

Wang, B., and T. Li, 1994: Convective Interaction with Boundary-Layer Dynamics in the Development of a Tropical Intraseasonal System. *Journal of the Atmospheric Sciences*, **51 (11)**, 1386–1400, doi: 10.1175/1520-0469(1994) 051<1386:CIWBLD>2.0.CO;2.

Wang, B., and H. Rui, 1990: Dynamics of the Coupled Moist Kelvin–Rossby Wave on an Equatorial Beta-Plane. *Journal of the Atmospheric Sciences*, **47 (4)**, 397– 413, doi: 10.1175/1520-0469(1990)047<0397:DOTCMK>2.0.CO;2.

Wang, C., C. Deser, J.-Y. Yu, P. DiNezio, and A. Clement, 2017: El Niño and Southern Oscillation (ENSO): A Review. *Coral Reefs of the Eastern Tropical Pacific*, P. W. Glynn, D. P. Manzello, and I. C. Enochs, Eds., Coral Reefs of the World, Vol. 8, Springer Netherlands, Dordrecht, ISBN: 978-94-017-7498-7, 85–106, doi: 10.1007/978-94-017-7499-4_4.

Warren, D. M., 1991: *Using indigenous knowledge in agricultural development*, World Bank discussion papers, Vol. 127. 1st ed., World Bank, Washington, DC, ISBN: 0821318845.

Washington, R., and M. C. Todd, 1999: Tropical-temperate links in southern African and Southwest Indian Ocean satellite-derived daily rainfall. *Interna-*

tional Journal of Climatology, **19 (14)**, 1601–1616, doi: 10.1002/(SICI)1097-0088(19991130)19:14<1601::AID-JOC407>3.0.CO;2-0.

Webster, P. J., and J. R. Holton, 1982: Cross-Equatorial Response to Middle-Latitude Forcing in a Zonally Varying Basic State. *Journal of the Atmospheric Sciences*, **39 (4)**, 722–733, doi: 10.1175/1520-0469(1982)039<0722:CERTML>2.0.CO;2.

Weickmann, K. M., G. R. Lussky, and J. E. Kutzbach, 1985: Intraseasonal (30–60 Day) Fluctuations of Outgoing Longwave Radiation and 250 mb Streamfunction during Northern Winter. *Monthly Weather Review*, **113 (6)**, 941–961, doi: 10.1175/1520-0493(1985)113<0941:IDFOOL>2.0.CO;2.

Wheeler, M., G. N. Kiladis, and P. J. Webster, 2000: Large-Scale Dynamical Fields Associated with Convectively Coupled Equatorial Waves. *Journal of the Atmospheric Sciences*, **57 (5)**, 613–640, doi: 10.1175/1520-0469(2000)057<0613:LSDFAW>2.0.CO;2.

Wheeler, M. C., and H. H. Hendon, 2004: An All-Season Real-Time Multivariate MJO Index: Development of an Index for Monitoring and Prediction. *Monthly Weather Review*, **132 (8)**, 1917–1932, doi: 10.1175/1520-0493(2004)132<1917:AARMMI>2.0.CO;2.

Wheeler, M. C., and G. N. Kiladis, 1999: Convectively Coupled Equatorial Waves: Analysis of Clouds and Temperature in the Wavenumber–Frequency Domain. *Journal of the Atmospheric Sciences*, **56 (3)**, 374–399, doi: 10.1175/1520-0469(1999)056<0374:CCEWAO>2.0.CO;2.

Wheeler, M. C., and H. Nguyen, 2015: Tropical Meteorology: Equatorial Waves. *Encyclopedia of atmospheric sciences*, G. R. North, Ed., Elsevier Acad. Press, Amsterdam, ISBN: 9780123822253, 102–112.

Wheeler, M. C., and K. M. Weickmann, 2001: Real-Time Monitoring and Prediction of Modes of Coherent Synoptic to Intraseasonal Tropical Variability. *Monthly Weather Review*, **129 (11)**, 2677–2694, doi: 10.1175/1520-0493(2001)129<2677:RTMAPO>2.0.CO;2.

White, C. J., and Coauthors, 2017: Potential applications of subseasonal-to-seasonal (S2S) predictions. *Meteorological Applications*, **24 (3)**, 315–325, doi: 10.1002/met.1654.

Williams, C. J. R., D. R. Kniveton, and R. Layberry, 2007: Climatic and oceanic associations with daily rainfall extremes over Southern Africa. *International Journal of Climatology*, **27 (1)**, 93–108, doi: 10.1002/joc.1376.

Williams, P. D., T. W. N. Haine, and P. L. Read, 2008: Inertia–Gravity Waves Emitted from Balanced Flow: Observations, Properties, and Consequences. *Journal of the Atmospheric Sciences*, **65 (11)**, 3543–3556, doi: 10.1175/ 2008JAS2480.1.

Wirth, V., M. Riemer, E. K. M. Chang, and O. Martius, 2018: Rossby Wave Packets on the Midlatitude Waveguide—A Review. *Monthly Weather Review*, **146 (7)**, 1965–2001, doi: 10.1175/MWR-D-16-0483.1.

World Bank, 2019: Poverty and Equity Data Portal (accessed 25 March 2019). Rome, Italy, URL http://povertydata.worldbank.org.

Yanai, M., and T. Maruyama, 1966: Stratospheric Wave Disturbances Propagating over the Equatorial Pacific. *Journal of the Meteorological Society of Japan. Ser. II*, **44 (5)**, 291–294, doi: 10.2151/jmsj1965.44.5_291.

Yanai, M., and M. Murakami, 1970: A Further Study of Tropical Wave Disturbances by the Use of Spectrum Analysis. *Journal of the Meteorological Society of Japan. Ser. II*, **48 (3)**, 185–197, doi: 10.2151/jmsj1965.48.3_185.

Yang, G.-Y., B. Hoskins, and J. Slingo, 2007a: Convectively Coupled Equatorial Waves. Part II: Propagation Characteristics. *Journal of the Atmospheric Sciences*, **64 (10)**, 3424–3437, doi: 10.1175/JAS4018.1.

Yang, G.-Y., and B. J. Hoskins, 2017: The Equivalent Barotropic Structure of Waves in the Tropical Atmosphere in the Western Hemisphere. *Journal of the Atmospheric Sciences*, **74 (6)**, 1689–1704, doi: 10.1175/JAS-D-16-0267.1.

Yang, G.-Y., B. J. Hoskins, and J. M. Slingo, 2003: Convectively Coupled Equatorial Waves: A New Methodology for Identifying Wave Structures in Observational Data. *Journal of the Atmospheric Sciences*, **60 (14)**, 1637–1654, doi: 10.1175/1520-0469(2003)060<1637:CCEWAN>2.0.CO;2.

Yang, G.-Y., B. J. Hoskins, and J. M. Slingo, 2007b: Convectively Coupled Equatorial Waves. Part I: Horizontal and Vertical Structures. *Journal of the Atmospheric Sciences*, **64 (10)**, 3406–3423, doi: 10.1175/JAS4017.1.

Yang, G.-Y., J. Methven, S. J. Woolnough, K. I. Hodges, and B. J. Hoskins, 2018: Linking African Easterly Wave Activity with Equatorial Waves and the Influence of Rossby Waves from the Southern Hemisphere. *Journal of the Atmospheric Sciences*, **75 (6)**, 1783–1809, doi: 10.1175/JAS-D-17-0184.1.

Yasunaga, K., and B. E. Mapes, 2012: Differences between More Divergent and More Rotational Types of Convectively Coupled Equatorial Waves. Part II: Composite Analysis based on Space–Time Filtering. *Journal of the Atmospheric Sciences*, **69 (1)**, 17–34, doi: 10.1175/JAS-D-11-034.1.

Yasunari, T., 1979: Cloudiness Fluctuations Associated with the Northern Hemisphere Summer Monsoon. *Journal of the Meteorological Society of Japan. Ser. II*, **57 (3)**, 227–242, doi: 10.2151/jmsj1965.57.3_227.

Ying, Y., and F. Zhang, 2017: Practical and Intrinsic Predictability of Multiscale Weather and Convectively Coupled Equatorial Waves during the Active Phase of an MJO. *Journal of the Atmospheric Sciences*, **74 (11)**, 3771–3785, doi: 10.1175/JAS-D-17-0157.1.

Žagar, N., 2012: Multivariate Data Assimilation in the Tropics by Using Equatorial Waves. *Pure and Applied Geophysics*, **169 (3)**, 367–379, doi: 10.1007/s00024-011-0375-2.

Žagar, N., 2017: A global perspective of the limits of prediction skill of NWP models. *Tellus A: Dynamic Meteorology and Oceanography*, **69 (1)**, 1317 573, doi: 10.1080/16000870.2017.1317573.

Žagar, N., E. Andersson, and M. Fisher, 2005: Balanced tropical data assimilation based on a study of equatorial waves in ECMWF short-range forecast errors. *Quarterly Journal of the Royal Meteorological Society*, **131 (607)**, 987–1011, doi: 10.1256/qj.04.54.

Žagar, N., M. Blaauw, B. Jesenko, and L. Magnusson, 2016: Diagnosing model performance in the tropics. *ECMWF Newsletter*, **(147)**, 26–33.

Žagar, N., and C. L. E. Franzke, 2015: Systematic decomposition of the Madden-Julian Oscillation into balanced and inertio-gravity components. *Geophysical Research Letters*, **42 (16)**, 6829–6835, doi: 10.1002/2015GL065130.

Žagar, N., D. Jelić, M. Blaauw, and P. Bechtold, 2017: Energy Spectra and Inertia–Gravity Waves in Global Analyses. *Journal of the Atmospheric Sciences*, **74 (8)**, 2447–2466, doi: 10.1175/JAS-D-16-0341.1.

Žagar, N., A. Kasahara, K. Terasaki, J. Tribbia, and H. Tanaka, 2015: Normal-mode function representation of global 3-D data sets: open-access software for the atmospheric research community. *Geoscientific Model Development*, **8 (4)**, 1169–1195, doi: 10.5194/gmd-8-1169-2015.

Žagar, N., J. Tribbia, J. L. Anderson, and K. Raeder, 2009: Uncertainties of Estimates of Inertia–Gravity Energy in the Atmosphere. Part I: Intercomparison of Four Analysis Systems. *Monthly Weather Review*, **137 (11)**, 3837–3857, doi: 10.1175/2009MWR2815.1.

Zaitchik, B. F., 2017: Madden-Julian Oscillation impacts on tropical African precipitation. *Atmospheric Research*, **184**, 88–102, doi: 10.1016/j.atmosres.2016.10.002.

Zhang, C., 2005: Madden-Julian Oscillation. *Reviews of Geophysics*, **43 (2)**, 676, doi: 10.1029/2004RG000158.

Zhang, C., 2013: Madden–Julian Oscillation: Bridging Weather and Climate. *Bulletin of the American Meteorological Society*, **94 (12)**, 1849–1870, doi: 10.1175/BAMS-D-12-00026.1.

Zhou, G., N. Minakawa, A. K. Githeko, and G. Yan, 2004: Association between climate variability and malaria epidemics in the East African highlands. *Proceedings of the National Academy of Sciences*, **101 (8)**, 2375–2380, doi: 10.1073/pnas.0308714100.

Zhou, S., and A. J. Miller, 2005: The Interaction of the Madden–Julian Oscillation and the Arctic Oscillation. *Journal of Climate*, **18 (1)**, 143–159, doi: 10.1175/JCLI3251.1.

Zhou, X., and B. Wang, 2007: Transition from an eastern Pacific upper-level mixed Rossby-gravity wave to a western Pacific tropical cyclone. *Geophysical Research Letters*, **34 (24)**, 2837, doi: 10.1029/2007GL031831.

Zipser, E. J., 1977: Mesoscale and Convective–Scale Downdrafts as Distinct Components of Squall-Line Structure. *Monthly Weather Review*, **105 (12)**, 1568–1589, doi: 10.1175/1520-0493(1977)105<1568:MACDAD>2.0.CO;2.

Acknowledgments

Above all, I thank God, my creator, for his unconditional love through Jesus Christ, which empowered and encouraged me throughout the entire dissertation. Everything I am and have comes from him.

I would like to express my sincere gratitude to my advisors Peter Knippertz and Andreas H. Fink for the continuous support during my PhD study, for their patience, motivation, enthusiastic encouragement and useful critiques. Their guidance helped me in all the time of research and writing of this thesis.

I am particularly grateful to my colleagues Michael Maier-Gerber, Marlon Maranan, Philipp Zschenderlein, and Florian Pantillon for the vivid and helpful discussions about weather dynamics, tropical meteorology, rainfall variability over Africa, and programming. Moreover, I thank Peter Vogel, Tilmann Gneiting, Manuel Klar, and Sebastian Lerch for the helpful discussions and comments during the regular project meetings, the joint work on statistical forecasting, and help with mathematical questions. I also thank Roderick van der Linden for providing code that was further developed to filter the waves and create the composite plots. I appreciate Michael Riemer, Volkmar Wirth and the rest of the Waves to Weather community for the helpful conversations during several meetings. Thanks also to Robert Redl, Benedikt Heyl, and Niklas Tönsing for creating the IGRA2reader package and for the help with the development of the SERAF website. I wish to acknowledge the helpful discussions with various colleagues during the research stay in the USA, including George Kiladis, Juliana Dias, Eric Maloney, Paul Roundy, Ryan Torn, Brian Mapes, and Yuan-Ming Cheng.

Finally, I thank most heartily my parents for their caring love, my siblings for being marvelous brothers and sisters and my wonderful wife for her exceeding cordial support and love.